Topics in Applied Physics 141

Kaoru Yamanouchi
Katsumi Midorikawa
Luis Roso *Editors*

Progress in Ultrafast Intense Laser Science XVI

Springer

Topics in Applied Physics

Volume 141

Topics in Applied Physics is a well-established series of review books, each of which presents a comprehensive survey of a selected topic within the domain of applied physics. Since 1973 it has served a broad readership across academia and industry, providing both newcomers and seasoned scholars easy but comprehensive access to the state of the art of a number of diverse research topics.

Edited and written by leading international scientists, each volume contains high-quality review contributions, extending from an introduction to the subject right up to the frontiers of contemporary research.

Topics in Applied Physics strives to provide its readership with a diverse and interdisciplinary collection of some of the most current topics across the full spectrum of applied physics research, including but not limited to:

- Quantum computation and information
- Photonics, optoelectronics and device physics
- Nanoscale science and technology
- Ultrafast physics
- Microscopy and advanced imaging
- Biomaterials and biophysics
- Liquids and soft matter
- Materials for energy
- Geophysics
- Computational physics and numerical methods
- Interdisciplinary physics and engineering

We welcome any suggestions for topics coming from the community of applied physicists, no matter what the field, and encourage prospective book editors to approach us with ideas. Potential authors who wish to submit a book proposal should contact Zach Evenson, Publishing Editor:

zachary.evenson@springer.com

Topics in Applied Physics is included in Web of Science (2020 Impact Factor: 0.643), and is indexed by Scopus

More information about this series at http://www.springer.com/series/560

Kaoru Yamanouchi · Katsumi Midorikawa ·
Luis Roso
Editors

Progress in Ultrafast Intense Laser Science XVI

Springer

Editors
Kaoru Yamanouchi
Department of Chemistry
School of Science, The University of Tokyo
Tokyo, Japan

Katsumi Midorikawa
Center for Advanced Photonics
RIKEN, Wako, Saitama, Japan

Luis Roso
Centro de Laseres Pulsados
Vega de Salamanca, Salamanca, Spain

ISSN 0303-4216 ISSN 1437-0859 (electronic)
Topics in Applied Physics
ISBN 978-3-030-75088-6 ISBN 978-3-030-75089-3 (eBook)
https://doi.org/10.1007/978-3-030-75089-3

This Springer imprint is published by the registered company Springer Nature Switzerland AG
The registered company address is: Gewerbestrasse 11, 6330 Cham, Switzerland

Preface

We are pleased to present the sixteenth volume of Progress in Ultrafast Intense Laser Science. As the frontiers of ultrafast intense laser science rapidly expand ever outward, there continues to be a growing demand for an introduction to this interdisciplinary research field that is at once widely accessible and capable of delivering cutting-edge developments. Our series aims to respond to this call by providing a compilation of concise review-style articles written by researchers at the forefront of this research field, so that researchers with different backgrounds as well as graduate students can easily grasp the essential aspects.

As in the previous volumes, each chapter of this book begins with an introductory part, in which a clear and concise overview of the topic and its significance is given, and moves onto a description of the authors' most recent research results. All chapters are peer-reviewed. The articles of this sixteenth volume cover a diverse range of the interdisciplinary research field, and the topics may be grouped into three categories: atoms and molecules in intense laser fields (Chaps. 1– 5), applications of circularly polarized laser pulses (Chaps. 6 and 7), and theoretical and technological developments for intense laser field experiments (Chaps. 8– 10).

From the third volume, the PUILS series has been edited in liaison with the activities of the Center for Ultrafast Intense Laser Science at the University of Tokyo, which has also been responsible for sponsoring the series and making the regular publication of its volumes possible. From the fifth volume, the Consortium on Education and Research on Advanced Laser Science, the University of Tokyo, has joined this publication activity as one of the sponsoring programs. The series, designed to stimulate interdisciplinary discussion at the forefront of ultrafast intense laser science, has also collaborated since its inception with the annual symposium series of ISUILS (http://www.isuils.jp/), sponsored by JILS (Japan Intense Light Field Science Society).

We would like to take this opportunity to thank all the authors who have kindly contributed to the PUILS series by describing their most recent work at the frontiers of ultrafast intense laser science. We also thank the reviewers who have read the submitted manuscripts carefully. One of the co-editors (KY) thanks Ms. Mihoshi Abe for her help with the editing processes.

We hope this volume will convey the excitement of ultrafast intense laser science to the readers and stimulate interdisciplinary interactions among researchers, thus paving the way to explorations of new frontiers.

Tokyo, Japan — Kaoru Yamanouchi
Saitama, Japan — Katsumi Midorikawa
Salamanca, Spain — Luis Roso
January 2021

Contents

Contributors

Hiroshi Akagi Kansai Photon Science Institute, National Institutes for Quantum and Radiological Science and Technology (QST), Kyoto, Japan

Toshiaki Ando Department of Chemistry, School of Science, The University of Tokyo, Tokyo, Japan

André D. Bandrauk Computational Chemistry & Molecular Photonics, Faculté des Sciences, Université de Sherbrooke,Laboratoire de Chimie Théorique, Sherbrooke, Canada

Junchi Chen State Key Laboratory of High Field Laser Physics and CAS Center for Excellence in Ultra-Intense Laser Science, Shanghai Institute of Optics and Fine Mechanics(SIOM), Chinese Academy of Sciences(CAS), Shanghai, China

Lingru Chen State Key Laboratory of High Field Laser Physics and CAS Center for Excellence in Ultra-Intense Laser Science, Shanghai Institute of Optics and Fine Mechanics(SIOM), Chinese Academy of Sciences(CAS), Shanghai, China

Farhad H. M. Faisal Fakultät Für Physik, Universität Bielefeld, Bielefeld, Germany

Robert Fedosejevs Electrical and Computer Engineering, University of Alberta, Edmonton, AB, Canada

Yao Fu State Key Laboratory of Integrated Optoelectronics, College of Electronic Science and Engineering, Jilin University, Changchun, China

Zebiao Gan State Key Laboratory of High Field Laser Physics and CAS Center for Excellence in Ultra-Intense Laser Science, Shanghai Institute of Optics and Fine Mechanics(SIOM), Chinese Academy of Sciences(CAS), Shanghai, China

Jing Guo Institute of Atomic and Molecular Physics, Jilin University, Changchun, China

Eisuke Haraguchi Department of Applied Physics, Hokkaido University, Sapporo, Japan

Feng He Key Laboratory for Laser Plasmas (Ministry of Education) and School of Physics and Astronomy, Collaborative Innovation Center for IFSA (CICIFSA), Shanghai Jiao Tong University, Shanghai, China;
CAS Center for Excellence in Ultra-intense Laser Science, Shanghai, China

Pei-Lun He Key Laboratory for Laser Plasmas (Ministry of Education), School of Physics and Astronomy, Shanghai, China;
Collaborative Innovation Center for IFSA (CICIFSA), Shanghai Jiao Tong University, Shanghai, China

Ryuji Itakura Kansai Photon Science Institute, National Institutes for Quantum and Radiological Science and Technology (QST), Kyoto, Japan

Kengo Ito Department of Applied Physics, Hokkaido University, Sapporo, Japan

Atsushi Iwasaki Department of Chemistry, School of Science, The University of Tokyo, Tokyo, Japan

Keisuke Kaneshima Department of Applied Physics, Hokkaido University, Sapporo, Japan

Tsuyoshi Kato Department of Chemistry, School of Science, The University of Tokyo, Tokyo, Japan

Toshiyuki Kawashima Central Research Laboratory, Industrial Development Center, Hamamatsu Photonics K.K., Hamamatsu City, Shizuoka, Japan

Yosuke Kayanuma Laboratory for Materials and Structures, Tokyo Institute of Technology, Nagatsuta, Yokohama, Japan;
Department of Physical Sciences, Osaka Prefecture University, Sakai, Osaka, Japan

Hirohiko Kono Department of Chemistry, Graduate School of Science, Tohoku University, Sendai, Japan

Shiro Koseki Department of Chemistry, Graduate School of Science, Osaka Prefecture University, Osaka, Japan

Norio Kurita Central Research Laboratory, Industrial Development Center, Hamamatsu Photonics K.K., Hamamatsu City, Shizuoka, Japan

Yuxin Leng State Key Laboratory of High Field Laser Physics and CAS Center for Excellence in Ultra-Intense Laser Science, Shanghai Institute of Optics and Fine Mechanics(SIOM), Chinese Academy of Sciences(CAS), Shanghai, China

Roberto Lera Center for Pulsed Lasers, CLPU, Villamayor, Salamanca, Spain

Helong Li State Key Laboratory of Integrated Optoelectronics, College of Electronic Science and Engineering, Jilin University, Changchun, China

Ruxin Li State Key Laboratory of High Field Laser Physics and CAS Center for Excellence in Ultra-Intense Laser Science, Shanghai Institute of Optics and Fine Mechanics(SIOM), Chinese Academy of Sciences(CAS), Shanghai, China

Shuai Li State Key Laboratory of High Field Laser Physics and CAS Center for Excellence in Ultra-Intense Laser Science, Shanghai Institute of Optics and Fine Mechanics(SIOM), Chinese Academy of Sciences(CAS), Shanghai, China

Wenqi Li State Key Laboratory of High Field Laser Physics and CAS Center for Excellence in Ultra-Intense Laser Science, Shanghai Institute of Optics and Fine Mechanics(SIOM), Chinese Academy of Sciences(CAS), Shanghai, China

Xiaoyan Liang State Key Laboratory of High Field Laser Physics and CAS Center for Excellence in Ultra-Intense Laser Science, Shanghai Institute of Optics and Fine Mechanics(SIOM), Chinese Academy of Sciences(CAS), Shanghai, China

Xinyan Liu State Key Laboratory of High Field Laser Physics and CAS Center for Excellence in Ultra-Intense Laser Science, Shanghai Institute of Optics and Fine Mechanics(SIOM), Chinese Academy of Sciences(CAS), Shanghai, China

Yanqi Liu State Key Laboratory of High Field Laser Physics and CAS Center for Excellence in Ultra-Intense Laser Science, Shanghai Institute of Optics and Fine Mechanics(SIOM), Chinese Academy of Sciences(CAS), Shanghai, China

Erik Lötstedt Department of Chemistry, School of Science, The University of Tokyo, Tokyo, Japan

Hideki Ohmura National Institute of Advanced Industrial Science and Technology (AIST), Tsukuba, Ibaraki, Japan

Shu Ohmura Department of Physical Science and Engineering, Nagoya Institute of Technology, Nagoya, Japan

Tomohito Otobe Kansai Photon Science Institute, National Institutes for Quantum and Radiological Science and Technology (QST), Kyoto, Japan

Yujie Peng State Key Laboratory of High Field Laser Physics and CAS Center for Excellence in Ultra-Intense Laser Science, Shanghai Institute of Optics and Fine Mechanics(SIOM), Chinese Academy of Sciences(CAS), Shanghai, China

José Antonio Pérez-Hernández Center for Pulsed Lasers, CLPU, Villamayor, Salamanca, Spain

Luis Roso Center for Pulsed Lasers, CLPU, Villamayor, Salamanca, Spain; Applied Physics Department, Universidad de Salamanca, Salamanca, Spain

Taro Sekikawa Department of Applied Physics, Hokkaido University, Sapporo, Japan

Takashi Sekine Central Research Laboratory, Industrial Development Center, Hamamatsu Photonics K.K., Hamamatsu City, Shizuoka, Japan

Yunhai Tang State Key Laboratory of High Field Laser Physics and CAS Center for Excellence in Ultra-Intense Laser Science, Shanghai Institute of Optics and Fine Mechanics(SIOM), Chinese Academy of Sciences(CAS), Shanghai, China

Cheng Wang State Key Laboratory of High Field Laser Physics and CAS Center for Excellence in Ultra-Intense Laser Science, Shanghai Institute of Optics and Fine Mechanics(SIOM), Chinese Academy of Sciences(CAS), Shanghai, China

Siqi Wang State Key Laboratory of Integrated Optoelectronics, College of Electronic Science and Engineering, Jilin University, Changchun, China

Xiaobin Wang State Key Laboratory of High Field Laser Physics and CAS Center for Excellence in Ultra-Intense Laser Science, Shanghai Institute of Optics and Fine Mechanics(SIOM), Chinese Academy of Sciences(CAS), Shanghai, China

Xinliang Wang State Key Laboratory of High Field Laser Physics and CAS Center for Excellence in Ultra-Intense Laser Science, Shanghai Institute of Optics and Fine Mechanics(SIOM), Chinese Academy of Sciences(CAS), Shanghai, China

Huailiang Xu State Key Laboratory of Integrated Optoelectronics, College of Electronic Science and Engineering, Jilin University, Changchun, China;
CAS Center for Excellence in Ultra-Intense Laser Science, Shanghai, China

Lu Xu State Key Laboratory of High Field Laser Physics and CAS Center for Excellence in Ultra-Intense Laser Science, Shanghai Institute of Optics and Fine Mechanics(SIOM), Chinese Academy of Sciences(CAS), Shanghai, China

Yi Xu State Key Laboratory of High Field Laser Physics and CAS Center for Excellence in Ultra-Intense Laser Science, Shanghai Institute of Optics and Fine Mechanics(SIOM), Chinese Academy of Sciences(CAS), Shanghai, China

Zhizhan Xu State Key Laboratory of High Field Laser Physics and CAS Center for Excellence in Ultra-Intense Laser Science, Shanghai Institute of Optics and Fine Mechanics(SIOM), Chinese Academy of Sciences(CAS), Shanghai, China

Kaoru Yamanouchi Department of Chemistry, School of Science, The University of Tokyo, Tokyo, Japan

Bo Yao State Key Laboratory of High Field Laser Physics and CAS Center for Excellence in Ultra-Intense Laser Science, Shanghai Institute of Optics and Fine Mechanics(SIOM), Chinese Academy of Sciences(CAS), Shanghai, China

Dinjun Yin State Key Laboratory of High Field Laser Physics and CAS Center for Excellence in Ultra-Intense Laser Science, Shanghai Institute of Optics and Fine Mechanics(SIOM), Chinese Academy of Sciences(CAS), Shanghai, China

Lianghong Yu State Key Laboratory of High Field Laser Physics and CAS Center for Excellence in Ultra-Intense Laser Science, Shanghai Institute of Optics and Fine Mechanics(SIOM), Chinese Academy of Sciences(CAS), Shanghai, China

Linpeng Yu State Key Laboratory of High Field Laser Physics and CAS Center for Excellence in Ultra-Intense Laser Science, Shanghai Institute of Optics and Fine Mechanics(SIOM), Chinese Academy of Sciences(CAS), Shanghai, China

Kai-Jun Yuan Institute of Atomic and Molecular Physics, Jilin University, Changchun, China;
Laboratoire de Chimie Théorique, Faculté des Sciences, Université de Sherbrooke, Québec, Sherbrooke, Canada

Xiaobo Zhang State Key Laboratory of High Field Laser Physics and CAS Center for Excellence in Ultra-Intense Laser Science, Shanghai Institute of Optics and Fine Mechanics(SIOM), Chinese Academy of Sciences(CAS), Shanghai, China

Zhao-Han Zhang Key Laboratory for Laser Plasmas (Ministry of Education), School of Physics and Astronomy, Shanghai, China;
Collaborative Innovation Center for IFSA (CICIFSA), Shanghai Jiao Tong University, Shanghai, China

Chapter 1
Robust Strategies for Affirming Kramers-Henneberger Atoms

Pei-Lun He, Zhao-Han Zhang, and Feng He

Abstract Atoms exposed to high-frequency strong laser fields experience ionization suppression due to the deformation of Kramers-Henneberger (KH) wave functions, which has not been confirmed yet in any experiment. We propose a bichromatic pump-probe strategy to affirm the existence of KH states, which are formed by the pump pulse and ionized by the probe pulse. In the case of the single-photon ionization triggered by a vacuum ultra-violet probe pulse, the double-slit character of the KH atom is mapped to the photoelectron momentum distribution. In the case of the tunneling ionization induced by an infrared probe pulse, streaking in anisotropic Coulomb potential gives rise to the rotation of the photoelectron momentum distribution in the laser polarization plane. Apart from bichromatic schemes, the non-Abelian geometric phase provides an alternative route to affirm the existence of KH states. Following specific loops in laser parameter space, a complete spin flipping transition could be achieved. Our proposal has the advantages of being robust against focal-intensity average as well as ionization depletion and is accessible with current laser facilities.

P.-L. He (✉) · Z.-H. Zhang
Key Laboratory for Laser Plasmas (Ministry of Education), School of Physics and Astronomy, Shanghai, China
e-mail: a225633@sjtu.edu.cn

Z.-H. Zhang
e-mail: zhangzhaohan@sjtu.edu.cn

Collaborative Innovation Center for IFSA (CICIFSA), Shanghai Jiao Tong University, Shanghai 200240, China

F. He
Key Laboratory for Laser Plasmas (Ministry of Education) and School of Physics and Astronomy, Collaborative Innovation Center for IFSA (CICIFSA), Shanghai Jiao Tong University, Shanghai 200240, China
e-mail: fhe@sjtu.edu.cn

CAS Center for Excellence in Ultra-intense Laser Science, Shanghai 201800, China

K. Yamanouchi et al. (eds.), *Progress in Ultrafast Intense Laser Science XVI*,
Topics in Applied Physics 141, https://doi.org/10.1007/978-3-030-75089-3_1

1.1 Introduction

Modern light-matter interaction researches date back to Einstein's explanation of the photoelectric effect, in which ionization happens only if the absorbed photon energy is larger than the binding energy. The advent of laser technologies has boosted light-matter interaction researches into a new era, where novel nonperturbative phenomena are discovered, for example, strong-field tunneling ionization [1], above-threshold ionization [2], high-harmonic generation [3–5], nonsequential double ionization [6], low-energy structures [7, 8], and photoelectron holography [9]. Among these fascinating scenarios, stabilization of atoms in intense laser fields, i.e., the counterintuitive decrease of the ionization probability with the increase of driving laser intensities, attracts the attention of the ultrafast community [10–12]. Two mechanisms are known for ionization stabilization. One is interference stabilization [13, 14], in which the released electron wave packets from populated Rydberg states interfere destructively. The other is adiabatic stabilization, in which the multiphoton ionization is suppressed due to the deformation of Kramers-Henneberger (KH) wave functions [15–18], which are defined to be the eigenstates of a time-averaged Hamiltonian [19].

Though theoretically predicted for decades, the experimental confirmation of adiabatic stabilization is obscure due to ionization depletion and the focal-intensity average of lasers. In real experiments, the fine structure related to the stabilization may be smeared out after integrating all ionized fragments driven by different laser intensities. Furthermore, while the field strength in the focused center reaches the threshold of stabilization, the lower intensity around the focusing spot may completely ionize the target. The target might also be completely ionized before the laser field reaches its peak intensity in the time domain [20]. Up to now, there is only tantalizing indirect experimental evidence [21, 22] for the adiabatic stabilization. For example, in [23], a large acceleration of neutral atoms was reported and regarded as a signal of stabilization [18]. However, this evidence is not convincing enough as frustrated ionization [24], in which the ionized electrons get recaptured by the parent nuclei, has similar output. The ionization stabilization of Rydberg atoms [25] is not convincing evidence since the nonadiabatic coupling [26, 27] in intense fields populates a superposition of Rydberg states thus the ionization suppression might be attributed to the interference stabilization [13].

There are vast researches on adiabatic stabilization [10–12]. However, only a few attempted to directly identify KH states. Popov et al. [28] proposed to affirm the existence of the KH states via the energy shift of the photoelectron [29–31]. Morales et al. identified specific fine structures in photoelectron momentum distribution contributed by excited KH states [32]. Jiang et al. suggested that the photoelectron momentum distribution carrying dynamical interference structures provides information on adiabatic stabilization [33]. However, these proposals are sensitive either to the laser intensity or to the pulse envelope and are not robust against ionization depletion. Thus, the experimental realization is still challenging.

In one of our recent publications, we discussed the possibility of realizing Young's double-slit experiment with a single atom via KH states [34]. Here, we proposed to detect KH states using a bichromatic pump-probe strategy, in which the KH state is formed by the pump pulse and ionized by the probe one. By detecting the photoelectron momentum distribution, one is able to extract the dichotomic structure of the target, and thereby affirm the existence of KH states. The spin flipping for atoms following a loop in the laser parameter space provides an alternative route.

1.2 Models and Methods

1.2.1 Dipole Kramers-Henneberger Transformation

Our start point is the time-dependent Schrödinger equation (TDSE) (atomic units are used throughout unless stated otherwise)

$$i\frac{\partial}{\partial t}\psi(\mathbf{x},t) = H\psi(\mathbf{x},t), \tag{1.1}$$

where $H = \frac{1}{2}\left(\mathbf{p}+\mathbf{A}(t)\right)^2 + V(\mathbf{x})$ for a dipole laser field. The Kramers-Henneberger (KH) transformation [19] provides a comoving frame for a free electron interacting with laser pulse field, which is implemented via a time-dependent translation operator

$$U_d = \exp\left(i\mathbf{p}\cdot\boldsymbol{\beta}(t)\right)\exp\left(-i\int^t d\tau \mathbf{A}^2(\tau)/2\right). \tag{1.2}$$

Define $\psi_{KH} = U_d\psi$, the Hamiltonian transforms into the form

$$H_d^{KH} = \frac{1}{2}\mathbf{p}^2 + V(\mathbf{x}+\boldsymbol{\beta}(t)), \tag{1.3}$$

here $\boldsymbol{\beta}(t) = \int^t d\tau \mathbf{A}(\tau)$ is the displacement of the photoelectron. For a linearly monochromatic plane wave laser field with a frequency ω, the displacement is given by

$$\boldsymbol{\beta} = \boldsymbol{\beta}_0 \sin(\omega t), \tag{1.4}$$

with $\boldsymbol{\beta}_0 = \beta_0\mathbf{e}_x$ and $\beta_0 = \frac{E_0}{\omega^2}$. One can thus expand the potential into Fourier series

$$V(\mathbf{x}+\boldsymbol{\beta}(t)) = \sum V_n(\mathbf{x};\boldsymbol{\beta}_0)e^{-in\omega t}. \tag{1.5}$$

The harmonic component is given by $V_n(\mathbf{x}) = \int_0^{2\pi} d\phi V\left(\mathbf{x}+\boldsymbol{\beta}(\phi)\right)e^{in\phi}/(2\pi)$. Ionization induced by the nonzero component is suppressed with increasing ω [35]. These observations inspire the concept of KH atom, *i.e.*, the atom in a series of

nontrivial metastable states that exist only when in the laser field. KH atom is the eigenstate of the Hamiltonian

$$H_0^{KH} = \frac{1}{2}\mathbf{p}^2 + V_0(\mathbf{x}; \boldsymbol{\beta}_0) \tag{1.6}$$

and is closely related to the ionization stabilization, see Sect. 1.2.3 for more discussions.

1.2.2 Nondipole Kramers-Henneberger Transformation

Before going into the detailed discussion of the KH states, here we study the Kramers-Henneberger transformation in its general form first. Førre et al. [36] generalized the Kramers-Henneberger transformation to include the nondipole effect when the laser pulse is monochromatic. For a complete discussion of the nondipole effect in the nonrelativistic regime, we further consider the case when the laser vector potential is given by the superpositions of propagating waves

$$\mathbf{A}(t, \mathbf{x}) = \sum_a A^a(t_-^a), \tag{1.7}$$

where t_-^a is the light-front time

$$t_-^a = t - \mathbf{x} \cdot \mathbf{n}^a / c \tag{1.8}$$

of the a-th pulse and $\mathbf{n}^a$ is the pulse's propagating direction. We use axial gauge $\mathbf{n}^a \cdot \mathbf{A}^a = 0$. The field decomposition follows from $\mathbf{E} = -\partial_t \mathbf{A} = \sum_a \mathbf{E}^a(t^a)$ and $\mathbf{B} = \nabla \times \mathbf{A} = \sum_a \mathbf{B}^a(t^a)$.

As the time dependent displacement $\boldsymbol{\beta}(t, \mathbf{x}) = \sum_a \int_{-\infty}^{t^a} d\tau_- \mathbf{A}^a(\tau_-^a)$ is spatially dependent, we need to properly order the operator when defining the nonuniform KH transformation as

$$\begin{aligned} U &=: \exp\left(i\boldsymbol{\beta}(t, \mathbf{x}) \cdot \mathbf{p}\right) : \\ &= 1 + i\beta^i p_i + \frac{i^2}{2!}\beta^i \beta^j p_i p_j + \frac{i^3}{3!}\beta^i \beta^j \beta^k p_i p_j p_k \ldots, \end{aligned} \tag{1.9}$$

where the Einstein summation rule is adopted for repeated indices in (1.9).

The commutators between the KH transformation operator U and momentum and position operators are summarized as follows

$$\begin{aligned} [U, \mathbf{x}] &= \boldsymbol{\beta}(t, \mathbf{x}) U \\ \left[U, \mathrm{p}^\mu\right] &= \sum_a \frac{\mathrm{n}^{\mu a}}{c} (\mathfrak{A}^a \cdot \mathbf{p}) U \end{aligned} \tag{1.10}$$

here $\mathrm{n}^{\mu a} = (1, \mathbf{n}^a)$ and $\mathrm{p}^{\mu} = (i\frac{\partial}{c\partial t}, -i\frac{\partial}{\partial \mathbf{x}})$. $\mu = 0$ gives time component and $\mu = 1, 2, 3$ gives the spatial component. $\mathfrak{A}^a$ is defined via series,

$$\begin{aligned}\mathfrak{A}^a(t, \mathbf{x}) = \mathbf{A}^a(t_-^a) &+ \sum_b \mathbf{A}^a(t_-^a)\cdot\mathbf{n}^b\mathbf{A}^b(t_-^b)/c \\ &+ \sum_{b,d} \mathbf{A}^a(t_-^a)\cdot\mathbf{n}^b\mathbf{A}^b(t_-^b)\cdot\mathbf{n}^d\mathbf{A}^d(t_-^d)/c^2 \\ &+ \sum_{b,d,f} \mathbf{A}^a(t_-^a)\cdot\mathbf{n}^b\mathbf{A}^b(t_-^b)\cdot\mathbf{n}^d\mathbf{A}^d(t_-^d)\cdot\mathbf{n}^f\mathbf{A}^f(t_-^f)/c^3 + \cdots\end{aligned} \tag{1.11}$$

When all fields propagate collinearly, $\mathfrak{A}^a$ equals $\mathbf{A}^a$. Let $\psi_{KH} = U\psi$, the equation of motion for ψ_{KH} is given by

$$\begin{aligned} i\frac{\partial}{\partial t}\psi_{KH} &= H_{KH}\psi_{KH} \\ &= H\psi_{KH} + \left[i\frac{\partial}{\partial t} - H, U\right]U^{\dagger}\psi_{KH}. \end{aligned} \tag{1.12}$$

H_{KH} can be calculated by the commutating relations (1.10). Define

$$\mathbf{x}_{KH} = \mathbf{x} + \boldsymbol{\beta}(t, \mathbf{x}), \tag{1.13}$$

the transformed Hamiltonian is

$$\begin{aligned} H_{KH} \approx &\frac{1}{2}(\mathbf{p}^2 + \mathbf{A}(\mathbf{x}_{KH}, t)^2) + V(\mathbf{x}_{KH}) \\ &+ \sum_a \frac{1}{c}\left[(\mathbf{p} + \mathbf{A}(t))\cdot\mathbf{n}^a(\mathbf{A}^a(t)\cdot\mathbf{p}) + \boldsymbol{\beta}(t)\cdot\mathbf{n}^a\mathbf{E}^a(t)\cdot\mathbf{p}\right], \end{aligned} \tag{1.14}$$

here we expand H_{KH} to the order of 1/c,

When the laser field is monochromatic, (1.14) is identical to the results obtained in [36]. New interacting terms $\mathbf{A}(t)\cdot\mathbf{n}^a\mathbf{A}^a(t)\cdot\mathbf{p}$ and $\boldsymbol{\beta}(t)\cdot\mathbf{n}^a\mathbf{E}^a(t)\cdot\mathbf{p}$ appear when there are multi-color non-collinearly propagating lasers. The nice feature of H_{KH} in (1.14) is that there are no coupling between momentum operators and spatial-dependent functions, thus one can use a fast Fourier transformation (fft) based split-operator algorithm to solve the TDSE.

Unfortunately, (1.14) is not suitable for studying nondipole effects when $\boldsymbol{\beta}(t)\cdot\mathbf{n}^a\mathbf{E}^a(t)\cdot\mathbf{p} \neq 0$, as $\boldsymbol{\beta}(t)$ is not always a small quantity. However, this difficulty could be avoided in the electric field gauge [39].

With the gauge transformation $\psi^L = \exp(i\mathbf{x}\cdot\mathbf{A}(t, \mathbf{x}))\,\psi$, the Hamiltonian in the electric field gauge reads

$$H^L = \tfrac{1}{2}\mathbf{p}^2 + V_C(\mathbf{r}) + \mathbf{x}\cdot\mathbf{E} - \textstyle\sum_a \mathbf{x}\cdot\mathbf{E}^a\mathbf{p}\cdot\mathbf{n}^a/c \tag{1.15}$$

Define the time dependent displacement

$$U_{KH}^{L} = \exp\left(\sum_{a} \mathbf{x}\cdot\mathbf{A}^{a}(t)\mathbf{p}\cdot\mathbf{n}^{a}/c\right), \tag{1.16}$$

and

$$\psi_{KH}^{L} = U_{KH}^{L}\psi^{L}, \tag{1.17}$$

we have the transformed Hamiltonian

$$\begin{aligned} H^{L} = {} & \frac{1}{2}\mathbf{p}^{2} + V_{C}\left(\mathbf{r} + 1/c\sum_{a}\mathbf{n}^{a}(\mathbf{x}\cdot\mathbf{A}^{a}(t))\right) + \mathbf{x}\cdot\mathbf{E}(t,\mathbf{x}) \\ & + \frac{1}{c}\sum_{a}\left[(\mathbf{E}(t)\cdot\mathbf{n}^{a})(\mathbf{x}\cdot\mathbf{A}^{a}(t)) - (\mathbf{p}\cdot\mathbf{n}^{a})(\mathbf{p}\cdot\mathbf{A}^{a}(t))\right]. \end{aligned} \tag{1.18}$$

1.2.3 The Kramers-Henneberger States

The KH states are defined to be the eigenstates of the KH Hamiltonian. Generally speaking, they are metastable states in the laser field while their stability increase when the laser frequency increases [35]. Thus, we expect the KH states could play an important role in the high frequency laser field. The dynamical information manifests itself already in (1.5). The adiabatic potential V_0 gets deformed by the laser field, which in turn deforms the bound state, and the nonzero order harmonic terms ionize the KH states. As we will see in Sect. 1.2.4, the above picture is extremely useful when the laser frequencies are high.

If the laser pulse is linearly polarized, V_0 has a dichotomic structure [17, 40]. Figure 1.1a plots V_0 when $\beta_0 = 10$ a.u., from which we see two local minimum located at $\pm\boldsymbol{\beta}_0$. Compared with the laser free case, V_0 is no longer isotropic and has only axial symmetries. As a consequence, the orbital angular momentum number is not conserved and the KH states could be labeled in the same manner as the homonuclear diatomic molecules. Due to the spin-orbital coupling, only the total magnetic moment is conserved. We will discuss the role of the spin-orbital coupling in Sect. 1.3.4 when we deal with the geometric phase.

The potential V_0 depends on the parameter $\boldsymbol{\beta}_0$, which means the KH states and their eigenenergies depend also on $\boldsymbol{\beta}_0$. We plot the eigenenergies of the ground state KH states in Fig. 1.1b. The eigenenergies increase when β_0 increases [29–31].

The adiabatic potential V_0 is dichotomic, so is the wave packet [16], see Fig. 1.1c. The wave function is localized at $\pm\boldsymbol{\beta}_0$ and has similar properties as homonuclear diatomic molecules. Thus, we could have charge resonance enhanced ionization [34, 37, 38] in atoms.

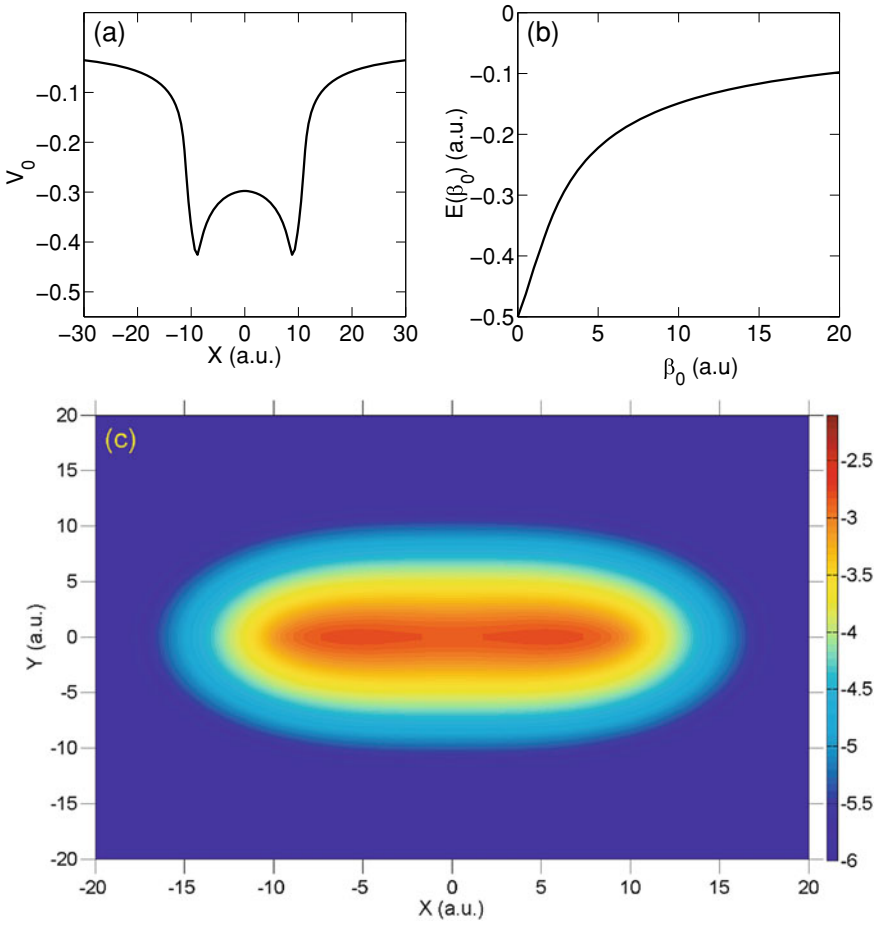

Fig. 1.1 The laser field is linearly polarized along the x-axis. **a** The plot of V_0 when $\beta_0 = 10$ a.u. **b** The eigenenergies of the ground state KH hydrogen atoms as a function of β_0. **c** The probability distribution of the ground state KH atom when $\beta_0 = 10$ a.u.

1.2.4 Dynamics of Kramers-Hennerberger States

In practice, we need to consider the effect of the pulse envelope. Thus, the expression for the displacement in (1.4) is replaced by

$$\boldsymbol{\beta}_0 = \beta_0 f(t)\mathbf{e}_x. \tag{1.19}$$

The corresponding laser field is given by $\mathbf{E}(t) = -\frac{\partial^2}{\partial t^2}\boldsymbol{\beta}$. We use the envelope $f(t) = \cos^2(\pi t/L)$ $(-L/2 < t < L/2)$ throughout this paper, where L stands for the pulse duration. The ground state of (1.1) is obtained using the imaginary time method [41],

and the split-operator method is adopted to propagate the wave function in real time. By Fourier transforming the ionized wave function, we obtained the photoelectron momentum distribution.

Researches on different aspects of high-frequency-laser ionization scatter in references [26, 27, 29, 36, 40, 42–45]. For our purpose here, we summarize the main conclusions with a special emphasis on the role played by KH states. We expanded the oscillating Coulomb potential as $V(\mathbf{x}+\boldsymbol{\beta}) \approx \sum_{\mathrm{n}} V_{\mathrm{n}}(\mathbf{x};\boldsymbol{\beta}_0)e^{-i\mathrm{n}\omega_0 t}$ [46, 47]. $V_0(\mathbf{x};\boldsymbol{\beta}_0)$ is interpreted as a laser-dressed adiabatic potential, while the nonzero harmonic components $V_{\mathrm{n}}(\mathbf{x};\boldsymbol{\beta}_0)$ induce photon absorption/emission. The Hamiltonian in (1.1) can now be regrouped into two parts, i.e., the adiabatic term$H_0 = \frac{\mathbf{p}^2}{2} + V_0(\mathbf{r};\boldsymbol{\beta}_0)$ and the remaining part $H_I = \sum_{\mathrm{n}} V_{\mathrm{n}}(\mathbf{x};\boldsymbol{\beta}_0)e^{-i\mathrm{n}\omega_0 t}$. The time-dependent electron wave packet can be expanded as

$$|\Psi(t)\rangle = \sum_N C_N(t)e^{-i\int^t d\tau E_N(\tau)}\left|N(\boldsymbol{\beta}_0)\right\rangle, \tag{1.20}$$

in which $\left|N(\boldsymbol{\beta}_0)\right\rangle$ is the instantaneous eigenstate of H_0 and satisfies the governing equation $H_0\left|N(\boldsymbol{\beta}_0)\right\rangle = E_N(\boldsymbol{\beta}_0)\left|N(\boldsymbol{\beta}_0)\right\rangle$. Inserting (1.20) into the Schrödinger equation yields

$$\dot{C}_N = \sum_M \langle N|\left(-\frac{\partial\boldsymbol{\beta}_0}{\partial t}\frac{\partial}{\partial\boldsymbol{\beta}_0} - iH_I\right)|M\rangle\, e^{-i\int^t d\tau(E_M-E_N)}C_M. \tag{1.21}$$

The term$\langle N|H_I|M\rangle$ is responsible for photons absorption/emission,and the skew-hermitian matrix$\langle N|\frac{\partial}{\partial\mathbf{fi}_0}|M\rangle$ providesthe nonadiabatic coupling [26, 27, 36] and the geometric phase [48]. As indicated by (1.22), KH states are of central importance here. The deformation of the KH wave function $\phi_N(\boldsymbol{\beta}_0)$ leads to the suppression of $\langle N|V_{\mathrm{n}}|M\rangle$, which is the fundamental reason for adiabatic stabilization [15, 17]. The phase accumulation due to the distorted KH state [18] leads to the dynamic interference [42–45]. Furthermore, KH states determine the strength of nonadiabatic coupling $\langle N|\frac{\partial}{\partial\beta_0}|M\rangle$.

1.3 Results and Discussions

1.3.1 Ionization in the High-Frequency Fields

Using the hydrogen atom as the prototypical target, we calculated the ionization probability as a function of β_0, as shown by the black solid line in Fig. 1.2a. Here, the laser pulse has a frequency of $\omega_0 = 3$ a.u., and a total duration L of sixty cycles. The "death valley" [20] structure is clearly shown.

With (1.22) in hand, we explored scenarios of ionization shown in Fig. 1.2 by dividing the ionization probability curve into three stages marked by A, B, and C. In

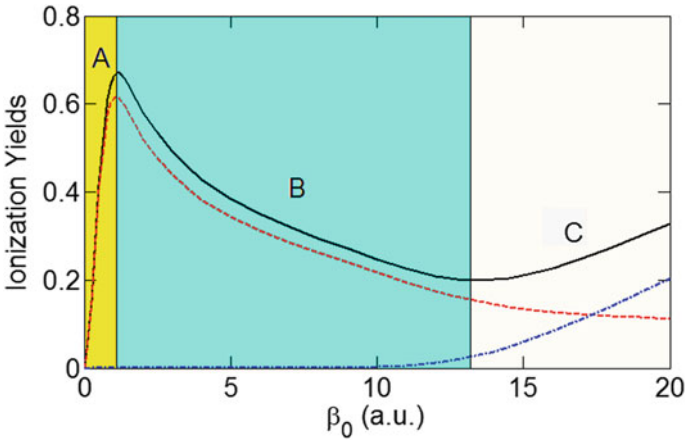

Fig. 1.2 The ionization probability as a function of β_0 obtained from TDSE simulations. The black solid line is for total ionization, the red dashed line is for one-photon ionization probability, and the blue dotted-dash line describes the nonadiabatic ionization

stage A, β_0 is small and so is the changing rate $\frac{\partial \beta_0}{\partial t}$, which means the deformation of KH wave functions and the nonadiabatic coupling are negligible. We extracted the single-photon ionization fragment from the total ionization spectra and presented it by the red dashed curve in Fig. 1.2. The single-photon-ionization probability overlaps with the total ionization probability as $\beta_0 < 1$ a.u., which suggests that the ionization can be well described by the conventional first-order perturbation theory and the nonadiabatic coupling is negligible. In stage B, the total ionization probability decreases due to the significant deformation of KH wave functions. The norm of $\langle N | V_n | M \rangle$ is suppressed with an increasing β_0. The dichotomic characteristic of KH states, i.e., the dimensionless number $\frac{Z}{\beta_0 I_p}$, serves as a measure of the deformation of wave functions. For the ground state hydrogen atom, the nuclear charge $Z = 1$ a.u. and the ionization energy $I_p = 0.5$ a.u. $\frac{Z}{\beta_0 I_p} \approx 1$ roughly corresponds to the point where the second order derivative of the laser-dressed ground state energy curve vanishes. $\frac{Z}{\beta_0 I_p} < 1$ implies the deformation of the wave function is significant. In stage C, the nonadiabatic ionization becomes more and more important [26, 27, 36]. There is no distinct boundary between B and C. The nonadiabatic coupling is determined by the product of $\left\langle N \left| \frac{\partial}{\partial \beta_0} \right| M \right\rangle$ and $\frac{\partial \beta_0}{\partial t}$, which implies an envelope dependence. Similar to the excited-state tunneling ionization [49], in the nonadiabatic ionization , the atom first transits to excited states, which are then mediated to continuum states. The effective ionization potential for the ground state decreases with the increasing of β_0 [29–31], and thus the nonadiabatic ionization is more important for a larger β_0. Ionization from excited states dominates since the ionization potential gets smaller in this situation.

We can analyze the PMD via the nonadiabatic perturbation theory. As the evolution of a certain eigenstate is described by

$$\dot{C}_N = \sum_M \langle N| \left(-\frac{\partial \boldsymbol{\beta}_0}{\partial t}\frac{\partial}{\partial \boldsymbol{\beta}_0} - i H_I\right)|M\rangle \times e^{-i\int^t d\tau (E_M - E_N)} C_M. \tag{1.22}$$

Here, the term $\langle N| H_I |M\rangle$ is responsible for absorption/emmison of photons, while $\langle N|\frac{\partial}{\partial \boldsymbol{\beta}_0}|M\rangle$ provides the nonadiabatic coupling and the geometric phase. We treat $\langle N| H_I |M\rangle$ as a perturbation and expand C_N in the way that $C_N = C_N^{(0)} + C_N^{(1)} + \cdots$. The zeroth-order equation is

$$\dot{C}_N^{(0)} = \sum_M \langle N| \left(-\frac{\partial \boldsymbol{\beta}_0}{\partial t}\frac{\partial}{\partial \boldsymbol{\beta}_0}\right)|M\rangle e^{-i\int^t d\tau (E_M - E_N)} C_M^{(0)}. \tag{1.23}$$

The nonadiabatic coupling described by (1.23) pumps the ground state to excited states. The first-order correction is $C_{\mathbf{p}}^{(1)}(t) = C_{\mathbf{p}}^{(1)a}(t) + C_{\mathbf{p}}^{(1)b}(t)$, where

$$C_{\mathbf{p}}^{(1)a}(t) = -i\sum_M \int_{t_0}^{t} d\tau \langle \mathbf{p}| H_I |M\rangle e^{-i\int^\tau d\tau' (E_M - E_{\mathbf{p}})} C_M^{(0)}(\tau), \tag{1.24}$$

$$C_{\mathbf{p}}^{(1)b}(t) = -\sum_M \int_{t_0}^{t} d\tau \langle \mathbf{p}| \frac{\partial}{\partial \boldsymbol{\beta}_0}|M\rangle \frac{\partial \boldsymbol{\beta}_0}{\partial \tau} e^{-i\int^\tau d\tau' (E_M - E_{\mathbf{k}})} C_M^{(0)}(\tau). \tag{1.25}$$

$C_{\mathbf{p}}^{(1)a}$ and $C_{\mathbf{p}}^{(1)b}$ are the transition amplitudes of single-photon absorption and the nonadiabatic coupling, respectively. Equations (1.25) and (1.26) are used to calculate the momentum distributions with specific laser parameters.

We plotted the photoelectron momentum distribution, i.e., $|C_{\mathbf{k}}^{(1)a}|^2$, in Fig. 1.3a, where dynamic interference appears. The dynamic interference occurs due to the phase accumulation by the distorted KH state and disappears if we enforced $C_N^{(0)}(t) = 1$ and $\mathrm{E}_M(\beta_0(\tau)) \to \mathrm{E}_M(\beta_0(\tau = 0))$. The nonadiabatic ionization has a significant contribution, with the given laser parameters in Fig. 1.3. Figure 1.3b, c plot $|C_{\mathbf{p}}^{(1)b}|^2$ when the electron gets ionized from the ground state and $2s\sigma_g$ state, respectively. Comparing the panel (b) with the panel (c), we found that the nonadiabatic ionization from excited states dominates since the corresponding ionization potential is smaller in this case. Please note that Fig. 1.3c is only qualitatively correct, as the depletion of the excited states is not negligible and should be included for accurate calculations.

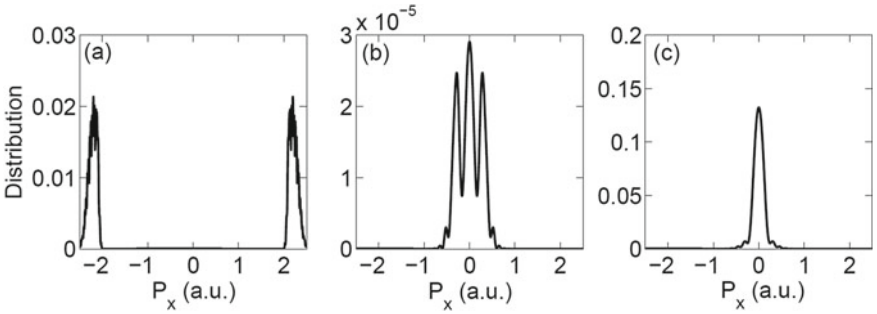

Fig. 1.3 Photoelectron momentum distribution obtained by the nonadiabatic perturbation theory. **a** photoelectron momentum distribution of single-photon ionization. **b** and **c** are the nonadiabatic ionization contributed by the ground and $2s\sigma_g$ states, respectively. The applied laser field consists of sixty cycles. The laser parameters are $\omega_0 = 3$ a.u. and $\beta_0 = 10$ a.u.

1.3.2 Imaging the Kramers-Hennerberger States

With these understandings about the central role played by KH states in the $\omega_0 \gg I_p$ regime, we now make the following proposal to experimentally affirm KH states. The strategy is basically a pump-probe scheme: a linearly or circularly polarized high-frequency strong laser pulse is used to irradiate on a prototypical hydrogen atom, which is to be ionized by another circularly polarized probe pulse. When the electron is released from the KH hydrogen atom, which plays the role of a double-slits [50–54], the photoelectron momentum distribution will inherit the double-slit interference structure [55]. In principle, this proposal can already be performed on advanced laser facilities [56–58]. In this strategy, the probe pulse should be strong enough to trigger noticeable ionization, but not so strong that the KH state formed by the pump pulse gets destroyed. This imposes a constraint $I_2 \ll (\frac{\omega_2}{\omega_1})^4 I_1$, where I_1 and I_2 are intensities of the pump and probe pulses. We denote their strength of the electric field as E_1 and E_2, and the amplitudes of the displacements are $\beta_1 = \frac{E_1}{\omega_1^2}$ and $\beta_2 = \frac{E_2}{\omega_2^2}$.

Note that the subscript 0 is preserved for the case of using only one pulse. Besides that, laser frequencies of the pump and probe pulses should be proper so that the photoelectron momentum distributions induced by the pump and probe pulses do not overlap. ω_2 should be sufficiently large to avoid interfering with very low energy electron produced by the nonadiabatic coupling [26, 36].

The upper row of Fig. 1.4 shows the above-threshold-ionization (ATI) containing the fragments released by absorbing $n\omega_1$ photons and $m\omega_2$ photons, where n and m are integers. Though the probability of absorbing ω_2 is small due to the relatively weak intensity of the probe pulse, the ionization induced by the probe pulse contributes distinct angular distribution and non-overlapping photoelectron energy with the ionization fragments induced by the pump pulse. Thus one can easily separate one-probe-photon ionization from the dominating pump-photon ionization, as shown

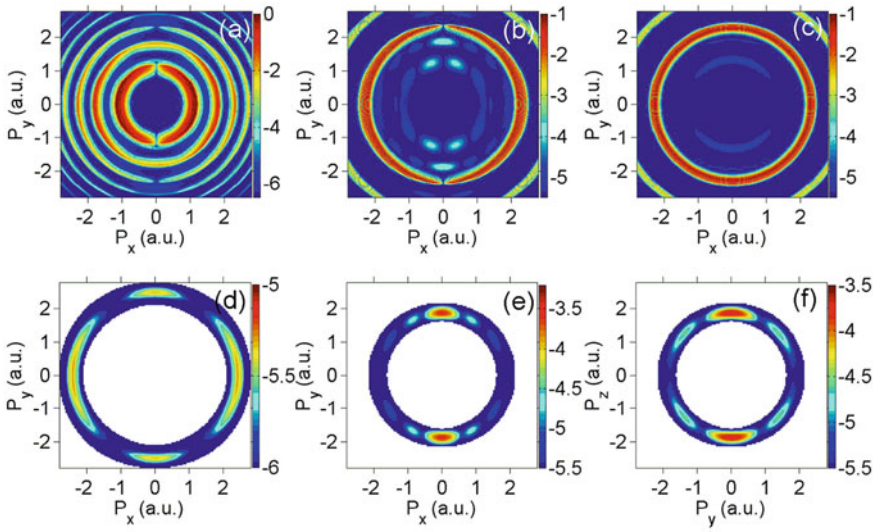

Fig. 1.4 Upper row: The photoelectron momentum distributions contributed by both the pump and probe pulses. Lower row: The photoelectron momentum distributions contributed by the one-probe-photon ionization, which are picked out from the upper row. Different laser parameters are used for the three columns. Left column: $\beta_1 = 2$ a.u., $\omega_1 = 1$ a.u., and $\omega_2 = 3.5$ a.u.; The pump pulse is linearly polarized along the x axis with a duration of twenty optical cycles, and the probe pulse is circularly polarized in the $x - y$ plane. Middle column: $\beta_1 = 5$ a.u., $\omega_1 = 3$ a.u., and $\omega_2 = 2$ a.u.; The pump pulse is linearly polarized along the x axis with a duration of sixty optical cycles, and the probe pulse is circularly polarized in the $x - y$ plane. Right Column: $\beta_1 = 3$ a.u., $\omega_1 = 3$ a.u., and $\omega_2 = 2$ a.u.; The pump pulse is circularly polarized in the $x - y$ plane with a duration of sixty optical cycles, and the probe pulse is circularly polarized in the $y - z$ plane. In all panels, the probe pulse has a duration of ten optical cycles and intensity $I_2 = 10^{16}$ W/cm^2. The delay between the pump and probe pulses is zero

in the lower row in Fig. 1.4. The number of nodes is determined by $\beta_1\sqrt{2E_{\mathbf{k}}}$ with $E_{\mathbf{k}}$ the photoelectron energy. Inversely, β_1 can be extracted from the angular distribution of the photoelectron induced by the one-probe-photon ionization. The comparison of (a), (b) and (c) shows that a larger ω_1 is more convenient for separating the ionization events from the pump and probe pulses. A larger frequency ω_1 is also better for avoiding the ionization depletion [35].

The unavoidable focal-intensity average in real experiments must be taken into account to judge the feasibility of the above proposal. By assuming that the intensity of the laser pulses has the spatially Gaussian distribution [59], we plotted the focal-intensity-averaged photoelectron angular distribution in Fig. 1.5. The frequencies are $\omega_1 = 1$ a.u. and $\omega_2 = 3.5$ a.u., corresponding to the parameters used in Fig. 1.4a, d. The laser intensities used for the three columns from left to right are $I_1 = 3.5 \times 10^{16}$ W/cm^2 ($\beta_1 = 1$ a.u.), $I_1 = 1.4 \times 10^{17}$ W/cm^2 ($\beta_1 = 2$ a.u.), and $I_1 = 3.2 \times 10^{17}$ W/cm^2 ($\beta_1 = 3$ a.u.), respectively. The photoelectron from unperturbed hydrogen atoms should be rotational invariant in the laser polarization plane,

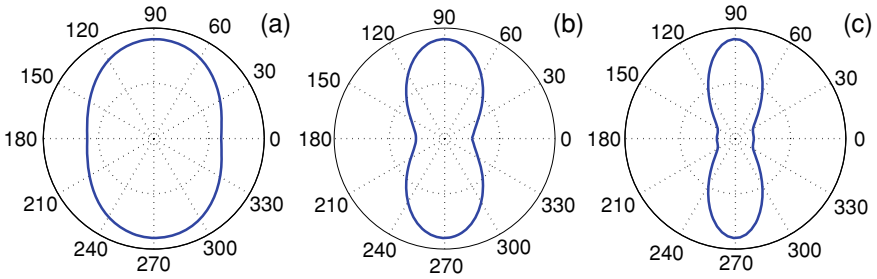

Fig. 1.5 Focal-intensity averaged photoelectron angular distributions. The laser frequencies are $\omega_1 = 1$ a.u., and $\omega_2 = 3.5$ a.u. The pump laser intensity is (a) $I_1 = 3.5 \times 10^{16}$ W/cm^2 ($\beta_1 = 1$ a.u.), (b) $I_1 = 1.4 \times 10^{17}$ W/cm^2 ($\beta_1 = 2$ a.u.), and (c) $I_1 = 3.2 \times 10^{17}$ W/cm^2 ($\beta_1 = 3$ a.u.). The probe laser has the intensity $I_2 = 1 \times 10^{16}$ W/cm^2, and the duration of ten optical cycles

hence, the anisotropic ionization probability, as shown in all these panels, confirms the existence of dichotomic distribution of the KH hydrogen atom, which in turn provides the evidence of adiabatic stabilization. The onset of adiabatic ionization implies that ionization is mainly contributed from small β_1, which explains why interference structures in photoelectron momentum distributions are not as distinct as that in Fig. 1.4. As the number of nodes is determined by $\beta_1\sqrt{2E_{\mathbf{k}}}$, a larger ω_2 is favored to produce distinctive angular distributions. This strategy works for diverse laser parameters and is robust against focal-intensity average. Moreover, the pump-probe delay can be tuned thus the probe pulse can contribute noticeable ionization before the KH atom is depleted.

1.3.3 Tunneling Ionization

Instead of the single-photon ionization triggered by the high-frequency probe pulse, the KH atom may be tunneling ionized by an infrared probe pulse as well. Figure 1.6 shows the focal-volume-averaged photoelectron momentum distributions for the probe laser intensity (a) $I_2 = 3 \times 10^{14}$ W/cm^2 and $\beta_1 = 2$ a.u. and (b) $I_2 = 2 \times 10^{14}$ W/cm^2 and $\beta_1 = 4$ a.u. Here, He^+ in the KH state is prepared and used as the target, and the two cases have the same Keldysh parameter. In contrast to the one-probe-photon ionization, signals from large β_1 are dominating in the tunneling regime.

The streaking of the photoelectron momentum distribution in the anisotropic Coulomb field produces a tilt angle, which is a function of β_1 and I_2 [60, 61]. The existence of β_1 can thus be mapped into the streaking tilt angle. We point out that it is also possible to use the laser induced electron diffraction [62, 63] to reconstruct β_1.

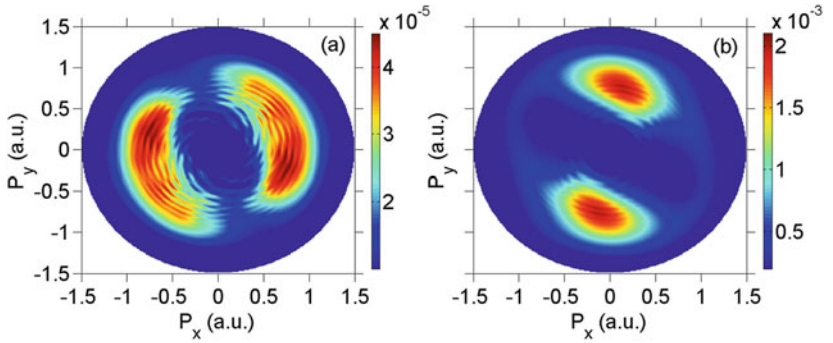

Fig. 1.6 Focal-intensity-averaged photoelectron momentum distributions that are tunneling ionized by infrared probe pulses. The pump and probe laser parameters are **a** $\beta_1 = 2$ a.u. and $I_2 = 3 \times 10^{14}$ W/cm^2, and **b** $\beta_1 = 4$ a.u. and $I_2 = 2 \times 10^{14}$ W/cm^2. The probe pulse has a duration of four optical cycles

1.3.4 Spin-Flipping

Besides utilizing the double-slit interference structure and the anisotropic angular streaking, the electron spin-flipping may also provide another route to affirm KH atoms. The physical principle is based on the non-Abelian geometric phase. Neglecting the ionization of KH atoms for a moment, the nonadiabatic coupling among those non-degenerate states, *i.e.*,

$$\langle N| \frac{\partial}{\partial \boldsymbol{\beta}_0} |M\rangle = \langle N| \frac{\partial H_0}{\partial \boldsymbol{\beta}_0} |M\rangle / (E_M - E_N) \tag{1.26}$$

can be suppressed in the adiabatic limit. However, situations are different for systems with energy degeneracies, where non-Abelian geometric phases play a role [64]. The deformation of KH states is crucial here. When the laser field is not very strong, i.e. $\beta_0 \ll 1$ a.u., the dynamical evolution of the state is determined by the dipole coupling matrix $\langle N| \mathbf{r} |M\rangle$. Typically, only a minor fraction of spin flipping could be achieved [65]. However, with an increasing β_0, couplings with the highly oscillating laser pulses are suppressed, which reduces (1.22) into

$$\frac{\partial C_N}{\partial \boldsymbol{\beta}_0} \approx -\sum\nolimits_{E_M = E_N} \langle N| \frac{\partial}{\partial \boldsymbol{\beta}_0} |M\rangle C_M \tag{1.27}$$

in the adiabatic limit.

The spin flipping in KH atom due to the adiabatically rotating electric field is isomorphic to that of in diatomic molecule due to the rotating molecule axis [66]. The nonzero spin flipping probability manifests the breaking of atom's isotropic symmetry, thus the existence of the axial symmetric KH atom. In this strategy, ensuring the adiabaticity implies that $\frac{\partial \boldsymbol{\beta}_0}{\partial t}$ should be small. Therefore, a pulse with a very long

duration is demanded. In this case, in order to avoid ionization depletion, a laser pulse with a large ω_0 is required.

Consider the situation that the laser field is linearly polarized along the z axis. Neglecting spin-orbital coupling for a moment. When the high-frequency pulse is turned on, the ground-state hydrogen is stretched to a $1s\sigma_g$ state, and the $2p_z$ state is stretched to a $2p\sigma_u$ state. The $2p_x$ and $2p_y$ state are stretched to a $2p\pi_u$ state. We label the eigenenergies of $1s\sigma_g$, $2p\sigma_u$, and $2p\pi_u$ by E_0, E_1, and E_2, respectively. Let $\mathbf{l}$ and $\mathbf{s}$ are orbital angular momentum and spin angular momentum respectively, m_l and m_s are their projections along the polarization axis. Due to the effect of spin-orbital coupling, only the projection of total angular momentum $\mathbf{J} = \mathbf{l} + \mathbf{s}$ along the polarization axis $M = m_l + m_s$ is conserved. We have the states mixing

$$\begin{aligned}
\left|\psi_0, M = \pm\frac{1}{2}\right\rangle &= \left|1s\sigma_g; m_l = 0, m_s = \pm\frac{1}{2}\right\rangle \\
\left|\psi_1, M = \pm\frac{1}{2}\right\rangle &= \left|2p\sigma_u; m_l = 0, m_s = \pm\frac{1}{2}\right\rangle \\
\left|\psi_2, M = \pm\frac{1}{2}\right\rangle &= \left|2p\pi_u; m_l = \pm 1, m_s = \mp\frac{1}{2}\right\rangle \\
&\quad + \frac{H_{SO}}{E_2 - E_1}\left|2p\sigma_u; m_l = 0, m_s = \pm\frac{1}{2}\right\rangle \\
\left|\psi_2, M = \pm\frac{3}{2}\right\rangle &= \left|2p\pi_u; m_l = \pm 1, m_s = \pm\frac{1}{2}\right\rangle
\end{aligned} , \tag{1.28}$$

where H_{SO} is the spin-orbital coupling and is of the order $O(\frac{1}{c^2})$. The energy between $\left|\psi_2, M = \pm\frac{1}{2}\right\rangle$ and $\left|\psi_2, M = \pm\frac{3}{2}\right\rangle$ is finely split, and $\left|\psi_2, M = \pm\frac{1}{2}\right\rangle$ has lower energy. The energy splitting due to the spin-orbital coupling is of the order $O(\frac{1}{c^2})$, which requires the pulse duration of the rotating pulse to be much longer than picoseconds to satisfy the adiabatic condition.

One then adiabatically rotates the polarization axis by $\theta_0 = \pi/2$ in the $z - x$ plane, then rotates it by ϕ_0 in the $x - y$ plane, and finally rotates it back to the z axis. In this case, the spin-up and spin-down states of $\left|\psi_0, M = \pm\frac{1}{2}\right\rangle$, $\left|\psi_1, M = \pm\frac{1}{2}\right\rangle$, and $\left|\psi_2, M = \pm\frac{1}{2}\right\rangle$ constitute of two-fold degenerate states $|\pm\rangle$. No spin-flipping could happen for $\left|\psi_2, M = \pm\frac{3}{2}\right\rangle$, as the geometric phase is Abelian [66]. Ulizing this effect,

Denoting the polarization axis of the laser pulse by $\mathbf{n} = (\sin\theta\cos\phi, \sin\theta \sin\phi, \cos\theta)$, we have degenerate KH states $|\pm(\theta, \phi)\rangle$ satisfying $\mathbf{n}\cdot\mathbf{J}\,|\pm(\theta, \phi)\rangle = \pm 1/2\,|\pm(\theta, \phi)\rangle$, where $\mathbf{J}$ is the addition of orbital angular momentum $\mathbf{L}$ and spin angular momentum $\mathbf{S}$. $|\pm(\theta, \phi)\rangle$ are connected to $|\pm(\theta = 0, \phi = 0)\rangle$ via rotations

$$|\pm(\theta, \phi)\rangle = \exp(-iJ_z\phi)\exp(-iJ_y\theta)\,|\pm(\theta = 0, \phi = 0)\rangle\,. \tag{1.29}$$

Components of non-Abelian connection 1-form $\mathfrak{A} = i\,\langle M|\mathbf{d}|N\rangle$, where $\mathbf{d}$ is exterior derivative, are thus given by

$$\mathfrak{A}_\theta = \tfrac{1}{2}\begin{pmatrix} 0 & i\kappa \\ -i\kappa & 0 \end{pmatrix},\ \mathfrak{A}_\phi = \tfrac{1}{2}\begin{pmatrix} \cos\theta & -\sin\theta\kappa \\ -\sin\theta\kappa & -\cos\theta \end{pmatrix}. \tag{1.30}$$

where

$$\kappa = 2\,\langle M = \frac{1}{2}|J_x|M = -\frac{1}{2}\rangle\Big|_{(\theta=0,\phi=0)}, \tag{1.31}$$

is a real-valued function of β_1 up to a possible trivial phase factor.

For the rotation process we considered, the holonomy is

$$W = T\left\{e^{i\oint \mathfrak{A}}\right\} \tag{1.32}$$
$$= \begin{pmatrix} \cos\left(\frac{\kappa\phi_0}{2}\right) + i\sin\left(\frac{\kappa\pi}{2}\right)\sin\left(\frac{\kappa\phi_0}{2}\right) & -i\cos\left(\frac{\kappa\pi}{2}\right)\sin\left(\frac{\kappa\phi_0}{2}\right) \\ -i\cos\left(\frac{\kappa\pi}{2}\right)\sin\left(\frac{\kappa\phi_0}{2}\right) & \cos\left(\frac{\kappa\phi_0}{2}\right) - i\sin\left(\frac{\kappa\pi}{2}\right)\sin\left(\frac{\kappa\phi_0}{2}\right) \end{pmatrix},$$

where T stands for the time ordering operator, as $\mathfrak{A}$ does not necessarily commute at different instants.

Equation (1.32) shows that the spin-flipping probability is given by $\cos^2\frac{\kappa\pi}{2}\sin^2\frac{\kappa\phi_0}{2}$. We have $\kappa \to 1$ for $\left|\psi_0, M = \pm\frac{1}{2}\right\rangle$ and $\left|\psi_1, M = \pm\frac{1}{2}\right\rangle$, thus only a negligible spin-flipping probability. For $\left|\psi_2, M = \pm\frac{1}{2}\right\rangle$ we have $\kappa \approx 0$. Taking $\phi_0 = \pi/\kappa$, a nearly complete spin-flipping could be achieved. We note the formation of the KH states is crucial here, otherwise, we will have κ exactly equals zero or one, thus no spin-flipping. The geometric phase for $\left|\psi_2, M = \pm\frac{1}{2}\right\rangle$ is non-Abelian, while the geometric phase for $\left|\psi_2, M = \pm\frac{3}{2}\right\rangle$ is Abelian. Ultilizing this nontrivial fact, we can manipulate the spin polarzation. Consider an ensemble of unpolarized ground-state hydrogen atoms. We resonantly excited it with a left-hand circularly polarized pulse, and obtain an ensemble with the states $\left|\psi_2, M = \frac{3}{2}\right\rangle$ and $\left|\psi_2, M = \frac{1}{2}\right\rangle$. Putting these states into the properly adiabatically rotating laser field, we end up with an ensemble of hydrogen atoms with spin up.

1.4 Conclusions

To summarize, a pump-probe scheme is suggested to detect the KH state. The pump pulse creates a KH atom, whose dichotomic structure is imprinted on the photoelectron momentum distribution. This strategy is robust against the focal-intensity average and ionization depletion. Alternatively, the spin flipping induced by the non-Abelian geometric phase in the adiabatically changing laser field can also provide evidence for the existence of KH atoms. An ideal implementation of our proposal requires $\frac{\omega_1}{I_p} > 1$ and $\frac{Z}{\beta_1 I_p} < 1$. In our strategy, the required laser intensity is about $I_1 = 10^{16} - 10^{17}$ W/cm^2, and the laser wavelength is around 10 – 50 nm, which is within the reach of current laser facilities. Relativistic and quantum electrodynamics

effects [67, 68] are negligible for the considered laser parameters. Moreover, we are concerned only about one-probe-photon ionization from KH states, thus the deviation from relativistic theory mainly differs by scaling factors [69]. We observed that the low-energy electron ionized by the nonadiabatic coupling is altered by the nondipole effect [70, 71]. However, this does not harm our proposal due to the non-overlapping energy. Our schemes not only provide accessible routes for detecting KH states, thus adiabatic stabilization, but are also useful for understanding upcoming high frequency strong laser-matter interaction.

Acknowledgements This work was supported by Innovation Program of Shanghai Municipal Education Commission (2017-01-07-00-02-E00034), National Key R&D Program of China (2018YFA0404802), National Natural Science Foundation of China (NSFC) (Grant No. 11925405, 91850203). Simulations were performed on the π supercomputer at Shanghai Jiao Tong University.

References

1. M. Uiberacker, T. Uphues, M. Schultze et al., Attosecond real-time observation of electron tunnelling in atoms. Nature **446**, 627 (2007)
2. P. Agostini, F. Fabre, G. Mainfray, G. Petit, N.K. Rahman, Free-free transitions following six-photon ionization of xenon atoms. Phys. Rev. Lett. **42**, 1127 (1979)
3. A. L'Huillier, P. Balcou, High-order harmonic generation in rare gases with a 1-ps 1053-nm laser. Phys. Rev. Lett. **70**, 774 (1993)
4. P.B. Corkum, Plasma perspective on strong field multiphoton ionization. Phys. Rev. Lett. **71**, 1994 (1993)
5. S. Ghimire, A.D. DiChiara, E. Sistrunk et al., Observation of high-order harmonic generation in a bulk crystal. Nat. Phys. **7**, 138 (2011)
6. A. L'Huillier, L.A. Lompre, G. Mainfray, et al., Multiply charged ions induced by multiphoton absorption in rare gases at 0.53 μm. Phys. Rev. A **27**, 2503 (1983)
7. C.I. Blaga, F. Catoire, P. Colosimo et al., Strong-field photoionization revisited. Nat. Phys. **5**, 335 (2009)
8. W. Quan, Z. Lin, M. Wu et al., Classical aspects in above-threshold ionization with a midinfrared strong laser field. Phys. Rev. Lett. **103** (2009)
9. Y. Huismans, A. Rouzée, A. Gijsbertsen et al., Time-resolved holography with photoelectrons. Science **331**, 61 (2011)
10. M. Gavrila, Atomic stabilization in superintense laser fields. J. Phys. B: At Mol. Opt. Phys. **35**, R147 (2002)
11. A.M. Popov, O.V. Tikhonova, E.A. Volkova, Strong-field atomic stabilization: numerical simulation and analytical modelling. J. Phys. B: At Mol. Opt. Phys. **36**, R125 (2003)
12. M. Richter, Imaging and controlling electronic and nuclear dynamics in strong laser fields. (Ph.D. Thesis, Tecnischen Universitat Berlin, 2016)
13. M.V. Fedorov, A.M. Movsesyan, Field-induced effects of narrowing of photoelectron spectra and stabilisation of Rydberg atoms. J. Phys. B: At. Mol. Opt. Phys. **21**, L155 (1988)
14. A.M. Movsesyan, M.V. Fedorov, Interference effects in the photoionization of Rydberg atoms in a strong electromagnetic field. Zh. Eksp. Teor. Fiz. **95**, 47 (1989)
15. M. Pont, M. Gavrila, Stabilization of atomic hydrogen in superintense, high-frequency laser fields of circular polarization. Phys. Rev. Lett. **65**, 2362 (1990)
16. K.C. Kulander, K.J. Schafer, J.L. Krause, Dynamic stabilization of hydrogen in an intense, high-frequency, pulsed laser field. Phys. Rev. Lett. **66**, 2601 (1991)
17. J.H. Eberly, K.C. Kulander, Atomic stabilization by super-intense lasers. Science **262**, 1229 (1993)

18. Q. Wei, P. Wang, S. Kais, D. Herschbach, Pursuit of the Kramers-Henneberger atom. Chem. Phys. Lett. **683**, 240 (2017)
19. W.C. Henneberger, Perturbation method for atoms in intense laser fields. Phys. Rev. Lett. **21**, 838 (1968)
20. P. Lambropoulos, Mechanisms for multiple ionization of atoms by strong pulsed lasers. Phys. Rev. Lett. **55**, 2141 (1985)
21. M. Richter, S. Patchkovskii, F. Morales, O. Smirnova1, and M. Ivanov1, The role of the Kramers-Henneberger atom in the higher-order Kerr effect, New J. Phys. **15**, 083012 (2013)
22. M. Matthews, F. Morales, A. Patas et al., Amplification of intense light fields by nearly free electrons. Nat. Phys. **14**, 695 (2018)
23. U. Eichmann, T. Nubbemeyer, H. Rottke, W. Sandner, Acceleration of neutral atoms in strong short-pulse laser fields. Nature **461**, 1261 (2009)
24. T. Nubbemeyer, K. Gorling, A. Saenz, U. Eichmann, W. Sandner, Strong-field tunneling without ionization. Phys. Rev. Lett. **101**, (2008)
25. M.P. De Boer, J.H. Hoogenraad, R.B. Vrijen, H.G. Muller, Indications of high-intensity adiabatic stabilization in neon. Phys. Rev. Lett. **71**, 3263 (1993)
26. K. Toyota, O.I. Tolstikhin, T. Morishita et al., Slow electrons generated by intense high-frequency laser pulses. Phys. Rev. Lett. **103**, (2009)
27. Q.C. Ning, U. Saalmann, J.M. Rost, Electron dynamics driven by light-pulse derivatives. Phys. Rev. Lett. **120**, (2018)
28. A.M. Popov, O.V. Tikhonova, E.A. Volkova, Applicability of the Kramers-Henneberger approximation in the theory of strong-field ionization. J. Phys. B: At. Mol. Opt. Phys. **32**, 3331 (1999)
29. M. Pont, Atomic distortion and ac-Stark shifts of H under extreme radiation conditions. Phys. Rev. A **40**, 5659 (1989)
30. M. Pont, N.R. Walet, M. Gavrila, Radiative distortion of the hydrogen atom in superintense, high-frequency fields of linear polarization. Phys. Rev. A **41**, 477 (1990)
31. M. Li, Q. Wei, Stark effect of Kramers-Henneberger atoms. J. Chem. Phys. **148**, (2018)
32. F. Morales, M. Richter, S. Patchkovskii, O. Smirnova, Imaging the Kramers-Henneberger atom. Proc. Natl. Acad. Sci. **108**, 16906 (2011)
33. W.C. Jiang, J. Burgdörfer, Dynamic interference as signature of atomic stabilization. Opt. Express **26**, 19921 (2018)
34. P.L. He, Z.H. Zhang, F. He, Young's Double-Slit Interference in a Hydrogen Atom. Phys. Rev. Lett. **124**, (2020)
35. J. Grochmalicki, M. Lewenstein, K. Rzaewski, Stabilization of atoms in superintense laser fields: is it real? Phys. Rev. Lett. **66**, 1038 (1991)
36. M. Førre, S. Selstø, J. P. Hansen, and L. B. Madsen, Exact nondipole Kramers-Henneberger form of the light-atom Hamiltonian: an application to atomic stabilization and photoelectron energy spectra, Phys. Rev. Lett. **95**, 043601 (2005)
37. T. Seideman, M.Y. Ivanov, P.B. Corkum, Role of electron localization in intense-field molecular ionization. Phys. Rev. Lett. **75**, 2819 (1995)
38. T. Zuo, A.D. Bandrauk, Charge-resonance-enhanced ionization of diatomic molecular ions by intense lasers. Phys. Rev. A **52**, R2511 (1995)
39. H.R. Reiss, Field intensity and relativistic considerations in the choice of gauge in electrodynamics. Phys. Rev. A **19**, 1140 (1979)
40. M. Pont, N.R. Walet, M. Gavrila, C.W. McCurdy, Dichotomy of the hydrogen atom in superintense, high-frequency laser fields. Phys. Rev. Lett. **61**, 939 (1988)
41. R. Kosloff, H. Tal-Ezer, A direct relaxation method for calculating eigenfunctions and eigenvalues of the Schrödinger equation on a grid. Chem. Phys. Lett **127**, 223 (1986)
42. P.V. Demekhin, L.S. Cederbaum, Dynamic interference of photoelectrons produced by high-frequency laser pulses. Phys. Rev. Lett. **108**, (2012)
43. P.V. Demekhin, L.S. Cederbaum, ac Stark effect in the electronic continuum and its impact on the photoionization of atoms by coherent intense short high-frequency laser pulses. Phys. Rev. A **88**, (2013)

44. M. Baghery, U. Saalmann, J.M. Rost, Essential conditions for dynamic interference. Phys. Rev. Lett. **118**, (2017)
45. M.X. Wang, H. Liang, X.R. Xiao et al., Nondipole effects in atomic dynamic interference. Phys. Rev. A **98**, (2018)
46. G. Yao, R.E. Wyatt, Stationary approaches for solving the Schrödinger equation with time-dependent Hamiltonians. J. Chem. Phys. **101**, 1904 (1994)
47. K. Toyota, U. Saalmann, J.M. Rost, The envelope Hamiltonian for electron interaction with ultrashort pulses. New J. Phys. **17**, (2015)
48. M. V. Berry, Quantal phase factors accompanying adiabatic changes, Proc. Roy. Soc. London, Ser. A **392**, 45 (1984)
49. E.E. Serebryannikov, A.M. Zheltikov, Strong-field photoionization as excited-state tunneling. Phys. Rev. Lett. **116**, (2016)
50. H.D. Cohen, U. Fano, Interference in the Photo-Ionization of Molecules. Phys. Rev. **150**, 30 (1966)
51. D. Akoury, K. Kreidi, T. Jahnke et al., The simplest double slit: interference and entanglement in double photoionization of H_2. Science **318**, 949 (2007)
52. J. Fernández, O. Fojón, A. Palacios, F. Martín, Interferences from fast electron emission in molecular photoionization. Phys. Rev. Lett. **98**, (2007)
53. D. Rolles, M. Braune, S. Cvejanović et al., Isotope-induced partial localization of core electrons in the homonuclear molecule N_2. Nature **437**, 711 (2005)
54. M. Kunitski, N. Eicke, P. Huber, J. Köhler et al., Double-slit photoelectron interference in strong-field ionization of the neon dimer. Nat. Comm. **10**, 1 (2019)
55. P.L. He, F. He, Ionization of H_2^+ in XUV pulses. Physica Scripta **90**, (2015)
56. A.A. Sorokin, S.V. Bobashev, T. Feigl et al., Photoelectric effect at ultrahigh intensities. Phys. Rev. Lett. **99**, (2007)
57. M. Fuchs, M. Trigo, J. Chen et al., Anomalous nonlinear X-ray Compton scattering. Nat. Phys. **11**, 964 (2015)
58. S. Huang, Y. Ding, Y. Feng et al., Generating single-spike hard X-ray pulses with nonlinear Bunch compression in free-electron lasers. Phys. Rev. Lett. **119**, (2017)
59. A.S. Alnaser, X.M. Tong, T. Osipov et al., Laser-peak-intensity calibration using recoil-ion momentum imaging. Phys. Rev. A **70**, (2004)
60. M. Odenweller, N. Takemoto, A. Vredenborg et al., Strong field electron emission from fixed in space H_2^+ ions. Phys. Rev. Lett. **107**, (2011)
61. P.L. He, N. Takemoto, F. He, Photoelectron momentum distributions of atomic and molecular systems in strong circularly or elliptically polarized laser fields. Phys. Rev. A **91**, (2015)
62. M. Meckel, D. Comtois, D. Zeidler et al., Laser-induced electron tunneling and diffraction. Science **320**, 1478 (2008)
63. C.I. Blaga, J. Xu, A.D. DiChiara et al., Imaging ultrafast molecular dynamics with laser-induced electron diffraction. Nature **483**, 194 (2012)
64. F. Wilczek, A. Zee, Appearance of gauge structure in simple dynamical systems. Phys. Rev. Lett. **52**, 2111 (1984)
65. P.L. He, D. Lao, F. He, Strong field theories beyond dipole approximations in nonrelativistic regimes. Phys. Rev. Lett. **118**, (2017)
66. J. Moody, A. Shapere, F. Wilczek, Realizations of magnetic-monopole gauge fields: Diatoms and spin precession. Phys. Rev. Lett. **56**, 893 (1986)
67. F. Ehlotzky, K. Krajewska, J.Z. Kamiński, Fundamental processes of quantum electrodynamics in laser fields of relativistic power. Rep. Prog. Phys. **72**, (2009)
68. A. Di Piazza, C. Müller, K.Z. Hatsagortsyan, C.H. Keitel, Extremely high-intensity laser interactions with fundamental quantum systems. Rev. Mod. Phys. **84**, 1177 (2012)
69. I.V. Ivanova, V.M. Shabaev, D.A. Telnov et al., Scaling relations of the time-dependent Dirac equation describing multiphoton ionization of hydrogenlike ions. Phys. Rev. A **98**, (2018)
70. C.T.L. Smeenk, L. Arissian, B. Zhou et al., Partitioning of the linear photon momentum in multiphoton ionization. Phys. Rev. Lett. **106**, (2011)
71. A. Ludwig, J. Maurer, B.W. Mayer et al., Breakdown of the dipole approximation in strong-field ionization. Phys. Rev. Lett. **113**, (2014)

Chapter 2
Observation of the Post-Ionization Optical Coupling in N_2^+ Lasing in Intense Laser Fields

Yao Fu, Helong Li, Siqi Wang, Erik Lötstedt, Toshiaki Ando, Atsushi Iwasaki, Farhad H. M. Faisal, Kaoru Yamanouchi, and Huailiang Xu

Abstract In this chapter, we introduce our recent studies on the mechanisms responsible for the optical amplification in N_2^+ induced by irradiating nitrogen molecules N_2 with intense laser fields. We demonstrate that the lasing intensities of N_2^+ at 391.4 nm, corresponding to the $B^2\Sigma_u^+$ ($\upsilon = 0$)-$X^2\Sigma_g^+$ ($\upsilon'' = 0$) transition, can be strongly modulated by manipulating the polarization state of the driven laser field, which is ascribed to the post-ionization coupling between the ground $X^2\Sigma_g^+$ state and the first excited $A^2\Pi_u$ state of N_2^+. By using pump-probe methods, we show direct evidences for the optical transition between the $X^2\Sigma_g^+$ and $A^2\Pi_u$ states of N_2^+ in intense laser field, based on which we show the optimization of N_2^+ lasing by designing intense laser fields.

2.1 Introduction

When a powerful femtosecond (fs) laser pulse is externally- or self-focused in pure nitrogen or air, it can induce a variety of dynamical processes of atmospheric constituents [1–4], resulting in electronically and rovibrationally excited atoms, molecules or ions, which are in some cases population-inverted and lead to amplification of the light covering the transitions [5–18]. This type of lasing phenomena in

Y. Fu · H. Li · S. Wang · H. Xu (✉)
State Key Laboratory of Integrated Optoelectronics, College of Electronic Science and Engineering, Jilin University, Changchun 130012, China
e-mail: huailiang@jlu.edu.cn

E. Lötstedt · T. Ando · A. Iwasaki · K. Yamanouchi
Department of Chemistry, School of Science, The University of Tokyo, 7-3-1 Hongo, Bunkyo-ku, Tokyo 113-0033, Japan
e-mail: kaoru@chem.s.u-tokyo.ac.jp

F. H. M. Faisal
Fakultät Für Physik, Universität Bielefeld, 33615 Bielefeld, Germany

H. Xu
CAS Center for Excellence in Ultra-Intense Laser Science, Shanghai 201800, China

K. Yamanouchi et al. (eds.), *Progress in Ultrafast Intense Laser Science XVI*,
Topics in Applied Physics 141, https://doi.org/10.1007/978-3-030-75089-3_2

air are popularly called "air lasing", and have been extensively investigated in recent years because of their high potential in atmospheric applications [16–18]. Recently, lasing in N_2^+ has been paid much attention because it was theoretically predicted that the ionization of N_2, whose ground-state electronic orbital configuration is KK $(\sigma_g 2s)^2(\sigma_u 2s)^2(\pi_u 2p)^4(\sigma_g 2p)^2$, by intense fs laser pulses [19] gives more population on the ground $X^2\Sigma_g^+$ state of N_2^+ [20, 21]. As a result, the stimulated amplification of light in the population-inverted N_2^+ could not occur only through the strong-field ionization of N_2. Therefore, considerable effort has been made to interpret the physical origin of the strong-field-induced N_2^+ lasing [22–29].

In 2015, we proposed, as shown in Fig. 2.1, a physical mechanism called "post-ionization optical coupling" to explain the strong-field-induced N_2^+ lasing phenomenon. In this scenario, it was suggested that the ionization of N_2 occurs in the strongest (central) part of the fs laser pulse, and most of N_2^+ cations are prepared in their ground $X^2\Sigma_g^+$ state as predicted theoretically. After the ionization, the resultant N_2^+ cations are still within the light field, and thus interact with the rear part of the fs laser pulse, which would induce an optical coupling among the lowest three states of N_2^+, i.e., $X^2\Sigma_g^+$, $A^2\Pi_u$ and $B^2\Sigma_u^+$, leading to population redistribution in N_2^+, and consequently, the population inversion between the $B^2\Sigma_u^+$ and $X^2\Sigma_g^+$ states. With this pumping mechanism, it was demonstrated that the population-inverted N_2^+ can be built up very rapidly within a time scale of a few femtoseconds, which agrees well with the experimental observation that N_2^+ lasing can be produced by the excitation of few-cycle 800 nm laser pulses [25].

In this chapter, we present further experimental evidences for the post-ionization coupling mechanism in N_2^+ lasing. We first demonstrate that the intensity (which represents the peak value of the measured signal) of the N_2^+ lasing at 391.4 nm can be significantly enhanced by designing a time-dependent polarized laser field using either the polarization gating (PG) technique [26] or a birefringent crystal [27], which can be convincingly explained by the post-ionization coupling where the modulated driven pulse efficiently transfers the population in the ground $X^2\Sigma_g^+$ state to the first

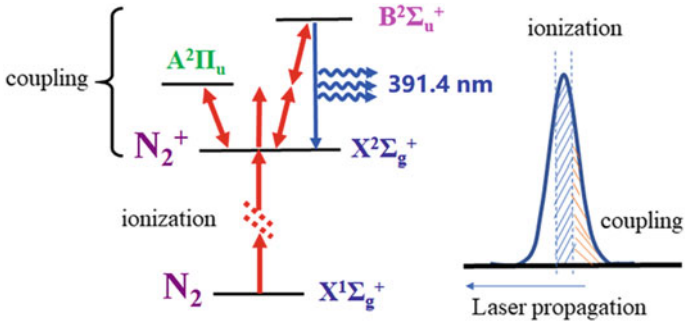

Fig. 2.1 Schematic diagram of post-ionization optical coupling that redistributes the populations among the $X^2\Sigma_g^+$, $B^2\Sigma_u^+$ and $A^2\Pi_u$ states and establishes the population inversion between the $X^2\Sigma_g^+$ and $B^2\Sigma_u^+$ states in N_2^+

excited $A^2\Pi_u$ state of N_2^+. This is an "indirect" evidence for the coupling, where the transition between the $X^2\Sigma_g^+$ and $A^2\Pi_u$ states is not directly observed. We then show, using pump-probe methods, the "direct" observations of the optical coupling by introducing an independent coupling pulse to induce the $X^2\Sigma_g^+$-$A^2\Pi_u$ transition, and find that the 391.4 nm lasing intensity can be controlled by modulating the strength, polarization and time delay of the coupling pulse [28, 29]. Based on the deeper understanding of the post-ionization coupling, we achieve the optimization of N_2^+ lasing in an elliptically modulated intense laser field.

2.2 Indirect Observation of $X^2\Sigma_g^+$-$A^2\Pi_u$ Coupling

When the ionization of N_2 occurs at the most intense part of a linearly polarized laser field, the N_2 molecules whose axes are parallel to the polarization direction of the linearly polarized laser field are preferentially ionized [30], and consequently, most of N_2^+ ions are aligned along the polarization direction of the laser field. However, in the post-ionization optical coupling model, the subsequent $X^2\Sigma_g^+$-$A^2\Pi_u$ coupling induced by the rear laser field has the maximum efficiency when the polarization direction of the coupling laser field is perpendicular to the direction of N_2^+ axis because of the perpendicular $X^2\Sigma_g^+$-$A^2\Pi_u$ transition nature of N_2^+ [31]. Therefore, it is expected that the intensity of N_2^+ lasing can be enhanced or reduced if one could control the polarization state of the rear part of the laser pulse. In the following, we will present experimental results of N_2^+ lasing in two types of designed laser fields, whose polarization states in the rear part of the laser pulse change in time, by using the PG technique [26] and birefringent crystal [27].

2.2.1 *N_2^+ Lasing Pumped with the Laser Pulse Modulated by the PG Technique*

To explore the effect of the laser polarization of the rear part of the pumping laser pulse on N_2^+ lasing, we employ a technique called polarization grating (PG) [32], which is often used in attosecond pulse generation, to modulate the polarization state of the pump laser pulse in time. As shown in Fig. 2.2a, the PG setup used in this study is composed of a 7-order quarter-wave plate (7-QWP) and a 0-order quarter wave plate (0-QWP). The angle between the optical axis of the 7-QWP and the polarization of the input laser pulse is set at 45°, so that the electric field of the laser field modulated by the 7-QWP can be expressed as [26],

$$E_{7-QWP}(t) = \frac{E_0}{\sqrt{2}} g\left(t - \frac{T_{d\_7-QWP}}{2}\right) e_{7-QWP\_o} + \frac{E_0}{\sqrt{2}} g\left(t + \frac{T_{d\_7-QWP}}{2}\right) e_{7-QWP\_e} \quad (2.1)$$

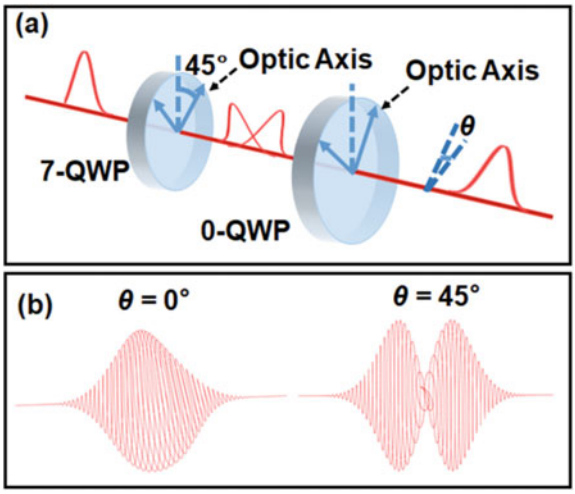

Fig. 2.2 **a** Schematic diagram of the PG, where 7-QWP and 0-QWP represent the 7-order and 0-order quarter wave plates. The angle θ represents the angle between the optical axes of the two quarter wave plates, **b** Amplitudes at $\theta = 0°$ and 45°, respectively

where E_0 is the amplitude of the input laser pulse, and T_{d_7-QWP} is the time delay between the o light and the e light induced by the 7-QWP with $T_{d\_7-QWP} = 2\pi(7 + 1/4)/\omega$ and $g(t) = e^{-2\ln 2t^2/\tau^2}\sin(\omega t + \varphi)$ is the Gaussian function of the laser pulse, and e_{7-QWP_o} and e_{7-QWP_e} are the unit vectors perpendicular (the o light) and parallel (the e light) to the optics axis of the 7-QWP, respectively. Then the laser pulse is further modulated by the 0-QWP, with the final electric field expressed as,

$$\begin{aligned} E_{PG}(t) = &\frac{E_0}{\sqrt{2}}\left[g\left(t - \frac{T_{d\_7-QWP} + T_{d\_0-QWP}}{2}\right)*\cos\theta + g\left(t + \frac{T_{d\_7-QWP} - T_{d\_0-QWP}}{2}\right) * \sin\theta\right] \\ &e_{0-QWP\_o} + \frac{E_0}{\sqrt{2}}\left[g\left(t - \frac{T_{d\_7-QWP} - T_{d\_0-QWP}}{2}\right)*\sin\theta\right. \\ &\left. -g\left(t + \frac{T_{d\_7-QWP} + T_{d\_0-QWP}}{2}\right) * \cos\theta\right]e_{0-QWP\_e} \end{aligned} \tag{2.2}$$

where T_{d_0-QWP} is the time delay between the o light and the e light induced by the 0-QWP with $T_{d\_0-QWP} = (2\pi * (1/4))/\omega$ and e_{0-QWP_o} and e_{0-QWP_e} are the unit vector perpendicular and parallel to the optical axis of the 0-QWP, respectively. It can be seen from (2.2) and Fig. 2.2b that when the angle, θ, between the optical axes of the two wave plates is changed, the polarization state of a linearly polarized pump laser field in the front and rear parts of the laser pulse can be changed from linear to circular or circular to linear, but the polarization state at the peak of the laser pulse (the central part) is kept as linear.

In this study, we carry out the experiments using the linearly polarized output of a Ti:sapphire amplifier (800 nm, 40 fs). After the laser beam passes through the PG, it is focused by a fused silica lens ($f = 40$ cm) into a vacuum chamber filled with pure nitrogen at 10 mbar. N_2^+ lasing is generated by both self- and external-seeding schemes, where self-seeding means that the seed pulse is directly produced by the pump pulse in N_2 gas during propagation, but the external seeding means that the

seed pulse is produced by frequency doubling of the pump pulse in a BBO crystal. The forward lasing is collimated by a fused silica lens (f = 30 cm), and recorded by a spectrometer (Andor, Shamrock) equipped with with an ICCD camera (Andor iStar).

With the laser field modulated by the PG with the angle of $\theta = 0°$, where the polarization of the rear part of the laser pulse is linear but its direction changes in time, it can be seen from Fig. 2.3a that the intensity of self-seeding N_2^+ lasing at 391.4 nm (solid line), corresponding to the $B^2\Sigma_u^+(\upsilon = 0)$-$X^2\Sigma_g^+$ ($\upsilon'' = 0$) transition, can be significantly enhanced when compared with that (dot line) obtained with the pump of the linear polarized light without the PG modulation. For both the cases, the pump laser energies are set at 1.0 mJ. In order to avoid the effect of self-generated seed on the lasing enhancement, we compare the lasing intensities measured in the external seed scheme. In this case, the energies of the pump laser pulses are reduced to 0.6 mJ, so that self-generated seed is negligible. As shown in Fig. 2.3b, the forward N_2^+ lasing produced by the PG-modulated laser pulse (solid line) in the presence of the external seed (dash line) is about one order of magnitude larger than that (dot line) by the linearly polarized laser pulse, which indicates that the population inversion between the $B^2\Sigma_u^+$ and $X^2\Sigma g^+$ states is dramatically changed by the PG-modulated fields.

On the other hand, we also measure the 391.4 nm fluorescence of N_2^+ on the $B^2\Sigma_u^+$-$X^2\Sigma_g^+$ transition by collecting it at a right angle of the laser propagation direction. It is found that the intensity of fluorescence pumped by the PG-modulated laser pulse is slightly weaker than (comparable with) that pumped by the linearly polarized laser pulse (not shown). Since the fluorescence intensity is determined by the population in $B^2\Sigma_u^+$ ($\upsilon = 0$) state of N_2^+, the enhancement of N_2^+ lasing at 391.4 nm can be thus ascribed to the efficient depletion of the population in the

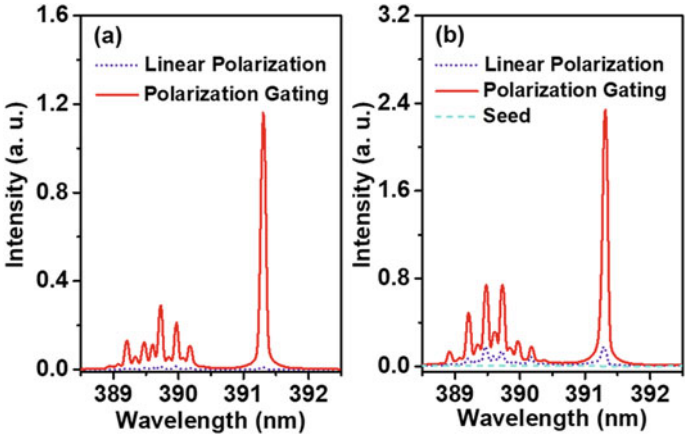

Fig. 2.3 The forward spectra of **a** self-seeding and **b** external seeding N_2^+ lasing obtained by the linearly polarized (dot lines) and PG-modulated (solid lines) laser pulses. The external seed (dash line) is also presented in (**b**). The angle θ is set at $\theta = 0°$

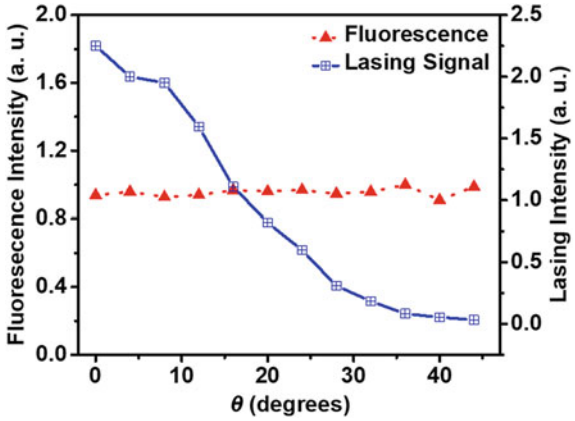

Fig. 2.4 The intensities of the N_2^+ lasing (square) and fluorescence (triangle) obtained with the PG pulse as a function of θ in the range of 0–45°

$X^2\Sigma_g^+(v'' = 0)$ by the optical coupling through the vertical $X^2\Sigma_g^+$-$A^2\Pi_u$ transition, in which the polarization of the coupling field in the rear part of the laser pulse is modulated by the PG.

In particular, it is known from the PG scheme that when we change the angle between the 0-QWP and 7-QWP from $\theta = 0°$ to 45°, the polarization state changes from linear to circular in both the front and rear parts, but the polarization state of the central part of the pulse keeps linear. Because the population in the $B^2\Sigma_u^+$ state is only dependent on the ionization of N_2 by the central part (strongest) of the laser pulse, it is expected that when the angle θ changes from 0° to 45° the fluorescence at 391.4 nm measured from the side direction keeps constant, but the lasing at 391.4 nm, which is dependent on both the populations in the $B^2\Sigma_u^+$ ($v = 0$) and $X^2\Sigma_g^+$ ($v'' = 0$) states, changes. This is really what we have observed. As shown in Fig. 2.4, when θ changes from 0° to 45°, the intensity of the 391.4 nm fluorescence (triangle) keeps constant in the entire range of θ, but the 391.4 nm lasing (square) decreases monotonously, which can be ascribed to the amplitude of the laser component perpendicular to the N_2^+ axis in the rear laser field decreases from linear polarization to circular polarization, leading to the less $X^2\Sigma_g^+$-$A^2\Pi_u$ perpendicular coupling.

2.2.2 *N_2^+ Lasing Pumped with the Laser Pulse Modulated by Multi-order Quarter-Wave Plate*

It can be seen from (2.2) that the laser field can be modulated by the PG. In fact, when the laser pulse only passes through the 7-QWP, the amplitude and polarization of the laser pulse can also be modulated as a function of the angle, $\boldsymbol{\alpha}$, between the polarization direction of the linear laser pulse and the fast axis of the 7-QWP, as shown in (2.3), but in this case the polarization state of the central part of the laser

pulse changes as well. In this section, we investigate how the lasing behaves in the laser field modulated only by the 7-QWP [27].

$$\boldsymbol{E}(\alpha, t) = E_0 \cos(\alpha) g\left(t - \frac{T_n}{2}\right) e_o + E_0 \sin(\alpha) g\left(t + \frac{T_n}{2}\right) \boldsymbol{e}_e. \tag{2.3}$$

As shown in Fig. 2.5a, the laser field can be separated into two electric field components, the ordinary light (E_y) and the extraordinary (E_x) light, with E_y being parallel to the fast axis of 7-QWP and thus having a larger amplitude at $-45° < \alpha < 45°$ (α represents the angle between the polarization direction of the linearly polarized laser pulse and the fast axis of 7-QWP). Due to the birefringence of the 7-QWP, the two components of the linearly polarized laser pulse will have a time delay of about 20 fs after passing through the 7-QWP, where E_x lags behind E_y. Therefore, in the coupling model [25], the stronger E_y component would induce the ionization of N_2 and the delayed and weaker E_x component would subsequently induce the post-ionization state coupling of N_2^+ through the perpendicular $X^2\Sigma_g^+$-$A^2\Pi_u$ transition. In Fig. 2.5b, we show the integrated intensity of the E_y component ($-\infty < t < \infty$) and that of the E_x component ($0 < t < \infty$) as a function of the angle α between the polarization direction of the linearly polarized laser pulse and the fast axis of 7-QWP.

As a result, we show in Fig. 2.6a the intensity of the N_2^+ lasing at 391.4 nm measured in the external seed scheme as a function of the angle α. The pressure is

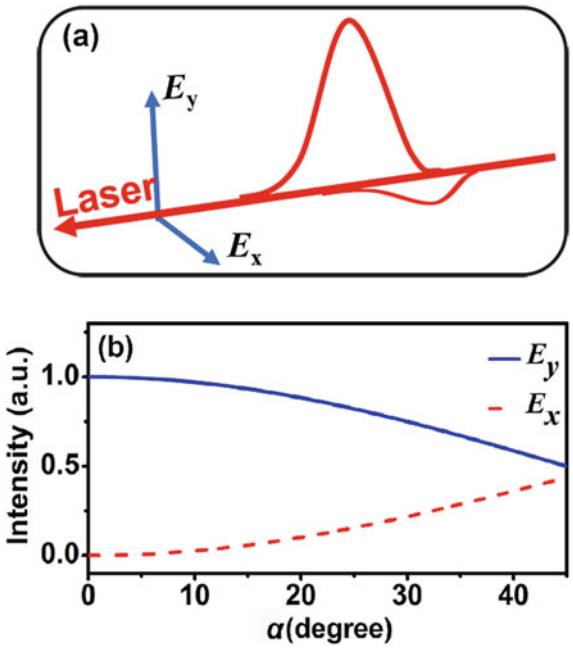

Fig. 2.5 **a** The amplitude of the E_x and E_y components of the laser electric fields with the direction of E_x and E_y perpendicular and parallel to the fast axis (ordinary light axis) of the 7-QWP at $\alpha = 10°$. **b** The intensity of the E_x component, which is proportional to the square of the amplitude, integrated over $0 < t < \infty$ (dash line) and that of E_y integrated over $-\infty < t < \infty$ (solid line) of the laser pulse vary as a function of α

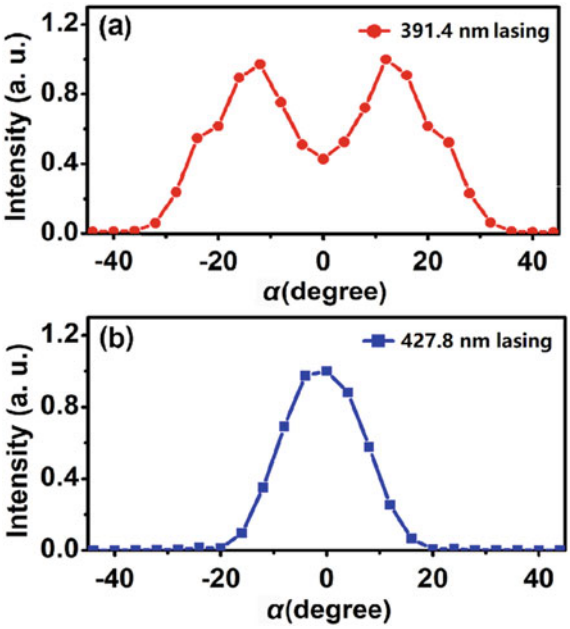

Fig. 2.6 **a** 391.4 nm and **b** 427.8 nm lasing intensity as a function of α in the 7-QWP modulated laser field

10 mbar and the laser energy is 0.7 mJ. It can be seen from Fig. 2.6a that as $|\boldsymbol{\alpha}|$ changes from 0° to 45°, the intensity of the 391.4 nm lasing first increases and then decreases, taking the maximums at the absolute value of $\alpha \sim 18°$, which may indicate that as the ellipticity of the laser pulse changes there exists a balance between the ionization rate and the coupling efficiency for the population inversion between the $X^2\Sigma_g^+(\upsilon'' = 0)$ and $B^2\Sigma_u^+(\upsilon = 0)$. That is, as $|\boldsymbol{\alpha}|$ varies from 0° to 45°, E_y decreases, leading to a decreasing ionization probability, and thus less N_2^+ ions. On the other hand, as $|\boldsymbol{\alpha}|$ changes from 0° to 45°, E_x increases, leading to a stronger coupling field for depleting the population in the $X^2\Sigma_g^+(\upsilon'' = 0)$ level through the $X^2\Sigma_g^+$-$A^2\Pi_u$ vertical transition after the ionization. Finally, a balance between the ionization and coupling for the population inversion is achieved.

Interestingly, it is found that as $|\boldsymbol{\alpha}|$ changes from 0° to 45°, the intensity of the lasing at 427.8 nm, corresponding to the $B^2\Sigma_u^+(\upsilon = 0)$-$X^2\Sigma_g^+(\upsilon'' = 1)$ transition, shows different behavior, i.e., monotonically decreasing with the maximum value at $\alpha \sim 0°$ (see Fig. 2.6b). Since the 391.4 and 427.8 nm lasing emissions result from the same upper level $B^2\Sigma_u^+(\upsilon = 0)$, the difference in the ellipticity dependences of these two lasing lines may be ascribed to the different variations of the population in the two vibrational levels $\upsilon'' = 0$ and $\upsilon'' = 1$ of the $X^2\Sigma_g^+$ state. In fact, it was previously demonstrated that the population in the $X^2\Sigma_g^+(\upsilon'' = 1)$ level is very small after ionization [33]. Therefore, the population in the $X^2\Sigma_g^+(\upsilon'' = 1)$ level could not be depleted further by the $E_x(t)$ component after the ionization, so that the 427.8 nm lasing is not sensitive to the $X^2\Sigma_g^+$-$A^2\Pi_u$ coupling, leading to the result

that the 427.8 nm lasing decreases monotonically due to the decreasing ionization probability as $|\boldsymbol{\alpha}|$ changes from 0° to 45°.

To verify the above conjecture on the ellipticity dependences of N_2^+ lasing, we perform numerical simulation of the population distribution of N_2^+ in a multi-order QWP modulated laser field based on the post-ionization optical coupling model [27]. We examine the final difference of the population between the $B^2\Sigma_u^+$ ($\upsilon = 0$) and $X^2\Sigma_g^+$ ($\upsilon'' = 0$) levels and that between $B^2\Sigma_u^+$ ($\upsilon = 0$) and $X^2\Sigma_g^+$ ($\upsilon'' = 1$) levels, as a function of the angle α, and find that for the 427.8 nm transition, the population difference exhibits a maximum at $\alpha = 0°$ and it decreases monotonically as $|\boldsymbol{\alpha}|$ increases, while for the 391.4 nm transition, the maximum values are located at the two symmetric positions of $0° < |\boldsymbol{\alpha}| < 45°$ with a dip at $\alpha = 0°$. These results are in good agreement with the experimental data shown in Fig. 2.6.

2.3 Direct Observation of $X^2\Sigma_g^+$-$A^2\Pi_u$ Coupling

We have demonstrated in Sect. 2.2 that the lasing intensities of N_2^+ can be significantly enhanced or reduced by modulating the polarization of the pump laser pulse, and that the ellipticity dependences of two lasing lines at 391.4 and 427.8 nm can be well explained by the post-ionization coupling among the $X^2\Sigma_g^+$, $A^2\Pi_u$, and $B^2\Sigma_u^+$ states of N_2^+. However, in the above-mentioned polarization modulation methods, both the stronger electric field component used for the ionization of N_2, and the weaker one used as the post-ionization coupling are from the same pump laser pulse, so that the ionization and coupling are entangled within the laser pulse and cannot be well separated and manipulated. Therefore, it would be helpful to provide deeper insight into the coupling mechanism if one could directly show the coupling effect by pump-probe methods, in which the coupling process can be independently operated without disturbing the ionization process. In the following, we will present experimental results for direct observation and manipulation of the coupling in N_2^+ lasing using pump-probe methods [28, 29].

2.3.1 Pump-Coupling-Probe Scheme

Here we design a pump-coupling-probe scheme (see Fig. 2.7), in which we employ an intense 800 nm pump laser pulse (40 fs, 700 μJ) to induce the ionization of N_2, a weak 800 nm laser pulse (40 fs, 20–200 μJ) to manipulate the $X^2\Sigma_g^+$ ($\upsilon'' = 0$)-$A^2\Pi_u$ ($\upsilon' = 2$) coupling of N_2^+, and then a much weaker 400 nm broadband pulse (40 ~ 60 fs, 50 nJ) to externally seed the N_2^+ gain medium [28]. Since the perpendicular $X^2\Sigma_g^+$-$A^2\Pi_u$ transition is sensitive to the polarization direction of the coupling field, it is expected that when we change the polarization direction of the coupling field with respect to that of the pump laser pulse, the population in the $X^2\Sigma_g^+$ ($\upsilon'' = 0$)

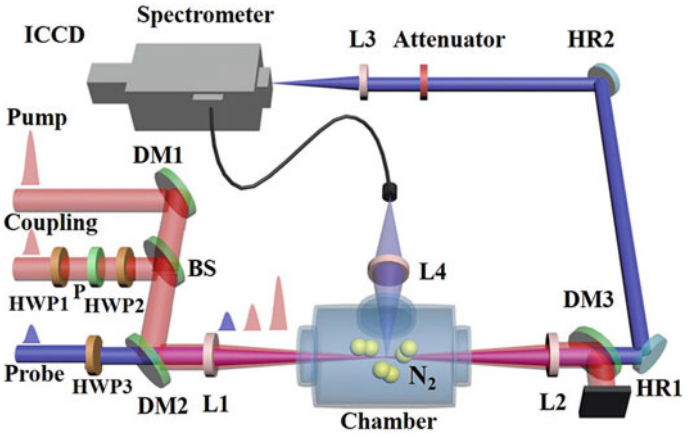

Fig. 2.7 Schematic diagram of the pump-coupling-probe experimental setup. HWP: half-wave plate (1, 2: for 800 nm; 3: for 400 nm); P: polarizer; DM: dichromic mirror; BS: beam splitter; L: fused silica lens (1: $f = 40$ cm; 2: $f = 30$ cm; 3: $f = 6$ cm; 4: $f = 6$ cm); F: filter; HR1 and HR2: 400 nm high reflection mirror

can be depleted to some extent accordingly, and thus the 391.4 nm lasing intensity can be modulated.

In this experiment [28], the delay time between the pump and the coupling pulses, and that between the pump and the seed pulses are set at 70 fs and 200 fs, respectively. With the delay time of 70 fs, the molecular axis of N_2^+ ions prepared along the polarization direction of the pump pulse will not change much after the ionization, and the interference effect between the pump and coupling fields can be negligible because these two pulses (40 fs) are almost separated completely. Figure 2.8 shows the intensity of the 391.4 nm lasing as a function of the angle β between the polarization directions of the pump and the coupling pulses. $\beta = 0°$ and 90° mean that

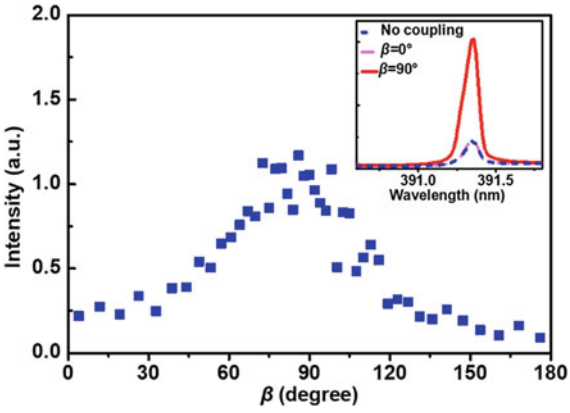

Fig. 2.8 The intensity of the 391.4 nm lasing as a function of β. Inset: The forward lasing spectra obtained in the presence of the coupling field for the cases of $\beta = 0°$ (pink dash) and $\beta = 90°$ (red solid), and that obtained in the absence of the coupling field (blue dash)

the polarization directions of these two pulses are parallel and perpendicular, respectively. In this measurement, the pressure of N_2 gas in the chamber is 10 mbar, and the coupling laser energy is 180 μJ. As an example, the lasing spectra measured at $\beta = 0°$ and $\beta = 90°$ are shown in the inset of Fig. 2.8, where the lasing spectrum in the absence of the coupling pulse is also presented. It can be seen from Fig. 2.8 that the 391.4 nm lasing intensity increases from $\beta = 0°$ to 90°, and the decreases from $\beta = 90°$ to 180°, with the maximum value taking at $\beta \sim 90°$.

This indicates that as the polarization directions of these two pulses are perpendicular, the population in the $X^2\Sigma_g^+$ ($\upsilon'' = 0$) can be depleted more efficiently, which is in good agreement with our conjecture that the perpendicular transition between the $X^2\Sigma_g^+$ ($\upsilon'' = 0$) and $A^2\Pi_u$ states is sensitive to the polarization direction of the coupling laser, so that the optimized population inversion between the $B^2\Sigma_u^+$ ($\upsilon = 0$) and $X^2\Sigma_g^+$ ($\upsilon'' = 0$) states takes place when the polarization direction of the coupling field is set to be perpendicular to that the pump laser pulse, with which the N_2 molecules having the molecular axis parallel to the pump laser polarization are preferentially ionized [30].

Furthermore, since the coupling laser wavelength is resonant with the $X^2\Sigma_g^+$ ($\upsilon'' = 0$)-$A^2\Pi_u$ ($\upsilon' = 2$) transition, it is also expected that the efficiency of the post-ionization optical coupling shall be strongly dependent on the intensity of the coupling field. Therefore, we measure in Fig. 2.9 the intensity of the 391.4 nm lasing as a function of the energy of the coupling laser pulse for the two cases of $\beta = 0°$ (red dot) and $\beta = 90°$ (blue rectangle), respectively. It can be clearly seen from Fig. 2.9 that in the case of $\beta = 90°$ the 391.4 nm lasing signal becomes stronger as the energy of the coupling pulse increases, but in the case of $\beta = 0°$ the 391.4 nm lasing signal does not change much as the energy of the coupling pulse varies. That is, as $\beta = 90°$ the 391.4 nm lasing is sensitive to the coupling laser energy, but as $\beta = 0°$ it is reverse. Based on the above results, we conclude that as the polarization directions of the pump and coupling pulses are parallel ($\beta = 0°$) there is almost no coupling

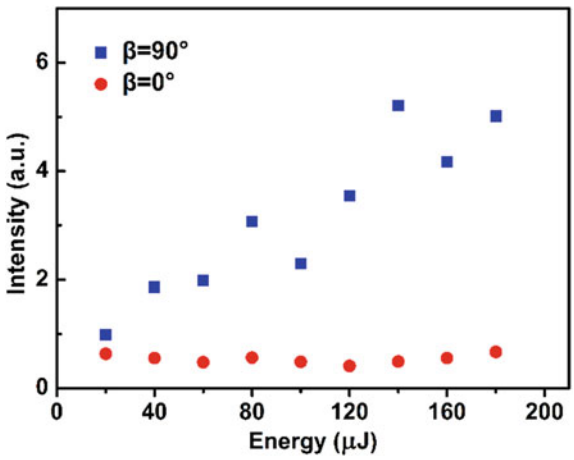

Fig. 2.9 Energy effect of the coupling field on the 391.4 nm lasing intensity for the cases of $\beta = 0°$ (red dot) and $\beta = 90°$ (blue rectangle)

between the $A^2\Pi_u$ ($\upsilon' = 2$) and $X^2\Sigma_g{}^+$ ($\upsilon'' = 0$) states, but as they are perpendicular, there exists the optical coupling that induce the depletion of the population in the $X^2\Sigma_g{}^+$ ($\upsilon'' = 0$) state, and thus the variation in the 391.4 nm lasing intensity.

2.3.2 *Broadband Few-Cycle Laser Ionization-Coupling Scheme*

It is well known that the energy separation information of two levels in an optical transition can be obtained by Fourier transform of its temporal oscillation waveform. Therefore, if when the coupling field is temporally scanned in a pump-probe scheme, one can observe temporal oscillations of $N_2{}^+$ lasing with the oscillation frequencies correspond to the $X^2\Sigma_g{}^+$ ($\upsilon'' = 0$)-$A^2\Pi_u$ (υ') transitions, it would provide a direct evidence for the modulation of the population in the $X^2\Sigma_g{}^+$ ($\upsilon'' = 0$) state through the optical coupling. To verify this idea, we design a broadband ionization-coupling scheme, in which we employ an intense few-cycle pulse (~7 fs) to induce the ionization of N_2 and generate the self-seed, and a weak few-cycle pulse, whose bandwidth can cover the $X^2\Sigma_g{}^+$ ($\upsilon'' = 0$)-$A^2{}_u$ ($\upsilon' = 1, 2, 3$) transitions, serves as a coupling field to modulate the population in the $X^2\Sigma_g{}^+$ ($\upsilon'' = 0$) state [29]. By measuring the intensity of the $B^2\Sigma_u{}^+$ ($\upsilon = 0$)-$X^2\Sigma_g{}^+$ ($\upsilon'' = 0$) lasing at 391.4 nm as a function of the pump-probe time delay, we can investigate how the $A^2\Sigma_u$-$X^2\Sigma_g{}^+$ coupling modulate the lasing temporally.

In Fig. 2.10, we show the dependences of the 391.4 nm lasing intensity on the delay time between the ionization (pump) and the coupling (probe) pulses. Both the ionization and coupling laser pulses are close to linear polarization with the ellipticity of ~0.1. The red and black curves in Fig. 2.10 represent that the time-dependent $N_2{}^+$ lasing is measured respectively under the conditions that the polarization directions

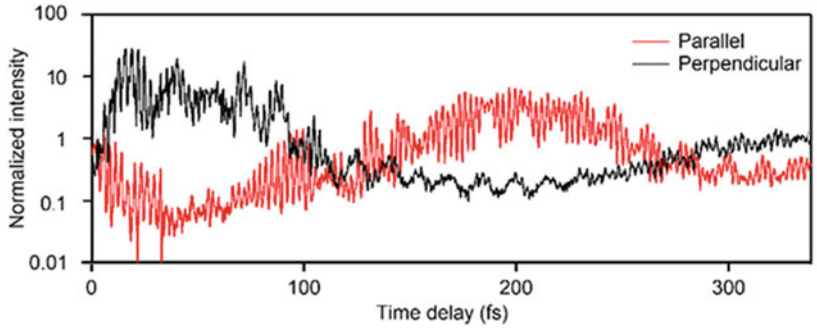

Fig. 2.10 The intensity of 391.4 nm lasing as a function of the time delay between the ionization (pump) and the coupling (probe) pulses measured as the polarization directions of the pump and probe are parallel (red curve) and perpendicular (black curve) to each other. The lasing intensity is normalized by the lasing intensity obtained by the pump laser pulse only

of the ionization and coupling pulses are parallel (red curve) and perpendicular (black curve) with each other. It can be seen from Fig. 2.10 that for both cases the laser intensities oscillate strongly. In the parallel condition, the lasing intensity takes the minimum value at ~20–45 fs and the maximum value at ~200 fs. In the perpendicular case, the lasing intensity takes the maximum value at ~5–45 fs and the minimum value at ~200 fs. At around 15~45 fs, the lasing intensity in the perpendicular condition is ~30 times stronger than that obtained by the pump pulse only, which is consistent with our previous study [26], where we observed ~100 times enhancement of the lasing intensity when we used the polarization modulated pulse whose polarization direction changes by 90° within 20 fs.

In addition, it can be seen from Fig. 2.10 that there is a slow modulation (~300 fs period) of the lasing intensity for both the conditions, which are anti-phased. The slow modulations can be attributed to the field-free rotation motion of N_2^+. The discussion on the contribution of the molecular alignment to the generation of the N_2^+ lasing can be found in [34]. Since the N–N molecular axis of N_2^+ will rotate after ionization, the probability of the perpendicular $X^2\Sigma_g^+$-$A^2\Pi_u$ transition induced by the coupling pulse with the fixed polarization direction will vary as a function of the delay time between the pump and the coupling pulses. As a result, the perpendicular transition of the $X^2\Sigma_g^+$-$A^2\Pi_u$ state effectively enhances the $X^2\Sigma_g^+$-$B^2\Sigma_u^+$ lasing at ~20–45 fs (see black curve) and 200 fs (see red curve). At the delay time of 16 fs, the lasing intensity obtained in the perpendicular case is 300 times larger than that obtained in the parallel case.

It can also be seen in Fig. 2.10 that the lasing intensities for both the parallel and perpendicular conditions exhibit the frequency oscillations with the periods of 2–3 fs, and of 13–20 fs. After the Fourier transform of the lasing oscillations, we obtain the frequency spectra of time-dependent N_2^+ lasing intensity under the (a) parallel and (b) perpendicular conditions, as shown in Fig. 2.11. From the frequency spectra, it can be observed that there are three peaks appearing in the range of 0.3–0.5

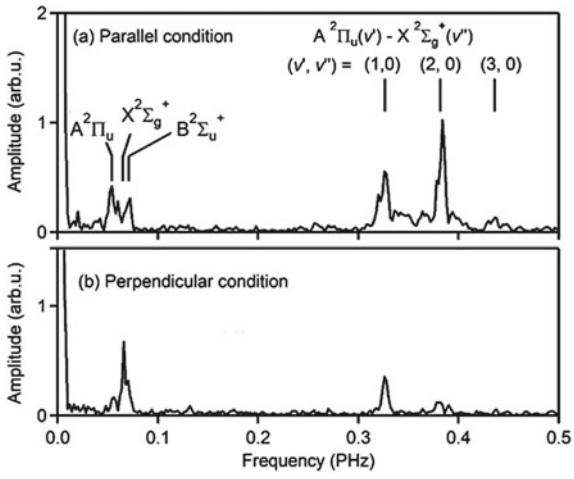

Fig. 2.11 Fourier transform spectra of time-dependent N_2^+ lasing intensity under the **a** parallel and **b** perpendicular conditions

PHz at 0.33, 0.38, and 0.44 PHz in the parallel condition, and two peaks appearing at 0.33 and 0.38 PHz in the perpendicular condition with relatively weak amplitudes. These peaks in the range 0.3–0.5 PHz can be assigned to the energy separations of the ro-vibrational levels between the $A^2\Pi_u$ ($v' = 1, 2, 3$) and $X^2\Sigma_g^+$ ($v'' = 0$) states. In addition, it can also be seen in Fig. 2.11 that there are peaks at the low frequency range of 0.05–0.08 PHz, which are assigned to the vibrational level separations of the three respective electronic states of $X^2\Sigma_g^+$, $A^2\Pi_u$, and $B^2\Sigma_u^+$. These results clearly show that the lowest three electronic states in N_2^+ are coupled coherently by the ionization pulse, resulting in the final modulations in the $B^2\Sigma_u^+$-$X^2\Sigma_g^+$ lasing by the coupling pulse.

2.4 Optimization of N_2^+ Lasing by Modulating the Polarization State of the Pump Laser Pulse

So far, we have revealed, based on the above results, that the strong-field-induced N_2^+ lasing can be convincingly explained by the post-ionization $B^2\Sigma_u^+$-$X^2\Sigma_g^+$-$A^2\Pi_u$ three-state coupling model. This interpretation will be very helpful for developing a variety of techniques to manipulate and optimize N_2^+ lasing. In particular, it is known from Sect. 2.2 that within the pump pulse two processes essentially take place to achieve the lasing emission: (i) the preparation of population in the lowest three $X^2\Sigma_g^+$, $A^2\Pi_u$ and $B^2\Sigma_u^+$ states through the ionization of N_2 by the central (strongest) part of the pulse, and (ii) the modulation of the population in the $X^2\Sigma_g^+$ state by the later part of the pulse. Therefore, in the following we will present two examples of optimizing N_2^+ lasing at 391.4 nm by modifying the relative amplitudes and the temporal separation of the two polarization components in an elliptically modulated ultrashort pulsed laser field.

2.4.1 Optimization of N_2^+ Lasing Using Different Orders of QWPs

As presented in Sect. 2.2.2, it is found that the 391.4 nm lasing intensity can be significantly enhanced by changing the angle α between the polarization direction of the pump laser pulse and the optical axis of the 7-QWP, which is ascribed to the balance between the ionization rate of N_2 and the coupling efficiency of N_2^+ induced respectively by the the two polarization components in the elliptically modulated ultrashort pulsed laser field by the 7-QWP. Here we further investigate the optimization of N_2^+ lasing using different orders of QWPs.

In Fig. 2.12, we present the lasing intensity at 391.4 nm measured with *n*-QWP in an external seed scheme as a function of the angle α, where $n = 0, 3, 7, 10$, respectively [27]. It can be seen from Fig. 2.12 that as α changes from 0° to 45°

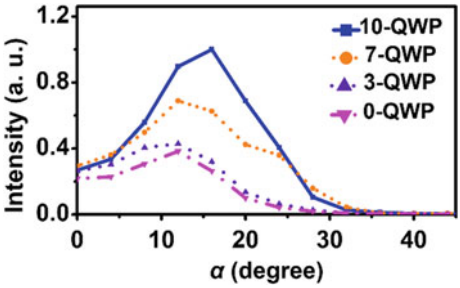

Fig. 2.12 The lasing intensity at 391.4 nm as a function of α with n = 0 (purple downward triangle), 3 (violet upward triangle), 7 (orange dot), 10 (blue rectangle)

the 391.4 nm lasing intensity first increases and then decreases for all the four QWP cases. It can also be noted that the maximum intensity of the 391.4 nm lasing increases monotonically as the order of the QWP increases from $n = 0$ to 10, and that the angle α, at which the lasing intensity becomes maximum, moves from $\alpha \sim 12°$ to $\alpha \sim 18°$.

The optimization of N_2^+ lasing using n-order QWPs can be well understood based on the coupling model due to the balance between the ionization and the coupling induced respectively by the the two polarization components in the elliptically pulsed laser field. As shown in Fig. 2.13, it can be seen that when n increases from 0 to 10, for a certain angle of α, although the relative amplitudes of the two polarization components, E_y and E_x, keep constant, their temporal separation in the pump pulse increases, which means that after the ionization of N_2 by the strongest part of the E_y component, the effective coupling part in the E_x component becomes more due to the more delayed $E_x(t)$ component. This gives rise to the more efficient depletion in the $X^2\Sigma_g^+$ ($\upsilon'' = 0$) state through the $X^2\Sigma_g^+$-$A^2\Pi_u$ vertical transition, leading to the enhanced lasing intensity with increasing n from 0 to 10.

Therefore, the key factor for the optimization of the $B^2\Sigma_u^+$ ($\upsilon = 0$)-$X^2\Sigma_g^+$ (υ"= 0) lasing is the $E_x(t)$ component of the laser field interacting with N_2^+ in the latter part of the laser field. However, it should be emphasized that although the experimental results shown in Fig. 2.12 demonstrate that the lasing intensity increases as the QWP order increases (up to $n = 10$), there should be an upper limit for the order n when the lasing intensity starts to decrease. Actually, it is estimated that when the order n increases up to about $n = 15$, the two components, E_x and E_y, of the pump laser pulse are separated in time almost completely, and therefore, the lasing signal intensity could not increase more even when the order increases more. Furthermore, if the

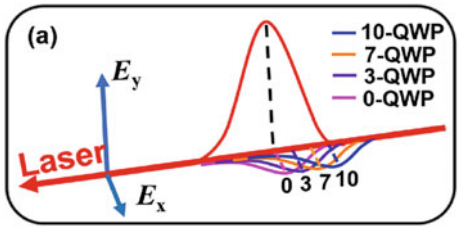

Fig. 2.13 Schematic diagram of the variation in the temporal separation between the two polarization components for the cases of $n = 0, 3, 7, 10$, respectively

order increases further, the intensity of these two components decreases because of the frequency chirp, and consequently, the lasing intensity will start dropping.

2.4.2 *Asymmetric Enhancement of N_2^+ Lasing in an Elliptically Modulated Laser Field.*

In Sect. 2.4.1, we demonstrate the optimization of N_2^+ lasing at 391.4 nm in an elliptical laser field modulated by *n*-QWPs for the angle α in a small range of $\alpha = 0°–45°$. Here we demonstrate that when we extend the angle α to a larger angle range of $\alpha \sim 0°–90°$, an asymmetric enhancement feature of the 391.4 nm lasing is observed, which further shows the effect of the relative amplitudes of the two polarization components on the ionization and coupling in the birefringence-modulated elliptically laser fields [35].

In Fig. 2.14, we plot the intensity of 391.4 nm lasing measured in an external seed scheme as a function of α, in the range of 0°–90° [35]. The N_2 gas pressure is 8 mbar, and the energies of the pump and probe laser pulses are 0.7 mJ and 100 nJ, respectively. It can be seen from Fig. 2.14 that the optimized intensities of the 391.4 nm lasing appear at $\alpha \sim 14°$ and 73° with the ellipticity of $\varepsilon \sim 0.3$, but the lasing enhancement at $\alpha \sim 14°$ is about 3 times larger than that at $\alpha \sim 73°$, even though the laser pulse at these two positions have almost the same ellipticity value of $\varepsilon \sim 0.3$.

The above asymmetric enhancements of the 391.4-lasing intensity in the α range of 10°–20° and 70°–80° for the 7-QWP case can be ascribed to the different population depletion in the $X^2\Sigma_g^+(\upsilon'' = 0)$ due to the different $X^2\Sigma_g^+$-$A^2\Pi_u$ coupling contribution provided by the rear laser field after ionization. Based on (2.3), after passing through 7-QWP, the laser pulse is divided into the two polarization components, where when $0° < \alpha < 45°$ (Fig. 2.15a), the amplitude of $\boldsymbol{E}_\mathbf{y}$ is larger than that of $\boldsymbol{E}_\mathbf{x}$, while when $45° < \alpha < 90°$ (Fig. 2.15b), the situation is reversed. It can be seen from Fig. 2.15 that when $0° < \alpha < 45°$ the ionization of N_2 is induced by the yellow part in the stronger component (yellow part) of the pulse, and subsequently, the vertical $X^2\Sigma_g^+$-$A^2\Pi_u$ coupling proceeds by the weaker component in the violet

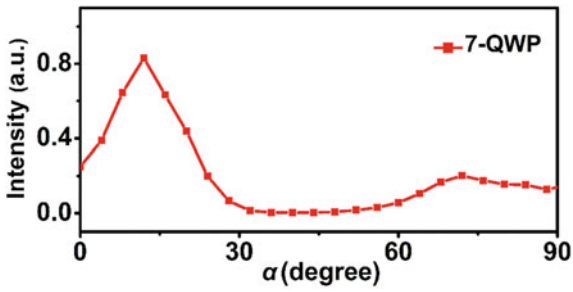

Fig. 2.14 The intensity of the 391.4 nm lasing measured in the 7-QWP modulated laser field as a function of the angle α between the polarization direction of the linearly polarized laser pulse and the fast axis of 7-QWP

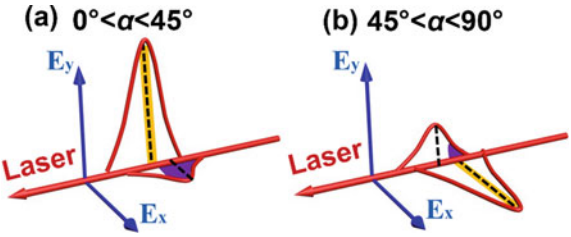

Fig. 2.15 Schematic diagram of the variation in the amplitudes of the two orthogonally-polarized laser components in the 7-QWP modulated laser field with **a** $0° < \alpha < 45°$ and **b** $45° < \alpha < 90°$

region. On the other hand, when $45° < \alpha < 90°$, if the ionization process occurs within the stronger component, only a small portion (violet region) of the weaker component of the pulse can contribute to the coupling process. Therefore, even though the laser fields in the two α ranges shown in Fig. 2.15a and b have the same ellipticity, the relative amplitudes of E_x and E_y is opposite in the two cases, leading to the different strengths of the $X^2\Sigma_g^+$-$A^2\Pi_u$ coupling after the ionization of N_2, and thus the different 391.4 nm lasing intensities.

2.5 Summary

In summary, we have investigated the N_2^+ lasing actions induced by intense laser fields, and presented indirect and direct experimental evidences for the post-ionization optical coupling in N_2^+ in intense laser fields by modulating the polarization state of the pump pulse, as well as by using pump-probe methods. We demonstrated that the N_2^+ lasing at 391.4 nm, corresponding to the $B^2\Sigma_u^+$ ($\upsilon = 0$)-$X^2\Sigma_g^+$ ($\upsilon'' = 0$) transition, is strongly sensitive to the polarization state of the rear part of the pump laser pulse, and contributed it to the efficient population transfer from the ground $X^2\Sigma_g^+$ ($\upsilon'' = 0$) state to the first excited $A^2\Pi_u$ state of N_2^+.

By using pump-probe methods, we further showed that the vertical transition between the $X_2\Sigma_g^+$ and $A^2\Pi_u$ states of N_2^+ are sensitive to the polarization direction and the energy of the resonant coupling pulse. In addition, by introducing the broadband coupling pulse, we were able to show the optical transitions between different vibrational levels of the $X^2\Sigma_g^+$ and $A^2\Pi_u$ states by Fourier transforms of the lasing intensity oscillations observed in the temporal domain.

With the knowledge of the balance between the ionization of N_2 and the coupling of N_2^+ in the elliptically polarized pulse, we showed the optimization of N_2^+ lasing at 391.4 nm by changing the temporal separation between the two perpendicular polarization components and their relative amplitudes by using multi-order QWPs. We also revealed that the N_2^+ lasing at 427.8 nm, corresponding to the $B^2\Sigma_u^+$ ($\upsilon = 0$)-$X^2\Sigma_g^+$ ($\upsilon'' = 0$) transition, cannot be well manipulated by modulating the polarization state of the rear part of the laser pulse. We have convincingly explained the different ellipticity dependence on the two N_2^+ lasing lines at 391.4 and 427.8 nm by the post-ionization coupling model.

The results presented in this chapter provide reliable evidences for understanding the N_2^+ lasing mechanism, based which the optimization of intense N_2^+ lasing can be realized, which will benefit for the promising application of air lasing in a variety of fields such as remote sensing and standoff spectroscopy.

Acknowledgements The work is supported in part by National Natural Science Foundation of China (NSFC) (61625501, 61427816) and by the two MEXT (Ministry of Education, Culture, Sports, Science and Technology) Grant-in-Aid for Specially Promoted Research (#19002006 and #15H05696).

References

1. A.L. Gaeta, Catastrophic collapse of ultrashort pulses. Phys. Rev. Lett. **84**, 3582 (2000). https://doi.org/10.1103/physrevlett.84.3582
2. H.L. Xu, A. Azarm, J. Bernhardt, Y. Kamali, S.L. Chin, The mechanism of nitrogen fluorescence inside a femtosecond laser filament in air. Chem. Phys. **360**, 171 (2009). https://doi.org/10.1016/j.chemphys.2009.05.001
3. J.L. Liu, J.M. Dai, S.L. Chin, X.C. Zhang, Broadband terahertz wave remote sensing using coherent manipulation of fluorescence from asymmetrically ionized gases. Nat. Photon. **4**, 627 (2010). https://doi.org/10.1038/nphoton.2010.165
4. H.L. Xu, S.L. Chin, Femtosecond laser filamentation for atmospheric sensing. Sensors **11**, 32 (2011). https://doi.org/10.3390/s110100032
5. Q. Luo, W. Liu, S.L. Chin, Lasing action in air induced by ultra-fast laser filamentation. Appl. Phys. B **76**, 337–340 (2003). https://doi.org/10.1007/s00340-003-1115-9
6. W. Chu, B. Zeng, J. Yao, H. Xu, J. Ni, G. Li, H. Zhang, F. He, C. Jing, Y. Cheng, Z. Xu, Multiwavelength amplified harmonic emissions from carbon dioxide pumped by mid-infrared femtosecond laser pulses. EPL—Europhys. Lett. **97**, 64004 (2012). https://doi.org/10.1209/0295-5075/97/64004
7. S. Yuan, T.J. Wang, Y. Teranishi, A. Sridharan, S.H. Lin, H.P. Zeng, S.L. Chin, Lasing action in water vapor induced by ultrashort laser filamentation. Appl. Phys. Lett. **102**, 224102 (2013). https://doi.org/10.1063/1.4809585
8. A. Dogariu, J.B. Michael, M O. Scully, R.B. Miles, High-gain backward lasing in air. Science **331**, 442-445 (2011). https://doi.org/10.1126/science.1199492
9. A. Laurain, M. Scheller, P. Polynkin, Low-threshold bidirectional air lasing. Phys. Rev. Lett. **113**, 253901 (2014). https://doi.org/10.1103/PhysRevLett.113.253901
10. D. Kartashov, S. Ališauskas, A. Baltuška, A. Schmitt-Sody, W. Roach, P. Polynkin, Remotely pumped stimulated emission at 337 nm in atmospheric nitrogen. Phys. Rev. A **88**, 041805 (2013). https://doi.org/10.1103/PhysRevA.88.041805
11. S. Mitryukovskiy, Y. Liu, P. Ding, A. Houard, A. Mysyrowicz, Backward stimulated radiation from filaments in nitrogen gas and air pumped by circularly polarized 800 nm femtosecond laser pulses. Opt. Express **22**, 12750–12759 (2014). https://doi.org/10.1364/OE.22.012750
12. J. Yao, H. Xie, B. Zeng, W. Chu, G. Li, J. Ni, H. Zhang, C. Jing, C. Zhang, H. Xu, Y. Cheng, Z. Xu, Gain dynamics of a free-space nitrogen laser pumped by circularly polarized femtosecond laser pulses. Opt. Express **22**, 19005–19013 (2014). https://doi.org/10.1364/OE.22.019005
13. J. Ni, W. Chu, H. Zhang, C. Jing, J. Yao, H. Xu, B. Zeng, G. Li, C. Zhang, S. Chin, Y. Cheng, Z. Xu, Harmonic-seeded remote laser emissions in N2-Ar, N2-Xe and N2-Ne mixtures: a comparative study. Opt. Express **20**, 20970–20979 (2012). https://doi.org/10.1364/OE.20.020970

14. J. Yao, B. Zeng, H. Xu, G. Li, W. Chu, J. Ni, H. Zhang, S. L. Chin, Y. Cheng, Z. Xu, High-brightness switchable multiwavelength remote laser in air. Phys. Rev. A **84**, 051802 (2011). https://doi.org/10.1103/PhysRevA.84.051802
15. H. Li, D. Yao, S. Wang, Y. Fu, H. Xu, Air lasing: phenomena and mechanisms. Chin. Phys. B **28**, 114204 (2019). https://doi.org/10.1088/1674-1056/ab47f5
16. H. Zhang, C. Jing, J. Yao, G. Li, B. Zeng, W. Chu, J. Ni, H. Xie, H. Xu, S. L. Chin, K. Yamanouchi, Y. Cheng, Z. Xu, Rotational coherence encoded in an "air-laser" spectrum of nitrogen molecular ions in an intense laser field. Phys. Rev. X **3**, 041009 (2013). https://doi.org/10.1103/PhysRevX.3.041009
17. Z. Liu, J. Yao, H. Zhang, B. Xu, J. Chen, F. Zhang, Z. Zhang, Y. Wan, W. Chu, Z. Wang, Y. Cheng, Extremely nonlinear Raman interaction of an ultrashort nitrogen ion laser with an impulsively excited molecular wave packet. Phys. Rev. A **101**, 043404 (2020). https://doi.org/10.1103/PhysRevA.101.043404
18. P.R. Hemmer, R.B. Miles, P. Polynkin, T. Siebert, A.V. Sokolov, P. Sprangle, M.O. Scully, Standoff spectroscopy via remote generation of a backward-propagating laser beam. Proc. Nat. Acad. Sci. USA **108**, 3130 (2011). https://doi.org/10.1073/pnas.1014401107
19. G. Herzberg, Molecular spectra and molecular structure. I. spectra of diatomic molecules. Am. J. Phys. **19**, 390(1951). https://doi.org/10.1119/1.1932852
20. A. Becker, A.D. Bandrauk, S.L. Chin, S-matrix analysis of non-resonant multiphoton ionisation of inner-valence electrons of the nitrogen molecule. Chem. Phys. Lett. **343**, 345–350 (2001). https://doi.org/10.1016/s0009-2614(01)00705-9
21. S.F. Zhao, C. Jin, A.T. Le, T.F. Jiang, C.D. Lin, Determination of structure parameters in strong-field tunneling ionization theory of molecules. Phys. Rev. A, 82, 049903 (2010) (Phys. Rev. A **81**, 033423 (2010)). https://doi.org/10.1103/PhysRevA.82.049903
22. A. Azarm, P. Corkum, P. Polynkin, Optical gain in rotationally excited nitrogen molecular ions. Phys. Rev. A **96**, 051401 (2017). https://doi.org/10.1103/PhysRevA.96.051401
23. Y. Liu, P. Ding, G. Lambert, A. Houard, V. Tikhonchuk, A. Mysyrowicz, Recollision-induced superradiance of ionized nitrogen molecules. Phys. Rev. Lett. **115**, 133203 (2015). https://doi.org/10.1103/PhysRevLett.115.133203
24. J. Yao, S. Jiang, W. Chu, B. Zeng, C. Wu, R. Lu, Z. Li, H. Xie, G. Li, C. Yu, Z. Wang, H. Jiang, Q. Gong, Y. Cheng, Population redistribution among multiple electronic states of molecular nitrogenions in strong laser fields. Phys. Rev. Lett. **116**, 143007 (2016). https://doi.org/10.1103/PhysRevLett.116.143007
25. H. Xu, E. Lötstedt, A. Iwasaki, K. Yamanouchi, Sub-10-fs population inversion in N2+ in air lasing through multiple state coupling. Nat. Commun. **6**, 8347 (2015). https://doi.org/10.1038/ncomms9347
26. H. Li, M. Hou, H. Zang, Y. Fu, E. Lötstedt, T. Ando, A. Iwasaki, K. Yamanouchi, H. Xu, Significant enhancement of N_2^+ lasing by polarization-modulated ultrashort laser pulses. Phys. Rev. Lett. **122**, 013202 (2019). https://doi.org/10.1103/PhysRevLett.122.013202
27. Y. Fu, E. Lötstedt, H. Li, S. Wang, D. Yao, T. Ando, A. Iwasaki, F.H.M. Faisal, K. Yamanouchi, H. Xu, Optimization of N_2^+ lasing through population depletion in the $X^2\Sigma_g^+$ state using elliptically-modulated ultrashort intense laser fields. Phys. Rev. R. **2**, 012007(R) (2020). https://doi.org/10.1103/PhysRevResearch.2.012007
28. S. Wang, Y. Fu, D. Yao, S. Chen, W. Zhang, H. Li, H. Xu, Observation of the optical $X^2\Sigma_g^+ - A^2\Pi_u$ coupling in N_2^+ lasing induced by intense laser field. Chin. Phys. B **28**, 123301 (2019). https://doi.org/10.1088/1674-1056/ab54b1
29. T. Ando, E. Lötstedt, A. Iwasaki, H. Li, Y. Fu, S. Wang, H. Xu, K. Yamanouchi, Rotational, vibrational, and electronic modulations in N_2^+ lasing at 391.4 nm: evidence of coherent $B^2\Sigma_u^+ - X^2\Sigma_g^+ - A^2\Pi_u$ coupling. Phys. Rev. Lett. **123**, 203201 (2019). https://doi.org/10.1103/PhysRevLett.123.203201
30. D. Pavičić, K.F. Lee, D.M. Rayner, P.B. Corkum, D.M. Villeneuve, Direct measurement of the angular dependence of ionization for N_2, O_2, and CO_2 in intense laser fields. Phys. Rev. Lett. **98**, 243001 (2007). https://doi.org/10.1103/PhysRevLett.98.243001

31. S.R. Langhoff, Jr C.W. Bauschlicher, H. Partridge, Theoretical study of the N_2^+ Meinel system. J. Chem. Phys. **87**, 4716 (1987). https://doi.org/10.1063/1.452835
32. Z.H. Chang, Single attosecond pulse and xuv supercontinuum in the high-order harmonic plateau. Phys. Rev. A **70**, 043802 (2004). https://doi.org/10.1103/physreva.70.043802
33. F.R. Gilmore, R.R. Laher, P.J. Espy, Franck–Condon factors, r-centroids, electronic transition moments, and Einstein coefficients for many nitrogen and oxygen band systems. J. Phys. Chem. Ref. Data **21**, 1005–1107 (1992). https://doi.org/10.1063/1.555910
34. H. Xu, E. Lötstedt, T. Ando, A. Iwasaki, K. Yamanouchi, Alignment-dependent population inversion in N_2^+ in intense few-cycle laser fields. Phys. Rev. A **96**, 041401 (2017). https://doi.org/10.1103/PhysRevA.96.041401
35. Y. Fu, S. Chen, S. Wang, W. Zhang, D. Yao, H. Zang, H. Li, H. Xu, Asymmetric enhancement of N_2^+ lasing in intense, birefringence-modulating elliptical laser fields. Opt. Express **28**, 23274–23283 (2020). https://doi.org/10.1364/OE.389284

Chapter 3
Volterra Integral Equation Approach to the Electron Dynamics in Intense Optical Pulses

Yosuke Kayanuma

Abstract Recent advances in laser technology have made it possible to utilized very high intensity optical pulses with wide range of wave-length to pump electrons in materials. This opened a new era in experimental physics to use pulse-lasers as a tool to manipulate electrons not only for the ultrafast probe into electronic states in materials, but also for a new means to obtain light with much higher frequebecause it is morencies than the pump-pulse. From theoretical side, this requires to establish a coherent theoretical framework to analyze the ultra fast dynamics of the electrons driven by high intensity light fields. In this article, I propose a novel theoretical technique to approach this subject. We formulate the Volterra integral equations of second kind for that purpose. Although this is equivalent to the differential equations of Schrödinger, it has an advantage to treat the light-matter interactions as two independent modules; the intra-band driving and the inter-band driving. The expression for the former can be obtained analytically in many cases and is incorporated into the theory as an integral kernel. The formalism is applied to two simple models, the population inversion in the molecules under intense laser beams in air, and the high harmonic generations in solids.

3.1 Introduction

Thanks to the advances of high intensity and ultrashort laser technology, various new aspects of the quantum dynamics in the electronic excited states have been revealed. In understanding these phenomena, it may be said that the wave-like picture of light of Maxwell revived rather than the corpuscular picture of photons of Einstein.

Y. Kayanuma (✉)
Laboratory for Materials and Structures, Tokyo Institute of Technology, Nagatsuta, Yokohama, Japan
e-mail: kayanuma.y.aa@m.titech.ac.jp

Department of Physical Sciences, Osaka Prefecture University, Sakai, Osaka, Japan

K. Yamanouchi et al. (eds.), *Progress in Ultrafast Intense Laser Science XVI*,
Topics in Applied Physics 141, https://doi.org/10.1007/978-3-030-75089-3_3

The primary interest is in the phenomena of photo-ionization by a long wavelength but intense light field. In this connection, one of the surprising achievements in this decade is the demonstration of carrier multiplication in semiconductors by terahertz pulses with magnitude of 1–MVcm^{-1} [1]. Such an excitation of electrons to the higher excited states may induce further extraordinary dynamical processes. For the salient examples in this category, we may name the phenomena called the high harmonic generation (HHG) from the strongly laser-driven atoms [2] and solids [3].

These developments in experimental physics require novel theoretical frameworks to treat such a highly nonlinear interactions of light and matter non-perturbatively. Since the pioneering work by Keldysh [4], a number of elaborate theories have been proposed on this subject, both in the atoms and molecules [5–8] and in solids [9, 10]. As noticed by Becker and Faisa [11], the highly nolinear electron dynamics in the intense fields can be formulated as a quest for the scattering matrix. An important point in calculating the scattering matrix is that the equation of motion for a free electron in the arbitrary time-dependent electric field has already been solved. The eigen state is called a Volkov state [12] in the free vacuum, and a Houston state [13] in the periodic lattice structure.

In the present article, I would like to add yet another contribution to this subject. In our approach, we formulate the time-dependent problem in the form of an integral equation of Volterra-type, where the integral kernel is explicitly obtained using the Houston state representation. Although this is equivalent to the numerical solution of the Schrödinger's differential equation, it has some advantages over the differential equation.

For the purpose of demonstration, I take two examples of application, the problem of population inversion in air-lasing, and the HHG in solids. These examples represent two typical situations of the spatial extension of light-matter interaction. In the first example, the optical transition is localized at the position of the molecule. In the case of HHG in solids, the transtion occurs throughout the bulk crystal from the valence band to the conduction band according to the translational symmetry of the crystal lattice. It will be be shown that, in both cases, a closed expression for the optical responses is obtained.

3.2 Population Inversion in N_2^+ Ions in the Intense Laser Beam

It is well known that, when an intense light beam passes through a transparent medium, say air, self focusing and filamentation of the beam often occur due to the nonlinear optical effects [14]. Sometimes this was a nuisance for experimentalists. Since the advent of high intensity ultrashort lase pulses, a possibility of application of this phenomenon emerged. The filaments in air are often accompanied with luminescence or even lasing to forward or backward [15] of the pumping beams. The spectrum of backward scattered fluorescence or lasing will be a source of remote sensing. In

the case of N_2 molecules in air, the forward lasing is the dominant pathway and the backward lasing is reported to be observed only under limited conditions [16]. In the ambient conditions of the air, the backward lasing is strongly depressed by the presence of oxygen molecules.

For the origin of lasing at 391.4 nm (3.17 eV) emission from N_2, a widely accepted view is that it is mainly due to the induced emission from the excited state of N_2^+ ions, mostly assigned to $B^2\Sigma_u^+ \rightarrow X^2\Sigma_g^+$ [15, 17]. The lasing of air can be initiated by the irradiation of fundamentals of Ti-sapphire laser. The photon energy (1.55 eV)is far below the ionization energy of N_2 (16 eV). Therefore, at least two question must be answered: What is the mechanism of ionization by below-threshold excitation? What is the mechanism of population inversion in the N_2^+ ions?

Population inversion in N_2^+ ions is a little surprising, because if the transition from the ground state to the excited state within the N_2 molecule occurs first, the photo-ionization from the excited state will follow much faster than that from the Σ_g state. In [18], the authors considered that the population inversion occurs within a single pump pulse in the reversed order. In the first half of the pulse, an electron of the highest occupied molecular orbital (HOMO) in a neutral N_2 molecule is ejected to the free state. Then the electronic configuration changes suddenly due to the transition $N_2 \rightarrow N_2^+$: The second ionization potential becomes much larger, while the excitation energy to the lowest unoccupied molecular orbital (denoted as B) becomes lower. An electron in the HOMO (denoted as X) of N_2^+ is excited to the B state by the electric field in the last half of the pulse. The abrupt emergence of the new electronic configuration gives rise to the double excitation as a highly nonadiabatic process. The authors carried out a simulation of the population change in a simple model within the assumption that a two-level system in the ground state is suddenly put in the intense off-resonant field at the moment of maximum intensity. Although it is noticed that the couplings between other excited states also plays a role [19–21], the essential mechanism would be the same.

In the following section, I would like to examine this model of air lasing by a simulation on a toy model with a very simple calculation. In order to mimic the ultrafast electron dynamics for a molecule in vacuum, we introduce a discrete structure into the vacuum with a small mesh of a nearest neighbor hopping. The quantum mechanical equation of motion for the ejected electron is then described by a tight-binding model, and the bound states of molecule are replaced by localized states in the lattice. This model is originally considered for the ultrafast electron dynamics in the crystals. For the technique of solving the Schrödinger equation, a method of Volterra integral equation of second kind [22, 23] is proposed. The advantage of this method is its simplicity and flexibility for the extension taking into account various effects.

A. **Volterra Integral Equation**

Let us assume a simple cubic "crystal structure" in three dimensions with the lattice constant a and hopping parameter $-B/2$. Furthermore, an additional site or "impurity state" is assumed at the origin. The Hamiltonian for the tight binding model in this space is written as

$$H_0 = -\frac{B}{2}\sum_{\alpha=x,y,z}{\sum_{j_\alpha}}'(|j_\alpha+1\rangle\langle j_\alpha| + H.c.) + \epsilon_c \sum_{j_x,j_y,j_z} |j_x, j_y, j_z\rangle\langle j_x, j_y, j_z| + \epsilon_0|g\rangle\langle g|. \tag{3.1}$$

In the above equation, $|j_x, j_y, j_z\rangle = |j_x\rangle \otimes |j_y\rangle \otimes |j_z\rangle$ means the state vector at the site index (j_x, j_y, j_z), where $\otimes$ is the direct product. The symbol $\sum'_{j_\alpha}$ means that the index j_α runs over N sites $j_\alpha = -\frac{N}{2}, -\frac{N}{2}+1, \ldots, 0, \ldots, \frac{N}{2}-2, \frac{N}{2}-1$ with N being a very large even number. The Symbol $\sum_{j_\alpha}$ indicates the sum over $N+1$ site from $-N/2$ to $N/2$. The state vector $|g\rangle$ is the "impurity state" located at $(0, 0, 0)$ site with the energy $\epsilon_0(=0)$ chosen as the origin of the energy. The band-center energy is denoted as ϵ_c.

The eigenstate of H_0 in the conduction band is written as $|k_x, k_y, k_z\rangle = |k_x\rangle \otimes |k_y\rangle \otimes |k_z\rangle$ where

$$|k_\alpha\rangle = 1/\sqrt{N}\sum_{j\alpha} |j_\alpha\rangle \exp[iak_\alpha j_\alpha], \qquad -\pi/a \le k_\alpha \le \pi/a \quad (\alpha = x, y, z)\,, \tag{3.2}$$

with the eigenvalue

$$\epsilon_{k_x,k_y,k_z} = \epsilon_c - B\left(\cos k_x a + \cos k_y a + \cos k_z a\right), \qquad -\pi/a \le k_\alpha \le \pi/a. \tag{3.3}$$

Hereafter, we use the convention $\vec{k} = (k_x, k_y, k_z)$ and $\vec{j} = (j_x, j_y, j_z)$.

The low energy states in the conduction band of the tight binding model can be regarded as describing the free states in vacuum. In fact, in the limit $|k_\alpha a| << 1$, the above equation can be approximated as

$$\epsilon_{\vec{k}} \simeq \epsilon_c - 3B + \frac{Ba^2}{2}\vec{k}^2. \tag{3.4}$$

Comparing this with the energy of a free electron in vacuum, $\epsilon_{\vec{k}} = \hbar^2\vec{k}^2/2m$, where m is the mass of electron, we find $m = \hbar^2/Ba^2$. In the case of N_2 molecule in vacuum, $|g\rangle$ corresponds to the HOMO, and $\epsilon_c - 3B$ is the ionization energy ($\simeq$ 16 eV).

We assume that a linearly polarized pump pulse with polarization in the x-direction hits the sample along the z-axis. The interaction with the intense electromagnetic field will induce two kind of action on the initially localized electrons. The one is the excitation of the localized electron to the continuum state. This effect will be called an *inter-band driving*. The second is the perturbation of the excited states due to the optical Stark effect, which will be called an *intra-band driving*.

The Hamiltonian for the intra-band driving is written as

$$H_1(t) = -eaE(t)\sum_{j_x} j_x |j_x\rangle\langle j_x|, \tag{3.5}$$

where $E(t)$ is the electric field of the laser pulse. The Hamiltonian for the inter-band driving is given by

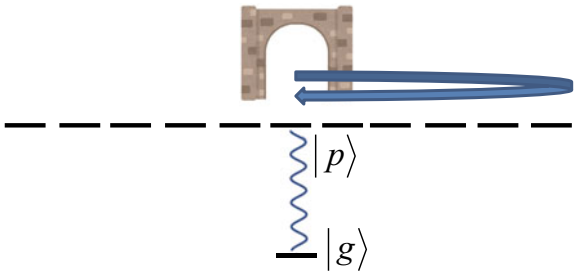

Fig. 3.1 Image of portal state

$$H_2(t) = E(t) \sum_k \left(\mu_k |k\rangle\langle g| + \mu_k^* |g\rangle\langle k|\right), \tag{3.6}$$

where μ_k is the transition dipole moment of the HOMO or impurity state to the state $|k\rangle$ in the conduction band defined in the length gauge as

$$\mu_k = -\langle k|er|g\rangle,$$

with $-er$ being the dipole moment of the molecule ($e > 0$). For the electric field of the pump-pulse, we assume the Gaussian form,

$$E(t) = E_0 \exp[-t^2/\sigma^2] \cos(\omega t + \varphi), \tag{3.7}$$

where σ is the pulse-width and φ is the carrier-envelope phase (CEP). For the pulse-width not extremely short, the CEP-dependence of the responses is negligible. Therefore, we set $\varphi = 0$ in the present work. We assumed an x-polarized light hits the material along the z-direction. The theory can be readily extended to the circularly polarized light.

It is noticeable that $H_2(t)$ is written as

$$H_2(t) = \mu E(t)\left(|p\rangle\langle g| + |g\rangle\langle p|\right), \tag{3.8}$$

where $|p\rangle$ is given by

$$|p\rangle = \mu^{-1} \sum_k \mu_k |k\rangle, \tag{3.9}$$

with $\mu = \sqrt{\sum_k |\mu_k|^2}$. We call $|p\rangle$ a *portal state* because the electron goes out from or comes back to the ground state $|g\rangle$ only through $|p\rangle$ as shown in Fig. 3.1.

The portal state is a localized state around $|g\rangle$ with spatial extension of the same order of $|g\rangle$. The actual functional form of $|p\rangle$ is given once the transition dipole moment μ_k is given. Although the following theory can be constructed for a general case of $|p\rangle$, we assume here, for simplicity, that $|g\rangle$ is well localized at the origin, so that μ_k is approximately independent of k. Then, $|p\rangle$ is given by the state $|0, 0, 0\rangle$ in the site-representation. In other words, we assume a vertical transition in real space.

At this point, a comment may be in order on the analogy and difference between the electron dynamics in solids and in true vacuum. In solids, Bloch's theory tells that the electronic states are described by linear combinations of the atomic like localized states (Wannier states). The magnitude and the selection rule for optical transitions are determined, roughly speaking, by the Wannier functions and the overlapping of the envelope functions. In the present article, the state $|k\rangle$ represents the envelope functions of the Bloch states, with atomic functions being implicitly accompanied. In the case of electrons in real vacuum, $|k\rangle$ should be a plane wave state or a scattering state.

Now we calculate the time-resolved photo-ionization probability of the localized electron with the integral equation method. For that purpose, the intra-band driving term $H_1(t)$ is included into an unperturbed Hamiltonian with definition,

$$\tilde{H}_0(t) \equiv H_0 + H_1(t).$$

The Schrödinger equation for the state vector $|\psi(t)\rangle$,

$$i\hbar\frac{d}{dt}|\psi(t)\rangle = \left\{\tilde{H}_0(t) + H_2(t)\right\}|\psi(t)\rangle \tag{3.10}$$

is transformed into an integral equation,

$$\begin{aligned}|\psi(t)\rangle = &-(i/\hbar)\int_{-\infty}^{t} \exp_+\left[-(i/\hbar)\int_{\tau}^{t}\tilde{H}_0(\tau')d\tau'\right]H_2(\tau)|\psi(\tau)\rangle d\tau \\ &+ \exp_+\left[-(i/\hbar)\int_{-\infty}^{t}\tilde{H}_0(\tau)d\tau\right]|g\rangle,\end{aligned} \tag{3.11}$$

where $\exp_+$ is the time-ordered exponential, and $|g\rangle$ is the initial state at $t = -\infty$. The proof of (3.11) can be easily done by differentiating both sides of (3.11) with respect to t, and show that it is equivalent to (3.10).

We calculate the probability amplitudes $C_p(t)$ and $C_g(t)$ that the electron is found at the portal state $C_p(t) = \langle p|\psi(t)\rangle$, and at the ground state $C_g(t) = \langle g|\psi(t)\rangle$ at time t. From (3.11), we find a pair of integral equations,

$$C_p(t) = -(i/\hbar)\int_{-\infty}^{t}\langle p|\exp_+\left[-(i/\hbar)\int_{\tau}^{t}\tilde{H}_0(\tau')d\tau'\right]|p\rangle\mu E(\tau)C_g(\tau)d\tau, \tag{3.12}$$

$$C_g(t) = -(i/\hbar)\int_{-\infty}^{t}\mu E(\tau)C_p(\tau)d\tau + 1. \tag{3.13}$$

In (3.12), the integral kernel

$$K_{p,p}(t,\tau) \equiv \langle p| \exp_+\Big[-(i/\hbar)\int_\tau^t \tilde{H}_0(\tau')d\tau'\Big]|p\rangle$$

can be calculated analytically in the limit $N \to \infty$. This is because the Hamiltonian $\tilde{H}_0(t)$ is a sum of independent terms in the x, y and z direction. We find

$$K_{p,p}(t,\tau) = e^{-(i/\hbar)\epsilon_g(t-\tau)} K_0(t,\tau)^2 K_1(t,\tau), \tag{3.14}$$

in which

$$K_0(t,\tau) = J_0(B|t-\tau|/\hbar), \tag{3.15}$$

$$K_1(t,\tau) = J_0(B|R(t,\tau)|/\hbar), \tag{3.16}$$

where $J_0(x)$ is the 0th order Bessel function, and $R(t,\tau)$ is given by the Lie algebraic argument [24] as

$$R(t,\tau) = \int_\tau^t \exp\Big[-i(ea/\hbar)\int_\tau^u E(s)ds\Big]du. \tag{3.17}$$

The numerical solution of the integral equations was done by discretizing the time into meshes with small intervals. The numerical integration is written as a summation using the trapezoidal approximation. This gives the iterative relations for the values $C_p(t)$ and $C_g(t)$ with those of former time-bin, and determined successively.

In the two types of kernels, $K_0(t,\tau)$ represents the quantum diffusion to y, and z direction. The kernel $K_1(t,\tau)$ represents the motion of the electron in the x direction under the influence of the oscillating electric field. It is noticed that this intra-band driving term is important in the below threshold photo ionization because it induces the tunneling excitation as schematically shown in Fig. 3.2. However, it is found that, at least within the present model calculation, the effect of this term becomes significant only for a one-dimensional model. In three-dimension, the photo ionization probability becomes enhanced appreciably only for very high intensities of the electric field. This term is extremely important for the process of the high harmonic generation. The existence of the long plateau in the HHG spectrum is solely attributed to the intra-band driving as shown later.

B. **Application to Population Inversion**

Zhang and coauthors [18] studied theoretically their conjecture on the fundamental mechanism of population inversion in N_2 molecules under intense pulse irradiation by a simple two-level model. They calculated the probability of excitation of a two-level system after the passage of a modified Gaussian pulse. The temporal shape of

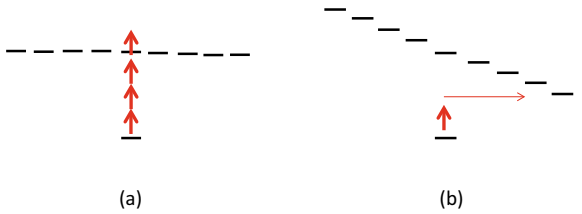

Fig. 3.2 Schematic picture for **a** the multi-photon excitation where the intra-band driving is absent, and **b** the tunneling excitation where the intra-band driving exists and plays an important role. Quantitatively, this effect is important for one-dimensional systems

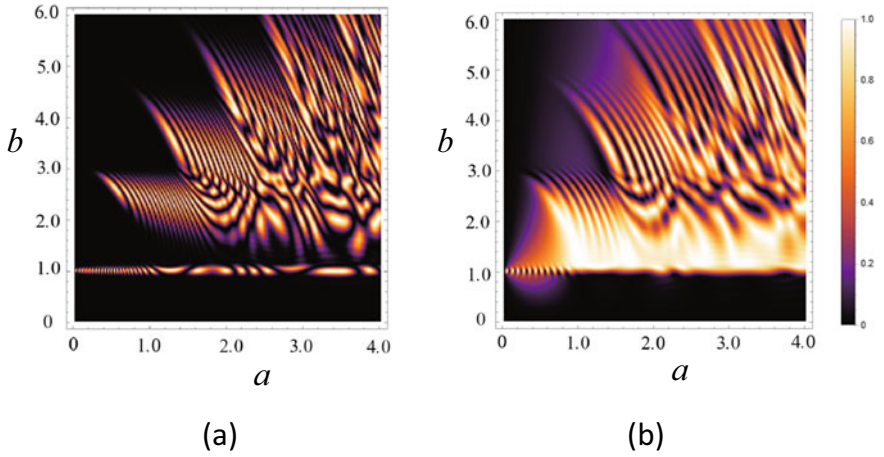

Fig. 3.3 Excitation probability of a two-level system plotted against the amplitude of the inter-band driving $a = \mu E_0/2\hbar\omega$ and the energy gap $b = \epsilon/\hbar\omega$. In **a**, the pump field is given by the Gaussian pulse $E(t) = E_0 e^{-t^2/\sigma^2}\cos\omega t$, and in **b** the pump field has a sudden rise as $E(t) = \theta(t)E_0 e^{-t^2/\sigma^2}\cos\omega t$ with $\theta(t)$ being the step function

the Gaussian pulse was strongly modified to a highly asymmetric form; the front half of the pulse has a sharp edge while the back half has an original Gaussian envelop. By the numerical simulation, they concluded that a necessary condition for the population inversion is the abrupt exposure to the intense optical field and the adiabatic fade away of the field strength.

In Fig. 3.3, the density plot of the excitation probability $P(a, b)$ in a two level system is shown in the two parameter space, $a = \mu E_0/2\hbar\omega$ and $b = \epsilon/\hbar\omega$, where ϵ is the energy difference of the two-level system. In Fig. 3.3a, $P(a, b)$ is shown for the original Gaussian pulse $E(t) = E_0 \exp[-t^2/\sigma^2]\cos(\omega t)$, while in (b), $P(a, b)$ is shown for the pulse shape $E(t) = \theta(t)E_0 \exp[-t^2/\sigma^2]\cos(\omega t)$, where $\theta(t)$ is a step function defined as $\theta(t) = 0$, for $t < 0$, and $\theta(t) = 1$ for $t \geq 0$. The pulse width is chosen as $\sigma = 20T$ where T is the oscillation period of the laser field. A part of Fig. 3.3b has been presented in [18].

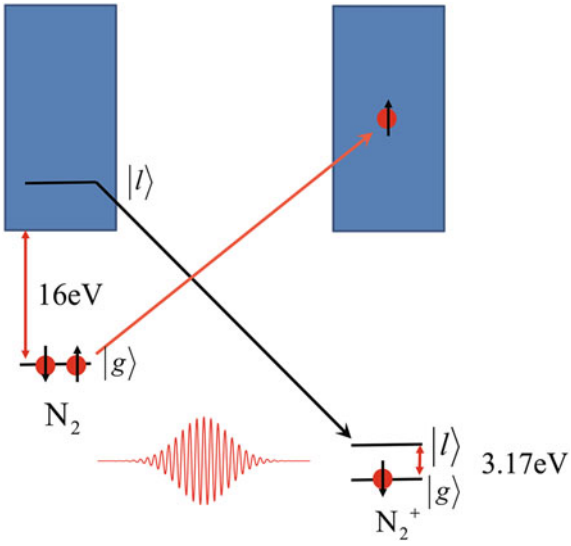

Fig. 3.4 A proposed model of correlated electrons for the intense field induced population inversion in N_2 molecules

From Fig. 3.3, it is obvious that the highly asymmetric pulse with abrupt turning on and smooth fading away (Fig. 3.3b) is far more favorable for the population inversion than that with the normal Gaussian shape (Fig. 3.3a). Interestingly, a systematic and periodic pattern can be recognized in Fig. 3.3a. This may be explained by the adiabatic Floquet theory and path interference in the Landau-Zener transitions at quasi-level crossings [25]. In the plot Fig. 3.3b also, the periodic pattern in $P(a, b)$ is discernible.

In order to see the whole process in a unified way, we applied our calculation scheme to the population inversion in N_2 molecules in the intense pulse laser field. In Fig. 3.4, our model for the double excitation of N_2 molecules in the intense off-resonant pulse laser field is schematically shown. We assume two electrons are occupying the HOMO of N_2. For convenience, they are named "up-spin electron" and "down-spin electron", although the spin does not play any specific role in this problem. In the initial state, the on-site Coulomb energy U works like Hubbard model. The intense optical pulse first ejects one of the electrons, say, up-spin electron to the free state. Then the disappearance of U increases the second ionization energy. Furthermore, due to the incomplete screening of the core potential, the higher molecular orbital comes down, roughly to 3eV above the X-state of N_2^+, and prompts the excitation of the down-spin electron. Our purpose is to see the conditions for this scenario to work.

Our model Hamiltonian for the correlated two electrons is given as

$$H(t) = H_0(t) + H_I(t), \tag{3.18}$$

$$H_0(t) = \epsilon_g \left(u_g^\dagger u_g + d_g^\dagger d_g\right) + U u_g^\dagger u_g d_g^\dagger d_g + \left(\epsilon_l^0 + V u_g^\dagger u_g\right) d_l^\dagger d_l + \sum_k \epsilon_k u_k^\dagger u_k - eaE(t) \sum_{j_x} j_x u_{j_x}^\dagger u_{j_x}, \tag{3.19}$$

$$H_I(t) = E(t) \left(\mu_1 \sum_k \left(u_k^\dagger u_g + u_g^\dagger u_k\right) + \mu_2 \left(d_l^\dagger d_g + d_g^\dagger d_l\right)\right). \tag{3.20}$$

In the above equations, $d_g^\dagger$ and $d_l^\dagger$ are creation operators of the down-spin in the HOMO with energy ϵ_g and the lowest excited state with energy $\epsilon_l = \epsilon_l^0 + V u_g^\dagger u_g$, in which $u_g^\dagger$ and $u_k^\dagger$ are the creation operators of the up-spin state in the HOMO and the free state with energy ϵ_k, respectively. U and V are the on-site Coulomb energies between the up-spin electron and the down-spin electron. The electric field $E(t)$ is assumed to be an x-polarized pulse with functional form given in (3.7). The transition dipole moments from the HOMO are denoted μ_1 for the free state and μ_2 for the first excited state, respectively. In actual simulations, we set $\mu_1 = \mu_2 = \mu$, for simplicity. Note that our Hamiltonian (3.19) contains the Hamiltonians (3.1), (3.5), and (3.6) in the part of up-spin variables.

Although it is possible to solve the two-electron dynamics described by the above Hamiltonian, only an approximate solution is shown here. The up-spin electron plays a key role to control the whole ultra fast process by changing the energy levels for the down-spin electron. Therefore, we neglect the back-reaction from the down-spin electron to the up-spin electron. Note that we only name the electron that was ejected to continuum an up-spin electron, and that excited to the LUMO a down-spin electron. The actual numerical calculation was done as follows. First, the time-dependent probability of photo-ionization of the up-spin electron was calculated. This gives the population probability to the HOMO $n_\uparrow(t) = \langle u_g^\dagger u_g \rangle$. The energy of the first excited state ϵ_l is then evaluated as $\epsilon_l(t) = \epsilon_l^0 + V n_\uparrow(t)$. The transition dynamics for the down-spin is simultaneously calculated by solving the Schrödinger equation numerically for the two-level system $|g\rangle = d_g^\dagger|0\rangle$ and $|l\rangle = d_l^\dagger|0\rangle$, with input of the value $\epsilon_l(t)$. The on-site Coulomb energy U is roughly equal to the difference between the first and the second ionization energy of N_2, and V is set to be $18\hbar\omega$ in the numerical calculation.

In Fig. 3.5, two examples of the pulse-induced population inversion are plotted for the one-dimensional model. In Fig. 3.5a, b, the field strength is set to be $\mu E_0/\hbar\omega = eaE_0/\hbar\omega = 6.0$. In (a), the population of the up-spin electron to the HOMO of N_2 is plotted as a function of t, and in (b), the population of the down-spin electron to the B-state of N_2^+ is shown. In this case, the up-spin electron is almost completely ejected to the free state before the peak value of the pulse with half width $\sigma = 10T$. The down-spin electron undergoes a nonadiabatic transition to the B-state with a violent oscillation and smooth adiabatic convergence. In Fig. 3.5c, d, on the other hand, the field strength is set to be slightly lower, $\mu E_0/\hbar\omega = eaE_0/\hbar\omega = 5.9$. The probability of photo-ionization of the up-spin electron is almost complete as shown in (c). However, the population inversion of the down-spin electron is not attained as seen in (d). Detailed inspection into the power dependence of the final transition

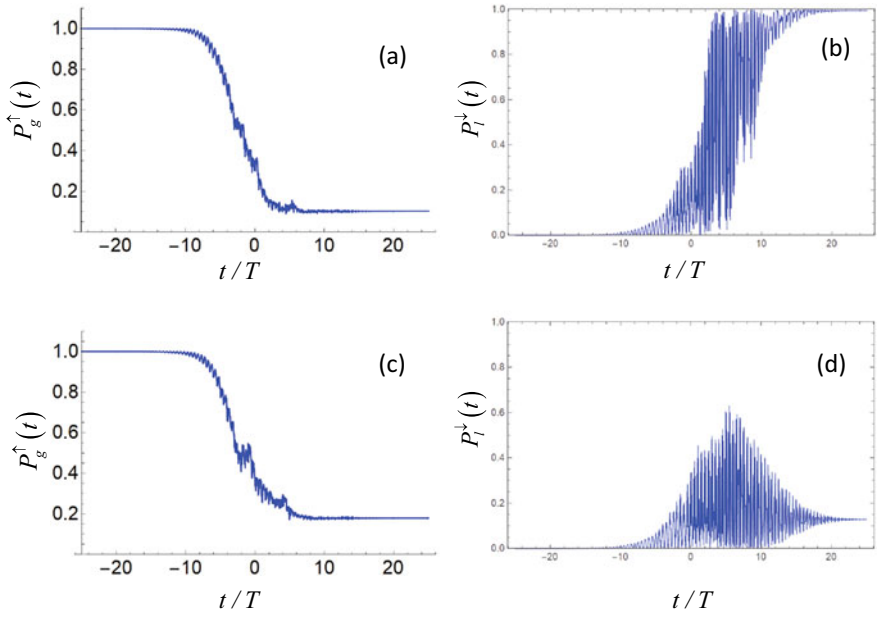

Fig. 3.5 The pulse-intensity dependence of the population change in the lowest excited state of N_2^+ ions. **a** The population to the highest occupied state of the up-spin electron of N_2 molecule, for $\mu E_0/\hbar\omega = eaE_0/\hbar\omega = 6.0$ and **b** the corresponding population to the lowest excited state of the down-spin electron. **c** The same as (**a**) with $\mu E_0/\hbar\omega = eaE_0/\hbar\omega = 5.9$ and **d** the corresponding population to the lowest excited state of the down-spin electron. Other parameter values are common to all of the figures, $B/\hbar\omega = 25$, $\epsilon_g/\hbar\omega = 35$, $\sigma/T = 10$

rate of the down-spin electron indicates that it is not a monotonic function of E_0 as can be expected from Fig. 3.3b.

3.3 High Harmonic Generations in Solids

Now, we extend the formalism developed in previous sections to the case of bulk solids in the intense pulse fields. A number of recent topics in the laser science can be classified in this category. Our interest is focused mainly on the above band-gap excitation of valence electrons in insulators, and subsequent high harmonic radiation. This subject has been attracting intense interest both of the experimentalists and theoreticians since the first report of HHG in solids [3]. For reviews on HHG in atoms and molecules in gas phase, see [26, 27] for example.

Following the success of the explanation of the HHG profile for the gas phase by a simple semi-classical model of Corkum [28] and its quantum mechanical version [29], a number of theories have been proposed for the HHG in solids. They may

be classified according to the methodology in the treatment of the interaction with an intense driving field in solids as the semiclassical one [30], semiconductor Bloch equation [31, 32], Floquet theory [33, 34], and so forth. Our purpose here is not to present a comprehensive review of these works, nor a detailed theoretical analysis of the experimental data, but to propose a new theoretical framework to overview this subject, based on a model as simple as possible.

A. **Crystal model of Two-Level Atoms**

Let us assume a simple cubic crystal of $N \times N \times N$ sites ($N >> 1$). Each site is occupied by a single atom with atomic orbitals, or Wannier functions, ϕ_c and ϕ_v. The energy difference between ϕ_c and ϕ_v is ϵ_c. Both of the ϕ_c and ϕ_v are coupled to the same kind of orbitals at the nearest neighbor atoms with the hopping parameters, $-B_c/2$ and $B_v/2$, respectively. This forms the conduction band and the valence band. This is the simplest toy-model of the band structure of a crystal lattice. The extension to a little more realistic model can be done, for example, by putting an s-orbital and three-fold degenerate p-orbitals at each site. This is the tight-binding model describing the band structures of carbon materials like graphene [35], or III-V semiconductors like GaAs [36].

Each site is designated with three indices j_x, j_y, j_z as before, and the indices c and v which designate the conduction and the valence band. The unperturbed Hamiltonian H_0 in this section is given by

$$H_0 = -\frac{B_c}{2} \sum_{\alpha=x,y,z} {\sum_{j_\alpha}}' (|j_\alpha + 1, c\rangle\langle j_\alpha, c| + H.c.) + \epsilon_0 \sum_{\vec{j}} |\vec{j}, c\rangle\langle\vec{j}, c| + \frac{B_v}{2} \sum_{\alpha=x,y,z} {\sum_{j_\alpha}}' (|j_\alpha + 1, v\rangle\langle j_\alpha, v| + H.c.), \tag{3.21}$$

where the convention of the summation is the same as before. The Hamiltonian H_0 can be diagonalized by introducing the Bloch states $|\vec{k}, c\rangle$ and $|\vec{k}, v\rangle$,

$$H_0 = \sum_{\vec{k}} \epsilon_c(\vec{k}) |\vec{k}, c\rangle\langle\vec{k}, c| + \sum_{\vec{k}} \epsilon_v(\vec{k}) |\vec{k}, v\rangle\langle\vec{k}, v|,$$

where

$$\epsilon_c(\vec{k}) = \epsilon_0 - B_c \left(\cos k_x a + \cos k_y a + \cos k_z a\right),$$

and

$$\epsilon_v(\vec{k}) = B_v \left(\cos k_x a + \cos k_y a + \cos k_z a\right).$$

The half-width of the conduction band and the valence band are $3B_c$ and $3B_v$, respectively. It is assumed that the band-gap $\epsilon_0 - 3(B_c + B_v)$ is much larger than the photon energy $\hbar\omega$.

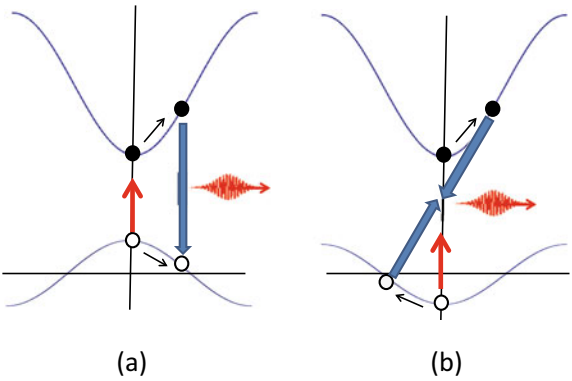

Fig. 3.6 Schematic picture of the recombination luminescence in **a** electron-vacancy picture and **b** electron-hole picture.

The electromagnetic field of the optical pulse is assumed to be linearly polarized in the x-direction. The interaction with the electron can be divided into two as before. The intra-band driving term is given by

$$H_1(t) = -eaE(t) \sum_{j_x} j_x \left(|j_x, c\rangle\langle j_x, c| + |j_x, v\rangle\langle j_x, v| \right), \tag{3.22}$$

and the inter-band driving is by

$$H_2(t) = \mu E(t) \sum_{j_\alpha = x,y,z} \left(|j_\alpha, c\rangle\langle j_\alpha, v| + H.c. \right), \tag{3.23}$$

where the functional form of $E(t)$ is the same as (3.7).

In Fig. 3.6, the optical pumping and HHG process in our model is schematically depicted. In Fig. 3.6a, the electron in the conduction band, and a "vacancy" of electron in the valence band are shown by a solid circle, and an open circle, respectively. This vacancy should not be confused with the so called "hole" in the high-energy physicist's sense. The vacancy has a positive charge and negative mass at the zone center, so that it is accelerated in the k-space to the same direction as the electron. The hole is defined as a quasi particle which has a positive charge and positive mass at zone center. Furthermore, it has an opposite momentum and inversed value of energy to the vacancy as shown in (b). In Fig. 3.6a, the radiative recombination process of an electron-vacancy pair is schematically shown. In this view, the radiative recombination process is described as the vertical transition in the Bloch space. In Fig. 3.6b, the same process is shown in the electron-hole picture. In this view, the recombination process is described as a radiative pair annihilation of an electron and a hole with opposite momentum. The electron-vacancy view is common in the society of solid state physics, while the electron-hole picture, or particle-anti particle picture, is common among the high-energy physicists.

Hereafter, we adopt the electron-hole picture, because it is more suitable to describe the two-particle dynamics. The Hamiltonians (3.19)–(3.23) are written in the second quantized form as

$$H_0 = -\frac{B_c}{2} \sum_{\alpha=x,y,z} {\sum_{j_\alpha}}' \left(a^\dagger_{j_\alpha+1} a_{j_\alpha} + H.c. \right) + \sum_{\vec{j}} \epsilon_0 a^\dagger_{\vec{j}} a_{\vec{j}} - \frac{B_v}{2} \sum_{\alpha} {\sum_{j_\alpha}}' \left(b^\dagger_{j_\alpha+1} b_{j_\alpha} + H.c. \right), \tag{3.24}$$

$$H_1(t) = -eaE(t) \sum_{j_x} j_x \left(a^\dagger_{j_x} a_{j_x} - b^\dagger_{j_x} b_{j_x} \right), \tag{3.25}$$

$$H_2(t) = \mu E(t) \sum_{\vec{j}} \left(a^\dagger_{\vec{j}} b^\dagger_{\vec{j}} + a_{\vec{j}} b_{\vec{j}} \right), \tag{3.26}$$

where $a^\dagger_{\vec{j}}$ and $b^\dagger_{\vec{j}}$ are creation operators for electron, and hole at $\vec{j}$th site, respectively, and the origin of energy is chosen at the vacuum of electrons and holes. It should be noted that the creation operators $a^\dagger_{\vec{j}}$ are defined as the direct product, $a^\dagger_{\vec{j}} = a^{x\,\dagger}_{j_x} \otimes a^{y\,\dagger}_{j_y} \otimes a^{z\,\dagger}_{j_z}$.

With the Fourier transformation,

$$a^\dagger_{\vec{j}} = \frac{1}{\sqrt{N^3}} \sum_{\vec{k}} a^\dagger_{\vec{k}} e^{-ia\vec{k}\vec{j}}, \quad b^\dagger_{\vec{j}} = \frac{1}{\sqrt{N^3}} \sum_{\vec{k}} b^\dagger_{\vec{k}} e^{-ia\vec{k}\vec{j}},$$

H_0 and $H_2(t)$ are rewritten as

$$H_0 = \sum_{\vec{k}} \left(\epsilon^c_{\vec{k}} a^\dagger_{\vec{k}} a_{\vec{k}} - \epsilon^v_{-\vec{k}} b^\dagger_{\vec{k}} b_{\vec{k}} \right), \tag{3.27}$$

$$H_2(t) = \mu E(t) \sum_{\vec{k}} \left(a^\dagger_{\vec{k}} b^\dagger_{-\vec{k}} + a_{\vec{k}} b_{-\vec{k}} \right), \tag{3.28}$$

which explicitly indicate the mechanism of generation of high energy photons by pair annihilations of an electron and a hole with opposite momentums, $\hbar\vec{k}$ and $-\hbar\vec{k}$ to yield a photon with zero momentum and energy $\epsilon^c_{\vec{k}} + \left(-\epsilon^v_{-\vec{k}} \right)$ as shown in Fig. 3.7.

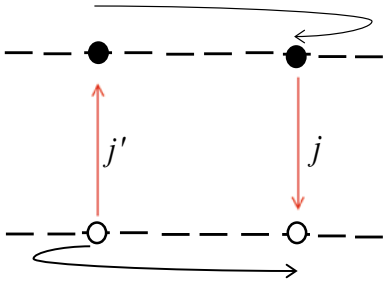

Fig. 3.7 Schematic picture for the electron-hole pair creation and pair-annihilation in the two-level model of crystals in the cite representation

B. **Calculation of HHG Probability**

Now we calculate the probability of HHG within the framework of the integral equation. For that purpose, the intra-band driving term $H_1(t)$ is included into an unperturbed Hamiltonian with definition,

$$\begin{aligned}\tilde{H}_0(t) &\equiv H_0 + H_1(t), \\ &= H_0^c(t) + H_0^v(t),\end{aligned} \tag{3.29}$$

with

$$\begin{aligned}H_0^c(t) &= \sum_{\vec{k}} \epsilon_{\vec{k}}^c a_{\vec{k}}^\dagger a_{\vec{k}} - eaE(t) \sum_{j_x} j_x a_{j_x}^\dagger a_{j_x}, \\ H_0^v(t) &= -\sum_{\vec{k}} \epsilon_{-\vec{k}}^v b_{\vec{k}}^\dagger b_{\vec{k}} + eaE(t) \sum_{j_x} j_x b_{j_x}^\dagger b_{j_x}.\end{aligned} \tag{3.30}$$

The Schrödinger equation for the state vector $|\psi(t)\rangle$,

$$i\hbar \frac{d}{dt}|\psi(t)\rangle = \left\{\tilde{H}_0(t) + H_2(t)\right\}|\psi(t)\rangle \tag{3.31}$$

is transformed into an integral equation,

$$\begin{aligned}|\psi(t)\rangle = &-(i/\hbar)\int_{-\infty}^{t} \exp\left[-(i/\hbar)\int_{\tau}^{t} \tilde{H}_0(\tau')d\tau'\right] H_2(\tau)|\psi(\tau)\rangle d\tau \\ &+ \exp\left[-(i/\hbar)\int_{-\infty}^{t} \tilde{H}_0(\tau)d\tau\right]|\psi_g\rangle,\end{aligned} \tag{3.32}$$

where $|\psi_g\rangle$ is the initial state at $t = -\infty$ and is given by the vacuum of electron and hole, $|\psi_g\rangle = |0\rangle$. We calculate the probability amplitude $C_{\vec{j}}(t) \equiv \langle 0|a_{\vec{j}} b_{\vec{j}}|\psi(t)\rangle$ that the electron and the hole are found at $\vec{j}$th site at time t. It should be noted that the

electron and the hole are always created at the same site, but once created, they are driven in the conduction band and the valence band independently, until they collide at another identical site and are annihilated simultaneously.

We adopt here a single-pair approximation, in which the simultaneous excitations of multiple electron-hole pairs are neglected. This is justified if the energy gap is large enough, and if the electromagnetic field is not extremely intense. Within this approximation the amplitude $C_{\vec{j}}(t)$ is calculated from (3.11) and (3.13) as

$$C_{\vec{j}}(t) = -(i/\hbar)\sum_{\vec{j}'}\int_{-\infty}^{t}\langle 0|a_{\vec{j}}\exp[-(i/\hbar)\int_{\tau}^{t}H_0^c(\tau')d\tau']a_{\vec{j}'}^{\dagger}|0\rangle$$
$$\times\ \langle 0|b_{\vec{j}}\exp[-(i/\hbar)\int_{\tau}^{t}H_0^v(\tau')d\tau']b_{\vec{j}'}^{\dagger}|0\rangle\langle 0|\psi(\tau)\rangle\mu E(\tau)d\tau. \quad (3.33)$$

For the amplitude in the ground state $C_g(t) \equiv \langle 0|\psi(t)\rangle$, we find

$$C_g(t) = -(i/\hbar)\sum_{\vec{j}}\int_{-\infty}^{t}C_{\vec{j}}(\tau)\mu E(\tau)d\tau + 1. \quad (3.34)$$

If we define the kernels for the electron,

$$K_{\vec{j},\vec{j}'}^{(c)}(t,\tau) \equiv \langle 0|a_{\vec{j}}\exp[-(i/\hbar)\int_{\tau}^{t}H_0^c(t')d\tau']a_{\vec{j}'}^{\dagger}|0\rangle$$

and for the hole,

$$K_{\vec{j},\vec{j}'}^{(v)}(t,\tau) \equiv \langle 0|b_{\vec{j}}\exp[-(i/\hbar)\int_{\tau}^{t}H_0^v(t')d\tau']b_{\vec{j}'}^{\dagger}|0\rangle,$$

the above equations are written as

$$C_{\vec{j}}(t) = -(i/\hbar)\sum_{\vec{j}'}\int_{-\infty}^{t}K_{\vec{j},\vec{j}'}^{(c)}(t,\tau)K_{\vec{j},\vec{j}'}^{(v)}(t,\tau)C_g(\tau)\mu E(\tau)d\tau, \quad (3.35)$$

$$C_g(t) = -(i/\hbar)\sum_{\vec{j}}\int_{-\infty}^{t}C_{\vec{j}}(\tau)\mu E(\tau)d\tau + 1. \quad (3.36)$$

The kernels $K^{(c)}_{\vec{j},\vec{j}'}(t,\tau)$ and $K^{(v)}_{\vec{j},\vec{j}'}(t,\tau)$ describe the transition amplitudes that the electron (hole) is found at the site $\vec{j}$ at time t under the condition it exists at the site $\vec{j}'$ at time τ with the influence of quantum hopping with uniform driving field. They can be obtained analytically as

$$K^{(c)}_{\vec{j},\vec{j}'} = e^{-(i/\hbar)\epsilon_0(t-\tau)} K^{(c)}_{j_x,j'_x}(t,\tau) K^{(c)}_{j_y,j'_y}(t,\tau) K^{(c)}_{j_z,j'_z}(t,\tau), \tag{3.37}$$

$$K^{(v)}_{\vec{j},\vec{j}'} = K^{(v)}_{j_x,j'_x}(t,\tau) K^{(v)}_{j_y,j'_y}(t,\tau) K^{(v)}_{j_z,j'_z}(t,\tau), \tag{3.38}$$

in which

$$K^{(c)}_{j_x,j'_x}(t,\tau) = \exp[i\frac{\pi}{2}(j_x - j'_x)] J_{j_x-j'_x}\left(B_c|R(t,\tau)|\right), \tag{3.39}$$

$$K^{(c)}_{j_y,j'_y}(t,\tau) = \exp[i\frac{\pi}{2}(j_y - j'_y)] J_{j_y-j'_y}\left(B_c|t-\tau|\right), \tag{3.40}$$

$$K^{(c)}_{j_z,j'_z}(t,\tau) = \exp[i\frac{\pi}{2}(j_z - j'_z)] J_{j_z-j'_z}\left(B_c|t-\tau|\right), \tag{3.41}$$

where $J_j(x)$ is jth order Bessel function, and $R(t,\tau)$ is given in (3.17). For the kernel of the hole, $K^{(v)}_{\vec{j},\vec{j}'}$, the analogous expressions to the above formula are obtained, with only difference that B_c must be replaced by B_v. Strictly speaking, the above formulas are derived for the infinitely large tight binding model, but it is approximately valid under the condition $N >> 1$. The fact that the integral kernels are completely decoupled into the three components of the direction of motion is an advantage of the present theory in the time domain. Furthermore, using Neumann's sum rule,

$$\sum_{n=-\infty}^{\infty} J_n(a) J_n(b) e^{in\theta} = J_0(\sqrt{a^2 + b^2 - 2ab\cos\theta}), \tag{3.42}$$

we can carry out the summation over the creation sites of the electron-hole pair, and finally obtain

$$C_{\vec{j}}(t) = -(i/\hbar) \int_{-\infty}^{t} e^{-(i/\hbar)\epsilon_g(t-\tau)} J_0\left((B_c + B_v)|R(t,\tau)|\right) \tag{3.43}$$

$$\times\, J_0\left((B_c + B_v)|t-\tau|\right)^2 C_g(\tau)\mu E(\tau) d\tau, \tag{3.44}$$

$$C_g(t) = -(i/\hbar) \sum_{\vec{j}} \int_{-\infty}^{t} C_{\vec{j}}(\tau)\mu E(\tau) d\tau + 1.$$

So far, we have not taken into account any relaxation phenomena in the dynamical processes. Furthermore, in actual experiments, the observed intensity of the high harmonics depends on the spot-size of the pump pulse. Therefore, we introduce here

the effective number of atoms N_{eff} that contribute to high harmonic generation. Since $C_{\vec{j}}(t)$ does not depend on $\vec{j}$, we may set $C_{\vec{j}}(t) = C_p(t)/\sqrt{N_{eff}}$, and find

$$C_p(t) = -(i/\hbar)\int_{-\infty}^{t} e^{-(i/\hbar)\epsilon_g(t-\tau)} J_0\left((B_c+B_v)|R(t,\tau)|\right) \times J_0\left((B_c+B_v)|t-\tau|\right)^2 C_g(\tau)\mu_{eff}E(\tau)d\tau, \quad (3.45)$$

$$C_g(t) = -(i/\hbar)\int_{-\infty}^{t} C_p(\tau)\mu_{eff}E(\tau)d\tau + 1. \quad (3.46)$$

where $\mu_{eff} = \sqrt{N_{eff}}\mu$ is the effective dipole moment.

For the source of harmonic radiation in solids, two mechanism of polarization can be considered. The one is the intra-band polarization, and the other is the inter-band polarization [37]. The electromagnetic radiation from the intra-band polarization is due to the non-parabolicity of the band dispersion. The inter-band polarization corresponds to the recombination emission. Numerical calculations show that the intra-band contribution is usually smaller than that of the inter-band one [30]. So, we consider only the contribution from the inter-band transition radiation here. The time-dependent amplitude of the emitted radiation $A(t)$ is proportional to the expectation value of the source term $\sum_{\vec{j}} a_{\vec{j}} b_{\vec{j}}$ as

$$A(t) = \langle\psi(t)|\sum_{\vec{j}} a_{\vec{j}} b_{\vec{j}}|\psi(t)\rangle. \quad (3.47)$$

Because the component of the excited states in $|\psi(t)\rangle$ is very small in the present parameter values, we can safely write

$$A(t) = \langle 0|\sum_{\vec{j}} a_{\vec{j}} b_{\vec{j}}|\psi(t)\rangle = \sum_{\vec{j}} C_{\vec{j}}(t).$$

The intensity of high harmonics photons of frequency Ω per unit density of atoms is then given by the Fourier transform of $C_p(t)$ as

$$I(\Omega) = \left|\int_{-\infty}^{\infty} C_p(t)\exp[i\Omega t]dt\right|^2. \quad (3.48)$$

It is remarkable that the above formulas (3.45) and (3.46) for the HHG in the bulk crystals are formally the same as the (3.12), (3.13), which are derived for the electron dynamics in the impurity state, or a molecule in the vacuum in the previous section. This suggests that the mechanism of the HHG in the crystal is essentially the same as that in a gas in vacuum. A difference is that the parameter for the half band-width in the latter model is the sum of B_c and B_v, in contrast to the former case, where only the half band-width B_c appears in the formula.

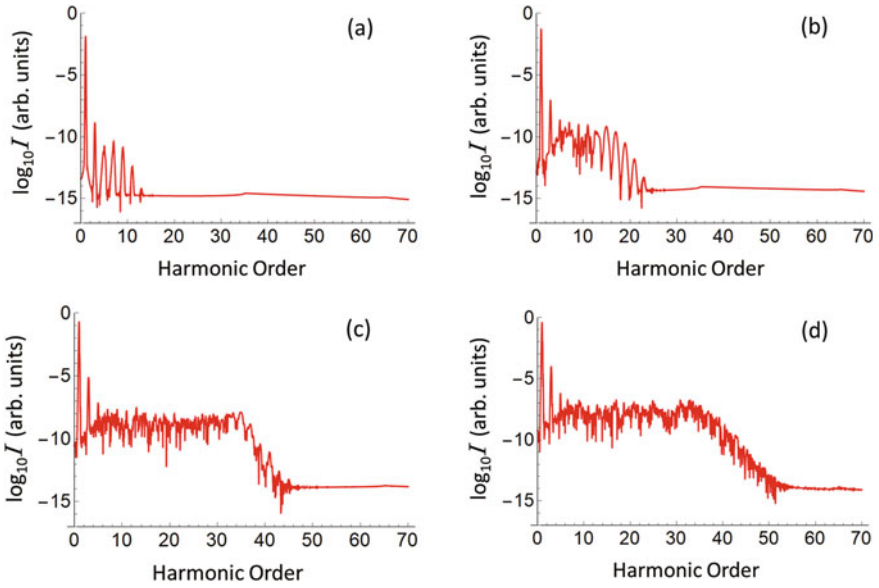

Fig. 3.8 Theoretical results for the high harmonic spectrum. The parameter values are $(B_c + B_v)/\hbar\omega = 15$, $\epsilon_g/\hbar\omega = 50$ which correspond to the band-gap $5\hbar\omega$, $\sigma = 5T$. The field intensities are **a** $eaE_0 = \mu_{eff}E_0 = 0.5\hbar\omega$, **b** $eaE_0 = \mu_{eff}E_0 = 1.0\hbar\omega$, **c** $eaE_0 = \mu_{eff}E_0 = 2.0\hbar\omega$, **d** $eaE_0 = \mu_{eff}E_0 = 3.0\hbar\omega$, respectively.

In Fig. 3.8, the dependence of the high harmonic spectra on the incident pulse-amplitude are shown for the three dimensional tight-binding model. The parameter values are $B_c + B_v = 15\hbar\omega$ (total half band-width= $45\hbar\omega$), $\epsilon_0 = 50\hbar\omega$ which corresponds to the band gap $5\hbar\omega$ at Γ-point. The incident pulse is linearly polarized in the x-direction, and the pulse-width is $\sigma = 5T$ where $T = 2\pi/\omega$. The amplitude of the electric field is chosen as (a) $eaE_0/\hbar\omega = \mu_{eff}E_0/\hbar\omega = 0.5$, (b) $eaE_0/\hbar\omega = \mu_{eff}E_0/\hbar\omega = 1.0$, (c) $eaE_0/\hbar\omega = \mu_{eff}E_0/\hbar\omega = 2.0$ and (d) $eaE_0/\hbar\omega = \mu_{eff}E_0/\hbar\omega = 3.0$.

The theoretical results in Fig. 3.8 reproduce the experimental features [3, 38] fairly well. The high harmonic spectrum has a long plateau and a sudden cutoff. Experimentally, it is observed that the spectrum obeys the optical selection rule that only the odd order harmonics have appreciable intensities for crystals with space-inversion symmetry. In the theoretical line shapes, however, such a selection rule seems to be blurred except for the low order harmonics and those near cutoff. This is paradoxical since the theoretical results derived on a simple symmetrical model gives much more noisy curves than the experimental data. The elucidation of this paradox has been attracting theoretical interest recently. It is reported that the selection rule is recovered [30, 39, 40] if one takes into account some mechanism of dephasing in his model. In a phenomenological model [30], it was shown that a surprisingly short dephasing time, as short as 1 femtosecond, is required in order to get agreement

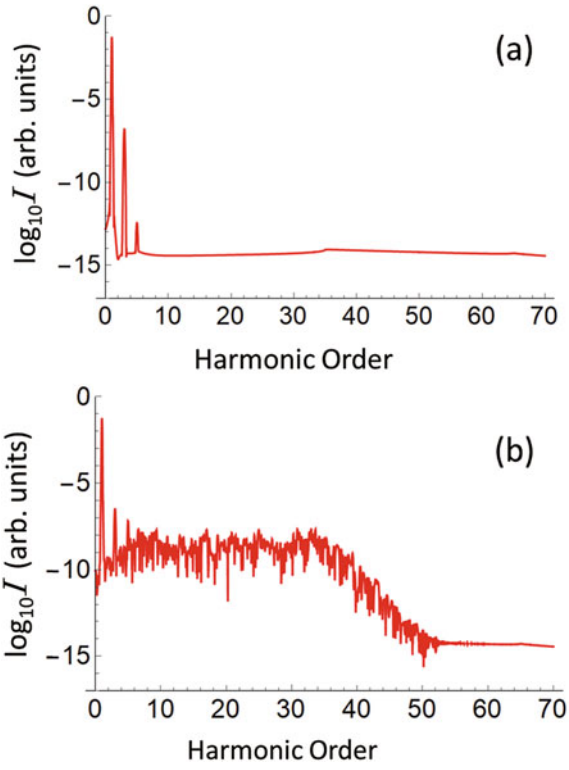

Fig. 3.9 The dependence on the intra-band driving of the HHG spectrum for $\mu_{eff} E_0/\hbar\omega = 1.0$ with **a** $eaE_0 = 0$ and **b** $eaE_0/\hbar\omega = 3.0$

with experimental data. It was also asserted that the pulse propagation in the dense and inhomogeneous media also plays a role to make the experimental HHG spectra *clean* [41]. This is an intriguing open question.

In order to clarify the distinct roles of the inter-band driving and the intra-band driving, the theoretical line shapes of the high harmonics are shown in Fig. 3.9 for two set of parameter values, namely for $\mu_{eff} E_0 = 1.0$ and $eaE_0 = 0$ (no intra-band driving) in (a) and $\mu_{eff} E_0 = 1.0$ and $eaE_0 = 3.0$ (strong intra-band driving) in (b). In Fig. 3.9a, only the 1st, 3rd and 5th harmonics are seen. In contrast, a long plateau of high harmonics is observed in Fig. 3.9b. Note that the line-shape is almost the same as shown in Fig. 3.8d. This means that the total line-shape of the high harmonics is entirely determined by the intra-band driving field, although its amplitude depends on the inter-band driving.

The features in these line-shape of HHG qualitatively agree with those reported [3, 38] and with the simple formula of the three-step model [28]. Quantitatively, however, the agreement with the formula by the three-step model in not good. The three-step model predicts the energy of the cutoff of the plateau E_c as

$$E_c = I_p + 3U_p, \tag{3.49}$$

where I_p is the ionization energy and U_p is the ponderomotive energy, $U_p = e^2E_0^2/4m\omega^2$. From (3.4), we may set $I_p = \epsilon_g - 3(B_c + B_v)$ and $m = \hbar^2/(B_c + B_v)a^2$. But this gives a too small value of E_c. The main reason of the disagreement is the breakdown of the effective mass approximation. In the present model of a two-level atom crystal, it is assumed that the transition dipole moment is a constant and the optical transition is allowed all over the first Brillouin zone vertically. Although the main contribution comes from the excitation around the Γ-point because the transition probability depends also on the energy gap, the contribution from other region will not be negligible. In the present model of cosine-band, the effective mass becomes much smaller and even formally be zero at the band-center. For a quantitative analysis of the HHG spectra in solids, information on the actual band structure will be needed.

On the other hand, it is reported experimentally that the high-energy cutoff in solids has a linear dependence on the amplitude of drive laser field [42]. This is in agreement with the present theoretical result shown in Fig. 3.8. It is noticed that, in the theory, the gap between the edge of the plateau and the cutoff is extended in the high intensity limit as shown in Fig. 3.8d. In order to clarify all these features, further investigation will be needed into the electron dynamics in solids induced by the high intensity pulse fields.

3.4 Conclusion and Prospect

I have proposed a simple formalism based on an integral equation of Volterra-type to calculate the electron dynamics driven by intense pulse fields. It is an analogy of the Dyson equation in time-domain, but has some advantages compared with other more elaborate methods. If the wave-length of the electromagnetic field is much larger than the atomic scales, as is usually the case, the integral kernel for the propagation of the electron in the free-space or in the crystal lattice structures can be analytically obtained. Because the integral kernels are exponential functions, it is easily extended to higher dimensions.

In this article, I have shown two examples for the application of this method. In the Section II, the electron is assumed to make transitions between a localized state and a delocalized "band". In the Section III, an electron and a hole make transitions between the two delocalized "bands" from the "vacuum". It is remarkable that the integral equations are reduced to a formally the same structure, if one introduces a "portal state". This suggests that the mechanism of the high harmonic generation in the system of atoms in vacuum and in the crystals are essentially the same. In the latter case, the translational symmetry plays an important role.

One of the difference in the two models treated here is the quantitative difference in the effective interaction amplitude with the external fields. In the case of crystals, the dipole moment for inter-band transition is enhanced by a factor $\sqrt{N_{eff}}$, where N_{eff} is the phenomenologically introduced effective number of atoms participating in the interaction with photons. The actual value of $\sqrt{N_{eff}}$ will be determined taking

into account the experimental conditions such as the spacial profile of the laser pulses, the relaxation times in the excited states and so forth. Anyway, it may be expected that the solids are promising candidate for the intense light source of high harmonics because of their higher atomic densities. Another difference of the electron dynamics in solids from that in vacuum is the existence of a periodic structure of lattice. Usually this is negligible in the low energy region. However, in the case of motion under the intense electromagnetic field, the discrete structure of the crystal lattice may become non-negligible. The criterion for this boundary is the ratio $aE_0/\hbar\omega$. In fact, in the simple tight-binding picture, the effective transfer energy B is reduced to zero for $aE_0/\hbar\omega = 2.405$ and even become negative i. e. the particle has a negative mass, for $2.405 < aE_0/\hbar\omega < 5.52$. This phenomenon is called a dynamic localization [43] or a band-collapsing [44]. This is due to the coherent path-interference [24] in the driven quantum system. This effect has been automatically incorporated in the expression of the integral kernels under uniform electromagnetic field. To the authors knowledge, clear experimental observation of the dynamic localization in real crystals is yet to be done. It may be a next target in the intense-laser science in solids.

References

1. H. Hirori, K. Shinokita, M. Shirai, S. Tani, K. Kadoya, K. Tanaka, Nat. Commun. **2**, 594 (2011)
2. C.-G. Wahlström, J. Larsson, A. Persson, T. Starczewcki, S. Svanberg, P. Salieres, Ph Balcou, Anne L' Huillier. Phys. Rev. A **48**, 4709 (1993)
3. S. Ghimire, A.D. DiChiara, E. Sistrunk, P. Agostini, L.F. DiMauro, D.A. Reis, Nat. Phys. **7**, 138 (2011)
4. L.V. Keldysh, Sov. Phys. JETP **20**, 1307 (1965)
5. F.H.M. Faisal, J. Phys. B **6**, L89 (1973)
6. H.R. Reiss, Phys. Rev. A **22**, 1786 (1980)
7. K. Yabana, G.F. Bertch, Phys. Rev. B **54**, 4484 (1996)
8. I. Kawata, H. Kono, Y. Fujimura, J. Chem. Phys. **110**, 11152 (1999)
9. T. Otobe, M. Yamagiwa, J.-I. Iwata, K. Yabana, T. Nakatsukasa, Phys. Rev. B **77**, (2008)
10. K. Yabana, T. Sugiyama, Y. Shinohara, T. Otobe, G.F. Bertch, Phys. Rev. B **85**, (2012)
11. A. Becker, F.H.M. Faisal, J. Phys. B: At. Mol. Opt. Phys. **38**, R1–R51 (2005)
12. D.M. Volkov, Z. Phys. **94**, 250 (1935)
13. W.V. Houston, Phys. Rev. **57**, 184 (1940)
14. For a contemporary review, *Femtosecond Laser Filamentation*, S. L. Chin (Springer Series on Atomic, Optical, and Plasma Physics 55, 2010)
15. A. Dogariu, J.B. Michael, O. Scully, R.B. Miles, Science **331**, 442 (2011)
16. X. Zhang, R. Danylo, Z. Fan, P. Ding, C. Kou, Q. Liang, A. Houard, V. Tikhonchuk, A. Mysyrowicz, Y. Liu, Appl. Phys. B **53**, 126 (2020)
17. J. Yao, B. Zeng, H. Xu, G. li, W. Chu, J. Ni, H. Zhang, S. L. Chin, Y. Cheng, Z. Xu, Phys. Rev. A **84**, 051802(R) (2011)
18. Y. Zhang, E. Lötstedt, K. Yamanouchi, J. Phys. B **52**, (2017)
19. H. Xu, E. Lötstedt, A. Iwasaki, K. Yamanouchi, Nat. Commun. **6**, (2015)
20. J. Yao, S. Jiang, W. Chu, B. Zeng, C. Wu, R. Lu, Z. Li, H. Xie, G. Li, c. Yu, Z. Wang, H. Jiang, Q. Gong, Y. Cheng, Phys. Rev. Lett. **116**, 143007 (2016)
21. H. Li, M. Hou, H. Zang, Y. Fu, E. Lötstedt, T. Ando, A. Iwasaki, K. Yamanouchi, H. Xu, Phys. Rev. Lett. **122**, 013202 (2019)
22. Y. Kayanuma, S. Fukuchi, J. Phys. Soc. Jpn. **53**, 1869 (1984)

23. A. Yasui, T. Uozumi, Y. Kayanuma, Phys. Rev. B **72**, (2005)
24. Y. Kayanuma, K. Saito, Phys. Rev. A **77**, 010101 (R) (2008)
25. For a review of the Floquet engineering in periodically driven systems, see M. Holthaus, J. Phys. B: At. Mol. Opt. Phys. **49**, 013001 (2016). I thank T. N. Ikeda, for drawing my attention to this work.
26. T. Barbec, F. Krausz, Rev. Mod. Phys. **72**, 545 (2000)
27. A.D. Bandrauk, S. Barmaki, S. Chelkowski, G.L. Kamta, progress in ultrafast intense laser science III, Chap. 9, in *Springer Series in Chemical Physics*, eds. by K. Yamanouchi, S.L. Chin, P. Agostini, G. Ferrante
28. P.B. Corkum, Phys. Rev. Lett. **71**, 1995 (1993)
29. M. Lewenstein, Ph. Balcou, M. Yu. Ivanov, Anne L'Huillier, P.B. Corkum, Phys. Rev. A **49**, 2117 (1994)
30. G. Vampa, C.R. McDonald, G. Orlando, P.B. Corkum, T. Bravec, Phys. Rev. B **91** (2015)
31. D. Golde, T. Meier, S.W. Koch, Phys. Rev. B **77**, (2008)
32. T. Tamaya, A. Ishikawa, T. Ogawa, K. Tanaka, Phys. Rev. Lett. **116**, (2016)
33. H. Yamane, S. Tanaka, Symmetry Basel **10**, 313 (2018)
34. T.N. Ikeda, K. Chinzei, H. Tsunetsugu, Phys. Rev. A **98**, (2018)
35. See for example, M. I. Katsnelson, *Graphen* (Cambridge University Press, Cambridge, 2013)
36. Y. Mizumoto, Y. Kayanuma, A. Srivastava, J. Kono, A.H. Chin, Phys. Rev. B **74** (2006)
37. See for example, C. Yu, S. Jiang, R. Lu, Adv. Phys. **4**, 1562982 (2019)
38. O. Schubert, M. Hohenleutner, F. Langer, E. Urbanek, C. Lange, U. Huttner, D. Golde, T. Meier, M. Kira, S.W. Koch, R. Huber, Nat. Photonics **8**, 119 (2014)
39. K. Chinzei, T.N. Ikeda, Phys. Rev. Res. **2**, (2020)
40. G. Orland, T. Ho, S. Chu, J. Opt. Soc. Am. **37**, 1540 (2020)
41. I. Floss, C. Lemell, G. Wachter, V. Smejkal, S.A. Sato, X.-M. Tong, K. Yabana, J. Burgdörfer, Phys. Rev. A **97**, 011401(R) (2018)
42. S. Ghimire, D.A. Reis, Nat. Phys. **15**, 10 (2019)
43. D.H. Dunlap, V.M. Kenkre, Phys. Rev. B **34**, 3625 (1986)
44. M. Holthaus, Phys. Rev. Lett. **68**, 351 (1992)

Chapter 4
Channel-Resolved Angular Correlation Between Photoelectron Emission and Fragment Ion Recoil of Ethanol in Intense Laser Fields

Ryuji Itakura, Hiroshi Akagi, and Tomohito Otobe

Abstract We investigate multi-channel dissociative ionization of ethanol in intense near-infrared laser fields with photoelectron-photoion coincidence three-dimensional momentum imaging. As the intensity of the linearly polarized laser field increases to 23 TW/cm^2, phoelectrons are dominantly emitted along the laser polarization. The photoelectron angular distributions (PADs) are not influenced by the orientation direction of ethanol with respect to the laser polarization direction. In the circularly polarized laser field with 80 TW/cm^2, the photoelectron angular distributions of CH_3CD_2OH in the recoil frame of the CD_2OH^+ and $CH_3CD_2^+$ channels are obtained. Photoelectrons in the CD_2OH^+ channel are preferentially emitted from the CH_3 moiety at the moment of birth. By the density functional theory (DFT), we calculate the ionization probability in the electric field as a function of its direction. The comparison between the observed and calculated recoil frame (RF)-PADs suggests that the inner valence 10a′ molecular orbital is deformed by the laser field prior to the photoelectron emission. It is clearly shown that there are two pathways, (i) photoelectron emission from 10a′ and (ii) photoelectron emission from the highest occupied 3a″ molecular orbital followed by photoexcitation. In the $CH_3CD_2^+$ channel, the RF-PAD is found to be isotropic, suggesting the stepwise processes of photoelectron emission and subsequent photoexcitation.

4.1 Introduction

Electronic structure and dynamics are the fundamental basis for all molecular processes in laser fields [1]. Electrons are driven by an intense laser field and then emitted out of molecules. Great progress of the experimental technique in ultrafast intense laser science allows us to image electronic structure by monitoring high-order harmonics, fragment ions, and photoelectrons.

R. Itakura (✉) · H. Akagi · T. Otobe
Kansai Photon Science Institute, National Institutes for Quantum and Radiological Science and Technology (QST), 8-1-7 Umemidai Kizugawa, Kyoto 619-0215, Japan
e-mail: itakura.ryuji@qst.go.jp

K. Yamanouchi et al. (eds.), *Progress in Ultrafast Intense Laser Science XVI*,
Topics in Applied Physics 141, https://doi.org/10.1007/978-3-030-75089-3_4

High harmonic spectroscopy of an aligned molecular ensemble enables us to perform tomography of molecular orbitals (MOs) [2]. This has been already extended to time-resolved measurement for deformation of degenerate hole orbitals [3], dynamical symmetry [4, 5] and identification of chiral molecules [6]. Ion momentum imaging with a sub-10-fs pulse is also useful to image the shape of the highest occupied molecular orbital (HOMO) from which an electron is emitted through tunneling without vibrational and rotational motion [7]. Recently, it is suggested that Rydberg MOs are strongly coupled to HOMO in the course of ionization of hydrocarbon molecules in intense laser fields [8]. The ion momentum imaging with a sub-10 fs pulse has been updated to visualize a photoexcited state and opens the door to tracing electronic dynamics with the pump-probe measurement [9].

Photoelectron imaging is another powerful method to probe the electronic structure. In a multielectron system, a photoelectron is emitted not only from the highest occupied molecular (atomic) orbital, but also from inner valence orbitals. Inherently, ionization is a multi-channel phenomenon. Photoelectron spectroscopy is superior in assigning an electronic state, that is, an orbital from which a photoelectron is emitted. Channel-resolved photoelectron spectra of dissociative ionization of ethanol were measured with photoelectron and photoion coincidence momentum imaging (PEPICO-MI) [10–12]. The photoelectron energy indicates the electronic and vibrational states of the molecular ion formed by the ionization, and the product ion species indicates the final electronic state of the molecular ion after the interaction with the laser field [13]. On the basis of the difference between the photoelectron spectra of respective product channels, ionization and subsequent electronic excitation pathways were revealed [10–12]. Additionally, the correlation between the photoelectron energy and the kinetic energy of the fragment ions helps us to resolve the ionization and electronic excitation pathways, even if a peak in the photoelectron spectrum is too broad to assign the electronic state [10].

In the present chapter, we describe how a photoelectron is emitted from the point view of the photoelectron angular distribution (PAD). First, channel-resolved PADs of ethanol in linearly polarized near-infrared laser fields are shown. The angular correlation between the photoelectron emission and the fragment recoil is extracted by PEPICO-MI. Next, we discuss the ionization induced by a circularly polarized laser field. From the PADs in the recoil frame where the z axis is defined by the recoil vector of the fragment ion, the ionization probability is obtained as a function of the angle of the molecular orientation. Theoretical calculation based on the density functional theory (DFT) exhibits how the MO is deformed by an intense laser field. From comparison between the theoretical and experimental results of the orientation dependent ionization probability, the branching of the ionization and subsequent electronic excitation pathways is also extracted [14].

4.2 Photoelectron Emission in Linearly Polarized Laser Fields

4.2.1 Channel-Resolved Photoelectron Momentum Imaging

The details of the experimental setup for PEPICO-MI was described in our previous publications [10, 12]. Briefly, we detected a photoelectron and a product ion in coincidence using a pair of position sensitive detectors composed of microchannel plates and delay-line anodes (RoentDek HEX80) [15] with a stack of holed electrode plates for three dimensional momentum focusing [16]. The detected event rate was set to be almost 0.3 events per laser shot by controlling the sample gas density. Laser pulses were provided from a Ti:Sapphire chirped pulse amplification system ($\lambda \simeq 783$ nm, 1 kHz, ≤ 2 mJ/pulse). The pulse width was measured to be 35 fs (full width at half maximum (FWHM)) by second harmonic generation frequency-resolved optical gating. The laser peak intensity at the focal point was estimated from the ponderomotive energy shift of the peak in the photoelectron spectra [10, 17]. The measurement was performed in the laser intensity range of 9–23 TW/cm^2. The angles showing the direction of the photoelectron momentum $\mathbf{p}^{\mathbf{ele}}$ and the fragment-ion momentum $\mathbf{p}^{\mathbf{ion}}$ are shown in Fig. 4.1. We analyzed only the photoelectron in the range of $|p_z^{\mathrm{ele}}| < 0.05$ atomic units (a.u.), where p_z^{ele} is the momentum component along the z axis (time-of-flight direction).

The two-dimensional (2D) cuts of the three-dimensional (3D) photoelectron mometum distributions correlated to the formation of respective production ions,

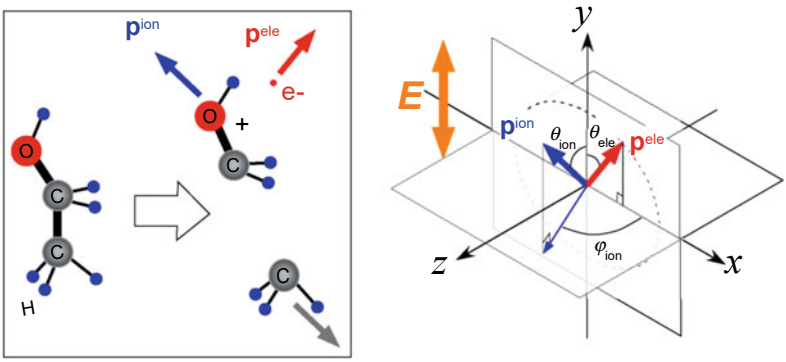

Fig. 4.1 Momenta of the photoelectron and the fragment ion in the laboratory frame (Right). The polarization direction of the linearly polarized laser field is vertical (y). Angles, θ_{ele} θ_{ion}, are the polar angles of the momenta of the photoelectron $\mathbf{p}^{\mathbf{ele}}$ and the fragment ions $\mathbf{p}^{\mathbf{ion}}$ with respect to the y axis. An angle φ_{ion} is the azimuth angle of $\mathbf{p}^{\mathbf{ion}}$. In the analysis, we select only the events that the photoelectron momentum is along the xy plane. The momentum component p_z^{ele} of the z axis (time-of-flight axis) is limited in the range of $|p_z^{\mathrm{ele}}| < 0.05$ atomic units. The left inset shows a dissociative ionization scheme with $\mathbf{p}^{\mathbf{ele}}$ and $\mathbf{p}^{\mathbf{ion}}$

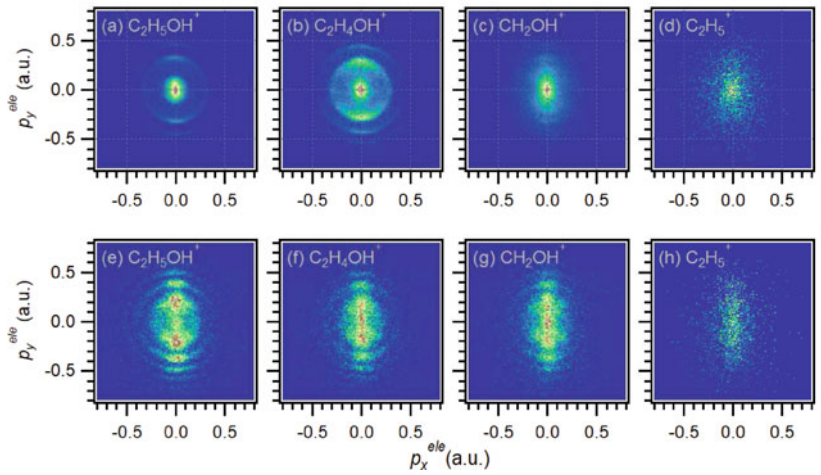

Fig. 4.2 Sliced photoelectron momentum images ($|p_z^{ele}| < 0.05$ a.u.) by linearly polarized 783-nm laser fields at the intensities of 9 TW/cm^2 ((**a**)–(**d**)) and 23 TW/cm^2 ((**e**)–(**h**)). Images are correlated with the product ions, $C_2H_5OH^+$ ((**a**) and (**e**)), $C_2H_4OH^+$ ((**b**) and (**f**)), CH_2OH^+ ((**c**) and (**g**)) and $C_2H_5^+$ ((**d**) and (**h**)). The unit of the coordinates is the atomic unit (a.u.).

$C_2H_5OH^+$, $C_2H_4OH^+$, CH_2OH^+, and $C_2H_5^+$ were obtained by counting the events in the range of $|p_z^{ele}| < 0.05$ a.u. as shown in Fig. 4.2. As the laser intensity increases from 9 TW/cm^2 to 23 TW/cm^2, the width of the photoelectron emission angle with respect to the laser polarization direction decreases, indicating the transition from the multiphoton ionization to the tunnel ionization.

4.2.2 *Angular Correlation Between Photoelectron Emission and Fragment Ion Recoil*

The angular correlations between the photoelectron emission and the recoil of CH_2OH^+ and $C_2H_5^+$ at the laser intensity of 23 TW/cm^2 are shown in Fig. 4.3. To reduce the influence of the position dependent sensitivity of the detector, we took an average of the raw count data at $(\theta_{ion}, \theta_{ele})$ and $(2\pi - \theta_{ion}, 2\pi - \theta_{ele})$ and mapped it at $(\theta_{ion}, \theta_{ele})$ for symmetrization, resulting in the $\theta_{ion} - \theta_{ele}$ maps in Figs. 4.3a and c. The sharp peaks are clearly shown at $\theta_{ele} = 0$ and 180° irrespective of θ_{ion}. There is no difference between the parallel configuration of $(\cos\theta_{ele} \times \cos\theta_{ion}) > 0$ and the anti-parallel configuration of $(\cos\theta_{ele} \times \cos\theta_{ion}) < 0$. In the tunnel ionization, the photoelectron has little kinetic energy at the moment of birth and is driven by the laser electric field. The final momentum of the photoelectron is determined by the vector potential of the laser electric field at the moment of birth. As a result, the photoelectron takes parallel and anti-parallel directions equivalently as its final direction even if the ionization probability strongly depends on the molecular orientation with

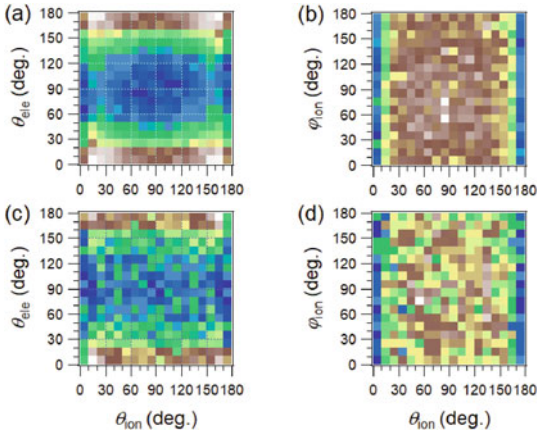

Fig. 4.3 Angular correlations between the momenta of the photoelectron and fragment ions, CH_2OH^+ ((**a**) and (**b**)) and $C_2H_5^+$ ((**c**) and (**d**)) at the laser intensity of 23 TW/cm^2. The correlation between the polar angles, θ_{ele} of the photoelectron and θ_{ion} of the fragment ions ((**a**) and (**c**)). The correlation between θ_{ion} and the azimuth angle φ_{ion} of the recoil momentum of the fragment ion with respect to the xy plane defined by the laser polarization direction (y) and the photoelectron momentum. See text for details.

respect to the direction of the electric field. At this intensity of 23 TW/cm^2, the PAD is governed dominantly by the laser electric field. It should be mentioned that for the $C_2H_5^+$ formation the probability at $(\theta_{ion}, \theta_{ele}) = (0°, 0°)$ and (180°, 180°), is smaller than the other directions. However, the statistical fluctuation at these directions is too large to discuss this small probability, because the counted event number is very small.

Figures 4.3b and d show the correlation between the polar angle θ_{ion} and the azimuth angle φ_{ion} of fragement ions with respect to the x axis. In the analysis, we treated only photoelectrons whose momenta are on the xy plane. As shown in Fig. 4.1, the azimuth angle φ_{ion} of $\mathbf{p}^{\mathbf{ion}}$ is equal to the difference between the azimuth angles of the photoelectron and the fragment ion in the laboratory frame. It is found that the probability as a function of φ_{ion} is constant, indicating no correlation in the azimuth angles.

From these angular correlations, it is found that the photoelectron emission is directed along the laser electric field irrespective of the molecular orientation. It is also confirmed that the probabilities of the photoelectron emission at the parallel and anti-parallel directions with respect to the fragment recoil are almost the same, which is consistent with the behavior of the tunnel ionization. From the angular correlation between a photoelectron and a fragment ion in linearly polarized laser fields, we can gain little insight into the electronic dynamics in molecules prior to the tunnel ionization.

4.3 Photoelectron Emission in a Circularly Polarized Laser Field

4.3.1 Laboratory Frame Photoelectron Momentum Distribution

We changed the polarization of the laser field to the circular one [14]. The pulse width and the wavelength were 60 fs (FWHM) and 800 nm, respectively. In this experiment with the circularly polarized laser field, we used partially deuterated ethanol CH_3CD_2OH to avoid production of different fragment ions with the same mass. Similarly to the experiment with the linearly polarized laser fields, we measured the 3D photoelectron momentum distribution (PMD) in a channel-resolved manner as shown in Fig. 4.4. In the laboratory frame where the laser polarization plane is parallel to the yz plane, the PMD have a torus shape dominantly along the polarization (yz) plane. The out-of-plane angular distribution of the photoelectron with respect to the yz plane shows the width of 31° (FWHM). In principle, the PMD projected on the yz plane should exhibit a isotropic ring shape when multi-cycle laser pulses are used. The slightly anisotropic ring shape in the observed distribution is caused by the non-uniform spatial dependence of the detector sensitivity and the ellipticity of the polarization. It is also noted that the PMDs of all three channels are almost the same with a single broad peak in the energy spectrum, suggesting the tunnel ionization is the dominant ionization mechanism.

From the observed photoelectron spectrum, the laser intensity was estimated to be 80 TW/cm^2 [18]. The corresponding electric field is 1.7×10^{10} V/m, which is 1.3

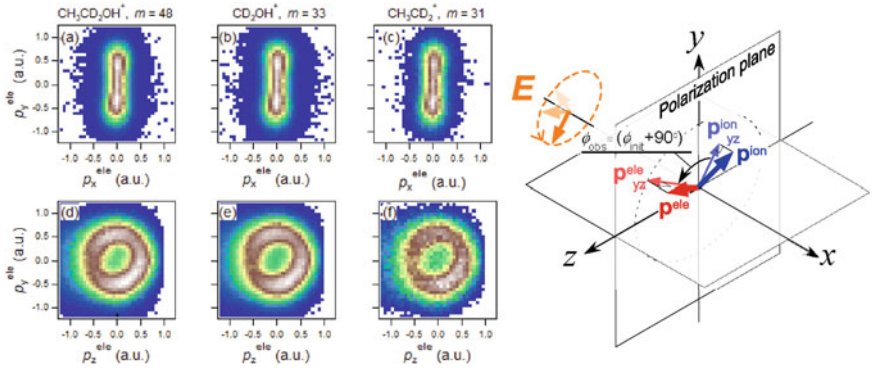

Fig. 4.4 Channel-resolved 3D PMD of CH_3CD_2OH ionized by a circularly polarized 800-nm laser field at the intensity of 80 TW/cm^2. Projected distributions on the xy plane ((**a**)–(**c**)) and on the yz plane ((**d**)–(**f**)). The laser electric field propagates along the x axis and rotates on the yz plane. Distributions are correlated with the formation of $CH_3CD_2OH^+$ ((**a**) and (**d**)), CD_2OH^+ ((**b**) and (**e**)), $CH_3CD_2^+$ ((**c**) and (**f**)). The inset (right) shows the laboratory frame coordinate and the observed angle $\phi_{obs} = (\phi_{init} + 90°)$ between $\mathbf{p}_{xy}^{ele}$ and $\mathbf{p}_{xy}^{ion}$ on the laser polarization (yz) plane

time as large as that of the linearly polarized laser field at the intensity of 23 TW/cm^2 in Sect. 4.2. The final momentum of the photoelectron formed through the tunnel ionization is governed by the laser field and independent of the fragment channel.

4.3.2 *Recoil Frame Photoelectron Momentum Distribution of the CD_2OH^+ Channel*

Using the recoil momentum of the fragment ion detected in coincidence, we can transform the laboratory frame (xyz) to the recoil frame (XYZ) that the YZ plane remains to be parallel to the polarization plane, and that the Y axis is defined by the projection $\mathbf{p}_{yz}^{ion}$ of the recoil momentum $\mathbf{p}^{ion}$ of the fragment ion on the YZ plane. The recoil direction of a fragment ion reflects the orientation of the ethanol molecule. The recoil frame PMD (RF-PMD) of the CD_2OH^+ channel is shown in Fig. 4.5a. The momentum distribution of the fragment ion, CD_2OH^+, is almost isotropic with the maximum at $\mathbf{p}^{ion} = 0$ in the laboratory frame as shown in Fig. 4.5b. In the analysis to extract the RF-PMD, we selected the events with the fragment recoil vector along the polarization plane. The imposed condition is that the out-of-plane angle of $\mathbf{p}^{ion}$ with respect to the polarization plane is smaller than 10°. To reduce the influence of the initial thermal velocity, we additionally imposed the restriction on the velocity of the fragment ion. We selected the events with the recoil velocity larger than 2×10^{-4} atomic units. The corresponding momentum is plotted as a red circle on the momentum distribution of CD_2OH^+ in Fig. 4.5b. This velocity was determined by the observed velocity spread of the parent ion, $CH_3CD_2OH^+$.

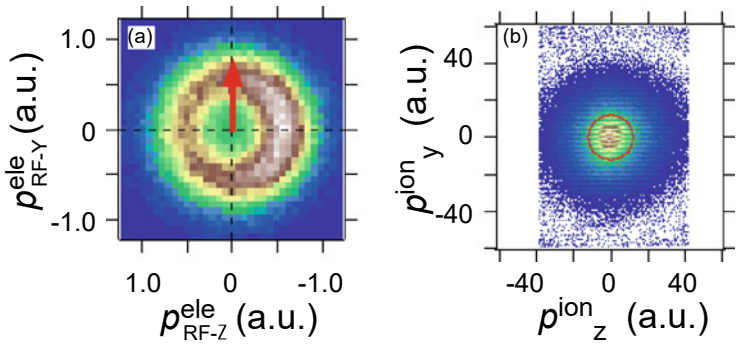

Fig. 4.5 **a** Observed RF-PMD of the CD_2OH^+ channel. The plotted distribution is the projection on the circular polarization (YZ) plane. The projected recoil direction of CD_2OH^+ on the laser polarization plane is shown by a red arrow along the Y axis in the recoil frame. **b** The projected momentum distribution of CD_2OH^+ on the yz plane in the laboratory frame. To extract the RF-PMD, we selectively analyzed the events that the velocity of the fragment ions is larger than 2×10^{-4} a.u. (a red circle) and the out-of-plane angle of the CD_2OH^+ recoil with respect to the polarization plane is smaller than 10°

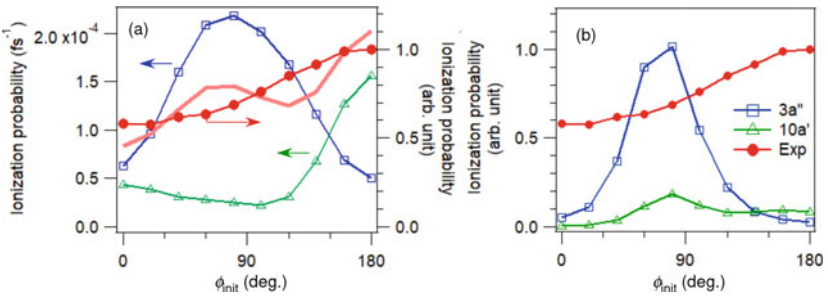

Fig. 4.6 **a** Observed RF-PAD $\Omega^{exp}_{CD_2OH^+}(\phi_{init})$ (red solid circle) for the CD_2OH^+ formation and calculated RF-PADs $\Omega_{i,CD_2OH^+}(\phi_{init})$ from the deformed $3a''$ (HOMO: blue open square) and $10a'$ (HOMO-1: green open triangle) orbitals. The fitting result of the linear combination of $\Omega_{3a'',CD_2OH^+}(\phi_{init})$ and $\Omega_{10a',CD_2OH^+}(\phi_{init})$ to the experimental RF-PAD $\Omega^{exp}_{CD_2OH^+}(\phi_{init})$ is plotted as a light red line. **b** Calculated RF-PADs $\Omega^{0}_{i,CD_2OH^+}(\phi_{init})$ from the frozen $3a''$ (blue open square) and $10a'$ (green open triangle) orbitals

To extract the angular distribution of the photoelectron at the moment of birth, we take account of the electron drift by the circularly polarized laser field to the perpendicular direction on the polarization plane [19, 20]. We define ϕ_{init} as the photoelectron emission angle on the YZ plane of the recoil frame at the moment of birth. Thus the observed angle ϕ_{obs} between $\mathbf{p}^{ion}_{yz}$ and $\mathbf{p}^{ele}_{yz}$ is described as $\phi_{obs} = (\phi_{init} + 90°)$. We rotated the image in Fig. 4.5a by 90° in a clockwise direction to obtain the recoil frame PAD (RF-PAD) as a function of ϕ_{init}. The RF-PMD image after the 90°-rotation shows the reflection symmetry with respect to the Y axis, suggesting that the influence of the Coulomb attraction in the photoelectron emission driven by the laser field [21] is negligible.

The experimentally observed RF-PAD $\Omega^{exp}_{CD_2OH^+}(\phi_{init})$ of the CD_2OH^+ channel is shown in Fig. 4.6. In the tunnel ionization, the photoelectron is emitted in the direction opposite to the electric field direction. The RF-PAD $\Omega^{exp}_{CD_2OH^+}(\phi_{init})$ exhibits a peak at $\phi_{init} = 180°$, suggesting that the ionization takes place preferentially when the electric field is in the direction parallel to the CD_2OH^+ recoil vector.

Using the DFT [14, 22] with the self-interaction correlation proposed by Krieger, Li, Iafrate [23, 24], we calculated the orientation dependent ionization probability as a function of the direction (Φ, Θ) of the static electric field with respect to the molecular structure as shown in the inset of Fig. 4.7. It is considered that the electron can move faster than the temporal variation of the laser electric field with the wavelength of 800 nm and that the tunnel of the electron takes place even faster than one-cycle of the laser field. The applied electric field is strong enough for the tunnel ionization to occur dominantly. Basically, the electronic dynamics proceeds adiabatically [25]. Therefore, the ionization probability in the static electric field is valid for discussing the ionization dynamics at a specific timing in the circularly polarized laser field. The static Kohn–Sham equation in the external electric field $\mathbf{E}$ is described as

$$\{h[n(\mathbf{r})] + V_{\text{ext}}(\mathbf{r})\}\phi_i(\mathbf{r}) = \epsilon_i\phi_i(\mathbf{r}) \tag{4.1}$$

where $V_{\text{ext}}(\mathbf{r})$ is an external dipole field, $V_{\text{ext}}(\mathbf{r}) = -e\mathbf{E}\cdot\mathbf{r}$. The static Kohn–Sham orbitals $\phi_i(\mathbf{r})$ satisfy the outgoing boundary condition without any incident waves. This is known as the Gamow state [26]. The orbital eigenvalues ϵ_i are complex as

$$\epsilon_i = \epsilon_i^{\text{R}} + i\Gamma_i, \tag{4.2}$$

where ϵ_i^{R} and Γ_i are the real and imaginary parts of ϵ_i, respectively. The imaginary part Γ_i is related to the ionization probability.

In the actual calculation, we used the absorbing potential $w(r)$ placed at a sufficiently large radius R from the molecular center with a thickness ΔR. We solved the following Kohn–Sham equation

$$\{h[n(\mathbf{r})] + V_{\text{ext}}(\mathbf{r}) - iw(r)\}\phi_i(\mathbf{r}) = (\epsilon_i^{\text{R}} + i\Gamma_i)\phi_i(\mathbf{r}) \tag{4.3}$$

with

$$-iw(r) = \begin{cases} 0 & (r < R) \\ -iw_0\dfrac{r-R}{R} & (R < r < R + \Delta R), \end{cases} \tag{4.4}$$

where w_0 and ΔR were determined so that $\phi_i(\mathbf{r})$ was completely absorbed. The ionization probability was obtained from the electron density absorbed by $w(r)$ [14].

The product ion CD_2OH^+ is known to be dominantly produced when $CH_3CD_2OH^+$ lies in the first electronically excited state which has a hole in 10a′ (HOMO-1) [13]. Therefore, we consider that the primary pathway for the formation of CD_2OH^+ originates from the photoelectron emission from 10a′.

The calculated ionization probability $W_{10a'}(\Phi, \Theta)$ is shown in Fig. 4.7a, indicating the maximum of $W_{10a'}(\Phi, \Theta)$ around $(\Phi, \Theta) = (158°, 90°)$. This electric field direction is almost parallel to the recoil vector of the CD_2OH^+ fragment ion, suggesting that the electron emission occurs from the CH_3 moiety around $\phi_{\text{init}} = 180°$. This calculated result agrees well with the experimental one shown in Fig. 4.6.

In the presence of the electric field on the C-C-O plane of ethanol, the MOs $\Upsilon_i(\Phi)$ are deformed prior to the photoelectron emission and are described as a linear combination of the field-free MOs of Ψ_i in Fig. 4.8. For the field-deformed MO $\Upsilon_{10a'}$ (HOMO-1), the calculated overlap populations $|\langle\Psi_i|\Upsilon_{10a'}(\Phi)\rangle|^2$ are shown in Fig. 4.9. Here, only a′ MOs are allowed to be mixed with 10a′ because the Cs symmetry is preserved by the electric field on the C-C-O plane. If the electric field is not on the C-C-O plane, the Cs symmetry is broken and thus the a′ orbitals can interact with a″ MOs. In the calculation assuming the electric field is not parallel to the C-C-O plane, the interaction between a′ and a″ orbitals is taken into account.

In the angular range of $\Phi = 150 - 180°$ where the ionization dominantly takes place, the field-deformed MO $\Upsilon_{10a'}$ contains $\Psi_{8a'}$ with $|\langle\Psi_{8a'}|\Upsilon_{10a'}\rangle|^2 = 0.05 - 0.07$ as shown in Fig. 4.9. The ionization probability is found to be significantly enhanced in spite of the small contribution from the neighboring MO. It is also interesting that

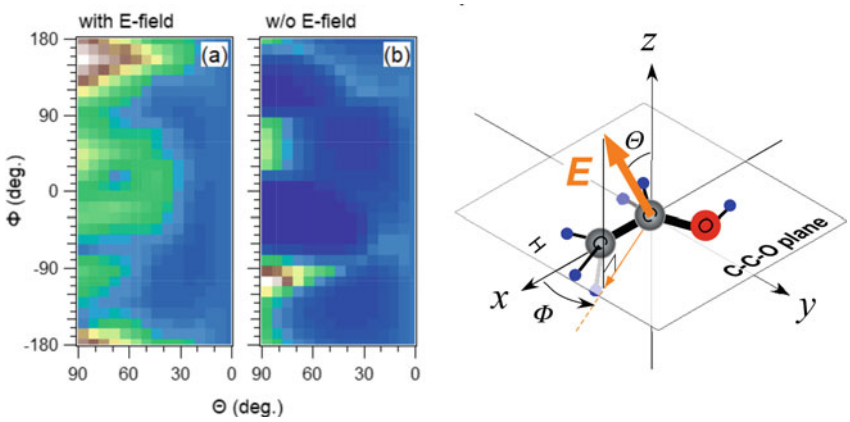

Fig. 4.7 Calculated ionization probabilities **a** $W_{10a'}(\Phi, \Theta)$ from the deformed 10a′ MO and **b** $W^0_{10a'}(\Phi, \Theta)$ from the frozen 10a′ in the electric field (1.7×10^{10} V/m). The direction of the electric field in the molecular frame is defined by the angles, Θ and Φ, in the inset (right)

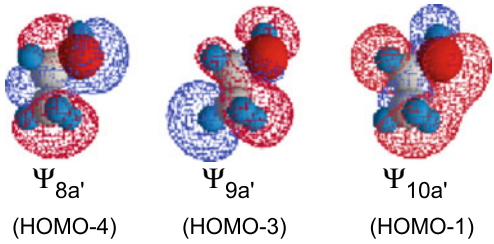

Fig. 4.8 Field-free a′ MOs of ethanol calculated by DFT

Fig. 4.9 Stacked graph of overlap populations $|\langle\Psi_i|\Upsilon_{10a'}\rangle|^2$ of $\Upsilon_{10a'}(\Phi)$ with the field free MOs $\Psi_{10a'}$, $\Psi_{9a'}$ and $\Psi_{8a'}$ from bottom. The electric field is on the C-C-O plane of ethanol ($\Theta = 90°$)

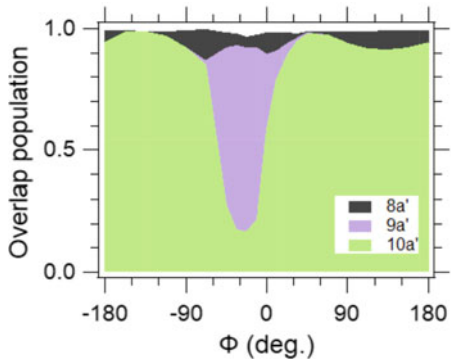

the contribution from $\Psi_{9a'}$ to $\Upsilon_{8a'}(\Phi)$ is significant around $\Phi = -30°$, meanwhile the ionization probability is not significantly enhanced. These results indicate that the degree of the MO mixing is not directly related to the tunnel ionization, which is enhanced by the extension of the lobe of MO in the anti-parallel direction to the electric field.

To confirm the effect of the orbital deformation by the electric field, we calculated the ionization probability $W^0_{10a'}(\Phi, \Theta)$ assuming the MOs are frozen in the course of ionization. By integrating the electron density of $|\Psi_{10a'}|^2$ in the spatial region outside the potential barrier formed by the electric field, $W^0_{10a'}(\Phi, \Theta)$ was obtained [14]. The potential barrier is defined using the potential by the external electric field, $V_{ext} = -e\mathbf{E} \cdot \mathbf{r}$, and the Kohn–Sham potential, $V_{KS} = V_H + V_{xc}$, where V_H is the Hartree potential and V_{xc} is the exchange-correlation potential. Using the pseudopotential of ions [27, 28], we determined the boundary where the total potential, $V_{ext} + V_{KS} + V_{ion}$, is equal to the binding energy of each MO in the outer region of the barrier.

As shown in Fig. 4.7b, $W^0_{10a'}(\Phi, \Theta)$ have a peak around $(\Phi, \Theta) = (-110°, 90°)$, but does not have a maximum around $(\Phi, \Theta) = (\pm 180°, 90°)$. This result reflects how far the lobe of the MO is extended toward the outer region at each direction, similarly to the theory of molecular tunnel ionization [29]. The peak around $(\Phi, \Theta) = (-110°, 90°)$ corresponds to the lone pair on the oxygen atom. Comparing the ionization probabilities $W_{10a'}(\Phi, \Theta)$ and $W^0_{10a'}(\Phi, \Theta)$, it is clearly found that the ionization is enhanced at $(\Phi, \Theta) = (160°, 90°)$ and suppressed at $(\Phi, \Theta) = (-110°, 90°)$ by deformation of 10a′ MO.

We compared the calculated results with the experimentally observed RF-PAD, $\Omega^{exp}_{CD_2OH^+}(\phi_{init})$, more quantitatively. It is a good approximation that the photoelectron tunnels toward the direction opposite to the laser electric field at the moment of birth. The observed RF-PAD, $\Omega^{exp}_{CD_2OH^+}(\phi_{init})$ shown in Fig. 4.6, results from the summation of the ionization probability over a certain angular range in the recoil frame. We transformed the ionization probabilities $W_{10a'}(\Phi, \Theta)$ and $W^0_{10a'}(\Phi, \Theta)$ obtained in the molecular frame of Fig. 4.7 to those in the recoil frame described in Fig. 4.4 [14]. The ionization probability in the recoil frame was integrated in the same angular range as the analysis of the experiment data. We took account of the solid angle of the photoelectron emission, which is assumed to have the same distribution as the out-of-plane distribution with the width of 31° (FWHM). Thus we obtained the calculated RF-PADs in the recoil frame of the CD_2OH^+ channel, $\Omega_{10a',CD_2OH^+}(\phi_{init})$ from the deformed MO $\Upsilon_{10a'}(\Phi)$ and $\Omega^0_{10a',CD_2OH^+}(\phi_{init})$ from the frozen MO $\Psi_{10a'}$ as shown in Fig. 4.6a and b, respectively. The peak angle of $\Omega_{10a',CD_2OH^+}(\phi_{init})$ at $\phi_{init} = 180°$ is in agreement with $\Omega^{exp}_{CD_2OH^+}(\phi_{init})$. However, as ϕ_{init} decreases from $\phi_{init} = 180°$, $\Omega_{10a',CD_2OH^+}(\phi_{init})$ decreases more rapidly than $\Omega^{exp}_{CD_2OH^+}(\phi_{init})$ and shows the minimum around $\phi_{init} = 100°$. Assuming 10a′ is frozen, $\Omega^0_{10a',CD_2OH^+}(\phi_{init})$ has a peak around $\phi_{init} = 80°$ and dose not reproduce the experimental result at all.

The discrepancy between $\Omega_{10a',CD_2OH^+}(\phi_{init})$ and $\Omega^{exp}_{CD_2OH^+}(\phi_{init})$ around $\phi_{init} = 90°$ is attributed to the sequential electronic excitation to the first electronically excited state $[(10a')^{-1}]$ following the photoelectron emission from 3a″ (HOMO) [10–12]. We consider that the experimental RF-PAD is the summation of the following

two pathways, photoelectron emission from $\Upsilon_{10a'}(\Phi)$ followed by dissociation to CD_2OH^+ and CH_3,

$$CH_3CD_2OH \rightarrow CH_3CD_2OH^+\left[(10a')^{-1}\right] + e^- \rightarrow CH_3 + CD_2OH^+ + e^-, \quad (4.5)$$

and photoelectron emission from $\Upsilon_{3a''}(\Phi)$ followed by photoexcitation and dissociation to CD_2OH^+ and CH_3^+,

$$\begin{aligned} &CH_3CD_2OH \rightarrow CH_3CD_2OH^+[(3a'')^{-1})] + e^- \\ &CH_3CD_2OH^+\left[(3a'')^{-1})\right] \rightarrow CH_3CD_2OH^+\left[(10a')^{-1}\right] \rightarrow CH_3 + CD_2OH^+. \end{aligned} \quad (4.6)$$

Using the DFT, we calculated the orientation dependent ionization probabilities from 3a″, $W_{3a''}(\Phi, \Theta)$ and $W^0_{3a''}(\Phi, \Theta)$ from $\Upsilon_{3a''}(\Phi)$ and $\Psi_{3a''}$, respectively. The RF-PADs from 3a″ of the CD_2OH^+ channel, $\Omega_{3a'',CD_2OH^+}(\phi_{init})$ and $\Omega^0_{3a'',CD_2OH^+}(\phi_{init})$ were also calculated in the same manner as those from 10a′. The excitation probability of the electronic ground state $[(3a'')^{-1}]$ to the first electronically excited state $[(10a')^{-1}]$ is defined by f_{exc}. In the circularly polarized laser field, f_{exc} is the averaged value over an optical cycle of the **E**-field rotation and independent of ϕ_{init}. Thus, $\Omega^{exp}_{CD_2OH^+}(\phi_{init})$ is described by a linear combination of $\Omega_{10a',CD_2OH^+}(\phi_{init})$ and $\Omega_{3a'',CD_2OH^+}(\phi_{init})$ as

$$\Omega^{exp}_{CD_2OH^+}(\phi_{init}) = \Omega_{10a',CD_2OH^+}(\phi_{init}) + f_{exc}\Omega_{3a'',CD_2OH^+}(\phi_{init}). \quad (4.7)$$

Through the least-squares fitting, $f_{exc} = 0.478(2)$ was obtained. The discrepancy between $\Omega^{exp}_{CD_2OH^+}(\phi_{init})$ and $\Omega_{10a',CD_2OH^+}(\phi_{init})$ can be largely compensated by $\Omega_{3a'',CD_2OH^+}(\phi_{init})$ as plotted in Fig. 4.6a. If we do not take the MO deformation into account, neither $\Omega^0_{10a',CD_2OH^+}(\phi_{init})$ nor $\Omega^0_{3a'',CD_2OH^+}(\phi_{init})$ exhibits the peak around $\phi_{init} = 180°$ as shown in Fig. 4.6b. This means that the experimental RF-PAD cannot be explained without the MO deformation. The MO deformation plays an essential role in ionization of the inner valence orbital 10a′.

The value of f_{exc} was evaluated on the basis of the ion yield ratio obtained from the time-of-flight mass spectrum shown in Fig. 4.10. The yield of CD_2OH^+ ($m = 33$ u), $I_{CD_2OH^+}$, is equal to the ionization probability integrated over 4π solid angle and described as

$$I_{CD_2OH^+} = P_{10a'} + f_{exc}P_{3a''} \quad (4.8)$$

where $P_{10a'}$ and $P_{3a''}$ are the integrated ionization probabilities from $\Upsilon_{10a'}(\Phi)$ and $\Upsilon_{3a''}(\Phi)$, respectively. The molecular ethanol ions in the electronic ground state are correlated to the formation of $CH_3CD_2OH^+$ and CH_3CDOH^+[13]. Therefore, the summation of the ion yields of $CH_3CD_2OH^+$ ($m = 48$ u) and CH_3CDOH^+ ($m = 46$ u), $I_{CH_3CD_2OH^+} + I_{CH_3CDOH^+}$, is expressed as

$$I_{CH_3D_2OH^+} + I_{CH_3DOH^+} = (1 - f_{exc})P_{3a''}. \quad (4.9)$$

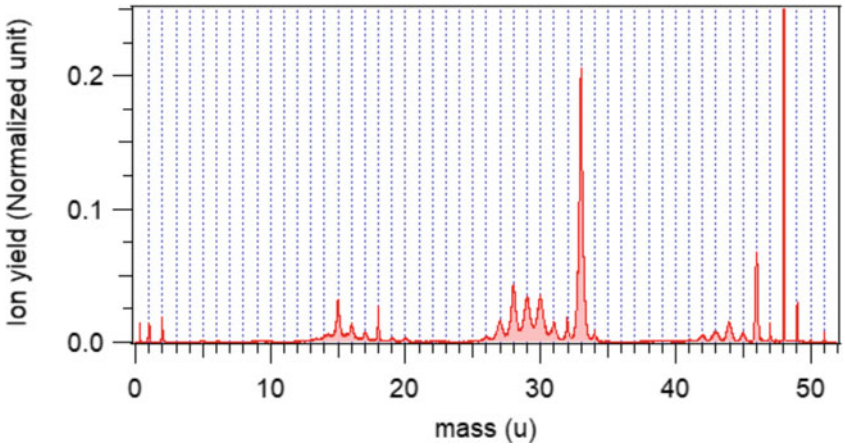

Fig. 4.10 Time-of-flight mass spectrum of CH_3CD_2OH. The ion yield is normalized by the peak intensity of $CH_3CD_2OH^+$ (m = 48 u)

Using Eqs. 4.8 and 4.9, f_{exc} is obtained as

$$f_{\mathrm{exc}} = \frac{R_{\mathrm{ion}} P_{3a''} - P_{10a'}}{(1 + R_{\mathrm{ion}}) P_{3a''}}, \tag{4.10}$$

where $R_{\mathrm{ion}} = I_{CD_2OH^+}/(I_{CH_3CD_2OH^+} + I_{CH_3CDOH^+})$. The other fragment ions such as $CH_3CD_2^+$, CH_2CD^+ and CDO^+ are known to be generated from the higher lying electronically excited states of $CH_3CD_2OH^+$ [13]. Considering that the observed ion yields of the other fragment ions are even smaller that the yield of CD_2OH^+ and $CH_3CD_2OH^+$, the excitation probability to the higher lying electronically excited states is estimated to be negligibly small.

The ion yield ratio of R_{ion} = 1.33 was obtained from the time-of-flight mass spectrum shown in Fig. 4.10. Inserting this R_{ion} value into Eq. 4.10 with $P_{10a'}$ and $P_{3a''}$ calculated by the DFT, the excitation probability becomes $f_{\mathrm{exc}} = 0.478$, which is in good agreement with the value obtained by the least-squares fitting using Eq. 4.7.

Considering the two pathways for the CD_2OH^+ formation, theoretically calculated RF-PAD becomes close to the experimental one. The residual discrepancy between the theoretical and experimental RF-PADs is caused partly by the deviation from the axial-recoil approximation in the fragmentation of $CH_3CD_2OH^+$ into CH_3 and CD_2OH^+.

The stepwise process that photoelectron emission from 3a″ followed by photoexcitation was revealed by channel-resolved photoelectron spectra and by energy correlations between photoelectrons and fragment ions at the intensity weaker than 23 TW/cm^2 of the linearly polarized laser fields [10, 12]. As the laser intensity increased to 23 TW/cm^2 and higher, the difference between channel-resolved photoelectron spectra was hardly identified and the kinetic energy distribution of the

fragment ions did not vary as a function of the photoelectron energy. Therefore, it was difficult to separate photoelectron emission and subsequent excitation pathways in the tunnel ionization regime. The angular correlation shown in this study provides the RF-PAD, through which we can compare the experimental measurement with the theoretical models. As a result, photoelectron emission and subsequent electronic excitation pathways are clearly revealed even in the tunnel ionization regime at 80 TW/cm^2 of the circularly polarized laser field.

4.3.3 *Recoil Frame Photoelectron Momentum Distribution of the $CH_3CD_2^+$ Channel*

We analyzed the $CH_3CD_2^+$ channel in the same manner as the CD_2OH^+ channel. The experimental RF-PMD is shown in Fig. 4.11a. Unlike the CD_2OH^+ channel, the isotropic ring shape is observed in the RF-PMD. The momentum distribution of $CH_3CD_2^+$ is also shown in Fig. 4.11b, indicating the isotropic distribution with the maximum at $\mathbf{p}^{\mathbf{ion}} = 0$, similarly to CD_2OH^+. In the recoil frame of this channel, the projection $\mathbf{p}^{\mathbf{ion}}_{\mathbf{yz}}$ of the recoil momentum $\mathbf{p}^{\mathbf{ion}}$ of $CH_3CD_2^+$ on the polarization (YZ) plane is parallel to the Y axis. The YX plane is common to the $CH_3CD_2^+$ and CD_2OH^+ channels, but the direction of the Y axis is almost opposite with respect to the molecular structure.

From the RF-PMD of the $CH_3CD_2^+$ channel, the RF-PAD $\Omega^{\mathrm{exp}}_{CH_3CD_2^+}(\phi_{\mathrm{init}})$ is obtained as shown in Fig. 4.12, indicating the flat distribution. It is known that

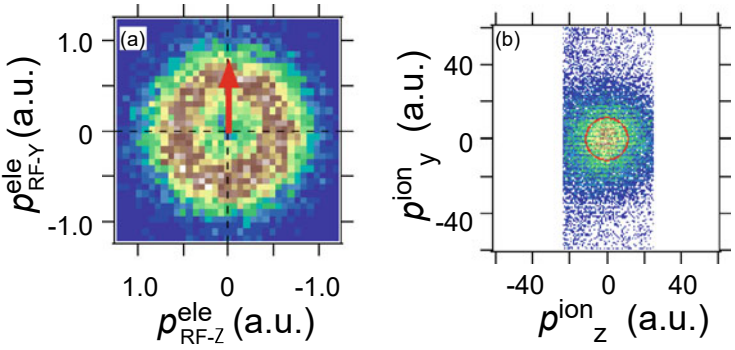

Fig. 4.11 **a** Observed RF-PMD of the $CH_3CD_2^+$ channel. The plotted distribution is the projection on the circularly polarization plane. The projected recoil direction of $CH_3CD_2^+$ on the laser polarization plane is shown by a red arrow along the Y axis in the recoil frame. **b** The projected momentum distribution of $CH_3CD_2^+$ on the yz plane in the laboratory frame. To extract RF-PMD, we selectively analyzed the events that the velocity of the fragment ions is larger than 2×10^{-4} a.u. (a red circle) and the out-of-plane angle of the $CH_3CD_2^+$ recoil with respect to the polarization plane is smaller than 10°

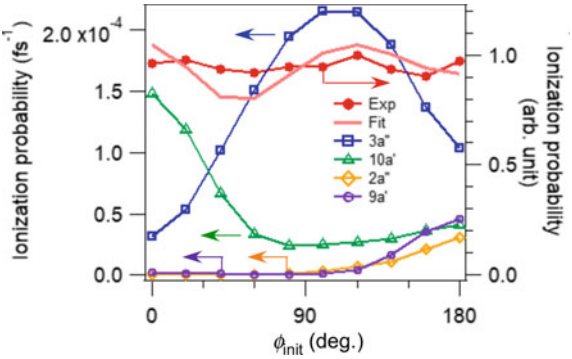

Fig. 4.12 **a** Observed RF-PAD $\Omega^{exp}_{CH_3CD_2^+}(\phi_{init})$ (red solid circle) for the $CH_3CD_2^+$ formation and calculated RF-PADs $\Omega_{i,CH_3CD_2^+}(\phi_{init})$ from the deformed $3a''$ (blue open square), $10a'$ (green open triangle), $2a''$ (yellow open diamond) and $9a'$ (purple open circle) orbitals. The fitting result of the linear combination of $\Omega_{3a'',CH_3CD_2^+}(\phi_{init})$, $\Omega_{10a',CH_3CD_2^+}(\phi_{init})$, $\Omega_{2a'',CH_3D_2^+}(\phi_{init})$ and $\Omega_{9a',CH_3CD_2^+}(\phi_{init})$ to the experimental RF-PAD $\Omega^{exp}_{CH_3CD_2^+}(\phi_{init})$ is plotted as a light red line

$CH_3CD_2^+$ is produced from the second, third and higher electronically excited states of $CH_3CD_2OH^+$ [13]. The second and third electronically excited states have a hole in $2a''$ (HOMO-2) and $9a'$ (HOMO-3), respectively. The RF-PADs, $\Omega_{2a'',CH_3CD_2^+}(\phi_{init})$ and $\Omega_{9a',CH_3CD_2^+}(\phi_{init})$, from $2a''$ and $9a'$ were calculated through the frame transformation of the ionization probabilities of $W_{2a''}(\Phi, \Theta)$ and $W_{9a'}(\Phi, \Theta)$, respectively, to the recoil frame of the $CH_3CD_2^+$ channel.

Both of $\Omega_{2a'',CH_3CD_2^+}(\phi_{init})$ and $\Omega_{9a',CH_3CD_2^+}(\phi_{init})$ exhibit the peak at $\phi_{init} = 180°$, corresponding to the tunnel ionization from the OH moiety in the $CH_3CD_2^+$ channel. These distributions are quite different from the experimental flat distribution of $\Omega^{exp}_{CH_3CD_2^+}(\phi_{init})$. In order to take account of the stepwise photoelectron emission and excitation as additional pathways, we additionally calculated the RF-PADs, $\Omega_{3a'',CH_3CD_2^+}(\phi_{init})$ and $\Omega_{10a',CH_3CD_2^+}(\phi_{init})$, from $3a''$ (HOMO) and $10a'$ (HOMO-1) in the $CH_3CD_2^+$ recoil frame from $W_{3a''}(\Phi, \Theta)$ and $W_{10a'}(\Phi, \Theta)$, respectively. It is found that the electron in $3a''$ is emitted from the lone pair on the O atom ($\phi_{init} \approx 100°$) and that the electron in $10a'$ is emitted from the CH_3 moiety ($\phi_{init} \approx 0°$) as described in Sect. 4.3.2.

We performed the least-squares fitting of the linear combination of these four RF-PADs $\Omega_{i,CH_3CD_2^+}(\phi_{init})$ to the experimental one, $\Omega^{exp}_{CH_3CD_2^+}(\phi_{init})$ as

$$\Omega^{exp}_{CH_3CD_2^+}(\phi_{init}) = \sum_i C_i \Omega_{i,CH_3CD_2^+}(\phi_{init}). \tag{4.11}$$

The fitting result of the coefficient ratio was

$$\{C_{3a''}, C_{10a'}, C_{2a''}, C_{9a'}\} = \{0.623(2), 1.000(5), 0.95(744), 0.26(296)\}.$$

The fitting errors of $C_{2a''}$ and $C_{9a'}$ are significantly large. The correlation between $\Omega_{2a'',CH_3CD_2^+}(\phi_{init})$ and $\Omega_{9a',CH_3CD_2^+}(\phi_{init})$ is strong in the fitting process, because the two RF-PADs are very similar. Considering such large fitting errors and correlation, the quantitative evaluation is difficult. In addition, the deviation from the axial-recoil approximation in the fragmentation should exist, similarly to the CD_2OH^+ channel. Nevertheless, it is certainly revealed that for the $CH_3CD_2^+$ formation there is a substantial contribution of the stepwise processes of the photoexcitation following the photoelectron emission from 3a″ (HOMO) and 10a′ (HOMO-1).

4.4 Summary

We investigated the electronic dynamics in dissociative ionization of ethanol in intense infrared laser fields. We focused our attention on the angular correlation between photoelectron emission and fragment recoil in the CH_2OH^+ and $C_2H_5^+$ channels. The PADs were measured by using PEPICO-MI in a channel-resolved manner. It was confirmed that the photoelectron emission tends to be directed along the laser electric field irrespective of the molecular orientation, as the intensity of the linearly polarized laser fields increases to the tunnel ionization regime. Similarly, using the circularly polarized laser field at 80 TW/cm^2, we could not find any difference between channel-resolved PMDs in the laboratory frame for the $CH_3CD_2OH^+$, CD_2OH^+ and $CH_3CD_2^+$ channels. However, the anisotropic PMD could be extracted in the recoil frame of the CD_2OH^+ channel. By taking account of the electron drift of 90°-rotation by the circularly polarized laser field, we could extract the RF-PAD at the moment of birth and indicated that the tunnel ionization preferentially occurs from the CH_3 moiety. The DFT calculation in the static electric field reproduced the experimentally observed RF-PAD. It was suggested that the deformation of the MO prior to the photoelectron emission is essential and that the photoelectron emission from 3a″ (HOMO) followed by the photoexcitation proceeds in addition to the photoelectron emission from the inner valence 10a′ MO. In the $CH_3CD_2^+$ channel, we experimentally obtained the isotropic RF-PAD. As compared with the calculated RF-PADs from the four valence orbitals, it was suggested that there is a substantial contribution of the stepwise processes that photoexcitation follows the electron emission from 3a″ (HOMO) and 10a′ (HOMO-1).

Finally, angular correlation measurement like RF-PADs allows us to know how electronic dynamics proceeds in molecules in the tunnel ionization regime, where we could not gain a deep insight from channel-resolved photoelectron spectra and energy correlation between the photoelectron and fragment ions.

Acknowledgements We thank Dr. K. Hosaka, Dr. A. Yokoyama and Prof. K. Yamanouchi for their support in the early stage of this work, Ms. Y. Hagihara for her support in the data analysis, and Dr. M. Tsubouchi and Prof. H. Kono for their valuable discussion. The present work was financially supported in part by JSPS KAKENHI (Grant Numbers 22685004, 26288013, and 17K05089).

References

1. A.D. Bandrauk, *Molecules in Laser Fields* (Marcel Dekker, New York, 1993)
2. J. Itatani, J. Levesque, D. Zeidler, H. Niikura, H. Pépin, J.C. Kieffer, P.B. Corkum, D.M. Villeneuve, Nature **432**(7019), 867 (2004)
3. P.M. Kraus, O.I. Tolstikhin, D. Baykusheva, A. Rupenyan, J. Schneider, C.Z. Bisgaard, T. Morishita, F. Jensen, L.B. Madsen, H.J. Wörner, Nat. Commun. **6**, 7039 (2015)
4. D. Baykusheva, M.S. Ahsan, N. Lin, H.J. Wörner, Phys. Rev. Lett. **116**(12), (2016)
5. D. Baykusheva, S. Brennecke, M. Lein, H.J. Wörner, Phys. Rev. Lett. **119**(20), (2017)
6. D. Baykusheva, H.J. Wörner, Phys. Rev. X **8**(3), (2018)
7. A.S. Alnaser, S. Voss, X.M. Tong, C.M. Maharjan, P. Ranitovic, B. Ulrich, T. Osipov, B. Shan, Z. Chang, C.L. Cocke, Phys. Rev. Lett. **93**(11), (2004)
8. B. Jochim, R. Siemering, M. Zohrabi, O. Voznyuk, J.B. Mahowald, D.G. Schmitz, K.J. Betsch, B. Berry, T. Severt, N.G. Kling, T.G. Burwitz, K.D. Carnes, M.F. Kling, I. Ben-Itzhak, E. Wells, R. de Vivie-Riedle, Sci. Rep. **7**(1), 4441 (2017)
9. T. Endo, A. Matsuda, M. Fushitani, T. Yasuike, O.I. Tolstikhin, T. Morishita, A. Hishikawa, Phys. Rev. Lett. **116**(16), (2016)
10. K. Hosaka, A. Yokoyama, K. Yamanouchi, R. Itakura, J. Chem. Phys. **138**(20), (2013)
11. T. Ikuta, K. Hosaka, H. Akagi, A. Yokoyama, K. Yamanouchi, F. Kannari, R. Itakura, J. Phys. B At. Mol. Opt. Phy. **44**(19), (2011)
12. K. Hosaka, R. Itakura, K. Yokoyama, K. Yamanouchi, A. Yokoyama, Chem. Phys. Lett. **475**(1–3), 19 (2009)
13. Y. Niwa, T. Nishimura, T. Tsuchiya, Int. J. Mass Spectrom. Ion Phys. **42**, 91 (1982)
14. H. Akagi, T. Otobe, R. Itakura, Sci. Adv. **5**(5), eaaw1885 (2019)
15. J. Ullrich, R. Moshammer, A. Dorn, R. Dorner, L.P.H. Schmidt, H. Schmidt-Bocking, Rep. Prog. Phys. **66**(9), 1463 (2003)
16. M. Lebech, J.C. Houver, D. Dowek, Rev. Sci. Instrum. **73**(4), 1866 (2002)
17. R.R. Freeman, P.H. Bucksbaum, H. Milchberg, S. Darack, D. Schumacher, M.E. Geusic, Phys. Rev. Lett. **59**(10), 1092 (1987)
18. P.B. Corkum, N.H. Burnett, F. Brunel, Phys. Rev. Lett. **62**(11), 1259 (1989)
19. A. Staudte, S. Patchkovskii, D. Pavičić, H. Akagi, O. Smirnova, D. Zeidler, M. Meckel, D.M. Villeneuve, R. Dörner, M.Y. Ivanov, P.B. Corkum, Phys. Rev. Lett. **102**(3), (2009)
20. H. Akagi, T. Otobe, A. Staudte, A. Shiner, F. Turner, R. Dorner, D.M. Villeneuve, P.B. Corkum, Science **325**(5946), 1364 (2009)
21. K.I. Dimitriou, D.G. Arbó, S. Yoshida, E. Persson, J. Burgdörfer, Phys. Rev. A **70**(6), (2004)
22. T. Otobe, K. Yabana, J.I. Iwata, Phys. Rev. A **69**(5), (2004)
23. J.B. Krieger, Y. Li, G.J. Iafrate, Phys. Rev. A **45**(1), 101 (1992)
24. X.M. Tong, S.I. Chu, Phys. Rev. A **55**(5), 3406 (1997)
25. H. Kono, Y. Sato, M. Kanno, K. Nakai, T. Kato, Bull. Chem. Soc. Jpn **79**(2), 196 (2006)
26. G. Gamow, Z. Phys. **51**(3), 204 (1928)
27. L. Kleinman, D.M. Bylander, Phys. Rev. Lett. **48**(20), 1425 (1982)
28. N. Troullier, J.L. Martins, Phys. Rev. B **43**(3), 1993 (1991)
29. X.M. Tong, Z.X. Zhao, C.D. Lin, Phys. Rev. A **66**(3), (2002)

Chapter 5
Effects of Electron Correlation on the Intense Field Ionization of Molecules: Effective Potentials of Time-Dependent Natural Orbitals

Hirohiko Kono, Shu Ohmura, Tsuyoshi Kato, Hideki Ohmura, and Shiro Koseki

Abstract We review our effective potential approach based on the multiconfiguration time-dependent (TD) Hartree–Fock (MCTDHF) method to simulate the multielectron dynamics of molecules. According to the formulation of MCTDHF, we introduce the equations of motion for TD natural orbitals $\{\phi_j(t)\}$ and TD effective potentials $v_j^{\mathrm{eff}}(t)$ that determine the fate of the dynamics of $\phi_j(t)$. $v_j^{\mathrm{eff}}(t)$ is separated into the one-body part $v_1(t)$ including the interaction with the laser electric field $\boldsymbol{\varepsilon}(t)$ and the two-body part $v_{2,j}(t)$ originating from electron–electron interaction. The estimated ionization rate for a CO molecule in an intense near-IR field is higher when $\boldsymbol{\varepsilon}(t)$ turns to the direction from C to O than when $\boldsymbol{\varepsilon}(t)$ is reversed, which is in agreement with experimentally observed preferential ionization from the C side. The mechanism of the directional anisotropy in tunnel ionization of CO is attributed to a narrow hump *near* the C nucleus formed in $v_{5\sigma}^{\mathrm{eff}}(t)$ of the 5σ HOMO which

H. Kono (✉)
Department of Chemistry, Graduate School of Science, Tohoku University, 6-3 Aramaki-Aza-Aoba, Aoba-ku, Sendai 980-8578, Japan
e-mail: hirohiko.kono.d6@tohoku.ac.jp

S. Ohmura
Department of Physical Science and Engineering, Nagoya Institute of Technology, Gokiso-cho, Showa-ku, Nagoya 466-8555, Japan
e-mail: s.ohmura@nitech.ac.jp

T. Kato
Department of Chemistry, School of Science, The University of Tokyo, 7-3-1 Hongo, Bunkyo-ku, Tokyo 113-0033, Japan
e-mail: tkato@chem.s.u-tokyo.ac.jp

H. Ohmura
National Institute of Advanced Industrial Science and Technology (AIST), 1-1-1 Higashi, Tsukuba, Ibaraki 305-8565, Japan
e-mail: hideki-ohmura@aist.go.jp

S. Koseki
Department of Chemistry, Graduate School of Science, Osaka Prefecture University, 1-1 Gakuen-cho, Naka-ku, Sakai, Osaka 599-8531, Japan
e-mail: shiro@c.s.osakafu-u.ac.jp

K. Yamanouchi et al. (eds.), *Progress in Ultrafast Intense Laser Science XVI*,
Topics in Applied Physics 141, https://doi.org/10.1007/978-3-030-75089-3_5

results from the field-induced change in $v_{2,5\sigma}(t)$. Analysis of effective potentials reveals that the suppression of 5σ ionization when $\boldsymbol{\varepsilon}(t)$ points from O to C is correlated with the enhancement in high-order harmonic generation from 4σ HOMO-2. A hump structure is also found in $v^{\text{eff}}_{\text{HOMO}}(t)$ of LiH interacting with an intense near-IR pulse, which identifies the ionization mechanism as "asymmetric charge-resonance enhanced ionization."

5.1 Introduction

Any material can be discharged by irradiation of light if the frequency of the light exceeds a certain threshold. This type of phenomenon was discovered in 1887 by Hertz and Hallwachs as a photoelectric effect and is now understood as ionization by photon absorption. In line with this discovery, Einstein proposed in 1905 the idea that a light beam consists of photons whose energies are proportional to the frequency of the light. In 1931, Goeppert-Mayer predicted that at high light intensity, more than one photon can be absorbed by a system. Thirty years later, Kaiser and Garrett experimentally verified two-photon absorption in a europium-doped crystal by utilizing a laser light source then developed [1]. A few years later, two-photon ionization was realized for photodetachment of I^- [2]. Multiphoton spectroscopy is currently one of the most versatile tools to investigate the structure and dynamics of intermediate electronic states in molecules [3–5].

New features have emerged above the horizon of the research of photoionization as the light intensity provided by laser systems available becomes as strong as Coulomb interaction in atoms or molecules. Ti: Sapphire near-infrared (near-IR) laser systems has now provided ultrashort few cycle pulses whose focused light intensity I are much greater than 10^{14} Wcm^{-2}. If I approaches ~10^{13} Wcm^{-2}, an atom or molecule is ionized with more than the energetically required number of photons. In this case, the photoelectron spectrum exhibits peaks that correspond to additional photons absorbed beyond the ionization threshold. This phenomenon, namely above threshold ionization, was first experimentally observed by Agostini et al. [6].

Laser fields of which the intensities are beyond 10^{14} Wcm^{-2} initiate large amplitude electronic motion, which results in a variety of physical or chemical phenomena in a wide range of timescale. Intense, ultrashort femtosecond (fs) or attosecond laser pulses are utilized to induce/manipulate electronic motions in atoms, molecules, etc. on extremely short timescales. Such systems are then highly excited or ionized in a nonperturbative manner. A typical phenomenon in the intensity regime of $I > 10^{14}$ Wcm^{-2} is tunnel ionization, which can be followed by efficient high-order harmonic generation (HHG) of emission. A number of experimental and theoretical works have been dedicated to explore the essence of the intense-field induced electron dynamics in atoms [7], molecules [8], solids [9], and biological systems [10], while aiming for practical application.

The temporal response of bound electronic/vibrational states in an atom or a molecule to an applied electric field can be categorized into two regimes, i.e., adiabatic and nonadiabatic [11]. It is possible to extend the concept of adiabaticity to ionization dynamics as well. Ionization induced by intense laser fields is usually characterized by the Keldysh parameter $\gamma = \left(\omega / f_{\max}\right)\left(2I_{\mathrm{P}}\right)^{1/2}$ [12] (in atomic units), where ω is the angular frequency of the applied field, $f_{\max}$ is the maximum of the electric field envelope of the pulse and I_{P} is the ionization potential. The mechanism of ionization is usually classified as adiabatic "quasistatic" tunnel ionization if $\gamma < 1$ and as multiphoton ionization if $\gamma > 1$. One can tune γ by making the most of light sources of different frequencies and intensities.

Diverse theoretical approaches have been developed to estimate or calculate the ionization rate or probability. In the case where the light intensity is beyond a certain limit, conventional perturbation theory does not function for the description of dynamics such as ionization. A landmark in the development of nonperturbative approaches is the one proposed by Keldysh [12], in which a formula for the rate of intense-field ionization, suited to practical use, is constructed as an electronic transition from the ground state of an atom to quantum states of an electron liberated in a driving electric field (Volkov states) [13]. In this approach, the wave function of the ground state is assumed to be not perturbed by the applied field; i.e., it is fixed. The details of the atomic energy structure, such as information on excited states or electron correlation, are not taken into account in formulating the ionization rate or probability. Another point to be noted in Keldysh's approach was the neglect of the Coulomb interaction between the released electron in the field and the remaining ion core. To cure the deficiency, Perelomov et al. developed a method, where the long-range Coulomb interaction is treated as the first-order correction in the quasiclassical action of the electron [14]. This Coulomb corrected approach is known as the Perelemov-Popov-Terent'ev (PPT) approach.

These types of approaches can be integrated as a category of *S*-matrix theory that formulates the transition probability of a quantum process. An element of the *S*-matrix in general equals to the transition amplitude obtained by projecting the total wave function of the system onto the final state in a dynamical process. Since the early days of the theoretical development for the description of nonperturbative ionization of atoms or molecules in intense laser fields, several versions of the S-matrix approach have been developed, which are together called the Keldysh-Faisal-Reiss (KFR) theory or Strong Field Approximation (SFA) [15, 16].

The Keldysh parameter γ approaches 0 as the electric field strength of the applied pulse becomes higher or the wavelength becomes longer (i.e., its optical period $2\pi / \omega$ becomes longer). In this case, an electron penetrates (or goes beyond) the distorted "quasistatic" barrier for ionization before the sign of the laser field is reversed; then, the Ammosov–Delone–Krainov (ADK) model [17], which is a quasistatic tunneling theory, is most commonly used. The ADK model is equivalent to the quasistatic limit ($\gamma \to 0$) of the PPT approach. Tong et al. have developed a molecular version of tunneling theory (now known as MO-ADK theory), where the symmetry property and asymptotic behaviour of the molecular electronic wave function are incorporated

into the treatment of the ADK model [18]. Tolstikhin and Morishita have established an adiabatic theory of intense field ionization for finite-range potentials [19].

The above approaches fall under the category of the single active electron (SAE) approximation; only one atomic or molecular orbital that is considered as the main ionizing orbital is allowed to evolve in time while interacting with the applied field. In the SAE approximation, the orbitals (or effects) of other electrons are mostly frozen at the shapes optimized at the ground-state calculation [20–22]; the one-electron time-dependent (TD) equation of motion for the least-bound electron is solved by the construction of an "effective potential" which is modelled after the interaction of an electron with the nuclei, the applied fields and the remaining electrons. One of the factors to be considered in the effective potential is dynamic multielectron polarization which results from field-induced polarization due to other electrons (orbitals) [23–25]. Semiempirical effective potentials for the ionizing orbital of a CO molecule were constructed in [26, 27] by modeling the dynamic polarization effects induced by the applied field.

Multielectron dynamics beyond the SAE picture, such as correlated electron dynamics [28, 29] and channel interference in HHG [30], is currently a primary target in the growing research field of attosecond science [31–33]. The physics in time-dependent processes beyond the SAE picture can be captured by solving the TD Schrödinger equation of a multielectron system with appropriate approximations. A relatively tractable one is the systematic expansion of the S-matrix for a dynamical quantum phenomenon (e.g., ionization) into relevant elementary processes involved [34]. In fact, only the first or second leading term in a series expansion of the S-matrix is evaluated because of practical difficulties associated with the higher order expansion.

Among first-principles approaches beyond the SAE picture is the TD version of the Hartree–Fock (HF) method, i.e., the TDHF method, where the multielectron wave function is approximated by a single Slater determinant alone and the time evolution of the molecular or atomic orbitals involved therein is evaluated under the mean field approximation. As in the HF method, the TDHF takes into account the electron–electron interaction in the mean field approximation but not correlated electron motion. For the simulation of electron dynamics, real-time real-space time-dependent density functional theory (TDDFT) is also utilized [35, 36]. In TDDFT, an exchange–correlation functional is incorporated in a fictitious reference system connected with a single TD Slater determinant, but its description of correlated electron motion is limited to a certain level because only the total electron density is legitimately determined.

As an orthodox method for including the correlated electron motion beyond the mean field approximation (electron correlation in dynamics), the multiconfiguration time-dependent Hartree–Fock (MCTDHF) method [37–47] has been developed in the past two decades. In MCTDHF, the multielectron wave function $\Psi(t)$ at time t is expressed as a linear combination of many Slater determinants corresponding to various electron configurations, as in the case of conventional quantum chemistry. The quantitative accuracy is systematically improved with increasing expansion length. In this method, both the orbitals and coefficients of Slater determinants

are optimized at each time step in compliance with TD variational schemes such as the Dirac–Frenkel variational principle [48–50].

The number of molecular orbitals (MOs) used in MCTDHF approaches has to be restricted in practical applications. The most commonly used scheme is the complete active space (CAS) method, where the orbitals used in the Slater determinants (or configuration state functions) are classified into two sets, i.e., inactive (core) and active orbitals. The two inactive spin-orbitals (SOs) that have the same spatial function are singly occupied respectively in all electron configurations; one can generate all possible electron configurations by distributing the other electrons among the active orbitals. The core orbitals are either frozen (frozen core) or subject to field-induced deformation (dynamically polarized core). This type of expansion scheme is called the time-dependent complete-active-space self-consistent-field (TD-CASSCF) method [51, 52]. Among recent advances in the MCTDHF method are the restricted configuration interaction expansion up to double or triple excitations [53–56] and the TD optimized coupled cluster expansion [57, 58], etc. Various types of wave-function-based multiconfigurational TD approaches to describe the dynamics of indistinguishable particles are introduced in a well-organized review [59].

More reliable and detailed results can generally be acquired as the theory employed is more accurate; accordingly, it become more complicated to unveil the intrinsic physics behind the numerical results. For example, the TD orbitals in the MCTDHF method are severely influenced by the effects of electron correlation originating from electron–electron (two-body) interaction, but those effects cannot be extracted straightforwardly from the time evolution of each orbital. It is difficult to assign the temporal change in orbitals separately to those due to the one-body interaction (interaction of an electron with nuclei and external fields) and those due to the two-body interaction.

In previous papers [60–64], we have attempted to establish a single orbital picture under the influence of electron correlation. To this end, we use the TD natural spin-orbitals $\{\phi_j(t)\}$ proposed by Löwdin [65], which diagonalize the first-order reduced density matrix of electrons constructed from the MCTDHF multielectron wave function $\Psi(t)$. The orbital-dependent effective potentials $\{v_j^{\mathrm{eff}}(\boldsymbol{r}, t)\}$ that govern the time evolution of $\{\phi_j(t)\}$ are then derived as a function of the spatial coordinate of an electron, $\boldsymbol{r}$ [62–64]. The TD effective potential $v_j^{\mathrm{eff}}(t)$ for $\phi_j(t)$ is the sum of two parts: $v_j^{\mathrm{eff}}(t) = v_1(t) + v_{2,j}(t)$, where $v_1(t)$ is the one-body interaction and $v_{2,j}(t)$ arises from the two-body interaction. Effective potential analysis of multielectron dynamics has been applied to the investigation of the directional anisotropy in intense-field induced ionization of heteronuclear diatomic molecules such as CO and LiH [62–64]. The role of electron correlation in dynamics can be scrutinized by comparing TDHF and MCTDHF effective potentials.

Thanks to the advance in modern laser technology, the form and phase of a laser field can be tailored for manipulating the dynamics of molecules on a femtosecond or even attosecond timescale. Space-asymmetric two-color fields are used to answer fundamental questions inherent in electron dynamics, e.g., as to what the origin of anisotropic electronic motion is. Directional anisotropy in ionization of CO has

been investigated extensively [66–69]. The emission direction of C^+ or O^+ from CO observed in $\omega + 2\omega$ two-color field ionization experiments demonstrates that ionization is enhanced to a great extent when the electric field is directed from the nucleus C to O [66–68]. This type of experiment can now be combined with the field-free molecular orientation technique, which has already been applied to CO [69]. In the SAE or single active orbital picture, ionization from the highest occupied molecular orbital (HOMO) of a molecule is treated as the main process of ionization. The role of the shape of the HOMO in anisotropic ionization is still under discussion. It has been suggested, e.g., in [70–72] that for CO the large-amplitude lobe of the HOMO around the nucleus C is correlated with the experimental fact that ionization preferentially occurs when the laser field points from C to O.

The direction of anisotropic ionization observed does not always accord with the prediction based solely on the shape and spatial extension of the HOMO. For carbonylsulphide OCS, the π HOMO has a large amplitude around the C–S axis. In the experiment performed by Holmegaad et al. [73], OCS molecules were fixed in space by combined laser and electrostatic fields and ionized with intense, circularly polarized 30-fs laser pulses. Contrary to the prediction from the shape of the HOMO, they found that ionization is enhanced when the electric field turns to the direction from O to S (i.e., an electron is then ejected from the O atom side).

For polar molecules such as CO and OCS, intense laser fields change the instantaneous energy levels of electronic states and the effects of linear Stark shifts on intense-field-induced ionization have been investigated [74–80]. The linear Stark effect increases or decreases the ionization potential when the electric field vector is parallel or antiparallel to the permanent dipole moment of the HOMO. The HOMO permanent dipole moment of OCS points from S to O and the HOMO ionization potential decreases when the electric field points from O to S, which is in accord with the experimental observation for OCS in a circularly polarized field that ionization dominantly proceeds from the O atom side [73]. In the $\omega + 2\omega$ two-color experiment reported by Ohmura et al. [72], the preferential direction was however from the S atom side (which was opposite to the ionization direction for circularly polarized pulses [73]).

The conventional MO-ADK theory [18] predicts that the ionization rate of the HOMO of CO is maximized when the electric field points from C to O [68], in agreement with the experimental result (preferential ionization from the C atom side). The results obtained by the Stark-shift-corrected MO-ADK theory indicates the opposite trend that the ionization rate of the HOMO is maximized when the electric field is reversed [68], which directly reflects the tendency that the linear Stark effect increases the ionization potential of CO when the electric field points from C to O and is thus apt to reduce the HOMO ionization rate from the C side. On the other hand, the prediction by the Stark-shift-corrected molecular SFA [68] is in accord with the experimental observation. The roles of permanent dipoles in anisotropic ionization have not been fully clarified yet. The results obtained by some theoretical approaches contradict the experimentally observed anisotropic ionization from the C atom side [81–83]. The diversity of theoretical predictions thus demands further and thorough investigation of the anisotropic ionization of CO.

Among other relevant factors to be considered are field-induced multielectron correlation effects [61] and the combined contribution to ionization from multiple orbitals [84–86]. Although the emission direction of C^+ or O^+ from CO in the two-color ionization experiments [66, 68, 84] suggests that the main ionization channel in CO is ionization from the 5σ HOMO, next lower lying orbitals such as 1π HOMO-1 and 4σ HOMO-2 contribute to the field-ionization of CO [84]. These factors also affect the efficiency of HHG. The effects of dynamic electron polarization on HHG have been discussed in [87, 88].

Effective potential is a competent and versatile tool to delve into intrinsic multi-electron nature in electronic dynamics. A straightforward application is to quantify correlation dynamics between natural orbitals by examining the temporal change in the corresponding effective potentials, though the effective potential itself is a single-electron representation. In a previous study [62–64], using the scheme of the TD-CASSCF, we calculated the effective potentials of natural orbitals for CO in an intense near-IR field ($\lambda = 760$ nm) and investigated the mechanism of anisotropic ionization of CO. The numerical results indicated that when the laser electric field points from C to O, tunnel ionization from the C atom side is significantly enhanced more than a few times compared to the field-reversed case. We found that a thin hump originating from two-body electron–electron interaction is then formed on the top of the field-induced distorted barrier in the HOMO effective potential. The hump emerges only $2a_0$ away outward from the nucleus C, which is specified as the interaction between the electron leaving the remaining core and the electrons swarming to the region of hump formation (ionization exit). We attributed the directional anisotropy in tunnel ionization of CO to this hump formation. The appearance of this kind of hump structure seems rather general. We simulated the electron dynamics of LiH in an intense field of $\lambda = 1520$ nm. The results indicate that a hump structure is formed in the 2σ HOMO effective potential of LiH and sets off anisotropic ionization.

In the present review on the effective potential approach, we also demonstrate for CO that the HHG starting from the ionization of 4σ HOMO-2 orbital is correlated with the 5σ ionization dynamics. In the following, we outline the effective potential approach and present the numerical results of the effective potentials for CO in Sects. 5.3.2 and 5.3.3 and for LiH in Sect. 5.3.4.

5.2 Theory

We present in this section the outline of the multiconfiguration time-dependent Hartree–Fock (MCTDHF) method for the simulation of multielectron dynamics of atoms and molecules. Our novel approach converts the multielectron dynamics obtained by numerically solving the equations of motion (EOMs) in the MCTDHF to a single orbital picture in the natural orbital representation and the TD effective potentials for natural orbitals are then derived from the EOMs. The roles of multi-electron dynamics together with electron correlation are quantified on the basis of the TD effective potentials in the single orbital picture.

5.2.1 The MCTDHF Method

The dynamics of an N_e-electron system in intense laser fields is governed by the TD Schrödinger equation

$$i\hbar\frac{\partial\Psi(t)}{\partial t} = \hat{H}(t)\Psi(t), \tag{5.1}$$

where $\Psi(t)$ is the multielectron TD wave function of the system at time t and $\hat{H}(t)$ is the electronic Hamiltonian that includes the interaction with the radiation field $\boldsymbol{\varepsilon}(t)$. (5.1) is solved by using the MCTDHF method where $\Psi(t)$ is expanded in terms of electron configurations $\{\Phi_I(t)\}$ necessary for the description of the dynamics under consideration ($\{\Phi_I(t)\}$ are either Slater determinants or configuration state functions) [38–47]:

$$\Psi(t) = \sum_{I=1}^{M} C_I(t)\Phi_I(t), \tag{5.2}$$

where $\{C_I(t)\}$ are the configuration interaction (CI) coefficients for $\{\Phi_I(t)\}$ and M is the total number of $\{\Phi_I(t)\}$. In the present study, the spin state is assumed to be a singlet. Each electron configuration has $N_e$spin-orbitals (SOs) $\{\psi_k(t)\}$. $\psi_k(t)$ for the kth single-orbital state $|k(t)\rangle$ is the product of a one-electron spatial orbital and a one-electron spin eigenfunction: $\psi_k(t) = \langle \boldsymbol{x} \mid k(t)\rangle$, where $\boldsymbol{x} = (\boldsymbol{r}, \mu)$ represents the set of the spatial coordinate $\boldsymbol{r}$ and the spin coordinate μ of an electron. The SOs used in the expansion are here referred to as occupied orbitals and the number of the occupied orbitals is denoted by N_o (in general, $N_o \geq N_e$). In TDHF, $N_o = N_e$.

The working EOMs for $\{\psi_k(t)\}$ and $\{C_I(t)\}$ have been derived by employing the Dirac-Frenkel TD variational principle [48–50]:

$$\langle\delta\,\Psi(t)|\left[\hat{H}(t) - i\hbar\frac{\partial}{\partial t}\right]|\Psi(t)\rangle = 0, \tag{5.3}$$

where $\delta\,\Psi(t)$ denotes all possible variations of the wave function (5.2) with respect to the degrees of freedom of the SOs and the CI-coefficients. We introduce a Lagrange multiplier matrix $\{\Lambda_{mk}(t)\}$ so that the initial orthonormalization condition at $t = t_0$ on $\{\psi_k(t)\}$ is maintained, i.e., $\langle\psi_k(t) \mid \psi_m(t)\rangle = \delta_{km}$ for $t \geq t_0$. The resulting EOMs for $\psi_k(t)$ are expressed as

$$\begin{aligned} i\hbar\frac{\partial}{\partial t}|\psi_k(t)\rangle &= \hat{h}(t)|\psi_k(t)\rangle \\ &\quad + \sum_{ij}^{N_o} A^{-1}(t)_{ki}\left[\hat{V}_{ij}(t) - \Lambda_{ij}(t)\right]\left|\psi_j(t)\right\rangle, \end{aligned} \tag{5.4}$$

where $\hat{h}(t)$ is the one-body Hamiltonian including the electric dipole interaction $\boldsymbol{r} \cdot \boldsymbol{\varepsilon}(t)$, $\hat{V}_{ij}(t)$ represents the orbital coupling between i and j mediated by other orbitals [39] and

$$A_{ij}(t) = \langle \Psi(t) | \hat{a}_i^{\dagger}(t) \hat{a}_j(t) | \Psi(t) \rangle \tag{5.5}$$

is the (i, j) matrix element of the 1st order reduced density matrix (1RDM) $\rho(\boldsymbol{x}, \boldsymbol{x}', t)$. The operators $\hat{a}_j(t)$ and $\hat{a}_j^{\dagger}(t)$ are, respectively, the annihilation and creation operators for an electron in $\psi_j(t)$. $\hat{V}_{ij}(t)$ is a function of $\boldsymbol{r}$ and dependent on $\{C_I(t)\}$. The 1RDM at t, which is a Hermitian matrix, can be calculated from $\{\psi_j(t)\}$ and $\{C_I(t)\}$, which is given by

$$\rho(\boldsymbol{x}, \boldsymbol{x}', t) = \sum_{ij}^{N_o} A_{ij}(t)\, \psi_i^*(\boldsymbol{x}, t)\, \psi_j(\boldsymbol{x}', t). \tag{5.6}$$

The trace of the 1RDM is normalized as $\Sigma_i A_{ii}(t) = N_e$ and $A^{-1}(t)_{ki}$ in (5.4) is the (k, i) element of the inverse of the1RDM.

The Lagrange multiplier $\Lambda_{ij}(t)$ may be expressed as

$$\Lambda_{ij}(t) = \sum_{k}^{N_o} \langle \psi_j(t) | \left[\hat{V}_{ik}(t) + A_{ik}(t) \hat{g}(t) \right] | \psi_k(t) \rangle, \tag{5.7}$$

where $\hat{g}(t)$ should be determined so that the orthonormalization condition $\langle \psi_j(t) \mid \psi_k(t) \rangle = \delta_{jk}$ is sustained. For (5.7), one can rewrite (5.4) as

$$\begin{aligned} i\hbar \frac{\partial |\psi_k(t)\rangle}{\partial t} = \Big[\hat{h}(t) - \hat{g}(t) \Big] |\psi_k(t)\rangle + \hat{Q}(t) \Big[\hat{g}(t) |\psi_k(t)\rangle \\ + \sum_{ij}^{N_o} A^{-1}(t)_{ki} \hat{V}_{ij}(t) |\psi_j(t)\rangle \Big], \end{aligned} \tag{5.8}$$

where $\hat{Q}(t) = 1 - \sum_k^{N_o} |\psi_k(t)\rangle\langle\psi_k(t)|$ is the projector onto the complement to the current orbital space $\{\psi_k(t)\}$. Since the time derivatives of SOs hold the following relation

$$i\hbar \langle \psi_j(t) | \frac{\partial}{\partial t} | \psi_k(t) \rangle = \langle \psi_j(t) | \Big[\hat{h}(t) - \hat{g}(t) \Big] | \psi_k(t) \rangle, \tag{5.9}$$

the time propagation becomes unitary if $\hat{g}(t)$ is a Hermitian operator like $\hat{g}(t) = \sum_{mn}^{N_o} |\psi_m(t)\rangle g_{mn}(t) \langle \psi_n(t)|$ with $g_{mn}(t) = g_{nm}^*(t)$. The derivation of EOMs for CI-coefficients starts with inserting $\langle \delta \Psi(t)| = \langle \partial \Psi(t) / \partial C_I | \delta C_I$ into the Dirac–Frenkel

variational principle (5.3) [38, 39, 41]. The EOM for C_I thus obtained contains $\{C_I(t)\}$, $\{g_{km}(t)\}$ and the matrix elements of the electron–electron interaction among SOs. The EOMS for $\{C_I(t)\}$ are coupled with (5.8).

For time propagation of $\Psi(t)$, we choose $\hat{g}(t) = \hat{h}(t)$ in (5.8) or (5.9) which is favorable for the numerical stability in solving the EOMs for $\{\psi_j(t)\}$ and $\{C_I(t)\}$; during the time-propagation of $|\psi_j(t)\rangle$, the orthonormalization condition then remains in the form of $\langle\psi_i(t) \mid \partial\psi_j(t)/\partial t\rangle = 0$ (for $i = j$ and $i \neq j$).

5.2.2 Derivation of Effective Potentials

For the choice of $\hat{g}(t) = \hat{h}(t)$, $A_{ij}(t) \neq 0$ in general. In fact, there is a way of obtaining a diagonal representation of the 1RDM. Diagonalization of the rhs of (5.6) by a unitary transformation of $\{\psi_j(t)\}$ is equivalent to seek an appropriate orbital set $\{\phi_j(t)\}$ that satisfies $A_{ij}(t) = 0$ for $i \neq j$. These orbitals $\{\phi_j(t)\}$ are nothing but natural orbitals [65]. The diagonal elements in the 1RDM for natural orbitals $\{\phi_j(t)\}$, $n_j(t) = A_{jj}(t)$, are called the occupation number of $\phi_j(t)$. The expectation value $s(t)$ of any one-body operator $\hat{s}$ is expressed as a sum of diagonal elements $s_j(t) = \langle\phi_j(t)|\hat{s}|\phi_j(t)\rangle$ [60]:

$$s(t) = \sum_j^{N_O} n_j(t) s_j(t) \tag{5.10}$$

For instance, the expectation value of the field-induced dipole moment $\hat{\boldsymbol{d}}$ satisfies (5.10).

The elements $\{A_{km}(t)\}$ of (5.5) for the wave function (5.2) can be expressed by using CI-coefficients. The EOM for $A_{km}(t)$ in the natural orbital representation we derived is as follows [62–64]:

$$\frac{\mathrm{d}A_{km}(t)}{\mathrm{d}t} = -\frac{i}{\hbar}\{W_{mk}(t) - W^*_{km}(t) + g_{mk}(t)[n_k(t) - n_m(t)]\}. \tag{5.11}$$

where $W_{km}(t)$ is defined as [89, 90]

$$\begin{aligned} W_{km}(t) = &\sum_{pqr} \big[\psi_k(t)\psi_q(t)\big|\psi_r(t)\psi_p(t)\big] \\ &\langle\Psi(t)|\hat{a}^\dagger_m(t)\hat{a}^\dagger_r(t)\hat{a}_p(t)\hat{a}_q(t)|\Psi(t)\rangle, \end{aligned} \tag{5.12}$$

with the conventional two-electron integral (in atomic units)

$$\big[\psi_k\psi_q\big|\psi_r\psi_p\big] = \int \mathrm{d}\boldsymbol{x}_1\mathrm{d}\boldsymbol{x}_2\, \psi^*_k(\boldsymbol{x}_1)\psi_q(\boldsymbol{x}_1)|\boldsymbol{r}_1 - \boldsymbol{r}_2|^{-1}\psi^*_r(\boldsymbol{x}_2)\psi_p(\boldsymbol{x}_2). \tag{5.13}$$

Let us start with the condition that $\psi_j(t_0) = \phi_j(t_0)$ at $t = t_0$. In order to satisfy $A_{km}(t) = 0$ for $k \neq m$ at $t \geq t_0$, we have to set $g_{mk}(t)$ in (5.11) as

$$g_{mk}(t) = \frac{W_{mk}(t) - W^*_{km}(t)}{n_m(t) - n_k(t)} \quad \text{for} \quad m \neq k. \tag{5.14}$$

The above constraint that $A_{km}(t) = 0$ for $k \neq m$ alone does not automatically determine the values of the diagonal elements of the operator $\hat{g}$. We here set the diagonal elements to be $g_{kk}(t) = 0$. According to this condition of $g_{kk}(t) = 0$, the phases of $\{C_I(t)\}$ and the global phases of $\{\phi_j(t)\}$ are consistently and uniquely determined through (5.8) and the EOMs for $\{C_I(t)\}$. In [89], the EOMs for natural SOs and their populations have been formulated by using the time-dependent density matrix functional theory.

Substitution of (5.14) and $g_{kk}(t) = 0$ into (5.8) yields the formal EOMs for the natural SOs $\{\phi_k(t)\}$ [62]

$$i\hbar \frac{\partial \phi_k(\boldsymbol{r}; t)}{\partial t} = \left[\hat{t} + v_k^{\text{eff}}(\boldsymbol{r}, t)\right] \phi_k(\boldsymbol{r}, t) \tag{5.15}$$

where $\hat{t}$ is the kinetic energy operator of an electron. The one-body quantity $v_k^{\text{eff}}(\boldsymbol{r}, t)$ is regarded as the orbital-dependent effective potential that determines the dynamics of $\phi_k(t)$ under multielectron interaction. We note that $v_k^{\text{eff}}(\boldsymbol{r}, t)$ consists of two independent terms: the one-body interaction term $v_1(\boldsymbol{r}, t)$ including $\boldsymbol{r} \cdot \boldsymbol{\varepsilon}(t)$ and the two-body term $v_{2,k}(\boldsymbol{r}, t)$ as

$$v_k^{\text{eff}}(\boldsymbol{r}, t) = v_1(\boldsymbol{r}, t) + \sum_j^{N_O} \frac{\langle \boldsymbol{r} | \hat{U}_{kj}(t) | \phi_j(t) \rangle}{\phi_k(\boldsymbol{r}, t)} = v_1(\boldsymbol{r}, t) + v_{2,k}(\boldsymbol{r}, t), \tag{5.16}$$

where $\hat{U}_{kj}(t)$ represents the coupling between $\phi_k(t)$ and $\phi_j(t)$

$$\hat{U}_{kj}(t) = \left(1 - \delta_{kj}\right) \frac{W_{jk}(t) - W^*_{kj}(t)}{n_k(t) - n_j(t)} + Q(t) \frac{\hat{V}_{kj}(t)}{n_k(t)} \tag{5.17}$$

Multielectron (correlation) dynamics can be examined by separately tracking the temporal change in $v_1(\boldsymbol{r}, t)$ and that in $v_{2,k}(\boldsymbol{r}, t)$. The expectation value of $\hat{t} + v_k^{\text{eff}}(\boldsymbol{r}, t)$ over $\phi_k(t)$ may be designated as a real-valued effective orbital energy $\varepsilon_k(t)$. In practice, we calculate the "instantaneous" (orthonormal) natural orbitals $\{\phi_j(t)\}$ at time t from $\{\psi_j(t)\}$ and $\{C_I(t)\}$ obtained in MCTDHF simulation under the condition of $\hat{g}(t) = \hat{h}(t)$. $v_k^{\text{eff}}(\boldsymbol{r}, t)$, as well as its components $v_1(\boldsymbol{r}, t)$ and $v_{2,k}(\boldsymbol{r}, t)$, can be plotted as a function of $\boldsymbol{r}$ by inserting $\{\phi_j(t)\}$ and the corresponding $\{C_I(t)\}$ (different from $\{C_I(t)\}$ obtained in the case of $\hat{g}(t) = \hat{h}(t)$) into (5.16).

5.3 Results and Discussion

We first present the numerical results of the ionization and HHG dynamics of a CO molecule in an intense near-IR field ($\lambda = 760$ nm) [62–64]. In Sects. 5.3.1–5.3.3, the characteristic features of the anisotropy in ionization and HHG of CO and the effects of electron correlation are examined in detail on the basis of the TD effective potentials for the 4σ and 5σ natural orbitals derived from the MCTDHF framework. The shapes of effective potentials are discussed from the viewpoint as to how electron correlation distinctly affects the electronic dynamics of CO. In the numerical simulations for CO [62–64], 10 spatial orbitals 1σ, 2σ, 3σ, 4σ, 2 × 1π, 5σ HOMO, 2 × 2π LUMO (lowest unoccupied molecular orbital) and 6σ are taken into account. We then adopted a TD-CASSCF scheme for the time evolution of the multiconfiguration expansion wavefunction [51]; the lower lying core SOs up to 4σ were treated as occupied by one electron and the time evolution of the four core orbitals obeys the EOMs derived for the core SOs. The high lying 6 SOs of 2 × 1π, 5σ, 2 × 2π, 6σ were chosen as the active orbitals that constitute the complete active space which accommodates the remaining 6 electrons. In this case, the expansion length M is 400.

The polarization direction of the applied electric field $\boldsymbol{\varepsilon}(t)$ was assumed to be parallel to the C–O axis. We adopted a two-cycle electric field $\varepsilon(t)$ (the C–O axis component of $\boldsymbol{\varepsilon}(t)$) of frequency of $\hbar\omega = 0.06E_\mathrm{h} = 1.64$ eV (wavelength $\lambda =$ 760 nm, optical period $T_\mathrm{c} = 2\pi/\omega = 2.53$ fs), where E_h is the Hartree. The carrier-envelope phase (CEP) φ is introduced as

$$\varepsilon(t) = f(t)\cos(\omega t - \varphi), \tag{5.18}$$

where the envelope function $f(t)$ is given by $f(t) = f_0 \sin^2\left(\pi t/2T_\mathrm{c}\right)$ with its maximum value of $f_0 = 0.0665\ E_\mathrm{h}/(ea_0) = 3.42 \times 10^{10}$ Vm^{-1} (the corresponding light intensity $I_0 = 1.54 \times 10^{14}$ W cm^{-2}). $\varepsilon(t)$ for $\varphi = -0.5\pi$ is shown in Fig. 5.1a and its sign is reversed when $\varphi = 0.5\pi$.

Since the polarization direction is parallel to the molecular axis, cylindrical symmetry is maintained; the cylindrical coordinates z and ρ are thus convenient for the numerical grid point representation of spatial orbitals; z is chosen parallel to the molecular axis. The nuclei C is placed at $z = -1.066\ a_0$ and O is placed at $z = 1.066\ a_0$ ($\rho = 0$), where a_0 is the Bohr radius (the C–O difference fixed is the equilibrium internuclear distance $R_\mathrm{e} = 2.132\ a_0$). The parameters necessary to numerically represent MOs such as grid intervals are given in [62].

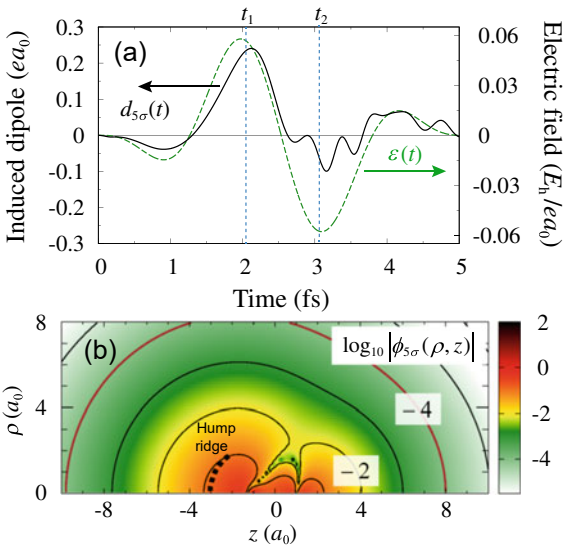

Fig. 5.1 **a** Electric field profile $\varepsilon(t)$ of the applied two-cycle pulse (5.18) of $\omega = 0.06E_h/\hbar$ with CEP of $\varphi = -0.5\pi$ (green broken line). The polarization direction is parallel to the C–O axis. The field strength is maximized at $t = 1.97$ fs as $\varepsilon_{max} = 0.0578\ E_h/(ea_0) = 2.97 \times 10^{10}$ Vm^{-1} and the field strength at $t = t_1 = 2.03$ fs is $\varepsilon(t) = 0.0572\ E_h/(ea_0) = 2.94 \times 10^{10}$ Vm^{-1}. The induced dipole moment $d_{5\sigma}(t)$ of the 5σ natural orbital is superimposed (black solid line) and that at t_1 is $d_{5\sigma}(t_1) = 0.23ea_0$. **b** Common logarithmic plot of the 5σ natural orbital $|\phi_{5\sigma}(t = 0)|$ of CO. The nuclei C and O are located at $z = -1.066a_0$ and $z = 1.066a_0$, respectively. The logarithmic contour interval is 1; for instance, the value of $|\phi_{5\sigma}(t = 0)|$ at the contour height of -4 is $10^{-4}a_0{}^{-3/2}$. See Sect. 5.3.3 and Fig. 5.4a for the hump ridge indicated by a dotted line. Adapted from Figs. 1 and 2 in [64] with permission from the publisher

5.3.1 *Intense-Field-Induced Ionization and Induced Dipole Moment of CO*

The temporal change in induced dipole moments seves as an index to characterize the overall electronic dynamics of a molecule. For the applied pulse (5.18) with $\varphi = -0.5\pi$, the induced dipole moment of the 5σ HOMO natural SO $\phi_{5\sigma}(t)$, denoted by $d_{5\sigma}(t)$, is plotted in Fig. 5.1a together with the time profile of $\varepsilon(t)$. The change in $d_{5\sigma}(t)$ is almost in proportion to $\varepsilon(t)$ up to the end of the first optical cycle (up to ~2.5 fs); the electronic response to $\varepsilon(t)$ is quasi-adiabatic. One of the reasons for this quasi-adiabatic feature is due to the fact that the energies of the excited singlet states of CO are 8.5 eV above the ground state, which is much higher than one photon energy of $\hbar\omega = 1.64$ eV [91]. In the adiabatic regime, the induced dipole moment is represented by a function of the applied electric field $\varepsilon(t)$, which is not necessarily a linear function of $\varepsilon(t)$. The electronic state can drastically alter in time as the interaction with the applied field proceeds. In the second optical cycle, the response to $\varepsilon(t)$ becomes nonadiabatic: electrons go back and forth during a half

optical cycle (excited bound states are involved if $d_{5\sigma}(t) \neq 0$ when the field returns to 0, i.e., when $\varepsilon(t) = 0$).

We found that ionization exclusively occurs from the 5σ orbital when the laser electric field points from the nucleus C to O, i.e., $\varepsilon(t) > 0$ (for instance, at $t \approx t_1 =$ 2.03 fs in Fig. 5.1a). The electric field then pushes electrons toward the side of $z < 0$ (from O to C). The ionization from 5σ was significantly reduced when $\varepsilon(t) < 0$. A criterion as to how adiabatically or nonadiabatically ionization proceeds is given by the Keldysh parameter γ. For the pulse (5.18), $\gamma \sim 1.0$. Recent theoretical and experimental studies have indicated that for few-cycle laser pulses, tunneling remains as the dominant mechanism in ionization even up to $\gamma \sim 3.0$ [92]. We thus classify the ionization process for the pulse (5.18) as tunnel ionization.

The ionization components from 4σ and 1π are less than that of 5σ [62], by orders of magnitude. The anisotropic ionization of CO is thus attributed to the nature of the 5σ HOMO. The TOF fragment analyses of $\omega + 2\omega$ experiments for CO [66–68] have also indicated that the ionization rate takes the maximum when the electric field $\varepsilon(t)$ points from C to O and takes the minimum when $\varepsilon(t)$ is reversed. For the pulse (5.18), the ionization rate estimated around the second peak of $\varepsilon(t)$ (at $t \approx t_1$) is five times larger for $\varphi = -0.5\pi$ than for $\varphi = 0.5\pi$ [62], which semiquantitatively agrees with the experimentally observed anisotropy [66].

The absolute value of the 5σ orbital amplitude, $|\phi_{5\sigma}(t = 0)|$, is depicted in Fig. 5.1b as a logarithmic contour map. In various studies [18, 68], the anisotropy in near-IR induced ionization has been attributed to the feature that the 5σ natural orbital has a large lobe protruding from the C atom. In Sect. 5.3.3, we focus on the crucial role of electron correlation in the anisotropic ionization in CO.

5.3.2 HHG Spectra of CO

We demonstrate in this subsection that HHG spectra $S(\omega_{\mathrm{H}})$ are affected by anisotropic ionization, where ω_{H} is the frequency of HHG. The HHG spectrum of a single molecule can be calculated from the Fourier transform $\mathscr{F}$ of the second order time derivative of the expectation value $\boldsymbol{d}(t)$ of the dipole moment operator $\hat{\boldsymbol{d}}$, i.e., the dipole acceleration $\ddot{\boldsymbol{d}}(t)$:

$$S(\omega_{\mathrm{H}}) = \left| \mathscr{F}\left[\ddot{\boldsymbol{d}}(t) \right] \right|^2 \tag{5.19}$$

The dipole moment $\boldsymbol{d}(t)$ in the natural orbital representation is expressed from (5.10) as

$$\boldsymbol{d}(t) = \sum_{j}^{N_{\mathrm{o}}} n_j(t) \left\langle \phi_j(t) \middle| \hat{\boldsymbol{d}} \middle| \phi_j(t) \right\rangle \tag{5.20}$$

The induced dipole moment such as $d_{5\sigma}(t)$ is given by $d_{5\sigma}(t) = \langle\phi_{5\sigma}(t)|\hat{\boldsymbol{d}}|\phi_{5\sigma}(t)\rangle - \langle\phi_{5\sigma}(0)|\hat{\boldsymbol{d}}|\phi_{5\sigma}(0)\rangle$. See $d_{5\sigma}(t)$ in Fig. 5.1a.

The HHG spectrum can be decomposed into different paths associated with respective natural orbitals by using the following expression [62]:

$$\boldsymbol{d}(t) \approx \sum_{j}^{N_o}\sum_{k}^{N_o} n_k(t)\langle\phi_j(0)|\hat{\boldsymbol{d}}|\phi_k(t)\rangle\langle\phi_k(t) \mid \phi_j(0)\rangle \tag{5.21}$$

where the overlap $\langle\phi_k(t) \mid \phi_j(0)\rangle$ denotes the transition from the initial orbital $|\phi_j(0)\rangle$ to the intermediate orbital $|\phi_k(t)\rangle$ driven by an applied field. This process is designated by the notation $k_t \leftarrow j_{t=0}$. The orbital $\phi_k(t)$ is allowed to include continuum components that may return to the ion core of the molecule. The transition matrix $\langle\phi_j(0)|\hat{\boldsymbol{d}}|\phi_k(t)\rangle$ represents the HHG upon electron recombination from the continuum component of $|\phi_k(t)\rangle$ back to the initial orbital $|\phi_j(0)\rangle$. This optical process is designated by $j_{t=0} \leftarrow k_t$. Each HHG process is weighted by the occupation numbers $\{n_k(t)\}$ of intermediate orbitals. A whole optical path in HHG can be denoted as $j_{t=0} \leftarrow k_t \leftarrow j_{t=0}$, which represents the HHG process that starts from $j_{t=0}$ to $j_{t=0}$ through k_t. Each path is thus denoted by a combination of the initial, intermediate and final natural orbitals. For instance, the path $5\sigma_{t=0} \leftarrow 5\sigma_t \leftarrow 5\sigma_{t=0}$ through $\phi_{5\sigma}(t)$ is denoted as the 5σ diagonal path. (5.21) can thus be interpreted as an extended formula for the three-step model [93, 94].

The HHG spectra $S(\omega_H)$ of CO for the pulses (5.18) with $\varphi = \mp 0.5\pi$, are presented in Fig. 5.2. As shown in Fig. 5.2a for $\varphi = -0.5\pi$, $S(\omega_H)$ of the 5σ diagonal path is much higher than that of the 4σ diagonal path, especially in the range of $\omega_H \leq 9\omega$. In the following, we omit "diagonal". The cutoff energy [93] of HHG is $\approx 21\,\hbar\omega$ for 5σ. The 5σ path in this range originates from the continuum component born in the 5σ orbital around $t = t_1$, of which the HHG is generated around $t = t_2 \approx 3$ fs. The continuum component from 5σ born at the third peak of $\varepsilon(t)$ (< 0 at $t \approx t_2$) is relatively small because of the anisotropic ionization of CO. Shown in Fig. 5.2b are the HHG spectra for $\varphi = 0.5\pi$. In this case, the HHG of the 5σ path, which stems from the electron released at $t \approx t_2$ ($\varepsilon(t_2) > 0$), is suppressed in comparison with the 5σ HHG for $\varphi = -0.5\pi$. This is because the fourth peak of $|\varepsilon(t)|$ is weaker than the third peak at $t \approx t_2$, whereas $\varepsilon(t_1) \approx |\varepsilon(t_2)|$ for $\varphi = -0.5\pi$. In either case of $\varphi = \pm 0.5\pi$, the HHG of the 5σ path is generated by an electron freed from the 5σ orbital when $\varepsilon(t) > 0$.

For the 4σ path, the opposite trend is observed as shown in Fig. 5.2. For this path, the 5th order peak for $\varphi = -0.5\pi$ results from ionization at $t \approx t_2$ and the 8th order peak for $\varphi = 0.5\pi$ results from ionization at $t \approx t_1$. Both peaks arise from the continuum component generated in the 4σ orbital when $\varepsilon(t) < 0$. For $\varphi = 0.5\pi$, prominent in the HHG of the 4σ path is the 8th order peak, which is much higher than the 8th order peak of the 5σ path. In addition to the 4σ and 5σ paths, the 1π path also exists; its HHG intensity is comparable to those of the 4σ and 5σ paths, though the 1π path is not the highest among all paths [62]. The HHG intensities of

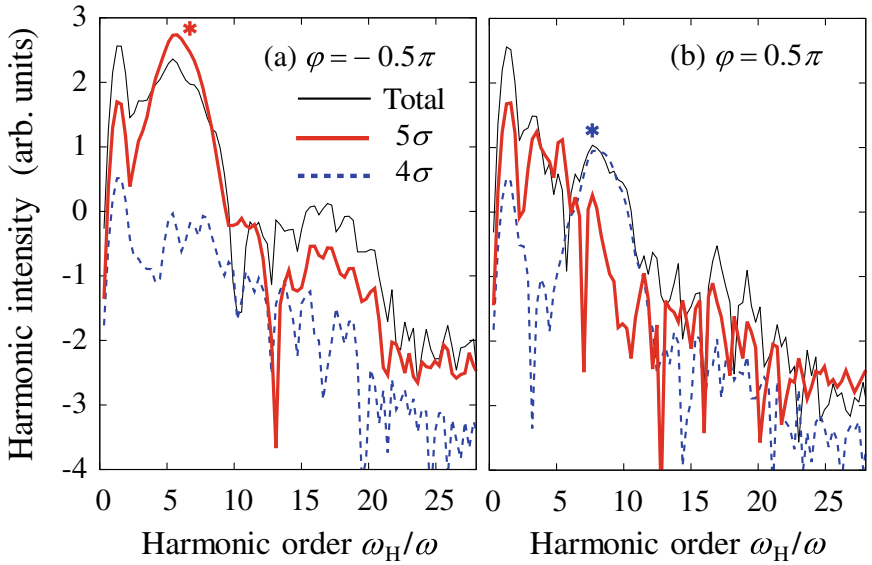

Fig. 5.2 High-harmonic spectra of the 4σ (blue broken lines) and 5σ (red solid lines) diagonal paths of CO for the pulses (5.18) with different CEPs: **a** $\varphi = -0.5\pi$ and **b** $\varphi = 0.5\pi$. The thin solid line denotes the total intensity $S(\omega_H)$ of HHG. The applied pulse for (**a**) $\varphi = -0.5\pi$ is shown in Fig. 5.1a. The highest peaks of the 4σ and 5σ paths in the two CEP cases are denoted by an asterisk "*". Adapted from Fig. 3 in [64] with permission from the publisher

off-diagonal paths such as $4\sigma_{t=0} \leftarrow 5\sigma_t \leftarrow 4\sigma_{t=0}$ are not drawn in Fig. 5.2, which are much weaker than the intensities of the dominant diagonal paths such as the 4σ and 5σ paths.

5.3.3 *Effective Potentials for Natural Orbitals of CO*

In this subsection, the mechanism of anisotropic near-IR induced ionization and multielectron (correlated) dynamics of CO are investigated by the use of the TD effective potentials of natural orbitals defined by (5.16). One can reveal the intrinsic multielectron nature in ionization dynamics by tracing the temporal change in the effective potential of each natural orbital. Plotted in Fig. 5.3 are 1-dimenisional cuts of 5σ effective potentials $v_{5\sigma}^{\rm eff}(t) = v_1(t) + v_{2,5\sigma}(t)$ at $t = t_1$ for the pulse (5.18) with $\varphi = \mp 0.5\pi$. In this figure, the effective potential is shown as a function of z while ρ is fixed at $0.755a_0$. Around this value of ρ, the electron density integrated over z takes a maximum. Figure 5.3a and b display the effective potentials for $\varphi = -0.5\pi$ obtained by TDHF and TD-CASSCF, respectively; Fig. 5.3c display those for $\varphi = 0.5\pi$ obtained by TD-CASSCF.

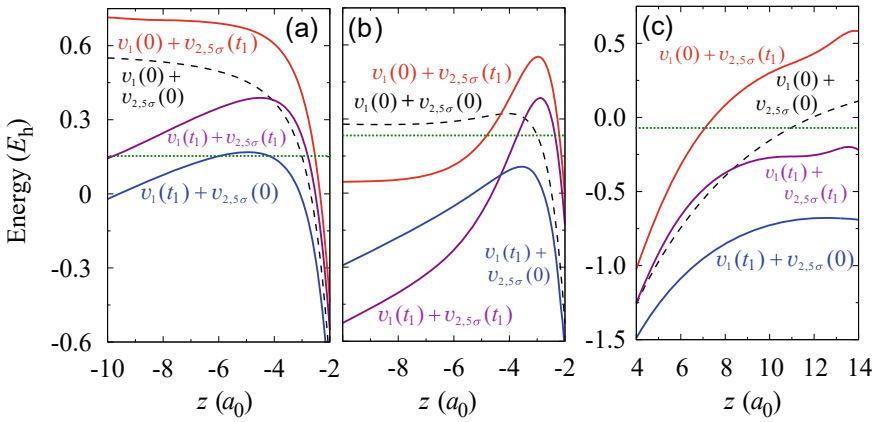

Fig. 5.3 1D cuts of 5σ effective potentials $v_{5\sigma}^{\rm eff}(t) = v_1(t) + v_{2,5\sigma}(t)$ at $t = t_1 \approx 2$ fs for the pulses (5.18) with $\varphi = \mp 0.5\pi$: **a** TDHF result for $\varphi = -0.5\pi$, **b** TD-CASSCF ($M = 400$) for $\varphi = -0.5\pi$ and **c** TD-CASSCF for $\varphi = 0.5\pi$. Four kinds of potential, of which the definitions are designated in panels, are plotted and each potential is drawn parallel to the z-axis at the fixed value of $\rho = 0.755a_0$. $v_1(t)$ is the one-body part in $v_{5\sigma}^{\rm eff}(t)$ and $v_{2,5\sigma}(t)$ is the two-body part. The green horizontal dotted line denotes the effective orbital energy $\varepsilon_{5\sigma}(t)$. Adapted from Fig. 4 in [64] with permission from the publisher

For $\varphi = -0.5\pi$, $\varepsilon(t)$ at $t \approx t_1$ points from C to O. The change in the one-body part $v_1(t)$ is governed by the dipole interaction, i.e., $v_1(t) = v_1(0) + z\varepsilon(t)$; thus, $v_1(t) + v_{2,5\sigma}(0)$ linearly slants, as shown in Fig. 5.3a and b. The change in the two-body part $v_{2,5\sigma}(t)$ differs between the two methods TDHF ($M = 1$) and TD-CASSCF. The effective potential $v_1(0) + v_{2,5\sigma}(t_1)$ for TD-CASSCF exhibits a hump structure around $z = -3a_0$, while $v_1(0) + v_{2,5\sigma}(t_1)$ for TDHF monotonically rises as $z \to -\infty$. As a result, the total one $v_{5\sigma}^{\rm eff}(t_1) = v_1(t_1) + v_{2,5\sigma}(t_1)$ shown in Fig. 5.3b has a thin hump barrier amenable to tunneling on the top of the field-induced distorted barrier of $v_1(t_1) + v_{2,5\sigma}(0)$.

The tunnel barrier is formed far away from the nuclei when the phase of $\varepsilon(t)$ is reversed at $t \approx t_2$, which explains suppressed tunnel ionization when $\varepsilon(t) < 0$ [62]. This feature is clearly demonstrated by effective potentials for $\varphi = 0.5\pi$ shown in Fig. 5.3c. In the case of $\varepsilon(t_1) < 0$, the field pushes electrons toward the direction from C to O. The two-body part $v_1(0) + v_{2,5\sigma}(t_1)$ monotonically increases up to the point of $z \approx 14a_0$. Consequently, the tunnel barrier of $v_{5\sigma}^{\rm eff}(t_1)$ appears at $z \approx 14\ a_0$. It should be noted in Fig. 5.3c that $v_{5\sigma}^{\rm eff}(t_1) > v_{5\sigma}^{\rm eff}(0)$ up to $z \approx 8a_0$, albeit the presence of the applied electric field of $\varepsilon(t_1) < 0$.

The above features of $v_{5\sigma}^{\rm eff}(t)$ well explain the directional anisotropy of tunnel ionization of CO. Since hump formation cannot be described by the mean field approximation in TDHF, as shown in Fig. 5.3a,we conclude that the origin of the hump is correlated electron motion. The ionization probability obtained by TDHF is less than 1/20 of the TD-CASSCF value [62], as expected from the comparison between Fig. 5.3a and b.

Figure 5.4a and b depict the TD-CASSCF effective potentials of $v_{5\sigma}^{\mathrm{eff}}(t_1)$ and $v_{4\sigma}^{\mathrm{eff}}(t_1)$ for $\varphi = -0.5\pi$ as functions of z and ρ. As indicated in Fig. 5.4a, the hump barrier around $z = -3\ a_0$ of $v_{5\sigma}^{\mathrm{eff}}(t)$ lowers with increasing ρ. The difference in total electron density between t=t_1 and t=0, shown in Fig. 5.4c, is locally peaked near the point $(z, \rho) = (-3a_0, 0)$, because electrons mostly move and swarm along the C–O axis when the polarization direction is parallel to it. This peak area in the electron density is regarded as an exit zone of ionization (an ionization exit with a crowd of electrons). The effective potential $v_1(0) + v_{2,\,5\sigma}(t_1)$ or $v_{5\sigma}^{\mathrm{eff}}(t_1)$ has thus a hump at the same ionization exit, ascribed to electron–electron repulsion or interactions between orbitals. The ridge of the hump in $v_{5\sigma}^{\mathrm{eff}}(t_1)$ is drawn by a broken line in Fig. 5.4a. The ridge elevates as $\varepsilon(t) > 0$ increases and incises the lobe of $\phi_{5\sigma}(t)$ (see Fig. 5.1b), which accelerates the ionization from $\phi_{5\sigma}(t)$ in the area outside the ridge ($z < -3a_0$).

As shown in Fig. 5.4b, $v_{4\sigma}^{\mathrm{eff}}(t)$ has a high barrier generated from the change in $v_{2,\,4\sigma}(t)$, which is ascribed to the electron–electron interaction with a 5σ electron on route to ionization. The high barrier formed at a radius of ~$7a_0$ ($z < 0$) from the nuclei drastically suppresses the ionization of a 4σ electron that contributes to HHG (see Fig. 5.2a). On the other hand, for $\varphi = 0.5\pi$, $\varepsilon(t_1) < 0$; then, $v_{4\sigma}^{\mathrm{eff}}(t_1)$ is nearly flat in the range of $2\ a_0 < z < 8\ a_0$. A barrier formed is far away ($z > 10\ a_0$) from the nuclei [62]. As a result, the electron released has wider space for quiver motion or

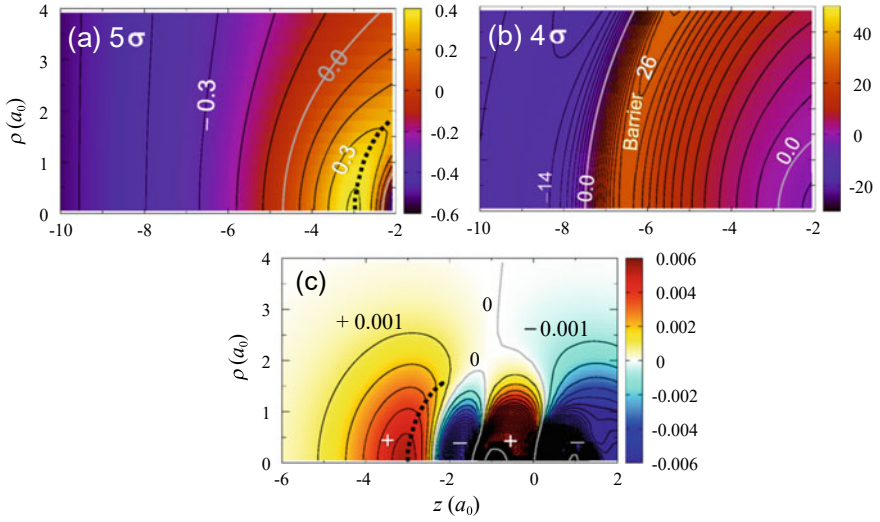

Fig. 5.4 2D plots of **a** $v_{5\sigma}^{\mathrm{eff}}(t)$ and **b** $v_{4\sigma}^{\mathrm{eff}}(t)$ effective potentials at $t = t_1 \approx 2$ fs for the pulse (5.18) with $\varphi = -0.5\pi$; **c** Contour map of the difference in total electron density between $t = t_1$ and $t = 0$. The contours lines are drawn at height intervals of $0.1E_{\mathrm{h}}$ in (**a**) and $2E_{\mathrm{h}}$ in (**b**). The dotted line in (**a**) indicates the ridgeline of the hump in $v_{5\sigma}^{\mathrm{eff}}(t)$. The contour lines in (**c**) are drawn at intervals of $0.001\ a_0^{-3}$. The region where the electron density increases is designated by the plus symbol "+", while the decrease is designated by " −". The hump ridge in (**a**) is superimposed on the contour plot (**c**) as a dotted line. Adapted from Figs. 6 and 7 in [64] with permission from the publisher

rescattering. This is the reason why the HHG of the 4σ path is enhanced for φ=0.5π, especially with respect to the 8th harmonic, as shown in Fig. 5.2b.

The one-body part $v_1(t)$ is simply equal to $v_1(0) + z\varepsilon(t)$. The crucial point of the effective potential $v^{\text{eff}}(t)$ resides in how field-induced electron–electron interaction affects the two-body part $v_2(t)$. As shown in Fig. 5.3b, $v_1(0)+v_{2,5\sigma}(t_1)$ exhibits a distinct feature, i.e., a hump near $z = -3a_0$, which is missing in the effective potential $v_1(0)+v_{2,5\sigma}(0)$ in the absence of the applied field. The hump height from the asymptotic value of $v_1(0)+v_{2,5\sigma}(t_1)$ at $z = -\infty$ to the barrier top, denoted by $\Delta v_{2,5\sigma}(t_1)$, is ~$0.50E_h$. The induced dipole moment $d_{5\sigma}(t_1)$ is $0.23ea_0$, as read in Fig. 5.1a. In the first optical cycle, the response to $\varepsilon(t)$ is nearly adiabatic. We confirmed that in the time domain around $t = t_1$, $\Delta v_{2,5\sigma}(t)$ increases with increasing $d_{5\sigma}(t)$. The decay profile of the hump as a function of z (<0) is however not reproduced by simply introducing the interaction associated with field-induced polarization, $V_{\text{int}} = d_{5\sigma}(t)/(z_0 - z)^2$ [23], where z_0 is the position of the point dipole. Global quantities such as induced dipole moments are insufficient to quantify the origin of the hump. The local structure of the electron distribution should be considered in detail, as discussed in the following paragraph.

The change in field-induced electron–electron interaction dominates the induced dipole moment, which is quantified by the change in total electron density $P(z, \rho; t)$. The difference $P(z, \rho; t) - P(z, \rho; 0)$ in TD-CASSCF total electron density is depicted in Fig. 5.4c as a contour map. The major change in electron density is a complicate vertical quadrupole form. The increase in electron density around $(z, \rho) = (-3a_0, 0)$ is found to be in the region of the hump formation in Fig. 5.4a. To conclude, the hump formation in $v_1(0)+v_{2,5\sigma}(t_1)$ is due to the penetration of an electron into the potential barrier caused by a field-induced local buildup in electron density. This newly emerging barrier, i.e., hump, plays a role as the tunnel ionization exit in the presence of electron correlation. For TDHF, the area where the electron density ascends is broad and obscure in comparison with the TD-CASSCF case, which is consistent with the fact that no hump structure emerges in Fig. 5.3a.

5.3.4 *A Hump Structure in the HOMO Effective Potential of LiH*

We present in this subsection the results of simulation for LiH interacting with an intense near-IR pulse in order to demonstrate that the emergence of hump structures is universal. We used three spatial orbitals for the expansion of the MCTDHF wavefunction $\Psi(t)$ as active orbitals: 1σ, 2σ HOMO and 3σ. The Li and H nuclei are placed at $z = -1.5a_0$ and $1.5a_0$ ($\approx$ the equilibrium internuclear distance $3.02a_0$), respectively. See the inset of Fig. 5.5.

The applied laser field $\varepsilon(t)$ is set to be parallel to the molecular axis. Here, we employed the same two-cycle shape of $\varepsilon(t)$ as in (5.18). The CEP was chosen as $\varphi = -0.5\pi$ but ω and f_0 are different from those in (5.18): $\omega = 0.03E_h/\hbar$ ($\lambda =$

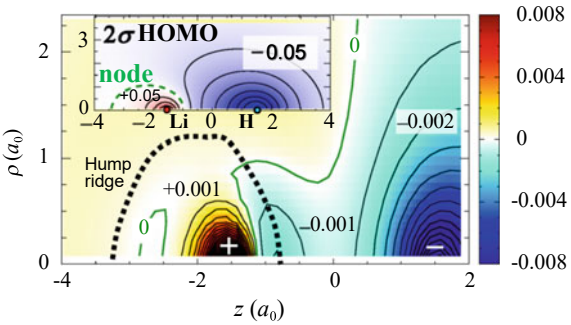

Fig. 5.5 Difference in total electron density between the two time points $t = 4.05$ fs and $t = 0$ for LiH interacting with the two-cycle pulse of $\lambda = 1520$ nm ($\varepsilon(t) > 0$ at $t = 4.05$ fs). The contour lines are drawn at intervals of $0.001a_0^{-3}$. The hump ridgeline in the effective potential $v_{2\sigma}^{\text{eff}}(t)$ of the 2σ HOMO is superimposed on the density difference as a dotted line. The inset is a contour map of the 2σ natural orbital $|\phi_{2\sigma}(t = 0)|$ (at intervals of $0.05a_0^{-3/2}$). The node of the 2σ orbital is drawn by a broken line in the inset. Adopted from Fig. 12 in [64] with permission from the publisher

1520 nm) and $f_0 = 0.02E_h/(ea_0) = 1.03 \times 10^{10}$ Vm^{-1} (light intensity $I_0 = 1.40 \times 10^{13}$ Wcm^{-2}). The pulse length is thus doubled as $2(2\pi/\omega) = 10.12$ fs.

When $\varepsilon(t)$ reaches the positive peak in the second half cycle ($t = 4.05$ fs), $\varepsilon(t) = 0.0172\ E_h/(ea_0) = 8.84 \times 10^9$ Vm^{-1}; the electron then receives a force toward the negative z direction. At $t \approx 4$ fs, a hump structure appears in $v_1(0) + v_{2,2\sigma}(t)$, which has a negative hole in the centre of $(z, \rho) \approx (-1.5a_0, 0)$. The external ridge of this caldera-like hump structure is indicated by a semicircle dotted line in Fig. 5.5, where the difference in total electron density between the two time points $t = 4.05$ fs and $t = 0$ is drawn by a contour plot. The hump ride agrees with the node of the 2σ orbital at $t = 0$ illustrated in the inset of Fig. 5.5.

The hump in the HOMO effective potential of LiH also plays a decisive role in the ionization process, as explained below. The inset of Fig. 5.5 shows that the electron density of the 2σ orbital in the absence of the applied field (at $t = 0$) is larger in the H atom side than in the Li atom side. The electron cloud around Li spreads only in a limited area of $-2.5a_0 < z < -1a_0$. When a field is applied and $\varepsilon(t) > 0$, the electron cloud is subject to a force in the negative z direction. This motion toward the negative z direction is however blocked by the external ridge which encircles the buildup in total electron density around the point $(z, \rho) = (-1.5a_0, 0)$, as shown in Fig. 5.5. The ridge does not emerge in the case of TDHF, reinforcing our conclusion that this ridge structure is due to electron correlation.

Electron density is thrusted into the Li atom region when $\varepsilon(t) > 0$, of which component is mostly retained near Li during the next half optical cycle; i.e., the electronic response to the applied field is no longer adiabatic, i.e., nonadiabatic [61] (the energy of the first excited state is as low as ~3.3 eV [95]). When $\varepsilon(t)$ reaches a negative peak at $t \approx 6$ fs, part of this component is liberated from the H side toward the positive z direction. This type of two-step nonadiabatic ionization has been found in the intense field ionization of H_2^+, which is widely known as charge-resonance

enhanced ionization [11, 96, 97]. In this two-step mechanism, ionization proceeds from the ascending well (the Li potential well when $\varepsilon(t) < 0$) of which the energy level is higher than the other descending well (the H potential well) because of the dipole interaction energy $z\varepsilon(t)$. This type of ionization mechanism may be called "asymmetric charge-resonance enhanced ionization". The ionization probability for $\varphi = 0.5\pi$ is reduced to ~1/3 in comparison with the $\varphi = -0.5\pi$ case.

5.4 Conclusions

We analyzed the multielectron dynamics of CO and LiH molecules in near-IR fields on the basis of the TD effective potential approach proposed in [62–64]. Within the framework of the MCTDHF method, the effective potentials $\{ v_j^{\text{eff}}(t)\}$ are defined as one-electron potentials that determine the temporal evolution of natural orbitals $\{\phi_j(t)\}$:$v_j^{\text{eff}}(t) = v_1(t) + v_{2,j}(t)$, where $v_1(t)$ is the one-body interaction including that with the applied laser field $\varepsilon(t)$ and $v_{2,j}(t)$ represents an effective two-body electron–electron interaction for a single electron.

The TD multiconfiguration expansion wave functions $\Psi(t)$ for CO in intense near-IR fields were calculated by the TD-CASSCF method and the TD effective potentials as a function of a single-electron spatial coordinate $\boldsymbol{r}$ were then obtained from the natural orbitals and corresponding CI expansion coefficients of $\Psi(t)$. The mechanism of the anisotropic ionization of CO in an intense two-cycle pulse of $\lambda = 760$ nm was investigated by monitoring the temporal change in $v_{5\sigma}^{\text{eff}}(t)$ for the 5σ HOMO. Two-body interaction can dramatically change the shape of the tunnel barrier in the 5σ effective potential, whereas the one-body potential $v_1(t)$ is simply slanted by the electric dipole interaction. When the electric field points from C to O ($\varepsilon(t) > 0$), a hump, which is due to field-induced electron–electron interaction, appears distinctly in $v_1(0) + v_{2,5\sigma}(t)$. A hump emerges in $v_{5\sigma}^{\text{eff}}(t)$ near the nucleus C, ~2 a_0 away outside from C along the coordinate z parallel to the molecular axis, where the total electron density is locally increased by the applied field. The formation of the hump, which does not appear in the results obtained in the TDHF calculations, is attributed to the electron correlation in dynamics. In conclusion, the hump formation in $v_1(0)+v_{2,5\sigma}(t_1)$ reflects the event that an electron penetrates through the potential barrier due a field-induced local rise of electron density. The height of the hump in $v_1(0)+v_{2,5\sigma}(t)$ is nearly proportional to the induced dipole moment $\phi_{5\sigma}(t)$. We have confirmed that this feature holds irrespective of whether the response is adiabatic or nonadiabatic (e.g., this is the case for $\lambda = 380$ nm nonadiabatic excitation [62]).

As the field strength increases ($\varepsilon(t) > 0$), the hump formed ascends in the region ($z < 0$) where the lobe of $\phi_{5\sigma}(t)$ spreads out extensively around the nucleus C. Electron density is then transferred from the interior to the exterior region outside the hump ridge (which is the border between the interior and exterior regions), and ionization proceeds together with a component already residing in the exterior region. When the sign of $\varepsilon(t)$ is reversed, ionization is relatively suppressed, because the tunnel

barrier is then located far away (~14a_0) from the O atom. This is the mechanism we proposed for the anisotropic ionization of CO.

The difference in ionization probability among few-cycle pulses with different CEPs can induce orientation-selective molecular ionization in an aligned molecular ensemble such as a mixed ensemble of C-O and O-C orientations. Orientation-selective molecular ionization can be experimentally observed even for a randomly oriented (unaligned) molecular ensemble as discussed in [62]. Experimental conditions similar to the present simulation could be realized by generating asymmetric fields with $\omega + 2\omega$ [66–68] or $\omega + 2\omega + 3\omega$ [98] phase-controlled laser pulses.

We have also investigated the ionization of LiH by an intense pulse of $\lambda = 1520$ nm. The effective potential for the 2σ HOMO obtained by the MCTDHF method exhibits a unique caldera-like hump structure. This hump hinders the ionizing current from the Li atom side when the electric field points from Li to H and the component retained near Li is liberated a half cycle later from the H atom side. This ionization mechanism may be called "asymmetric charge-resonance enhanced ionization". In contrast, the ionization of CO is direct; part of the HOMO electron density already resides in the negative z side of the hump ridge before ionization, as demonstrated in Fig. 5.1b.

Correlation between ionization and HHG can be well understood by tracing the temporal change in effective potentials. We revealed for CO that the suppression of 5σ ionization is associated with the enhancement of 4σ HHG, which can be experimentally confirmed by combining orientation experiments of CO with two-cycle near-IR pulses of different CEPs [69]. If both the orientation-dependent ionization and HHG induced by phase-controlled $\omega + 2\omega$ pulses are simultaneously detected, measuring the phase-dependent behaviour would clarify the correlation between orientation-dependent molecular ionization and enhancement/suppression of the orbital-specific HHG. It is challenging to extract the information of two-body parts $\{v_{2,j}(t)\}$ from experimental observables such as the phase-dependent yields and release-direction propensities of fragment ions.

Directional asymmetry was also experimentally observed in the photoelectron momentum distribution of CO [66, 99]. More than half of photoelectrons were finally detected in the same direction of O^+ for the asymmetric $\omega + 2\omega$ field with the zero relative phase difference. This "counterintuitive" feature was explained by a Coulomb-corrected tunnel ionization model in which an electron initially ejected from the C atom side is more strongly pulled back to the ion core by its Coulomb attractive force [100]. The numerical solution of the TD-Schrödinger equation for a 1D [100] or 3D [66, 99] hydrogen atom qualitatively reproduced the counterintuitive feature. It is of great interest to investigate how various hump structures in effective potentials affect the timing of tunnel ionization and eventually the photoelectron energies or momenta on the basis of the MCTDHF wavefunction in the natural spin orbital representation, though MCTDHF calculation of the photoelectron spectra in near-IR induced ionization is still computationally demanding [101].

In 1951, Slater derived an averaged potential field, regarded as a single (orbital-independent) effective potential for electrons, from the Hartree–Fock equation [102] by approximately treating the non-local exchange potential as a local potential. This

intuitive treatment by Slater, which became germination of modern density functional theory developed by Hohenberg, Sham, and Kohn [103, 104], has been soon mathematically rationalized by Sharp and Horton [105] as an optimized effective potential method. Slater has also provided an effective potential for an electronic ground state wave function in the form of a multiconfiguration expansion [106]. The present approach introduced in this review is considered in line with a time-dependent extension of Slater's idea. Recently, Kato and Yamanouchi have derived a time-dependent effective potential for electrons, which is formulated as a target to be optimized in the framework of multiconfiguration expansion [107]. Further development of various effective potential approaches is indispensable to grasp the physics behind multielectron correlation dynamics and to exploit practical single-electron theories for multielectron dynamics.

Acknowledgements This work was supported in part by JSPS KAKENHI Grant Number JP16H04091.

References

1. W. Kaiser, C.G.B. Garrett, Phys. Rev. Lett. **7**, 229 (1961)
2. J.L. Hall, E.J. Robinson, L.M. Branscomb, Phys. Rev. Lett. **14**, 1013 (1965)
3. *Advances in Multi-photon Processes and Spectroscopy*, vol.1, ed. by S.H. Lin (World Scientific, Singapole, 1984)
4. M.S. Schuurman, A. Stolow, Annu. Rev. Phys. Chem. **69**, 427 (2018)
5. S. Karashima, Y. Yamamoto, T. Suzuki, J. Phys. Chem. Lett. **10**, 4499 (2019)
6. P. Agostini et al., Phys. Rev. Lett. **42**, 1127 (1979)
7. C.J. Joachain, N.J. Kylstra, R.M. Potvliege, *Atoms in Intense Laser Fields* (Cambridge University Press, Cambridge, 2012)
8. M. Nisoli et al., Chem. Rev. **117**, 10760 (2017)
9. A. Schiffrin et al., Nature **493**, 70 (2013)
10. P. Vasa, D. Mathur, *Ultrafast Biophotonics* (Springer, Switzerland, 2016)
11. I. Kawata, H. Kono, Y. Fujimura, J. Chem. Phys. **110**, 11152 (1999)
12. L.V. Keldysh, Zh. Eksp. Teor. Fiz. **47**, 1945 (1964). (Sov. Phys. JETP **20**, 1307 (1964))
13. D.M. Wolkov, Z. Phys. **94**, 350 (1935)
14. A.M. Perelemov, V.S. Popov, M.V. Terent'ev, Zh. Eksp. Teor. Fiz. **50**, 1393 (1966). (Sov. Phys. JETP **23**, 924 (1966))
15. F.H.M. Faisal, J. Phys. B **6**, L89 (1973)
16. H.R. Reiss, Phys. Rev. A **22**, 1786 (1980)
17. M.V. Ammosov, N.B. Delone, V.P. Krainov, Sov. Phys. JETP **64**, 1191 (1986)
18. X.M. Tong, Z. Zhao, C.D. Lin, Phys. Rev. A **66**, 033402 (2002)
19. O.I. Tolstikhin, T. Morishita, Phys. Rev. A **86**, 043417 (2012)
20. X.M. Tong, C.D. Lin, J. Phys. B **38**, 2593 (2005)
21. M. Abu-samha, L.B. Madsen, Phys. Rev. A **81**, 033416 (2010)
22. M. Awasthi, A. Saenz, Phys. Rev. A **81**, 063406 (2010)
23. Z. Zhao, T. Brabec, J. Mod. Opt. **54**, 981 (2007)
24. V.-H. Hoang et al., Phys. Rev. A **95**, 023407 (2017)
25. H.-P. Kang et al., J. Phys. B At. Mol. Opt. Phys. **51**, 105601 (2018)
26. B. Zhang, J. Yuan, Z. Zhao, Phys. Rev. Lett. **111**, 163001 (2013)
27. M. Abu-samha, L.B. Madsen, Phys. Rev. A **101**, 013433 (2020)

28. K. Harumiya, I. Kawata, H. Kono, Y. Fujimura, J. Chem. Phys. **113**, 8953 (2000)
29. K. Harumiya et al., Phys. Rev. A **66**, 043403 (2002)
30. O. Smirnova et al., Nature (London) **460**, 972 (2009)
31. F. Krausz, M. Ivanov, Rev. Mod. Phys. **81**, 163 (2009)
32. M. Kling, M. Vrakking, Annu. Rev. Phys. Chem. **59**, 463 (2008)
33. M.J.J. Vrakking, F. Lepine, *Attosecond Molecular Dynamics*. (Royal Society of Chemistry, London, 2018)
34. A. Becker, F.H.M. Faisal, J. Phys. B At. Mol. Opt. Phys. **38**, R1 (2005)
35. M.A.L. Marques, C. Ullrich, F. Nogueira, A. Rubio, K. Burke, E.K.U. Gross (eds.), *Time-Dependent Density Functional Theory* (Springer, Berlin, 2006)
36. K. Yabana et al., Phys.Rev. B**85**, 045134 (2012)
37. J. Zanghellini et al., Laser Phys. **13**, 1064 (2003)
38. T. Kato, H. Kono, Chem. Phys. Lett. **392**, 533 (2004)
39. T. Kato, H. Kono, J. Chem. Phys. **128**, 184102 (2008)
40. E. Lötstedt, T. Kato, K. Yamanouchi, J. Chem. Phys. **144**, 154116 (2016)
41. M. Nest, T. Klamroth, P. Saalfrank, J. Chem. Phys. **122**, 124102 (2005)
42. T. Nguyen-Dang et al., J. Chem. Phys. **127**, 174107 (2007)
43. G. Jordan, J. Caillat, C. Ede, A. Scrinzi, J. Phys. B At. Mol. Opt. Phys. **39**, S341 (2006)
44. M. Nest, R. Padmanaban, P. Saalfrank, J. Chem. Phys. **126**, 214106 (2007)
45. S. Sukiasyan et al., Phys. Rev. Lett. **102**, 223002 (2009)
46. P. Redkin, R. Ganeev, Phys. Rev. A **81**, 063825 (2010)
47. D. Hochstuhl, S. Bauch, M. Bonitz, J. Phys. Conf. Ser. **220**, 012019 (2010)
48. P.A.M. Dirac, The principles of quantum mechanics, in *International Series of Monographs on Physics 27*, 4th edn. (Oxford Science, Oxford, 1958)
49. J. Frenkel, *Wave Mechanics* (Advanced General Theory, Claredon Press, OxFord, 1934)
50. A. Raab, Chem. Phys. Lett. **319**, 674 (2000)
51. T. Sato, K.L. Ishikawa, Phys. Rev. A **88**, 023402 (2013)
52. H. Miyagi, L.B. Madsen, Phys. Rev. A **87**, 062511 (2013)
53. H. Miyagi, L.B. Madsen, Phys. Rev. A **89**, 063416 (2014)
54. D.J. Haxton, C.W. McCurdy, Phys. Rev. A **91**, 012509 (2015)
55. T. Sato, K.L. Ishikawa, Phys. Rev. A **91**, 023417 (2015)
56. J.J. Omiste, W. Li, L.B. Madsen, Phys. Rev. A **95**, 023415 (2017)
57. T. Sato et al., J. Chem. Phys. **148**, 051101 (2018)
58. S. Kvaal, J. Chem. Phys. **136**, 194109 (2012)
59. A.U.J. Lode, C. Lévêque, L.B. Madsen, Rev. Mod. Phys. **92**, 011001 (2020)
60. T. Kato, H. Kono, Chem. Phys. **366**, 46 (2009)
61. S. Ohmura, H. Kono, T. Oyamada, T. Kato, K. Nakai, S. Koseki, J. Chem. Phys. **141**, 114105 (2014)
62. S. Ohmura, T. Kato, T. Oyamada, S. Koseki, H. Ohmura, H. Kono, J. Phys. B At. Mol. Opt. Phys. **51**, 034001 (2018)
63. T. Kato, K. Yamanouchi, H. Kono, *Attosecond Molecular Dynamics*. (Royal Society of Chemistry, London, 2018), pp. 139–181
64. S. Ohmura et al., J. Phys. B At. Mol. Opt. Phys. B**53**, 184001 (2020)
65. P. Löwdin, Phys. Rev. **97**, 1474 (1955)
66. H. Ohmura, N. Saito, T. Morishita, Phys. Rev. A **83**, 063407 (2011)
67. S. De et al., Phys. Rev. Lett. **103**, 153002 (2009)
68. H. Li et al., Phys. Rev. A **84**, 043429 (2011)
69. P.M. Kraus, D. Baykusheva, H.J. Wörner, J. Phys. B At. Mol. Opt. Phys. **47**, 124030 (2014)
70. H. Ohmura, N. Saito, M. Tachiya, Phys. Rev. Lett. **96**, 173001 (2006)
71. H. Ohmura et al., Phys. Rev. A **77**, 053405 (2008)
72. H. Ohmura, N. Saito, T. Morishita, Phys. Rev. A **89**, 013405 (2014)
73. L. Holmegaard et al., Nat. Phys. **6**, 428 (2010)
74. V.P. Majety, A. Scrinzi, J. Phys. B At. Mol. Opt. Phys. **48**, 245603 (2015)
75. R. Johansen et al., J. Phys. B At. Mol. Opt. Phys. **49**, 205601 (2016)

76. Y. Sakemi, S. Minemoto, H. Sakai, Phys. Rev. A **96**, 011401(R) (2017)
77. P. Sándor et al., Phys. Rev. A **98**, 043425 (2018)
78. L.B. Madsen, Phys. Rev. A **87**, 013406 (2013)
79. M.D. Śpiewanowski, L.B. Madsen, Phys. Rev. A**91**, 043406 (2015)
80. D. Dimitrovski, C.P.J Martiny, L.B. Madsen, Phys. Rev. A **82**, 053404 (2010)
81. M. Abu-samha, L.B. Madsen, Phys. Rev. A **82**, 043413 (2010)
82. O.I. Tolstikhin, T. Morishita, L.B. Madsen, Phys. Rev. A **84**, 053423 (2011)
83. L.B. Madsen et al., Phys. Rev. A **85**, 053404 (2012)
84. J. Wu et al., Phys. Rev. Lett. **108**, 183001 (2012)
85. P. von den Hoff, Appl. Phys. B **98**, 659 (2010)
86. H. Akagi, T. Otobe, R. Itakura, Sci. Adv. **5**, eaaw1885 (2019)
87. C.-T. Le, V.-H. Hoang, L.-P. Tran, V.-H. Le, Phys. Rev. A **97**, 043405 (2018)
88. B. Zhang, J. Yuan, Z. Zhao, Phys. Rev. A **111**, 035402 (2014)
89. K. Pernal, O. Gritsenko, E.J. Baerends, Phys. Rev. A **75**, 012506 (2007)
90. C.L. Benavides-Rivero, M.A.L. Marques, J. Chem. Phys. **151**, 044112 (2019)
91. E.S. Nielsen et al., J. Chem. Phys. **73**, 6238 (1980)
92. M. Uiberacker et al., Nature **446**, 627 (2007)
93. P.B. Corkum, Phys. Rev. Lett. **71**, 1994 (1993)
94. M. Lewenstein et al., Phys. Rev. A **49**, 2117 (1994)
95. W.C. Stwalley, W.T. Zemke, J. Phys. Rev. Data **22**, 87 (1993)
96. T. Zuo, A.D. Bandrauk, Phys. Rev. A **52**, R2511 (1995)
97. A.D. Bandrauk, H. Kono, in *Advances in Multi-Photon Processes and Spectroscopy*, vol. 15, ed. by S.H. Lin et al. (World Scientific, Singapore, 2003), pp. 147–214
98. H. Ohmura, N. Saito, Phys. Rev. A **101**, 043419 (2020)
99. H. Ohmura, in *Advances in Multi-Photon Processes and Spectroscopy*, vol. 21, ed. by S.H. Lin et al. (World Scientific, Singapore, 2003), pp. 55–102
100. S. Chelkowski, M. Zamojski, A.D. Bandrauk, Phys. Rev. A **63**, 023409 (2001)
101. Y. Orimo, T. Sato, K.L. Ishikawa, Phys. Rev. A **100**, 013419 (2019)
102. J.C. Slater, Phys. Rev. **81**, 385 (1951)
103. P. Hohenberg, W. Kohn, Phys. Rev. **136**, B864 (1964)
104. W. Kohn, L.J. Sham, Phys. Rev. **140**, A1133 (1965)
105. R.T. Sharp, G.K. Horton, Phys. Rev. **90**, 317 (1953)
106. J.C. Slater, Phys. Rev. **91**, 528 (1953)
107. T. Kato, K. Yamanouchi, Phys. Rev. A **98**, 023405 (2018)

Chapter 6
Ultrafast Magnetic Field Generation in Molecular π-Orbital Resonance by Circularly Polarized Laser Pulses

Kai-Jun Yuan, Jing Guo, and André D. Bandrauk

Abstract Optically induced magnetic fields,from the femtosecond nuclear to attosecond electron time scales are shown to be produced by intense ultrashort laser pulses due to highly nonlinear nonperturbative optical response. The light-matter interaction results in coherent electron currents, giving rise to magnetic field generation. Schemes with bichromatic high-frequency co-rotating and counter-rotating circularly polarized UV light pulses are used to produce the spatial and temporal evolution of the generated magnetic field. The one-electron molecular ion H_2^+ as a benchmark model is used to describe the ultrafast photophysics process. Under the condition of molecular resonance excitation, results obtained from ab-inito simulations show a strong dependence on the molecular alignment. In bicircular polarization processes, the interference effects between multiple resonant excitations modulate the evolution of the generated magnetic field, thus leading to pulse relative phase dependence. It is found that the modulation of generated magnetic fields is dependent on the pulse frequency and helicity combination. Molecular resonant excitation induces coherent ring electron currents, resulting in suppression of the phase dependence. Pulse helicity effects illustrate laser induced electron dynamics in bichromatic circular polarization processes. These highly nonlinear phenomena are described by attosecond ionisation and coherent electron current models. The results offer a

Kai-Jun Yuan is a deceased author.

K.-J. Yuan
Institute of Atomic and Molecular Physics, Jilin University, Changchun 130012, China

Laboratoire de Chimie Théorique, Faculté des Sciences, Université de Sherbrooke, Québec, Sherbrooke J1K 2R1, Canada

J. Guo
Institute of Atomic and Molecular Physics, Jilin University, Changchun 130012, China

A. D. Bandrauk (✉)
Computational Chemistry & Molecular Photonics, Faculté des Sciences, Université de Sherbrooke,Laboratoire de Chimie Théorique, Québec, Sherbrooke J1K 2R1, Canada
e-mail: andre.bandrauk@usherbrooke.ca

K. Yamanouchi et al. (eds.), *Progress in Ultrafast Intense Laser Science XVI*,
Topics in Applied Physics 141, https://doi.org/10.1007/978-3-030-75089-3_6

guiding principle for generating ultrafast magnetic fields and for studying coherent electron dynamics in complex molecular systems.

6.1 Introduction

Advances in synthesizing ultrashort intense pulses [1, 2] allow one to visualize and control electrons on the their natural attosecond (1 as $= 10^{-18}$ s) time scale and sub-nanometer dimension in photophysical processes [3–6]. Currently, 43 as pulses are the shortest available pulses for new ultrafast optical imaging [7]. Magnetic fields have also been adopted as a tool for investigations of new phenomena in molecular and material sciences, including molecular paramagnetic bonding [8], nonequilibrium electronic processes [9], demagnetization processes [10], coherent ultrafast magnetism [11], and optical magnetic recording [12]. These magnetization phenomena are currently studied with femtosecond circular-polarization x-ray sources due to their nanometer resolution and ultra-rapid response shorter than physical relaxation times [13–16].

Laser induced electronic ring currents have been proposed to generate strong magnetic fields in atomic and molecular systems [17–22]. By creating unidirectional constant valence-type electronic currents in molecules with circularly polarized π UV laser pulses, static magnetic fields [17–19] can be efficiently generated by means of resonant with degenerate π orbitals. These laser induced magnetic fields are much larger than those obtained by traditional static field methods [23]. It has been found that the generated magnetic field from electronic rings in atomic orbitals is strongly dependent on the quantum numbers and the nuclear charge [18]. The strategy thus allows to produce strong magnetic fields by controlling the orbital angular momentum in atoms and molecules. In these previous studies, coherent rotational electronic states are prepared resonantly, and lead to ring electronic currents and static magnetic fields. One also finds that ring electronic currents are dependent on the symmetry of the molecular orbitals, i.e., the helicity of the driving circularly polarized pulses [24], which can be used to reconstruct attosecond charge migration [25–28]. Linearly polarized laser pulses can also induce excited ring currents by controlling the rotation direction of π electrons in planar/nonplanar aromatic molecules [29–32]. Spinning continuum electrons can be generated locally on sub-nanometer molecular dimensional scales [33, 34]. As a result, time-dependent circular coherent electron wave packets (CEWPs) and currents are created in the continuum, which are the source of intense time-dependent internal magnetic fields generated on attosecond time scales. The optically induced attosecond magnetic field has been shown to be a function of the pulse intensity, wavelength, duration, and so on [35–38], thus offering new tools for control of ultrafast optical magnetism generation [39–41].

Coherent resonant excitation is an important process in photochemical reactions. We review attosecond magnetic field generation and electron currents under molecular resonant excitation in attosecond circular polarization processes. Results are performed on the aligned molecular ion H_2^+ at equilibrium by numerically solv-

ing the corresponding three-dimensional (3D) time-dependent Schrödinger equation (TDSE). A coherent superposition of the ground σ_g and excited π_u electronic states gives rise to time-dependent electronic ring currents inside molecules and oscillating magnetic field pulse generation in real time on the attosecond scale. Such ultrafast intramolecular electronic currents are controlled by the symmetry of the molecular orbitals. The orbital properties of molecules are thus the knob for controlling ultrafast magnetic field generation. In bichromatic circularly polarized laser fields, the interference effect between multiple pathway excitation-ionization processes influences the magnetic fields. These results allow to control ultrafast magnetic fields and reconstruct molecular attosecond charge migration dynamics. Since molecular vibrational and rotational effects on the femtosecond (1 fs $= 10^{-15}$ s) and picosecond (1 ps $= 10^{-12}$ s) time scales, the fixed nuclei simulations are valid to describe these ultrafast magnetic field generation processes on the attosecond time scale.

The chapter is organized as follows: We first introduce laser induced electron currents in molecular coherent $\sigma_g - \pi_u$ resonant excitation processes in Sect. 6.2. Results of ultrafast magnetic fields by intense circularly polarized attosecond XUV laser pulses are presented and discussed in Sect. 6.3. In Sect. 6.4 we show optically induced magnetic fields by bichromatic circularly polarized laser pulses. Pulse helicity and phase dependence effects are analyzed. Finally we summarize our findings in Sect. 6.5. Throughout this paper, atomic units (a.u.) which are defined by setting $\hbar = e^2 = m_e = 1$, are used unless otherwise stated.

6.2 Molecular Coherent $\sigma_g - \pi_u$ Resonant Excitation

We use the single electron molecular ion H_2^+ at equilibrium as a benchmark model, which can be fully studied [42], to present coherent excitation by an intense laser pulse at frequency ω. Two processes are compared with different molecular alignments: the molecular internuclear axis parallel and perpendicular to the laser propagation direction, as illustrated in Fig. 6.1. The circularly polarized laser pulse $\mathbf{E}(t)$ propagates along the z axis with its field polarization direction in the (x, y) plane, (6.18).

In a resonant excitation by an ultrafast ω pulse, a coherent superposition of the two electronic states with energy difference $\Delta E = E_e - E_g = \omega$, where $E_{g/e}$ is the eigenenergy of the ground/excited electronic state, is created. The wavefunction of the coherent superposition state within fixed nuclei approximation can be expressed as

$$\psi_c(\mathbf{r}, t) = c_g(t)\psi_g(\mathbf{r})e^{-iE_g t} + c_e(t)\psi_e(\mathbf{r})e^{-iE_e t}, \tag{6.1}$$

where $\psi_{g/e}(\mathbf{r})$ is the eigenfunction of the electronic state, and $c_{g/e}(t)$ is the corresponding occupation coefficient. The corresponding time dependent coherent electron density distributions are described by,

$$\begin{aligned}\mathscr{D}(\mathbf{r},t) &= |\psi_c(\mathbf{r},t)|^2 = \mathscr{D}_g(\mathbf{r},t) + \mathscr{D}_e(\mathbf{r},t) + \mathscr{D}_{(g,e)}(\mathbf{r},t) \\ &= |c_g(t)\psi_g(\mathbf{r})|^2 + |c_e(t)\psi_e(\mathbf{r})|^2 \\ &\quad + c_g(t)c_e(t)\psi_g(\mathbf{r})\psi_e(\mathbf{r})e^{-i\Delta Et} + c.c.. \end{aligned} \tag{6.2}$$

After the resonant ω_1 pulse, the coefficients $c_g(t)$ and $c_e(t)$ are constant. Then density distributions $\mathscr{D}_g(\mathbf{r},t) = |c_g(t)\psi_g(\mathbf{r})|^2$ and $\mathscr{D}_e(\mathbf{r},t) = |c_e^2(t)\psi_e(\mathbf{r})|^2$ are time independent, arising separately from the ground $\psi_g(\mathbf{r})$ and excited $\psi_e(\mathbf{r})$ electronic states. The superposition term $\mathscr{D}_{(g,e)}(\mathbf{r},t)$ oscillates with time t. The evolution of the coherent electron wavepackets with time depends on the molecular structure and orbitals [43, 44]. The period of the electron motion is $2\pi/\Delta E$ on the attosecond time scale. Therefore, exploring ultrafast charge migration dynamical processes requires demanding spatiotemporal resolutions [45, 46].

Figure 6.2 shows results of density distributions of coherent electron wave packets in (6.1) at different molecular alignments illustrated in Fig. 6.1, obtained by solving TDSEs in (6.17). Here we use the laser field in the form

$$E(t) = Ef(t)[\hat{e}_x \cos(\omega t) + \xi \hat{e}_y \sin(\omega t)]$$

where $f(t) = \sin^2(\pi t/n\tau)$ is the pulse envelope and $\tau = 2\pi/\omega$ is the laser period. A right handed ($\xi = 1$) circularly polarized 70 nm UV pulse at intensity $I = 3.5 \times 10^{14}$ W/cm^2 ($E = 0.1$ a.u.) and duration n = 5 cycles (580 as full width at half maximum, FWHM) is used to excite the molecule H_2^+. One sees that the time resolved electron density distributions are sensitive to the molecular alignments, Fig. 6.2a versus Fig. 6.2b.

For the around-axis case, i.e., $R \parallel z$, the excited-state orbital in cylindrical coordinates can be given by,

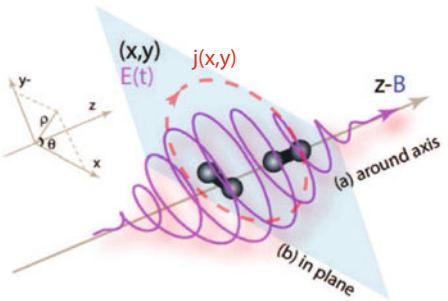

Fig. 6.1 Illustration of ultrafast magnetic field generation by circularly polarized UV laser pulses with their field vectors polarized in the ($x = \rho\cos\theta$, $y = \rho\sin\theta$) plane, propagating along the z axis. Laser induced electron currents $j(x, y)$ evolve in the laser polarization plane and the generated magnetic field B_z is along the z axis. Two cases with different molecular alignments, the molecular internuclear axis parallel and perpendicular to the laser propagation z direction i.e., **a** $R \parallel z$, around axis, and **b** $R \perp z$, in plane, are compared

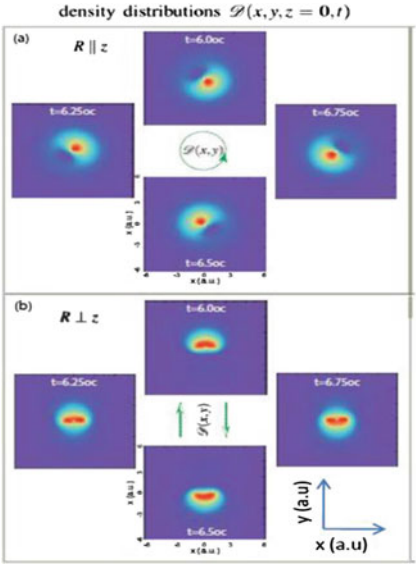

Fig. 6.2 **a**, **b** Density distributions $\mathscr{D}(x, y, z = 0, t)$ of coherent electron wave packets at different moments of the molecular ion H_2^+ at equilibrium $R_e = 2$ a.u. after the excitation by a $\lambda = 70$ nm circularly polarized pulse $\mathbf{E}(t)$ with its field vector polarized in the (x, y) plane. The pulse intensity and duration are fixed at $I = 3.5 \times 10^{14}$ W/cm^2 ($E = 0.1$ a.u.) and 5 cycles (580 as FWHM). Two cases of the molecule alignment are shown, **a** with the molecular R axis parallel to z (laser propagation direction) and **b** with the molecular R-axis perpendicular to the laser propagation direction with R along the x axis, c.f. Fig. 6.1. The circles and arrows in (**a**) indicate rotation of density whereas in (**b**) the arrows correspond to direct perpendicular electron transfer due to the perpendicular E_y field component of a circular pulse. The vertical axis in each panel is the y-axis, Arbitrary units of distributions are used

$$\psi_e = \psi_e^x + i\psi_e^y = \psi(x, y)e^{im\theta},$$

where $m = \pm 1$ is the magnetic quantum number which depends on the helicity ξ of the driving pulse. The electronic density distributions are localized around the molecular axis. The coherent superposition term of the electron density distribution gives

$$\mathscr{D}^{\parallel}_{(e,g)}(\mathbf{r}, t) \sim c_g(t)c_e(t)\psi_g(\mathbf{r})\psi_e(\mathbf{r})\cos(\Delta E t + m\theta). \tag{6.3}$$

Therefore, varying the time leads to a rotation of the electron density distribution around the axis with anticlockwise ($m = 1$) or clockwise ($m = -1$). The oscillation period is $\Delta\tau^{(0)} = 2\pi/\Delta E = 231$ as, and the maximum occurs at $\cos(\Delta E t + m\theta) = 1$, i.e., $\Delta E t + m\theta = 2n\pi$. The numerical results in Fig. 6.2a are in agreement with the predictions

For the in-plane case, i.e., $R \perp z$, a perpendicular y (to the molecular axis) resonant excitation is dominant. The corresponding electron wavefunction of the coherent excited state is then given by [47]

$$\psi_e(r) = -i[\psi_e^+(\mathbf{r}) - \psi_e^-(\mathbf{r})]/\sqrt{2} = \psi_e^y(\mathbf{r}), \tag{6.4}$$

where $\psi_e^{\pm}(r) = [\psi_e^z(r) \pm \psi_e^y(r)]/\sqrt{2}$. The corresponding time-dependent electron density distribution of the interference term reads as

$$\mathscr{D}_{(e,g)}^{\perp}(\mathbf{r}, t) \sim c_g(t)c_e^{\pm}(t)\psi_g(\mathbf{r})\tilde{\psi}_e^{\pm}(\mathbf{r})\cos(\Delta E t)\sin(\eta), \tag{6.5}$$

where $|\tilde{\psi}_e^{\pm}(\mathbf{r})|^2 = [|\psi_{\mathbf{e}}^{\mathbf{z}}(\mathbf{r})|^2 + |\psi_{\mathbf{e}}^{\mathbf{y}}(\mathbf{r})|]/\mathbf{2}$ and $\psi_e^z(\mathbf{r})$ and $\psi_e^y(\mathbf{r})$ are the degenerate real orbitals and η is the phase of the excited electronic state, dependent on the helicity ξ of the ω_1 pulse. This excitation is similar to a linear y polarization process. The coherent electron wave packets evolve along the perpendicular y direction, as displayed in Fig. 6.2b. The period of the coherent electron wave packet is also $2\pi/\Delta E = 231$ as.

6.3 Magnetic Field Generation in Resonant Excitation Processes

We consider the processes of ultrafast magnetic field generation under the $\sigma_g - \pi_u$ resonant excitation in the molecule H_2^+ at equilibrium by a right handed (ξ) circularly polarized laser pulse [48]. The molecule is aligned along the z axis, $R \parallel z$ and the x axis, $R \perp z$. Figure 6.3 shows results of induced magnetic fields at the nuclear centers $\mathbf{r} = \pm\mathbf{R}/2$ and the molecular center $\mathbf{r} = 0$ by a $\lambda = 70$ nm ($\omega = 0.65$ a.u.) circularly polarized laser pulse in (6.18). The pulse intensity $I = 3.5 \times 10^{14}$ W/cm^2 ($E = 0.1$ a.u.) and duration 5 oc (1 oc$= 2\pi/\omega$, optical cycles), corresponding to 580 as FWHM are used.

From [48] (in its Fig. 6.3) one sees that periodical oscillations of magnetic fields are generated for both alignments. For the case of $R \parallel z$, Fig. 6.3a, the same magnetic fields are produced at two nuclei, $B_z(\mathbf{r} = -\mathbf{R}/2, t) = B_z(\mathbf{r} = +\mathbf{R}/2, t)$ with the maximum value 0.61 T. The magnetic field at the molecular center $B_z(\mathbf{r} = 0, t)$ is slightly larger than those at the nuclei $\pm\mathbf{R}/2$. However, for the case of $R \perp z$, Fig. 6.3b, the generated magnetic field $B_z(\mathbf{r}, t)$ is strongly dependent on the measurement position $\mathbf{r}$. It is found that the time-dependent magnetic fields at the nuclei $\mathbf{r} = \pm\mathbf{R}/2$ oscillate periodically with opposite phases, $B_z(\mathbf{r} = -\mathbf{R}/2, t) \approx -B_z(\mathbf{r} = +\mathbf{R}/2, t)$ with maximum field strength 0.83 T. At the molecular center the induced magnetic field $B_z(\mathbf{R} = 0, t)$ is suppressed where the maximum field is 0.3 T. The dependence of induced magnetic fields on the molecular alignment indicates the different orbital combinations and evolutions of the coherent electronic wave packets.

In the $\sigma_g - \pi_u$ resonant excitation process, the induced electron currents in molecules can be described by the electronic angular continuity equation [24, 25]

$$\frac{d}{dt}\mathscr{D}(t) + \frac{\partial}{\partial\theta}j_\theta(t) = 0. \tag{6.6}$$

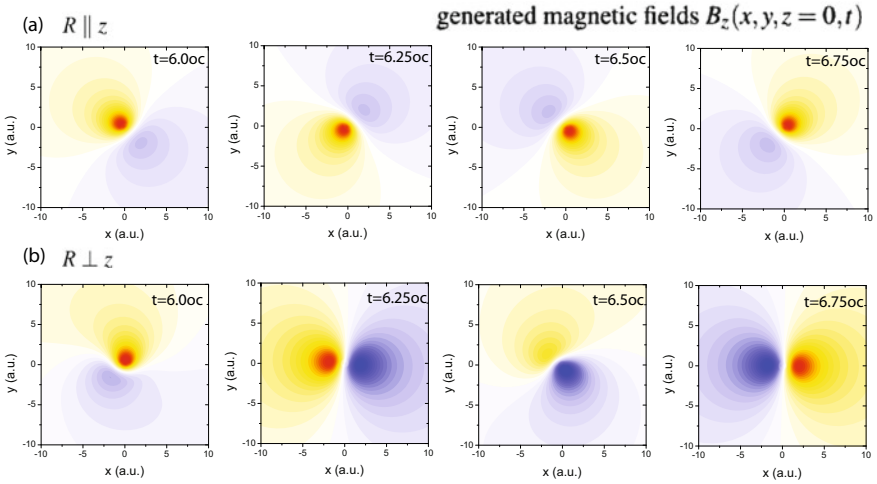

Fig. 6.3 Evolutions of generated magnetic fields $B_z(x, y, z = 0, t)$ at different moments of the molecular ion H_2^+ at equilibrium $R_e = 2$ a.u. after the $\lambda = 70$ nm and 5 oc circularly polarized pulse $\mathbf{E}(t)$ with its field vector polarized in the (x, y) plane. Two cases of the molecule aligned along the (top row, a) z and (bottom row, b) x axes, i.e., parallel and perpendicular to the laser propagation direction, $R \parallel z$ and $R \perp z$; c.f. Fig. 6.1. Arbitrary units of distributions are used

For the perpendicular polarization case of $R \parallel z$, Fig. 6.1a, the angular electron currents in (6.6) can be expressed as ($m = 1$)

$$j_\theta^{\parallel} = \mathscr{C}(\rho, z)\cos(\Delta E t - \theta), \tag{6.7}$$

where $\mathscr{C}(\rho, z) = -2|c_g(t)c_e(t)|\psi_g(\rho, z)\psi_e(\rho, z)\Delta E$. As predicted in (6.2) and (6.7), both $\mathscr{D}(t)$ and $j_\theta^{\parallel}(t)$ depend on the traiangular function of $\Delta E t$ and θ, showing the maxima of the distributions occur at $\theta \approx \pm\Delta E t$. As a result, the evolution of the electronic currents $j_\theta^{\parallel}(t)$ exhibits a periodical rotation with a period of $\Delta\tau^{(0)} = 2\pi/\Delta E = 232$ as. The induced magnetic field is therefore a function of time t, i.e, $B_z(t) \sim \cos(\Delta E t)$.

In the $R \parallel z$ case, the induced electron currents evolve with an anticlockwise direction around the molecular axis, generating unidirectional magnetic fields along the molecular axis, as displayed in Fig. 6.3a. According to molecular orbital theory, the electronic densities on the two nuclei $\pm\mathbf{R}/2$ are equivalent, i.e., $|\psi(-\mathbf{R}/2, t)|^2 = |\psi(+\mathbf{R}/2, t)|^2$. As a result, the same magnetic fields are produced, $B_z(-\mathbf{R}/2, t) = B_z(+\mathbf{R}/2, t)$. However, at the molecular center $\mathbf{r} = 0$, the electron wave function is the overlap between the two nuclear orbitals. The generated magnetic fields are simply the sum of those at the nuclei $\pm\mathbf{R}/2$, i.e., $B_z(\mathbf{r} = 0, t) \sim B_z(\mathbf{r} = -\mathbf{R}/2, t) + B_z(\mathbf{r} = \mathbf{R}/2, t)$. Their overlap enhances the magnetic fields at the molecular center.

In the case of $R \perp z$, the resonant $\sigma_g - \pi_u$ excitation corresponds to a perpendicular transition. Combining (6.5) and (6.6), one obtains the corresponding angular

electron currents with the form

$$j_{\theta}^{\perp}(t) = \mathscr{C}' \sin(\Delta E t)\cos(\theta), \tag{6.8}$$

where $\mathscr{C}' = -2|c_g(t)c_e^{\pm}(t)|\psi_g\psi_e^y\Delta E$. From (6.8) one sees that the angular electron currents evolve with time t following a function $\sin(\Delta E t)$. The oscillation period is therefore $\Delta\tau^{(0)} = 2\pi/\Delta E = 231$ as (1 as=10^{-18} s). The maximum value occurs at $\theta \approx n\pi$. As a result, the induced magnetic fields are mainly localized along the x axis The generated magnetic fields on the two nuclei $\pm\mathbf{R}/2$ vary with a period of $2\pi/\Delta E = 231$ as and show opposite phases. As shown in Fig. 6.2b, the magnetic field on the left nuclear center is positive whereas that on the right side nuclear center is negative at time $t = 6.25$ oc. Their superposition with opposite phases gives rise to suppression of generated magnetic fields at the molecular center $B_z(\mathbf{r} = 0, t)$. Due to the helicity effect of the circularly polarized laser pulse, the strengths of the generated magnetic fields on the two nuclei are not equal at the same time, $B_z(-\mathbf{R}/2, t)| \neq |B_z(+\mathbf{R}/\mathbf{2}, \mathbf{t})|$. Consequently, the time-dependent magnetic field $B_z(\mathbf{r} = 0, t)$ at the molecular center has been induced in Fig. 6.2b.

We discuss briefly now the issue of ionization which if it occurs too fast may hinder the effects we discussed so far. We note that the ionization probability is still low, at chosen intensity $I = 3.5x10^{14}$ W/cm^2 in our investigation so far. The ionization probability P_I can be estimated from [56] (in its Fig. 6.2a). in which the populations of ground and excited states are given which yield $P_I < 0.1$ for the in plane case and $P_I < 0.4$ for the molecular axis perpendicular to the polarization plane.

Note that as shown by Manz and Barth, [17–21] we expect to generate high magnetic fields by preparing high populations in states having orbital momentum l=1 states. Clearly, high laser intensities are necessary to populate efficiently excited molecular states on short time scales. Short time scale is necessary to reduce the influence of nuclear femtosecond motion, as well as, to populate efficiently excited molecular states without too much ionization. The chosen laser pulse intensity and duration realizes this goal as seen in [56] (in Fig. 6.2a, c) where the populations of the Π-states 0.5 and 0.4, respectively, are achieved.

6.4 Magnetic Field Generation by Bicircular Pulses

We next present the process in a bichromatic circularly polarized laser pulse. The bicircular field has now led to a useful application to generate high harmonics the source of attosecond pulses [49–52] and electronic vortices in photoionization [53, 54]. Vortices are time dependent quantum electronic currents and can be used to generate ultrashort attosecond magnetic field pulses inside molecules [38, 55, 56], thus offering new tools to control magneto-optics and spin-electronics in molecules and materials [57–59]. We show below the dependence of magnetic fields on the pulse helicity and relative phase at different molecular alignments.

In Fig. 6.4 we simulate the temporal evolution of the generated magnetic fields $B_z(\mathbf{r} = 0, t)$ at the molecular center of the H_2^+ molecule (Fig. 6.1) generated by 5-optical cycle pulses for various frequency combinations, single frequencies ω, and their combinations $(\omega, 2\omega)$, $(\omega, 3\omega)$ with co-rotating ($\xi = 1$) and counter-rotating ($\xi = -1$) components. The fundamental pulse wavelengths are used at $\lambda = 70$ nm ($\omega = 0.65$ a.u.), thus leading to resonant excitation between the $1s\sigma_g$ and $2p\pi_u$ electronic states and coherent electron currents in the (x, y) plane.

In Fig. 6.4a in the case of $R \parallel z$, the results of time-dependent magnetic fields by bicircular pulses at different pulse frequency combinations are similar as the single ω process. The induced magnetic field increases monotonously with time. However, in the $R \perp z$ process in Fig. 6.4b, the generated magnetic fields oscillate, which change their sign at the middle duration time (~2.5 oc) of all pulses. Minima-maxima occur again at the optical cycles. One also finds that the maximum magnetic field is $B_z = 0.65$ T in the $R \parallel z$ case whereas in the the $R \perp z$ process $B_z = 0.4$ T. The main difference at 70 nm between around-axis and in-plane magnetic fields is that around axis ($R \parallel z$), Fig. 6.4a, a single magnetic quantum number state $m = +1$ or -1 is excited resonantly whereas for in-plane excitation ($R \perp z$), Fig. 6.4b, both degenerate $m = \pm 1$ states are excited coherently. The excitation to the single electronic state induces unidirectional electron currents, thus leading to monotonous increase of magnetic fields. The maximum of the magnetic field appears at the end of the pulse. On the contrary, the degenerate excitations with $\Delta m = \pm 1$ have opposite phases. As a result, their interference gives rise to oscillations of the magnetic field generation. The maximum value is 0.4 T at $t = 3.75$.

In Fig. 6.5 we also present the spatial evolution of the generated attosecond magnetic fields during excitation processes. The density distributions of the generated

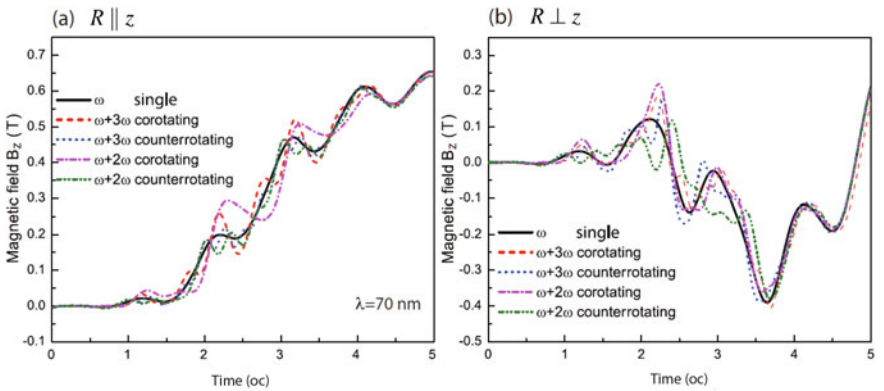

Fig. 6.4 Evolutions of generated magnetic fields $B_z(x, y, z = 0, t)$ at different moments of the molecular ion H_2^+ at equilibrium $R_e = 2$ a.u. after the $\lambda = 70$ nm and 5 oc circularly polarized pulse $\mathbf{E}(t)$ with its field vector polarized in the (x, y) plane. Two cases of the molecule aligned along the (top row, a) z and (bottom row, b) x axes, i.e., parallel and perpendicular to the laser propagation direction, $R \parallel z$ and $R \perp z$; c.f. Fig. 6.1. Arbitrary units of distributions are used

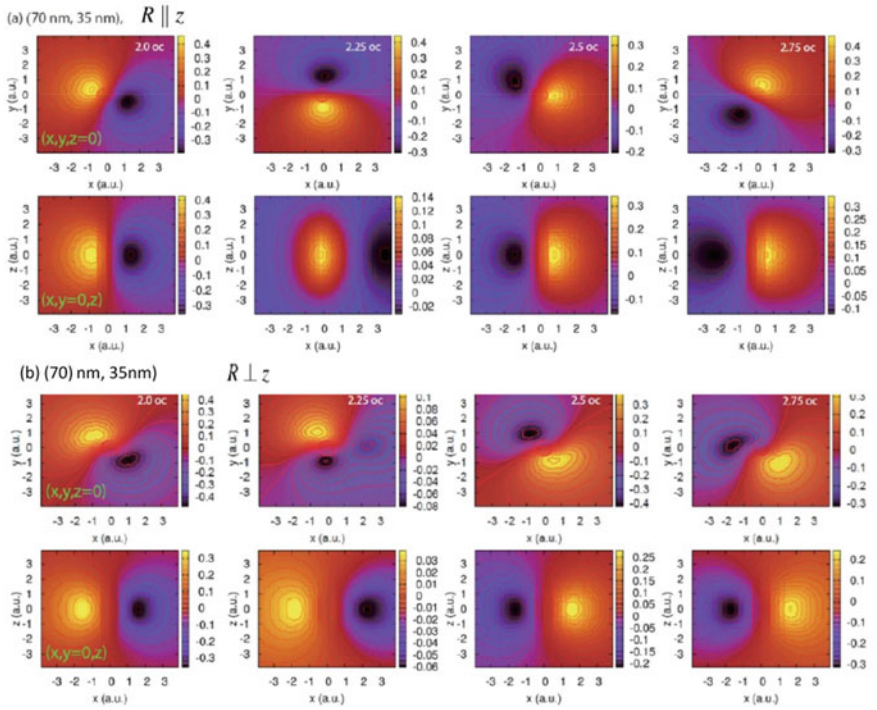

Fig. 6.5 Density plots of spatiotemporal magnetic fields $B_z(\mathbf{r}, t)$ in the $(x, y, z = 0)$ and $(x, y = 0, z)$ planes at different moments (from left to right) $t = 2.0$ oc, 2.25 oc, 2.5 oc, and 2.75 oc, where 1 optical cycle (oc) $= 2\pi/\omega$ by the bichromatic $(\omega, 2\omega)$ counter-rotating circularly polarized laser pulses with their field vectors in the molecular (x, y) plane. The molecule is aligned along the z and x axis, cf. Fig. 6.4, λ=70 nm ($\omega = 0.65au$)

magnetic field $B_z(\mathbf{r}, t)$ in the two planes, $(x, y, z = 0)$ and $(x, y = 0, z)$ planes by bichromatic counter-rotating $(\omega, 2\omega)$ circularly polarized laser pulses at different moments (from left to right panels) $t = 2.0$ oc, 2.25 oc, 2.5 oc, and 2.75 oc with a time interval of 0.25 oc for the two cases with molecular alignments (a) $R \parallel z$ and (b) $R \perp z$ are compared. The results are similar to the single ω processes in Fig. 6.3. The spatial distributions of the generated magnetic field in the $(x, y, z = 0)$ plane reflect the symmetry of the molecular orbitals of the excited states. For the process by the bicircular 70 and 35 nm pulse, the $1s\sigma_g - 2p\pi_u$ resonant excitation dominates with π_u symmetry. For the in-plane case with $R \perp z$, the excited electronic states are degenerate with $m = \pm 1$. The perpendicular excitation therefore leads to an oscillation of the generated magnetic field $B_z(x, y)$ in the up $(y > 0)$ and down $(y < 0)$ half planes, perpendicular to the molecular R/x axis, in Fig. 6.5b. For the around-axis case with $R \parallel z$, the electronic density distributions are localized around the molecular axis. As a result, the time-dependent magnetic field $B_z(\mathbf{r}, t)$ shows a rotation around the molecular R axis as illustrated in Fig. 6.5a.

The evolution of the generated magnetic field with time results from the corresponding time-dependent induced electron currents, i.e., coherent electron wave packets, for which a semiclassical model can be used to provide estimates of the radii of the circular electron currents at single frequencies ω and field amplitudes E_0 [33]. Assuming zero initial electron velocities, maximum induced electron velocities $v = 2E_0/\omega$ give circular radii

$$r_n(t) = 2E_0/\omega[1 + (n + 1/2)^2\pi^2]^{1/2}, n = 0, 1, 2, 3, \ldots \tag{6.9}$$

at times $t = (2n + 1)\pi/\omega$. At $\lambda = 70$ nm, one has $r_0 = 0.87$ a.u. and $r_1 = 2.27$ a.u.. In the case of $n = 0$ with minimum r_n, largest magnetic field can be produced due to small radii at shorter time t_n.

For the $R \perp z$ case the protons are situated at $x = \pm R/2 = \pm 1$ a.u. The magnetic fields B_z are maximum at $z = 0$, i.e., along the x-aligned R nuclear axis, but appear generally at each proton, with different phases. For the case of z axis parallel to R, the protons are situated at $z = \pm R/2 = \pm 1$ a.u. As shown in Fig. 6.5a, the magnetic field lies at positions with maximum values of $x = 0.9$ a.u. for the (70, 35 nm) process. For instance, at time 2.75 oc, one finds that the maximum magnetic field Bz appears at position (0,0.9,0) a.u. in 6.5b. The maximum displacements of the magnetic fields depend on the pulse wavelengths, reflecting the dimensions of the laser-induced electron currents, predicted from (6.9). In the circular laser field at frequency ω and field strength E_0, the first maximum laser-induced electron radius is given by the semiclassical ionization model. At 70 nm, the corresponding radius is $r_0 = 0.87$ a.u., in agreement with the numerical simulations, where the electron rotates around the molecular R axis with radius r_0 in the $(x, y, z = 0)$ plane, in Fig. 6.2a.

In the bicircular process, the generated magnetic fields are also shown to be sensitive to their relative phase. Figure 6.6 shows results of generated maximum magnetic fields B at the molecular center by intense bichromatic circularly polarized attosecond pulses with counter-rotating ($\xi = -1$) and co-rotating ($\xi = 1$) components, (6.19). Two cases of molecular excitation-ionization processes in the molecular ion H_2^+ aligned along (a,c) the x axis, $\mathbf{R} \parallel \mathbf{E}$ or $\mathbf{R} \perp z$, and (b, d) the z axis, $\mathbf{R} \perp \mathbf{E}$ or $\mathbf{R} \parallel z$, are compared by the bichromatic laser pulses with their field polarization vectors in the (x, y) plane, as illustrated in Fig. 6.1. The corresponding generated magnetic fields mainly lie along the z axis. The pulse wavelengths are respectively $\lambda_1 = 70$ nm ($\omega_1 = 0.65$ a.u.) and $\lambda_2 = 35$ nm ($\omega_2 = 1.3$ a.u.). We always fix the pulse intensities $I = 1 \times 10^{14}$ W/cm^2 ($E = 0.5338$ a.u.) and durations $T_{lp} = 48.3$ a.u.=1.16 fs, corresponding to 580 as FWHM, i.e., $5\tau_1$ for the ω_1 pulse and $10\tau_2$ for the ω_2 pulse. We also set the pulse carrier-envelope phase (CEP) $\phi_1 = 0$ and vary the CEP ϕ_2 from 0 to 2π, i.e., the relative CEP is $\phi = \phi_2 - \phi_1 = \phi_2$. Results in Fig. 6.6 show that the pulse phase ϕ dependence of the generated magnetic fields is a function of the molecular alignment and pulse helicity ξ.

For the case of $\mathbf{R} \perp z$ in Fig. 6.6a, the generated magnetic field B at the molecular center oscillates periodically as a cosine function of the pulse CEP ϕ. The maximum and minimum values of the magnetic field are $B = 0.225$ T and 0.165 T at $\phi \approx 0$ (or

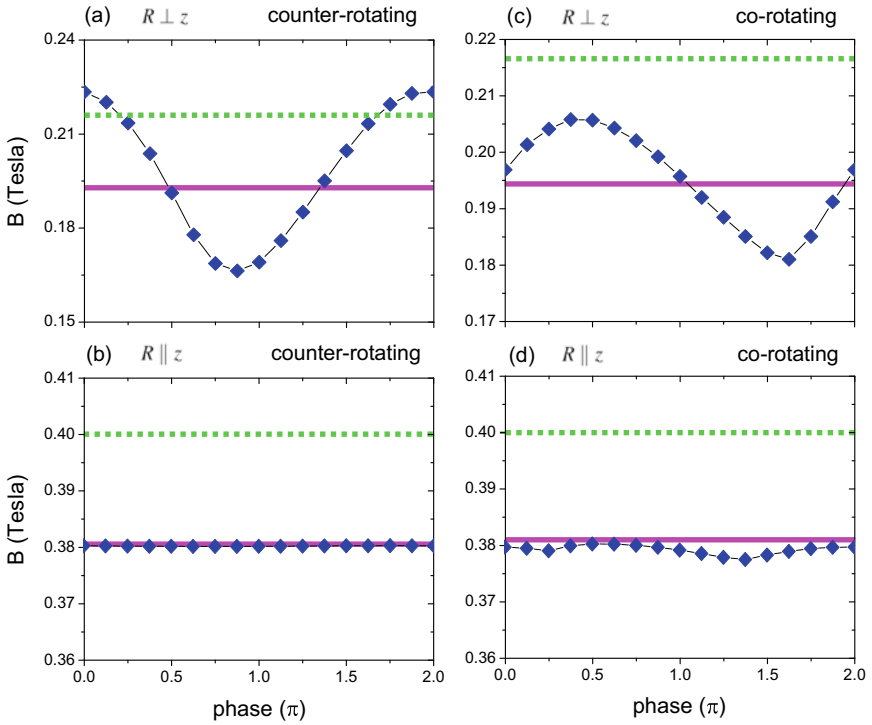

Fig. 6.6 Dependence of generated magnetic fields B (blue squares) at the molecular center on the relative pulse CEP $\phi = \phi_2 - \phi_1$ for the aligned molecule H_2^+ by bichromatic counter-rotating ($\xi = -1$) and co-rotating ($\xi = 1$) circularly polarized laser pulses with their field vectors polarized in the (x, y) plane. Two cases are compared for the molecule aligned along (**a**, **c**) the x axis and (**b**, **d**) the z axis, i.e., $\mathbf{R} \perp z$ in plane, and $\mathbf{R} \parallel z$, around axis. Pulse wavelengths $\lambda_1 = 70$ nm ($\omega_1 = 0.65$ a.u.) and $\lambda_2 = 35$ nm ($\omega_2 = 1.3$ a.u.), intensities $I = 1 \times 10^{14}$ W/cm^2 ($E = 0.5338$ a.u.), and duration $T_{lp} = 5\tau_1 = 10\tau_2$ (580 as FWHM) are fixed. Magenta solid lines denote the generated magnetic field by a single $\lambda = 70$ nm circularly polarized laser pulse, and green dashed lines present the sum values of the magnetic fields generated separately by the 70 and 35 nm circular pulses

2π) and π. For comparison, we also simulate the results of induced magnetic fields B with single-color circularly polarized attosecond pulses at separated wavelengths $\lambda = 70$ and 35 nm. The other parameters are the same as those used in Fig. 6.6a. For the two processes, the corresponding maximum strengths of induced magnetic fields at the molecular center are, respectively, $B_{\omega_1} = 0.194$ T and $B_{\omega_2} = 0.022$ T. Due to the $\sigma_g - \pi_u^+$ resonant excitation, the magnetic field induced by the 70 nm pulse is much stronger than the field generated by the 35 nm pulse, $B_{\omega_1} \approx 8.8 B_{\omega_2}$. Their sum value of the generated magnetic field $B_s = B_{\omega_1} + B_{\omega_2}$ is smaller that the maximum field $B = 0.225$ T of the bichromatic process. Comparing to the single-color circular processes, one notes that the sensitivity of the induced magnetic field B to the CEP

ϕ in Fig. 6.6a results from the interference effects between the two $\lambda_1 = 70$ nm and $\lambda_2 = 35$ nm processes, as derived in Appendix A.

With the bichromatic counter-rotating circularly polarized pulse at $\lambda_1 = 70$ nm and $\lambda_2 = 35$ nm, two processes can be triggered. The molecule is resonantly excited from the $1s\sigma_g$ state to the $2p\pi_u$ state by the $\lambda_1 = 70$ nm pulse with $\omega_1 = E_e - E_g$. Obviously, such process is insensitive to the pulse phase. Meanwhile, the absorptions of two ω_1 photons and one $\omega_2 = 2\omega_1$ photon give rise to photoelectron wave packets with the same kinetic energies E_e in the continuum. The total photoionization probability is the sum of the two ionization processes and their interference. As shown in Appendix A, the two corresponding direct transition probabilities $\mathscr{P}^{(1)}$ and $\mathscr{P}^{(2)}$ are insensitive to the pulse phases, whereas the interference term $\mathscr{P}^{(1,2)}$ depends on the phase difference $\Delta\eta$, i.e., $\mathscr{P}^{(1,2)} \sim \cos(\Delta\eta)$, where $\Delta\eta = \Delta\phi + \Delta\xi$, see see Eq (6.16) in the Appendix A. As a result, the total ionization probability $\mathscr{P} = \mathscr{P}^{(1)} + \mathscr{P}^{(2)} + \mathscr{P}^{(1,2)}$ is also a cosine function of the relative pulse phase ϕ with the form $\mathscr{P} \sim \cos(\phi)$. The interference effect between the two ionization processes modulates the total transition probability, i.e., $B \sim \cos(\phi)$, giving rise to a CEP dependence of the generated magnetic field, as illustrated in Fig. 6.6a. In Fig. 6.6b, the magnetic field is almost insensitive to the phase ϕ, with a constant value of $B = 0.38$ T. The magnetic fields generated by the bichromatic pulses are less than the sum of the two single 70 and 35 nm processes, i.e., $B < B_s = B_{\omega_1} + B_{\omega_2} = 0.4$ T, where $B_{\omega_1} = 0.382$ T and $B_{\omega_2} = 0.019$ T. The bichromatic magnetic fields mainly arise from the single 70 nm process, $B = B_{\omega_1}$, whereas the contribution from the absoprtion of single 35 nm (ω_2) or two 70 nm (ω_1) photons is weak and negligible, in Fig. 6.6b. This implies that the interference effect between the two ionization processes does not influence the bichromatic magnetic field generation.

Similar results are obtained in the co-rotating case in Fig. 6.6c, d. For the case of $\mathbf{R} \perp z$ the magnetic field B varies as a sine function of the phase ϕ due to the multiple pathway ionization interference, whereas for the case of $\mathbf{R} \parallel z$ the generated magnetic field is nearly a constant at $B = 0.38$ T where the $\sigma_g - \pi_u^+$ resonant excitation with $\Delta m = 1$ gives rise to ring electron currents in molecules and the contribution from the coherent electron wave packets $\psi_0(\mathbf{r}, t)$ in (6.1) dominates. It should be noted that in Fig. 6.6c at $\xi = +1$ the maximum magnetic field is $B = 0.206$ T at $\phi = 0.4\pi$, slightly weaker than that at $\xi = -1$ in Fig. 6.6a where $B = 0.225$ T at $\phi = 0$. The induced magnetic field is proportional to the ratio of the current (electron) velocity and radius in the continuum. As shown previously, the induced electron currents and generated magnetic fields depend on the quantum numbers. The difference between the co-rotating and counter-rotating generated magnetic fields in Fig. 6.6a, c results from the laser induced electron electron dynamics, which depends on the helicity of driving pulses [33], see also [55] where the counter vs co-rotating cases are discussed in detail. The phases in recollisions for the two cases are different and their sensitivity to CEP's shows a nearly the π phase difference.

6.5 Conclusions

We theoretically present optically induced magnetic fields from coherent electron currents in molecules. Numerical results are obtained from solutions of TDSE for the molecule H_2^+. We measure magnetic field generation under resonant excitation. Circularly polarized UV laser pulses are used to induce coherent electron currents with π orbital symmetry in molecules by resonant excitation of the $2p\pi_u$ electronic state. It is found that the generated magnetic field depends on the molecular alignments. In the around axis case, $R \parallel z$, a single quantum state is excited, giving rise to unidirectional electron currents. The magnetic field monotonously increases with time during excitation processes. However for the in-plane process, $R \perp z$, degenerate electronic states with $m = \pm 1$ are excited coherently. Their interference results in oscillations of magnetic fields. In bichromatic circularly polarized laser fields, the generated magnetic fields are also sensitive to the pulse helicity and phase. The results show a promising ability for coherent control magnetic field generation in the attosecond time scale.

Our investigations in this work have been restricted to the one electron systems, H_2^+. We believe that the main features of the magnetic field generation remain unchanged for two or more electrons systems in the regime in which one active electron approximation can be applied. Investigation of electron-electron interactions is currently under study- with focus on an important molecular effect, competition of electron delocalization versus entanglement in high intensity photophysics which has been reported recently: see [34].

Appendix A: Interference in Multi-pathway Photoionization

We here derive the multi-pathway electron interference modes in bichromatic fields based on the perturbation ionization theory [60–62]. The pulse frequencies $\omega_2 = 2\omega_1$, where $\omega_1 < I_p$ and $\omega_2 > I_p$, and I_p the molecular ionization potential, are used. The bichromatic circularly polarized laser pulses can produce photoelectron wave packets with the same kinetic energies $E_e = 2\omega_1 - I_p = \omega_2 - I_p$, which then interfere each other in the continuum.

For direct one ω_2 photon ionization processes by laser pulses, the relevant transition matrix element $\mathscr{A}^{(2)}$ can be expressed simply in the dipole form

$$\mathscr{A}^{(2)} = \langle \psi_I | \mathbf{D} \cdot \mathbf{F}_2(\omega_2) | \psi_0 \rangle = \mathscr{W}^{(2)} \mathscr{F}_2(\omega_2), \tag{6.10}$$

with the first order ionization amplitude

$$\mathscr{W}^{(2)} = \langle \psi_I | \mathbf{D} \cdot \mathbf{e} | \psi_{\mathbf{0}} \rangle, \tag{6.11}$$

where ψ_0 and ψ_I are respectively the initial ground state and the continuum state. **D** is the electric dipole operator. $\mathbf{F}_2(\omega_2) = \mathbf{e}\mathscr{F}_2(\omega_2) = E(\omega_2)e^{i\phi_2}$ is the ionizing pulse amplitude with unit vector **e** and field $E(\omega_2)$.

For the ω_1 laser pulse, at least a two $\omega_1 + \omega_1$ photon absorption is required to ionize H_2^+. The transition matrix element reads as

$$\mathscr{A}^{(1)} = \mathscr{W}^{(1)}\mathscr{F}_1^2(\omega_1) \tag{6.12}$$

with the amplitude

$$\mathscr{W}^{(1)} \sim \int dE \frac{\langle\psi_I|\mathbf{D}\cdot\mathbf{e}|\psi_\mathbf{n}\rangle\langle\psi_\mathbf{n}|\mathbf{D}\cdot\mathbf{e}|\psi_\mathbf{0}\rangle}{E_{1s\sigma_g} - E_{ni} + \omega_1 + i\Delta\epsilon}, \tag{6.13}$$

where ψ_n and E_{ni} are the wavefunction and energy of the intermediate (virtual) electronic state and $\Delta\epsilon$ is the level width, and laser fields $\mathscr{F}_1(\omega_1) = E(\omega_1)e^{i\phi_1}$. In equation (6.13) we see that the ionization amplitude $\mathscr{W}^{(1)}$ is determined by the field-free structure of the molecule and the laser pulse [63].

For a two ω_1 photon ionization with an intermediate resonant excited state, the transition matrix element $\mathscr{A}^{(1)}$ can be written as [64]

$$\mathscr{A}^{(1)} = \mathscr{A}^{iR}T_R\mathscr{A}^{Rc}, \tag{6.14}$$

where T_R is the life time of the intermediate resonant state. $\mathscr{A}^{iR}$ is the one photon transition between the initial ground state and the intermediate resonant electronic state, which is determined by the pulse area theorem. $\mathscr{A}^{Rc}$ is the photoionization of the intermediate resonant electronic state.

For photoionization by bichromatic laser pulses, that is, simultaneous two $\omega_1 + \omega_1$ photon and one $\omega_2 = 2\omega_1$ photon ionization, the total transition probability $\mathscr{P}$ is the square of the two amplitudes with an interference term of the cross products of the two one- and two-photon ionization amplitudes, that is,

$$\mathscr{P} = \mathscr{P}^{(1)} + \mathscr{P}^{(2)} + \mathscr{P}^{(1,2)}, \tag{6.15}$$

where $\mathscr{P}^{(1)} = ||A^{(1)}|^2$, $\mathscr{P}^{(2)} = \mathscr{A}^{(2)}are|^2$, and $\mathscr{P}^{(1,2)}$ is the interference term which can be simply written as

$$\begin{aligned}\mathscr{P}^{(1,2)} &= \mathscr{A}^{(1)*}\mathscr{A}^{(2)} + \mathscr{A}^{(1)}\mathscr{A}^{(2)*} \\ &= 2\mathscr{W}^{(1)}\mathscr{W}^{(2)}E^2(\omega_1)E(\omega_2)\cos(\Delta\eta),\end{aligned} \tag{6.16}$$

where $\mathscr{W}^{(1)}$ and $\mathscr{W}^{(2)}$ are the two ω_1 and one ω_2 photon transition amplitudes corresponding to (6.11) and (6.13). The phase difference $\Delta\eta = \Delta\phi + \Delta\xi$. It should be noted that the phase difference depends on the helicity of bichromatic fields. For a co-rotating case, the relative pulse phase difference $\Delta\phi = \phi_2 - 2\phi_1$ and $\Delta\xi = \xi_{\omega_2} - \xi_{\omega_1}$, where ξ_{ω_1} and ξ_{ω_2} are respectively the phases of the continuum

electron wave packets from two ω_1 and one ω_2 photoionization, whereas for a counter-rotating case, $\Delta\phi = \phi_2 + 2\phi_1$ and $\Delta\xi = \xi_{\omega_2} + \xi_{\omega_1}$. The phase difference $\Delta\xi$ is determined by the molecular intrinsic characteristic.

Appendix B: Numerical Methods

For the aligned molecule ion H_2^+ within Born-Oppenheimer approximation and static nuclear frames, the corresponding 3D TDSE in cylindrical coordinates $\mathbf{r} = (\rho, \theta, z)$ reads as,

$$i\frac{\partial}{\partial t}\psi(\mathbf{r}, t) = \left[-\frac{1}{2}\bigtriangledown_{\mathbf{r}}^2 + V_{en}(\mathbf{r}) + V_L(\mathbf{r}, t)\right]\psi(\mathbf{r}, t). \tag{6.17}$$

$\bigtriangledown_{\mathbf{r}}$ is the Laplacian operator, and V_{en} is the electron-nuclear potential. The circularly polarized laser pulse propagates along the z axis, perpendicular to the (x, y) plane with $x = \rho\cos\theta$ and $y = \rho\sin\theta$, Fig. 6.1. The radiative interaction between the laser field and the electron $V_L(\mathbf{r}) = \mathbf{r}\cdot\mathbf{E}(t)$ is described in the length gauge for a single color circularly polarized pulse,

$$\mathbf{E}(t) = Ef(t)[\hat{e}_x\cos(\omega t) + \hat{e}_y\xi\sin(\omega t)], \tag{6.18}$$

where $\hat{e}_{x/y}$ is the laser polarization direction and the symbol $\xi = \pm 1$ denotes the helicity of the field, $\xi = 1$ for right hand and $\xi = -1$ for left hand, or a bichromatic circularly polarized pulse

$$\begin{aligned}\mathbf{E}(t) &= \mathbf{E}_1(t) + \mathbf{E}_2(t)\\ &= Ef(t)\begin{cases}\hat{e}_x[\cos(\omega_1 t + \phi_1) + \cos(\omega_2 t + \phi_2)]\\ \hat{e}_y[\sin(\omega_1 t + \phi_1) + \xi\sin(\omega_2 t + \phi_2)]\end{cases},\end{aligned} \tag{6.19}$$

where ξ presents the helicity of the combined field, i.e., co-rotating ($\xi = 1$) and counter-rotating ($\xi = -1$) components. ϕ_1 and ϕ_2 are CEPs of the pulses $\mathbf{E}_1(t)$ and $\mathbf{E}_2(t)$. A smooth $\sin^2(\pi t/T_{lp})$ pulse envelope $f(t)$ for maximum amplitude E, intensity $I = I_x = I_y = c\varepsilon_0 E^2/2$ and duration $T_{lp} = n\tau_1$ is adopted, where one optical cycle period $\tau_{1,2} = 2\pi/\omega_{1,2}$, n=5 cycles. This pulse satisfies the total zero area $\int E(t)dt = 0$ in order to exclude static field effects [1].

The 3D TDSE in (6.17) is propagated by a second order split operator method which conserves unitarity in the time step Δt combined with a fifth order finite difference method and Fourier transform technique in the spatial steps $\Delta\rho$, Δz, and $\Delta\theta$ [65, 66]. The initial electron wavefunction $\psi(\mathbf{r}, t = 0)$ is prepared in the ground $1s\sigma_g$ state calculated by propagating an initial appropriate wavefunction in imaginary time using the zero-field TDSE in (6.17). The time step is taken to be $\Delta t = 0.01$ a.u.=0.24 as. The spatial discretization is $\Delta\rho = \Delta z = 0.25$ a.u. for a radial grid range $0 \le \rho \le 128$ a.u. (6.77 nm) and $|z| \le 32$ a.u. (1.69 nm), and the angle grid size $\Delta\theta = 0.025$ radian. To prevent unphysical effects due to the reflection of the

wave packet from the boundary, we multiply $\psi(\rho, \theta, z, t)$ by a "mask function" or absorber in the radial coordinates ρ with the form $\cos^{1/8}[\pi(\rho - \rho_a)/2\rho_{abs}]$. For all results reported here we set the absorber domain at $\rho_a = \rho_{max} - \rho_{abs}$=104 a.u. with $\rho_{abs} = 24$ a.u., exceeding well the field induced electron oscillation $\alpha_d = E/\omega_{1/2}^2$ of the electron [35].

The time dependent electronic current density is defined by the quantum expression in the length gauge,

$$\mathbf{j}(\mathbf{r}, t) = \frac{i}{2}[\psi(\mathbf{r}, t)\nabla_{\mathbf{r}}\psi^*(\mathbf{r}, t) - \psi^*(\mathbf{r}, t)\nabla_{\mathbf{r}}\psi(\mathbf{r}, t)], \tag{6.20}$$

$\psi(\mathbf{r}, t)$ is the exact Born-Oppenheimer (static nuclei) electron wave function obtained from the TDSE and $\nabla_{\mathbf{r}} = \mathbf{e}_\rho \nabla_\rho + \mathbf{e}_\theta \frac{1}{\rho}\nabla_\theta + \mathbf{e}_z \nabla_z$ in cylindrical coordinates. Then the corresponding *time dependent* magnetic field is calculated using the following classical Jefimenko's equation [67],

$$\mathbf{B}(\mathbf{r}, t) = \frac{\mu_0}{4\pi}\int \left[\frac{\mathbf{j}(\mathbf{r}', t_r)}{|\mathbf{r} - \mathbf{r}'|^3} + \frac{1}{|\mathbf{r} - \mathbf{r}'|^2 c}\frac{\partial \mathbf{j}(\mathbf{r}', t_r)}{\partial t}\right] \times (\mathbf{r} - \mathbf{r}')d^3\mathbf{r}', \tag{6.21}$$

where $t_r = t - r/c$ is the retarded time and $\mu_0 = 4\pi \times 10^{-7}$ NA^{-2} (6.692×10^{-4} a.u.) is called the permeability of free space. Units of $B(\mathbf{r}, t)$ are Teslas (1T=10^4 Gauss). For the static zero-field time-independent conditions occurring after the pulse, then (6.21) reduces to the classical Biot-Savart law [67].

Acknowledgements This work has been supported in part by the National Natural Science Foundation of China (Grants Nos. 11974007 and 11574117). The authors also thank Compute Canada for access to massively parallel computer clusters, and the Natural Sciences and Engineering Research Council of Canada and the Fonds de Recherche du Québec—Nature et Technologies for supporting their research work.

References

1. F. Krausz, M. Ivanov, Attosecond physics. Rev. Mod. Phys. **81**, 163 (2009)
2. Z. Chang, P.B. Corkum, S.R. Leone, Attosecond optics and technology: progress to date and future prospects. J. Opt. Soc. Am. B **33**, 1081 (2016)
3. S. Chelkowski, G.L. Yudin, A.D. Bandrauk, Observing electron motion in molecules. J. Phys. B **39**, S409 (2006)
4. H. Niikura, D.M. Villeneuve, P.B. Corkum, Mapping attosecond electron wave packet motion. Phys. Rev. Lett. **94** (2005)
5. H.C. Shao, A.F. Starace, Detecting electron motion in atoms and molecules. Phys. Rev. Lett. **105** (2010)
6. M.J.J. Vrakking, T.E. Elsaesser, Nature Photon. X-Ray Photonics: X-Rays Inspire Electron Movies **6**, 645 (2012)
7. T. Gaumnitz, A. Jain, Y. Pertot, M. Huppert, I. Jordan, F. Ardana-Lamas, H.J. Wörner, Streaking of 43-attosecond soft-X-ray pulses generated by a passively CEP-stable mid-infrared driver. Opt. Exp. **25**, 27506 (2017)

8. K.K. Lange, E.I. Tellgren, M.R. Hoffmann, T. Helgaker, A paramagnetic bonding mechanism for diatomics in strong magnetic fields. Science **337**, 327 (2012)
9. A. Matos-Abiague, J. Berakdar, Photoinduced charge currents in mesoscopic rings. Phys. Rev. Lett. **94** (2005)
10. C. La-O-Vorakiat, E. Turgut, C.A. Teale, H.C. Kapteyn, M.M. Murnane, S. Mathias, M. Aeschlimann, C.M. Schneider, J.M. Shaw, H.T. Nembach, T.J. Silva, Ultrafast demagnetization measurements using extreme ultraviolet light: comparison of electronic and magnetic contributions. Phys. Rev. X **2** (2012)
11. J.-Y. Bigot, M. Vomir, E. Beaurepaire, Coherent ultrafast magnetism induced by femtosecond laser pulses. Nat. Phys. **5**, 515 (2009)
12. C.D. Stanciu, F. Hansteen, A.V. Kimel, A. Kirilyuk, A.T. Tsukamoto, A. Itoh, T. Rasing, All-optical magnetic recording with circularly polarized light. Phys. Rev. Lett. **99** (2007)
13. C.-H. Lambert1, S. Mangin, B.S.D.C.S. Varaprasad, Y.K. Takahashi, M. Hehn, M. Cinchetti, G. Malinowski, K. Hono, Y. Fainman, M. Aeschlimann, E.E. Fullerton, All-optical control of ferromagnetic thin films and nanostructures. Science **345**, 1337 (2014)
14. B. Vodungbo, J. Gautier, G. Lambert, A. B. Sardinha, M. Lozano, S. Sebban, M. Ducousso, W. Boutu, K. Li, B. Tudu, M. Tortarolo, R. Hawaldar, R. Delaunay, V. L ¨ ®pez-Flores, J. Arabski, C. Boeglin, H. Merdji, P. Zeitoun, J. Luning, Laser-induced ultrafast demagnetization in the presence of a nanoscale magnetic domain network. Nat. Commun. **3**, 999 (2012)
15. G.P. Zhang, W. Hübner, G. Lefkidis, Y. Bai, T.F. George, Paradigm of the time-resolved magneto-optical Kerr effect for femtosecond magnetism. Nat. Phys. **5**, 499 (2009)
16. G.P. Zhan, Y. Bai, W. Hübner, G. Lefkidis, T.F. George, Understanding laser-induced ultrafast magnetization in ferromagnets: first-principles investigation. J. Appl. Phys. **103**, 07B113 (2008)
17. I. Barth, J. Manz, Y. Shigeta, K. Yagi, Unidirectional electronic ring current driven by a few cycle circularly polarized laser pulse: quantum model simulations for Mg-porphyrin. J. Am. Chem. Soc. **128**, 7043 (2006)
18. I. Barth, J. Manz, Electric ring currents in atomic orbitals and magnetic fields induced by short intense circularly polarized π laser pulses. Phys. Rev. A **75** (2007)
19. I. Barth, L. Serrano-Andrés, T. Seideman, Nonadiabatic orientation, toroidal current, and induced magnetic field in BeO molecules. J. Chem. Phys. **129** (2008)
20. I. Barth, C. Bressler, S. Koseki, J. Manz, Strong nuclear ring currents and magnetic fields in pseudorotating OsH_4 molecules induced by circularly polarized laser pulses. Chem. Asian J. **7**, 1261 (2012)
21. I. Barth, J. Manz, L. Serrano-Andrés, Quantum simulations of toroidal electric ring currents and magnetic fields in linear molecules induced by circularly polarized laser pulses. Chem. Phys. **347**, 263–271 (2008)
22. K. Köksal, F. Koç, The effect of twisted light on the ring-shaped molecules: the manipulation of the photoinduced current and the magnetic moment by transferring spin and orbital angular momentum of high frequency light. Comput. Theor. Chem. **1009**, 203 (2017)
23. K. Nobusada, K. Yabana, Photoinduced electric currents in ring-shaped molecules by circularly polarized laser pulses. Phys. Rev. A **75** (2007)
24. D. Jia, J. Manz, B. Paulus, V. Pohl, J.C. Tremblay, Y. Yang, Quantum control of electronic fluxes during adiabatic attosecond charge migration in degenerate superposition states of benzene. Chem. Phys. **482**, 146 (2017)
25. G. Hermann, C. Liu, J. Manz, B. Paulus, J.F. Pérez-Torres, V. Pohl, J.C. Tremblay, Multidirectional angular electronic flux during adiabatic attosecond charge migration in excited benzene. J. Phys. Chem. A **120**, 5360 (2016)
26. G. Hermann, C. Liu, J. Manz, B. Paulus, V. Pohl, J.C. Tremblay, Attosecond angular flux of partial charges on the carbon atoms of benzene in non-aromatic excited state. Chem. Phys. Lett. **683**, 553 (2017)
27. H. Ding, D. Jia, J. Manz, Y. Yang, Reconstruction of the electronic flux during adiabatic attosecond charge migration in $HCCI^+$. Mol. Phys. **115**, 1813 (2017)
28. D. Jia, J. Manz, Y. Yang, Generation of electronic flux during the femtosecond laser pulse tailored to induce adiabatic attosecond charge migration in $HCCI^+$. J. Mod. Opt. **64**, 960 (2017)

29. M. Kanno, H. Kono, Y. Fujimura, S.H. Lin, Nonadiabatic response model of laser-induced ultrafast π-electron rotations in chiral aromatic molecules. Phys. Rev. Lett. **104**, (2010)
30. H. Mineo, S.H. Lin, Y. Fujimura, Coherent -electron dynamics of (p)-2,2ä-biphenol induced by ultrashort linearly polarized UV pulses: angular momentum and ring current. J. Chem. Phys. **138** (2013)
31. H. Mineo, Y. Fujimura, Quantum design of π-electron ring currents in polycyclic aromatic hydrocarbons: Parallel and antiparallel ring currents in naphthalene. J. Phys. Chem. Lett. **8**, 2019 (2017)
32. M. Kanno 1, H. Kono, Y. Fujimura, Laser-control of ultrafast π-electron ring currents in aromatic molecules: Roles of molecular symmetry and light polarization. Appl. Sci. **8**, 2347 (2018)
33. K.J. Yuan, A.D. Bandrauk, Circularly polarized attosecond pulses from molecular high-order harmonic generation by ultrashort intense bichromatic circularly and linearly polarized laser pulses. J. Phys. B **45** (2012)
34. K.J. Yuan, H. Lu, A.D. Bandrauk, High-order-harmonic generation in molecular sequential double ionization by intense circularly polarized laser pulses. Phys. Rev. A **92** (2015)
35. K.J. Yuan, A.D. Bandrauk, Attosecond-magnetic-field-pulse generation by intense few-cycle circularly polarized UV laser pulses. Phys. Rev. A **88** (2013)
36. K.J. Yuan, A.D. Bandrauk, Attosecond-magnetic-field-pulse generation by coherent circular molecular electron wave packets. Phys. Rev. A **91** (2015)
37. A.D. Bandrauk, K.J. Yuan, Circularly polarised attosecond pulses: Generation and applications. Mol. Phys. **114**, 344 (2016)
38. A.D. Bandrauk, J. Guo, A.D. Bandrauk, Circularly polarized attosecond pulse generation and applications to ultrafast magnetism. J. Opt. **19** (2017)
39. J.-W. Kim, M. Vomir, J.-Y. Bigot, Ultrafast magnetoacoustics in nickel films. Phys. Rev. Lett. **109** (2012)
40. J.-Y. Bigot, Ultrafast magnetism: down to the nanometre scale. Nat. Mater. **12**, 283 (2013)
41. X. Zhang, X. Zhu, D. Wang, L. Li, X. Liu, Q. Liao, P. Lan, P. Lu, Ultrafast oscillating-magnetic-field generation based on electronic-current dynamics. Phys. Rev. A **99** (2019)
42. H. Ibrahim, C. Lefebvre, A.D. Bandrauk, A. Staudte, F. Légaré, H_2: The benchmark molecule for ultrafast science and technologies. J. Phys. B **51** (2018)
43. K.J. Yuan, A.D. Bandrauk, Exploring coherent electron excitation and migration dynamics by electron diffraction with ultrashort X-ray pulses. Phys. Chem. Chem. Phys. **19**, 25846 (2017)
44. K.J. Yuan, A.D. Bandrauk, Ultrafast X-ray photoelectron imaging of attosecond electron dynamics in molecular coherent excitation. J. Phys. Chem. A **123**, 1328 (2019)
45. S.R. Leone, C.W. McCurdy, J. Burgdörfer, L.S. Cederbaum, Z. Chang, N. Dudovich, J. Feist, C.H. Greene, M. Ivanov, R. Kienberger, U. Keller, M.F. Kling, Z.-H. Loh, T. Pfeifer, A.N. Pfeiffer, R. Santra, K. Schafer, A. Stolow, U. Thumm, M.J.J. Vrakking, What will it take to observe processes in 'real time'? Nat. Photon. **8**, 162 (2014)
46. P.M. Kraus, B. Mignolet, D. Baykusheva, A. Rupenyan, L. Horný, E.F. Penka, G. Grassi, O.I. Tolstikhin, J. Schneider, F. Jensen, L.B. Madsen, A.D. Bandrauk, F. Remacle, H.J. Wörner, Measurement and laser control of attosecond charge migration in ionized iodoacetylene. Science **790**, 350 (2015)
47. M. Kanno, H. Kono, S.H. Lin, Y. Fujimura, Laser-induced electronic and nuclear coherent motions in chiral aromatic molecules, in *Quantum Systems in Chemistry and Physics, Progress in Methods and Applications*, eds. by K. Nishikawa, J. Maruani, E. J. Brändas, G. Delgado-Barrio, P. Piecuch, (Springer, Dordrecht, Netherlands, 2012), pp 121–148
48. K.J. Yuan, J. Guo, A.D. Bandrauk, Generation of ultrafast magnetic fields from molecular coherent electron currents. Phys. Rev. A **98** (2018)
49. T. Zuo, A.D. Bandrauk, High-order harmonic generation in intense laser and magnetic fields. J. Nonlinear Opt. Phys. Mater. **04**, 533 (1995)
50. A.D. Bandrauk, H.Z. Lu, Controlling harmonic generation in molecules with intense laser and static magnetic fields: Orientation effects. Phys. Rev. A **68** (2003)

51. S. Long, W. Becker, J.K. McIver, Model calculations of polarization-dependent two-color high-harmonic generation. Phys. Rev. A **52**, 2262 (1995)
52. D.B. Milošević, W. Becker, R. Kopold, Generation of circularly polarized high-order harmonics by two-color coplanar field mixing. Phys. Rev. A **61** (2000)
53. J.M. Ngoko Djiokap, S.X. Hu, L.B. Madsen, N.L. Manakov, A.V. Meremianin, A.F. Starace, Electron vortices in photoionization by circularly polarized attosecond pulses. Phys. Rev. Lett. **115**, 113004 (2015)
54. J.M. Ngoko Djiokap, A.V. Meremianin, N.L. Manakov, S.X. Hu, L.B. Madsen, A.F. Starace, Multistart spiral electron vortices in ionization by circularly polarized UV pulses. Phys. Rev. A **91**, 013408 (2016)
55. K.J. Yuan, A.D. Bandrauk, Attosecond-magnetic-field-pulse generation by electronic currents in bichromatic circularly polarized UV laser fields. Phys. Rev. A **92** (2015)
56. J. Guo, K.J. Yuan, H. Lu, A.D. Bandrauk, Spatiotemporal evolution of ultrafast magnetic field generation in molecules with intense bichromatic circularly polarized uv laser pulses. Phys. Rev. A **99** (2019)
57. S. Eisebitt, M. Lörgen, W. Eberhardt, J. Luning, J. Stöhr, C.T. Rettner, O. Hellwig, E.E. Fullerton, G. Denbeaux, Polarization effects in coherent scattering from magnetic specimen: Implications for x-ray holography, lensless imaging, and correlation spectroscopy. Phys. Rev. B **68** (2003)
58. D. Baykusheva, M.S. Ahsan, N. Lin, H.J. Wörner, Bicircular high-harmonic spectroscopy reveals dynamical symmetries of atoms and molecules. Phys. Rev. Lett. **116** (2016)
59. K. Lin, X. Gong, Q. Song, Q. Ji, W. Zhang, J. Ma, P. Lu, H. Pan, J. Ding, H. Zeng, J. Wu, Directional bond breaking by polarization-gated two-color ultrashort laser pulses. J. Phys, B **49** (2016)
60. E.A. Pronin, A.F. Starace, M.V. Frolov, N.L. Manakov, Perturbation theory analysis of attosecond photoionization. Phys. Rev. A **80** (2009)
61. E.A. Pronin, A.F. Starace, L.Y. Peng, Perturbation-theory analysis of ionization by a chirped few-cycle attosecond pulse. Phys. Rev. A **84** (2011)
62. K.-J. Yuan, A.D. Bandrauk, Molecular above-threshold-ionization angular distributions with attosecond bichromatic intense XUV laser pulses. Phys. Rev. A **85** (2012)
63. J. Bakos, A. Kiss, L. Szabó, M. Tendler, Light intensity dependence of the multiphoton ionization probability in the resonance case. Phys. Lett. A **41**, 163 (1972)
64. P. Agostini, P. Bensoussan, Resonant three-photon ionization of potassium with circularly and linearly polarized light. Appl. Phys. Lett. **24**, 216 (1974)
65. A.D. Bandrauk, H. Shen, Exponential split operator methods for solving coupled time-dependent Schrödinger equations. J. Chem. Phys. **99**, 1185 (1993)
66. A.D. Bandrauk, H.Z. Lu, Exponential propagators (integrators) for the time-dependent Schrödinger equation. J. Theor. Comput. Chem. **12**, 1340001 (2013)
67. O.D. Jefimenko, *Electricity and magnetism: An Introduction to the Theory of Electric and Magnetic Fields*, 2nd edn. (Electret Scientific Co., Star City, West Virginia, 1989)

Chapter 7
Circularly Polarized High Harmonic Generation for Probing Molecular Chirality

Taro Sekikawa, Kengo Ito, Eisuke Haraguchi, and Keisuke Kaneshima

Abstract Chirality of molecules play an important role in biological activity. Chiral molecules are not superimposable on their own mirror images, called enantiomers, and do not have a symmetry plane nor a center of inversion symmetry. The chemical reactivity of the enantiomers sometimes depends on the chirality. Hence the distinguishing the enantiomers is important and circularly polarized light has been used to discern the enantiomers for a long time. The development of ultrashort pulse technology enables us to investigate nonlinear interactions of chiral molecules with an intense light field. Among various nonlinear optical interactions, we focus on high harmonic generation as the probe into molecular chirality. Here, we describe two our recent results: one is circularly polarized high harmonic generation (CP-HHG) from a chiral molecule, limonene, driven by a CP counter-rotating two-color laser field. The other is the development of elliptically polarized single-order high harmonic light source for the application to photoelectron spectroscopy of chiral molecules.

The physical properties of the enantiomers of chiral molecules are same. However, the chemical reactivity exhibits a strong enantiomeric selectivity. Therefore, the chirality plays a decisive role in biological systems. Discerning the enantiomers is important for understanding the activities of chiral molecules in biological systems. It is interesting that the interaction between circularly polarized (CP) light and chiral molecules depend on the chirality. Therefore, CP light has been used to investigate the magnetic properties and chirality of materials. The development of high peak power lasers provides us new opportunities to explore nonperturbative nonlinear interactions of chiral molecules with an optical field.

Among many nonlinear optical interactions, we are interested in high harmonic generation (HHG) as a probe into molecular chirality. Recently, using the approach based on HHG, the observation of molecular chirality was reported [1–3]. HHG is the light field emission by the nonlinear interactions between a laser electric field and the interacting molecules [4]. The process of HHG is intuitively understood by

T. Sekikawa (✉) · K. Ito · E. Haraguchi · K. Kaneshima
Department of Applied Physics, Hokkaido University, Sapporo 060-8628, Japan
e-mail: sekikawa@eng.hokudai.ac.jp

K. Yamanouchi et al. (eds.), *Progress in Ultrafast Intense Laser Science XVI*,
Topics in Applied Physics 141, https://doi.org/10.1007/978-3-030-75089-3_7

the three-step model, where an electron (1) is ionized by tunneling from an atom or molecule in the presence of a strong laser field, (2) is accelerated in the laser field, and (3) recombines with the parent ion and then emits a higher harmonic photon with an energy corresponding to the sum of the kinetic and ionization energies [5]. Because the HHG yield depends on the electronic states of the interacting molecules through tunneling and recombination probabilities, HHG can be used to probe the electronic states of the molecules, including the symmetry or the chirality of the molecular orbitals. This spectroscopic approach is known as high harmonic spectroscopy (HHS).

HHG can also be used as a light source to probe the chirality. Extreme ultraviolet (EUV) light, which has a high photon energy, allows element selective probing. Accordingly, CP EUV light enables the investigation of element selective electromagnetic and chiral phenomena [6]. High harmonics (HHs) of ultrashort laser pulses [7, 8] are promising for such investigations owing to their spatial and temporal coherence transferred from the driving laser. The electromagnetic fields of HHs are well polarized, and the temporal width of the HH pulses breaks into the attosecond regime [9–13].

In this article, we describe our recent investigation on the circular dichroism (CD) in HHG from chiral molecules [14] and on the polarimetry of elliptically polarized HHG [15]. The former is a kind of HHS to gain insight into chirality. The latter is for the development of a single-order CP EUV light source for the observation of the CD of chiral molecules.

7.1 Circular Dichroism in High Harmonic Generation from Chiral Molecules

7.1.1 Introduction

To distinguish between the enantiomers in a condensed phase, optical approaches such as the CD of photoabsorption and the optical rotation of light polarization have been used. These effects are induced by the interference term $\vec{\mu} \cdot \vec{m}$ between the electric $\vec{\mu}$ and magnetic $\vec{m}$ dipoles in the transition moment [16]. As $\left|\vec{m}\right|$ is generally small, the magnitude of the CD of photoabsorption is typically on the order of 10^{-4}–10^{-5}. Therefore, discerning the enantiomers is a demanding task. However, in the gas phase, the spatial distribution of the photoelectron emission from chiral molecules was found to have a larger anisotropy than the CD of photoabsorption by two or three orders of magnitude, enabling the observation or determination of the molecular chirality with a higher sensitivity [17–20].

HHG provides us unique opportunities for the investigation of chirality. In [1], HHS was applied to detect the chirality based on the observation that the HHG yield from chiral molecules is asymmetric with respect to the sign of the degree of the ellipticity of the driving laser. The ellipticity maximizing the anisotropy was found

to be ±1–2%. This anisotropy comes from the transition between electronic states in the cation, dependent on $\overrightarrow{m}$ pertinent to the molecule, during the second step of the three-step model. The recombining state of the cation with the free electron during the third step could be different from the initial state upon tunneling ionization, resulting in a difference in HHG yield. The interstate transition during the second step is sensitive to the sign of $\overrightarrow{m}$. Thus, the HHG yield is chiral-sensitive.

Previously, we investigated the CD of the CP-HHG by a two-color bicircular laser field from chiral molecules [14]. We used a photoelectron spectrometer using Kr gas as a target. However, the sensitivity to HHG was low. Therefore, in this study, we employed an EUV spectrometer equipped with a charge-coupled device (CCD) camera and observed the CD with better sensitivity to HHG.

CP HHG from a single-color CP laser beam is prohibited by the conservation of spin angular momentum. Considering the three-step model, the released electron cannot return to the parent ion under a CP light field, resulting in no HHG. Therefore, in [1], the polarization of the used laser pulses was very close to linear, as described above. In contrast, a two-color CP laser fields with counter-rotating polarizations generate CP high harmonic pulses [21–30]. The synthesized laser field by the fundamental (ω) and its second-harmonic (2ω) CP light exhibits a three-fold spatiotemporal symmetry. Therefore, the $3m$-order harmonics are missing in isotropic media, where m is a positive integer [23, 25]. The circular polarizations of the $3m + 1$ and $3m + 2$ harmonics are the same as those of ω and 2ω, respectively, and are opposite to each other because of the conservation of spin angular momentum. In this study, we observed the CD of CP HHG from the enantiomers of 1-methyl-4-(prop-1-en-2-yl)cyclohex-1-ene (limonene, inset of Fig. 7.1).

These enantiomers act differently in our smell of sense, e.g., each enantiomer has a peculiar smell: (*R*)- and (*S*)-limonene have the fragrance of oranges and pine, respectively. When light with a linear polarization passes through a pure enantiomer, the plane of polarization is rotated [31]. This is known as optical rotation. (*R*)- and (*S*)-limonene molecules rotate the plane clockwise or counterclockwise as viewed by an observer facing the oncoming wave, respectively.

In the quantum mechanical expression of the three-step model of HHG, the third step is expressed as the complex conjugate of the transition dipole moment between the ground state and ionized state [21, 24, 27, 32, 33]. Therefore, the CP HHG yield is expected to depend on the symmetry of the wavefunction of the outermost atomic or molecular orbital [9, 12]. Experimentally, the relative intensities of the allowed neighboring harmonics, $3m + 1$ and $3m + 2$, in CP HHG were found to depend on the atomic species [27, 29]. In the early stage of the investigation, these relative intensities appeared to be understood by the following propensity rule: single photoionization with a field corotating with the initial state is much more likely than with a counter-rotating field [24, 27]. However, the underlying mechanism was found to be more complicated, and precise theoretical calculations are necessary to understand it completely [29].

Although the quantitative prediction of the relative intensities is not simple, the sensitivity of CP HHG to the outermost atomic orbital suggests that CP HHG is also susceptible to the highest occupied molecular orbital (HOMO) of a chiral molecule,

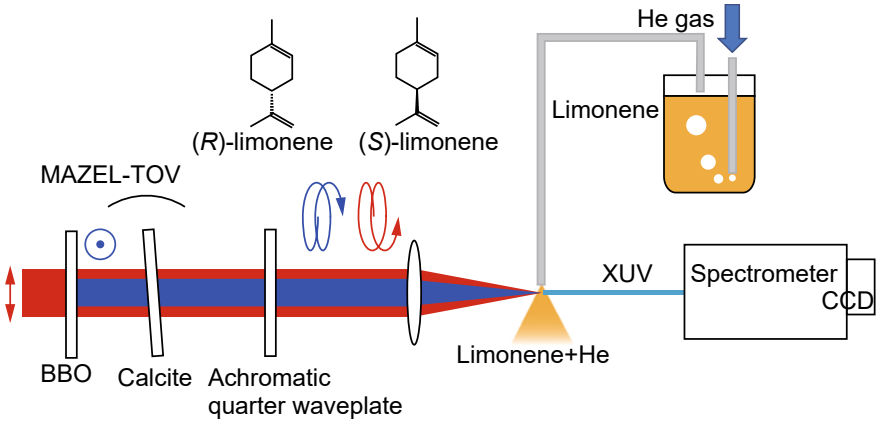

Fig. 7.1 Experimental setup for the observation of CP HHG. MAZEL-TOV is the optical system used to generate the two-color counter-rotating CP laser field consisting of a BBO crystal, a calcite plate, and an AQW [34]. The superposition of the two-color counter-rotating polarized laser fields, of which the rotation directions of the fundamental and second-harmonic light field are represented by the counterclockwise and clockwise arrows, respectively, forms triangular polarization with threefold symmetry. The inset is the molecular structures of limonene molecules

the direction of which should be determined by the rotation direction of the electrons in the HOMO. Even for randomly oriented molecules, the chirality is active. This indicates that CP HHG can be used to discern molecular chirality. Still, the response of a large molecule to a laser field would not be as simple as that of an atomic orbital. Therefore, the purpose of the present work is the experimental exploration of the sensitivity of CP HHG to molecular chirality.

7.1.2 Experiment

The experimental setup for CP HHG is illustrated in Fig. 7.1. A Ti:sapphire laser system delivers 1.4 mJ, 35 fs pulses with a center wavelength of 800 nm at a repetition rate of 1 kHz. The two-color counter-rotating CP laser field was synthesized by the inline setup called MAZEL-TOV [34]: the linearly polarized 800 nm pulses were partially converted to 400-nm pulses with a polarization perpendicular to ω by a β-BaB_2O_4 (BBO) crystal with a thickness of 300 μm. The pulse energies of the ω and 2ω pulses were 0.9 and 0.5 mJ, respectively. After compensating the group-delay between the ω and 2ω pulses by a calcite plate, their polarizations were changed to circular by an achromatic quarter-waveplate (AQW) (Kogakugiken corp.). Here, the rotation directions of the ω and 2ω were opposite to each other and were switched just by rotating the crystal axis of the AQW by 90°. Because of the inline setup, the spatial overlap between the ω and 2ω beams was suitable to form a triangular electric field. The generation of the $3m$-th harmonics was almost suppressed. In this paper,

counterclockwise polarization is defined by an observer facing an oncoming wave and vice versa.

The two-color synthesized laser field was focused into a gas jet using a concave mirror with a focal length of 0.5 m. The gas jet was formed by a glass capillary with an inner diameter of 300 μm. The capillary tip was set at the focal point of the mirror. The peak intensities of the ω and 2ω beams were estimated to be 5.0×10^{14} and 1.4×10^{14} W/cm^2, respectively. The enantiomers of limonene molecules, purchased from Wako Pure Chemical Industries Ltd., were stored in a glass bubbler and warmed to 333 K to increase their vapor pressure. The limonene vapor was sent through a heated pipeline to the glass capillary mixed with 1.6 atm helium gas. The flow of the limonene molecules mixed with helium was continuous. The spectra of the high harmonics were recorded by an EUV spectrometer with a CCD camera. The intensity of each harmonic was obtained by integrating the counts of each peak, and the ambiguity of the intensity was estimated by the square root of the total counts.

7.1.3 Results and Discussion

Figure 7.2a and b present the spectra of the CP HHG from (*S*)-limonene, and (*R*)-limonene, respectively. The clockwise (counterclockwise) circular arrow in Fig. 7.2 indicates the rotation direction of the polarization of the ω (2ω) used for HHG. The dotted (solid) lines indicate the CP HHG spectra generated by the combination of a clockwise (counterclockwise) rotating ω and counterclockwise (clockwise) rotating 2ω represented by the solid and dotted arrows, respectively. The following two features in the spectra are identified: (1) The $3m + 1$ harmonics of the (*R*)-limonene signal are relatively more enhanced than the $3m + 2$ when the ω has a clockwise polarization. (2) However, for the counterclockwise polarization of the ω, the $3m + 1$ harmonics of the (*S*)-limonene signal are more enhanced.

To quantitatively evaluate the CD, the Kuhn g-factor 2(IL - IR)/(IL + IR), where IL and IR are the intensities with counterclockwise and clockwise polarization, respectively, was estimated by summing up the counts for each harmonic order after normalizing the total counts of the observed spectrum to the same value for each polarization and is shown in Fig. 7.3. (*R*)-limonene (triangle) generates more high harmonics with clockwise circular polarization than with counterclockwise circular polarization, while (*S*)-limonene (circle) prefers the generation of harmonics with counterclockwise circular polarization. The Kuhn g-factors are almost symmetrical with respect to the baseline, indicating the CD in HHG. These results are consistent with the previous results [14].

Under the present experimental conditions, the interaction length between the laser field and chiral molecules was 300 μm and the gas density of the chiral molecules was low. Therefore, the phase-mismatch among the driving laser pulses and high harmonic pulses was negligible [25, 27, 35], which will be evaluated later. The response of a single molecule should be crucial for dichroism. The observed CD would be explained by the same processes proposed in [1] and [33]: the transition

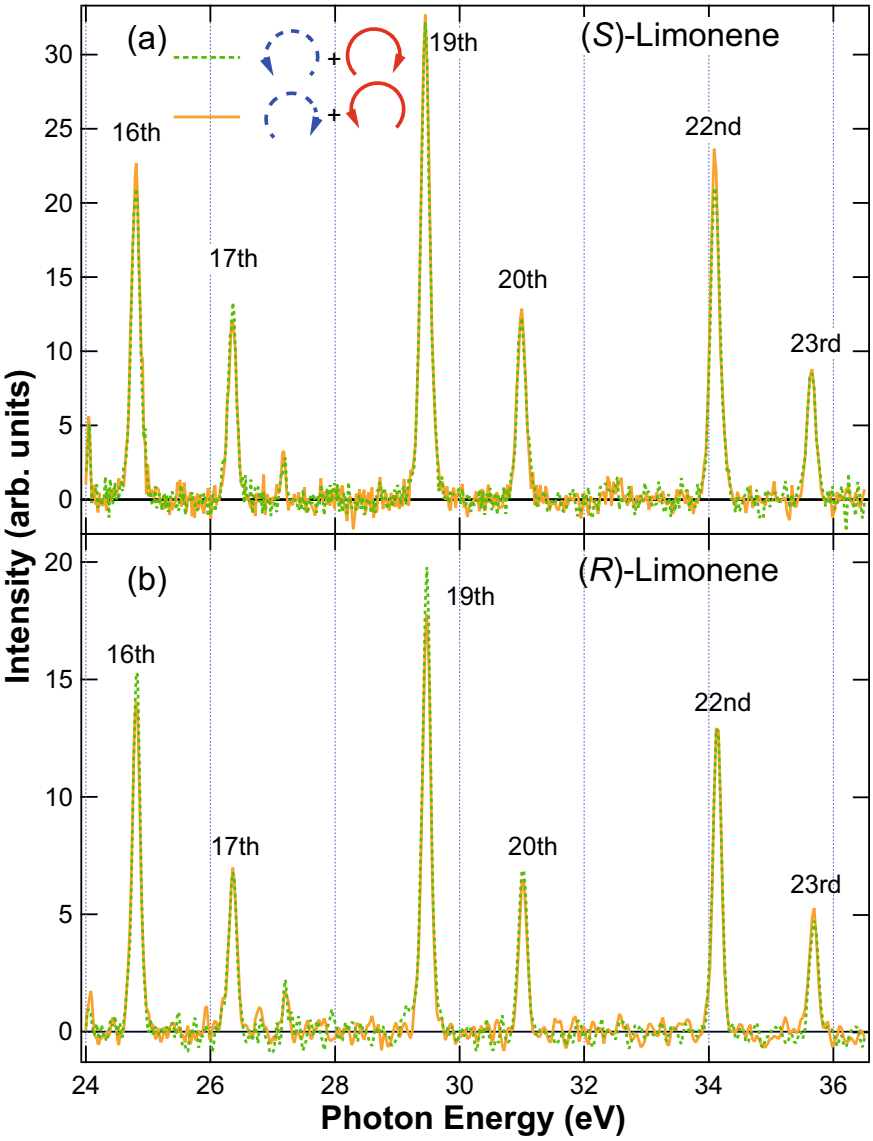

Fig. 7.2 High harmonics spectra from **a** He, **b** (*S*)-limonene, and **c** (*R*)-limonene, generated by the synthesized laser field by the CP ω and 2ω. The spectra shown by the dotted (solid) lines have been generated by the combination of ω and 2ω, of which the rotational directions of the polarization are clockwise (counterclockwise), represented by solid arrow, and counterclockwise (clockwise), represented by dotted arrow, respectively

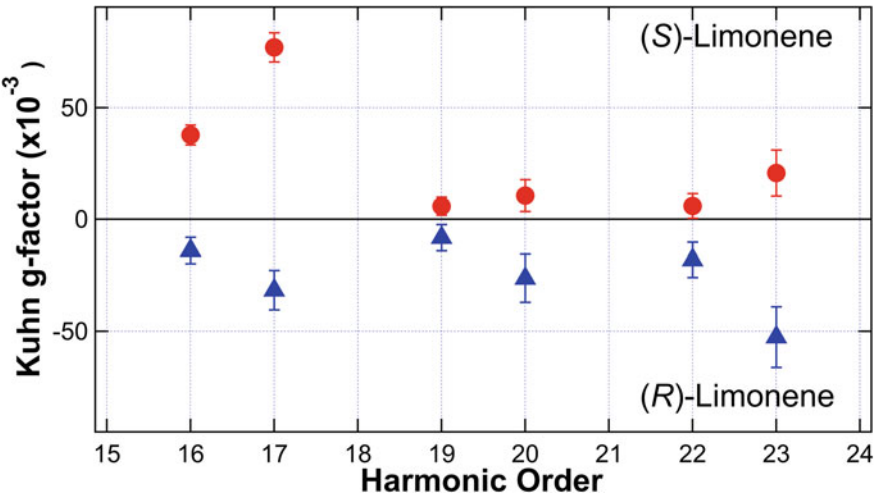

Fig. 7.3 Kuhn g-factors from the enantiomers for each higher harmonic order

to another state by $\overrightarrow{m}$ in the cation during the second step of the three-step model modulates the efficiency of HHG.

Here, however, more intuitive perspectives may be provided. One is the propensity rule of the ionization probability dictating the third process of the three-step model [24, 27, 29]: the emitted radiation is more likely to acquire a polarization with the same rotation direction of the outermost atomic orbitals [24]. Therefore, the preferred CP HHG is determined by the rotation direction of the HOMO wavefunction of an enantiomer, although it is not straightforward to predict the direction of the rotation or the ring current in the molecule from the molecular structure or the distribution of the HOMO electrons. Further investigation on HHG from chiral molecules will reveal the relationship between them.

As another perspective, the resonance with the intermediate states with CD could be responsible for the CD in HHG. In perturbative nonlinear optics, it is well-known that the resonance with the electronic states of nonlinear media enhances the nonlinear susceptibility. Even in HHG, the resonance with an electronic state raises the generation efficiency [36]. The photoabsorption of limonene appears in a wavelength region shorter than about 220 nm with CD [37]. Thus, both ω and 2ω can be resonant with the states at 200 nm. Because (*R*)-limonene has a larger absorption coefficient for clockwise polarization at 200 nm [37], the nonlinear responses to the clockwise polarized light could be larger at 200 nm than to the counterclockwise polarization. Experimentally, the Kuhn g-factors are found to have a negative sign for (*R*)-limonene, as shown in Fig. 7.3. That is, the HHs with clockwise polarization were generated more efficiently from (*R*)-limonene. Considering that the $3m + 1$ and $3m + 2$ orders have the same polarization as ω and 2ω, respectively [25], the resonance of ω or 2ω, with clockwise polarization, with the dichroic states enhances the HHs with clockwise polarization from (*R*)-limonene.

CD of the states at about 200 nm in limonene was observed in the photoelectron spatial distribution: Fanood et al. observed the wavelength dependence of the anisotropy of the photoelectron emission by the (2+1) resonance multiphoton ionization by the CP photons [38]. They found that the sign of the asymmetry factor of the photoemission from the HOMO was reversed when the center wavelength of the laser was changed from 420 to 392 nm. Interestingly, at these wavelengths, the sign of the CD of linear absorption also reversed [37]. This correspondence between the CD of the photoelectron emission and that of the linear absorption is attributed to the resonance with different vibrational levels and different electronic ion core configurations in the intermediate Rydberg states [38]. The intermediate states with CD should also influence the HHG through the resonance effects.

The enhancement of CP HHG by the resonance with the intermediate states with CD also appears to be the case in [1]. It was found that an elliptically polarized driving laser rotating in the clockwise direction with photon energies of 0.70 and 0.67 eV generates high harmonics more efficiently from (*S*)-epoxypropane and (*R*)-fenchone than the laser field rotating in the opposite direction. According to [39, 40], (*S*)-epoxypropane and (*R*)-fenchone are resonant and have larger absorption coefficients at 11 (=7.7 eV) and 6 photons (=4.0 eV) for the clockwise polarization, respectively. The correspondence found in limonene predicts that HHs are generated more efficiently by the driving laser with the clockwise polarization from these enantiomers, and successfully explains the experimental observation.

Finally, the phase mismatch in CP-HHG was estimated as follows. The angle of the optical rotation α and the difference in the refractive indices of the circular polarizations Δn have the relation of $\alpha = \pi \Delta n l/\lambda$, where λ and l are the wavelength and interaction length, respectively. Using α and n given in [31], Δn at ω and 2ω was deduced to be 2.1×10^{-6} and 5.2×10^{-6}, respectively, for a 1 cm-long liquid. As Δn is proportional to the density of limonene, Δn in the gas phase was estimated considering the vapor pressure [41]; at 358 K, the vapor pressure was 4.92 kPa. If the total gas pressure just below the capillary tube was 2700 Pa [42], the pressure of limonene was estimated as 82 Pa. When the temperature was cooled to 100 K by supersonic expansion, the gas density of limonene was 1.4×10^{-5} g/cm^3. As Δn is proportional to the density and the interaction length l of 300 μm, Δn at 2ω and ω are 8.2×10^{-11} and 3.3×10^{-11}, respectively. Meanwhile, the corresponding average refractive indices are 1.00026 and 1.00025, respectively. Therefore, under the assumption that the refractive indices in the EUV range are unity, the difference in the phase mismatch coming from the CD is negligibly small and phase matching is not the primary effect.

In summary, the CP HHG limonene enantiomer spectra were found to exhibit CD in the intensities. CP HHG is sensitive to the chirality of the interacting molecules with a synthesized CP light field. CP HHG appears to be very promising for discriminating enantiomers. As CP HHG includes processes taking place on the attosecond timescale, CP HHG might also be applicable to probe the attosecond transient chirality of molecules.

7.2 Polarimetry of a Single-Order Circularly Polarized High Harmonic Separated by a Time-Delay Compensated Monochromator

7.2.1 Introduction

To generate CP EUV light, the polarization conversion from linear to circular polarization was demonstrated by a reflective polarizer, although the conversion efficiency was ~4% [6]. Recently, the generation scheme of CP HHs directly driven by laser field was established [23, 25, 34, 43–45]. The driving laser field synthesized by two-color CP light fields with counter-rotating circular polarizations enables the efficient generation of CP HHs, while the one-color single beam CP laser field does not generate HHs, underlain by the three-step model of HH generation [5] and by the conservation of the spin angular momentum of photons. The conversion efficiency is comparable to the linearly polarized HH generation [23]. In the case of noncollinear geometry [43, 44], the HHs generated by two noncolinear beams with the same color are spatially dispersed. The propagating direction of each HH is determined by the conservation of the spin angular momentum of photons.

The application of CP HHs sometimes requires focusing the single-order harmonic on a target. However, in collinear geometry, all harmonics spatially overlap. Thus, it is necessary to spatially separate the harmonics. Although the harmonic orders are spatially dispersed in noncollinear geometry [43], it is not tractable to focus a specific harmonic order on targets. The usage of a grating is more convenient to both separate and focus the beam, as has already been demonstrated in the observation of nanoscale magnetic imaging [46].

Here, the monochromatization and focusing of a CP harmonic generated in the collinear scheme was implemented by a time-delay compensated monochromator (TDCM) [47–49], consisting of a pair of toroidal gratings and a slit [15]. The TDCM preserves the pulse duration of the selected harmonic [47–49] and focuses the harmonic pulses on target [48]. The TDCM is extensively used for time-resolved photoelectron spectroscopy using a linearly polarized harmonic [50–52]. To assess the applicability of the TDCM to isolate a single-order CP harmonic, the ellipticity of the selected harmonic was evaluated, because the grazing incidence to the toroidal gratings in the TDCM distorts the circular polarization to elliptical owing to the anisotropy of the complex coefficient of the diffraction on the grating. To obtain a CP HH, elliptically polarized harmonic pulses were generated by manipulating the polarization of the driving laser field and were corrected by the diffraction by the gratings. The first practical isolation and characterization of a CP single-order harmonic is demonstrated.

7.2.2 Experiment

The experimental setup is shown in Fig. 7.4. The driving laser field was synthesized by the MAZEL-TOV scheme described in Sect. 7.1.2 [34]. The 900 μJ, 35 fs linearly polarized ω light delivered at 1 kHz by a Ti:sapphire laser system was partially converted to 300 μJ 2ω light with perpendicular polarization to ω by a BBO crystal. The circular polarizations of HHs were switched by rotating the AQW by 90°. The ellipticity of ω and 2ω were 0.99 and 0.98, respectively, measured using a linear polarizer and a quarter waveplate. In this section, the rotating direction of the circular polarization is also defined as viewed by an observer facing the oncoming light, which is same in the previous section. The counterclockwise and clockwise rotations of the light polarization are called left-handed (LH) and right-handed (RH) polarization, respectively. Because MAZEL-TOV is composed of static optical elements, the relative phase between ω and 2ω was fixed. The two CP beams were focused in a Kr gas jet by a concave mirror with a 50 cm focal length. The inset in Fig. 7.4 shows the photoelectron spectrum of Kr atoms irradiated by HHs. Each labeled harmonic order has two peaks because of the spin–orbit splitting of the cation. The generation of the 18th harmonic was suppressed, and its intensity was 18% and 0.7% of the 19th and 17th harmonics, respectively, reinforcing the three-fold symmetry of the synthesized driving laser field. Therefore, the generated HHs were expected to be highly CP. The TDCM consists of a pair of Pt-coated toroidal gratings (HORIBA JOBIN YVON, 54,000,910) and the slit [48, 49]. The first grating disperses the harmonics spatially, and the slit selects a single-order harmonic. The second grating compensates for the pulse front tilt introduced by the diffraction to compress the pulse duration. The reflection angle of the grating is 142°. The harmonic order

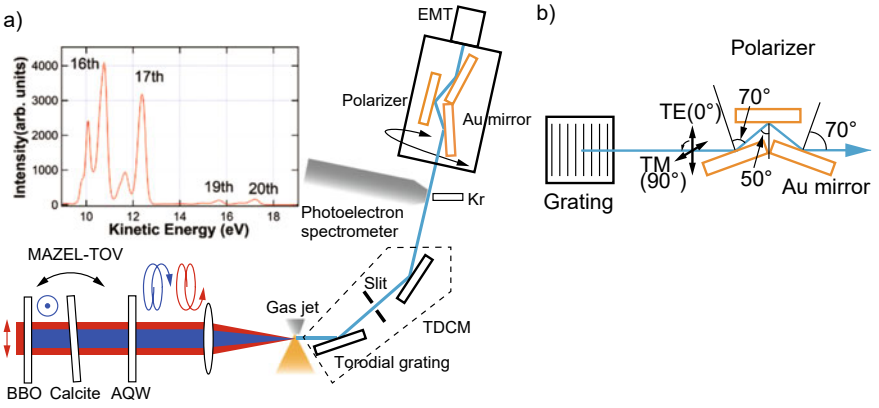

Fig. 7.4 **a** Experimental setup. AQW is an achromatic quarter waveplate, and EMT is an electron multiplier. TDCM is a time-delay compensated monochromator. The inset shows the photoelectron spectrum of Kr atoms irradiated by the labeled high harmonics. **b** Schematics of a linear polarizer consisting of three Au mirrors and a grating with the grooves in the vertical direction

was monitored by a photoelectron spectrometer and the single order selection was always confirmed. The photon flux of the 17th harmonic with circularly polarization was ~106 photons/pulse, comparable to that of linearly polarized light. The selected harmonic was detected by an electron multiplier (R2362, Hamamatsu Photonics) after the linear polarized described in the next section. The transmitted intensity $I(\phi)$ as a function of rotation angle of the polarizer ϕ was measured with an accumulation time of 3 s. every 10° between 0 and 180° for circular polarization and every 5° for linear polarization with an assumption that $I(\phi) = I(\phi - 180)$.

7.2.3 Characterization of Polarization

To characterize the polarization state of HHs, a linear polarizer for EUV light was constructed by three Au mirrors schematically shown in Fig. 7.4 [53], which has been used in EUV spectroscopy [54]. Intuitively, s-polarized light goes through the polarizer more because of the anisotropy in the reflectance of the Au mirror between s and p polarizations as listed in Table 7.1. These were calculated using the values in [55] and the Au mirrors with no coating were used to ensure the optical response of Au. In the constructed polarizer, the incident angles to the first and the third mirror were set as 70°, and that to the second mirror was set as 50° [53].

The Stokes vector of the completely polarized light beam $\overrightarrow{S} = (S_0, S_1, S_2, S_3)$ is associated with $I(\phi)$ as follows: when the phase difference between the x and y components of a polarized electric field of light is δ, of which sign determines the handedness of a circular polarization,

$$I(\phi) = \frac{I(0°) + I(90°)}{2} + \frac{I(90°) - I(0°)}{2}\cos(2\phi) + \sqrt{I(0°)}\sqrt{I(90°)}\sin(2\phi)\cos\delta. \tag{7.1}$$

The Stokes vector is associated with $I(\phi)$ by

$$\left(I(0°) + I(90°),\ \ I(90°) - I(0°),\ \ 2\sqrt{I(0°)}\sqrt{I(90°)}\cos\delta,\ \ 2\sqrt{I(0°)}\sqrt{I(90°)}\sin\delta\right) \tag{7.2}$$

Table 7.1 Reflectance and reflectance phase of Au [55]

Wavelength (nm)	Angle of incidence (°)	Reflectance		Phase (°)	
		$r_s{}^2$	$r_p{}^2$	δ_s	δ_p
50	70	0.515	0.251	−146	177
	50	0.251	0.0550	−16	151
47	70	0.455	0.199	− 46	179
	50	0.204	0.0332	−18	151

Hence, experimentally, S_2 is directly obtained by $I(45°) - I(-45°)$ and then, the absolute value of S_3 can also be evaluated. The sign of δ is usually determined by inserting a quarter waveplate. The ellipticity ε is given by $\varepsilon = \left|\tan\left(\frac{1}{2}\arctan\left(\frac{S_3}{\sqrt{S_1^2+S_2^2}}\right)\right)\right|$. Among the elements of the Stokes vector, there is a relationship of $S_0^2 = S_1^2 + S_2^2 + S_3^2$. However, when the beam contains the unpolarized component, these relationships are not directly applicable, because of $S_0^2 > S_1^2 + S_2^2 + S_3^2$, where S_0 corresponds to the total beam flux.

To take account of the unpolarized components and the diffraction by the gratings quantitatively, the transmittance of the optical system is evaluated by operating the Mueller matrixes, characterizing the optical components, on the Stokes vector [56]. The first element of the Stokes vector S_0 is proportional to $I(\phi)$, from which the Stokes vector and the optical parameters of the toroidal gratings are evaluated in this work. Using the complex reflection coefficients of an optical component $r_s \exp(i\delta_s)$ and $r_p \exp(i\delta_p)$ for s and p polarization, respectively, the Mueller matrix $\mathbf{M}$ for reflection is expressed as

$$\mathbf{M} = {}^1\!/_2\left(r_s^2 + r_p^2\right)\begin{pmatrix} 1 & -\cos 2\psi & 0 & 0 \\ -\cos 2\psi & 1 & 0 & 0 \\ 0 & 0 & \sin 2\psi \cos\Delta & \sin 2\psi \sin\Delta \\ 0 & 0 & -\sin 2\psi \sin\Delta & \sin 2\psi \cos\Delta \end{pmatrix}, \tag{7.3}$$

where $\tan\psi = r_p/r_s$ and $\Delta = \delta_p - \delta_s$ [53]. Because ψ and Δ depend on an incident angle θ, $\mathbf{M}$ at θ for Au is denoted as $\mathbf{M}_\theta$. In this work, to describe the diffraction by the grating, the matrix $\mathbf{M}_\mathrm{G}$ with the same formula as (7.3), using ψ_G and Δ_G defined by $\tan\psi_G = r_{TM}/r_{TE}$ and $\Delta_G = \delta_{TM} - \delta_{TE}$, respectively, is employed. Here, the complex coefficients for the transverse electric (TE) and transverse magnetic (TM) diffracted light are expressed as $r_{TE}\exp(i\delta_{TE})$ and $r_{TM}\exp(i\delta_{TM})$, respectively. Because the second toroidal grating in the TDCM is installed mirror-symmetrically including the groove geometry so that the light propagates in the backward direction of the diffraction [48], the Mueller matrix of the TDCM is expressed as $\mathbf{M}_\mathrm{G}\,\mathbf{M}_\mathrm{G}$ by the reciprocal theorem [57]. The rotation of the polarizer around the propagation direction of the light by ϕ is expressed as

$$\mathbf{R}(\phi) = \begin{pmatrix} 1 & 0 & 0 & 0 \\ 0 & \cos 2\phi & \sin 2\phi & 0 \\ 0 & -\sin 2\phi & \cos 2\phi & 0 \\ 0 & 0 & 0 & 1 \end{pmatrix}. \tag{7.4}$$

The Mueller matrix of the reflective polarizer rotated by ϕ is $\mathbf{R}(-\phi)\mathbf{M}_{70}\mathbf{M}_{50}\mathbf{M}_{70}\mathbf{R}(\phi)$. Here, $\mathbf{M}_{50}$ and $\mathbf{M}_{70}$ are calculated from the optical constants listed in Table 7.1. Consequently, $\overrightarrow{S}$ of the incident beam to the TDCM and the polarizer is transformed into $\overrightarrow{S'} = \mathbf{R}(-\phi)\mathbf{M}_{70}\mathbf{M}_{50}\mathbf{M}_{70}\mathbf{R}(\phi)\mathbf{M}_G\mathbf{M}_G\overrightarrow{S}$.

7.2.4 Polarization After the Time-Delay Compensated Monochoromator

Firstly, to examine whether the reflection polarizer works correctly, $I(\phi)$ of linearly polarized 17th harmonic (47 nm) with TE and TM polarizations were measured, as shown in Fig. 7.5a. Here, the direction of 0° is parallel to the groove of the toroidal grating and TE polarization. The TM polarization is perpendicular to the TE polarization. Transmitted intensity approaches to maximum in the same direction of the electric field, while the intensity of the perpendicular direction to the electric field was 0.033 of the maximum as expected from the extinction ratio of the polarizer calculated using the optical constants tabulated in Table 7.1. Hence, quantitatively, the three sets of Au mirrors work as a linear polarizer.

For the linear TE and TM polarizations of $\vec{S}_{\substack{TE\\TM}} = (1, \mp 1, 0, 0)$, the first element of $\vec{S}'_{\substack{TE\\TM}}$ after the TDCM and the polarizer is proportional to $\alpha \pm \beta\cos(2\phi)$ accordingly, where $\alpha = 1.69$ and $\beta = 1.58$ for the 17th harmonic obtained using ψ and Δ of Au. The difference between α and β is due to the finite reflectivity of the Au mirror of the orthogonal component in the polarizer. The solid lines in Fig. 7.5a indicate the fitting results for these equations. Although only the proportional coefficient was a fitting parameter, the angle dependence was reproduced. Therefore, the reflectance and the phase in Table 7.1 appropriately describes the responses of the Au mirrors installed in the reflection polarizer.

When the polarizations of the HHs were switched to circular polarizations, the angle dependences of the 17th harmonic selected by the TDCM were changed to those of Fig. 7.5c. The angle dependence shows that the polarizations after the TDCM are no longer circular polarization. In contrast with linear polarization, however, the LH CP light (●) has a maximum transmittance in the 325° direction, while the RH CP light (▲) has a maximum transmittance in the 35° direction. The angle dependence of the 16th harmonic was similar to that of the 17th harmonic as shown in Fig. 7.5b.

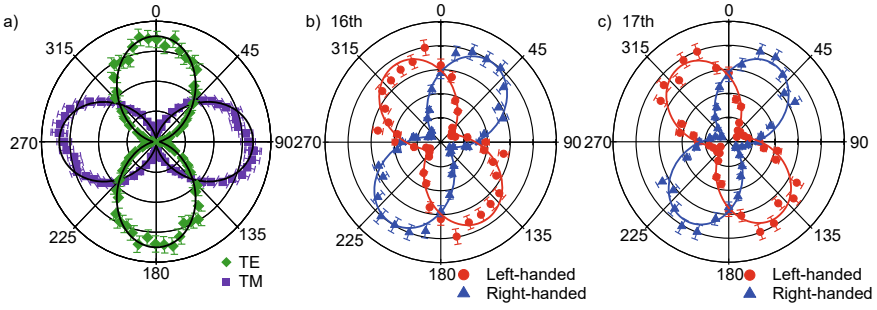

Fig. 7.5 **a** Transmitted intensities of TE (◆) and TM (■) polarizations of the 17th harmonic as a function of the rotating angle of the polarizer ϕ, respectively. The solid lines denote the fitting results. **b**, **c** Transmitted intensities of the left- (●) and right-handed (▲) CP 16th and 17th harmonics as a function of ϕ, respectively. The solid lines are the fitting results

Here, note that the circular polarization of the 16th and 17th harmonics are orthogonal to each other under the same generation condition. The difference in the tilt direction from 0° of the angular distribution between the 16th and17th harmonics confirms that they have the opposite circular polarization experimentally. The sensitive response of the angle dependence to circular polarization also suggests that the observed HHs are highly polarized. If the harmonics are non-polarized, the transmittance should have the minimum at 90° and 270°, while the experimentally observed minimum was observed in directions of ±55° and ±235°.

To understand the angle dependence of the transmittance of the RH and LH CP light including the unpolarized component with $\overrightarrow{S}_{\substack{RH\\LH}} = A(1,\ 0,\ 0,\ \pm 1) + B(1,\ 0,\ 0,\ 0)$, respectively, the first element of the Stokes vector $\overrightarrow{S}'_{\substack{RH\\LH}} = \mathbf{R}(-\phi)\mathbf{M}_{70}\mathbf{M}_{50}\mathbf{M}_{70}\mathbf{R}(\phi)\mathbf{M}_G\mathbf{M}_G \overrightarrow{S}_{\substack{RH\\LH}}$ is calculated. Here, A and B are proportional to the intensities of the polarized and nonpolarized components, respectively. The transmitted intensities of the RH and LH CP harmonics $I_{\substack{RH\\LH}}(\phi)$, i.e. the first element of $\overrightarrow{S}'_{\substack{RH\\LH}}$, are given as

$$I_{\substack{RH\\LH}}(\phi) = P + Q\cos(2\phi) \pm R\sin(2\phi) \tag{7.5}$$

where

$$P = (A + B)\alpha(1 + \cos^2(2\psi_G)), \tag{7.6}$$

$$Q = 2(A + B)\beta\cos(2\psi_G), \tag{7.7}$$

and

$$R = -A\beta\sin(2\Delta_G)\sin^2(2\psi_G). \tag{7.8}$$

For the 16th harmonic, $\alpha = 1.56$ and $\beta = 1.41$. Because R depends on Δ_G, the tilt direction of the principle axis of the transmittance depends on the circular polarization.

To evaluate the optical constants ψ_G and Δ_G, P, Q, and R are determined by fitting (7.5) to the experimental results. The fitting results are shown by the solid lines in Fig. 7.5b and c. ψ_G is uniquely determined by (7.6) and (7.7), while the other parameters, A, B, and Δ_G, cannot be determined uniquely. However, (7.7) and (7.8) limit the range of A as follows: (7.7) gives the maximum of A as $Q/(2\beta\cos(2\psi_G))$, where a HH is completely polarized, i.e. $B = 0$. Equation (7.8) also gives the lower limit of A as $R/\left(\beta\sin^2(2\psi_G)\right)$ to satisfy $R/\left(A\beta\sin^2(2\psi_G)\right) \leq 1$. Consequently, the range of A is given by

$$|R|/\left(\beta\sin^2(2\psi_G)\right) \leq A \leq Q/(2\beta\cos(2\psi_G)). \tag{7.9}$$

The corresponding range of B is given by (7.6) or (7.7) and, consequently, $\overrightarrow{S}_{\substack{RH\\LH}}$ and $\overrightarrow{S}'_{\substack{RH\\LH}}$ are also determined. Using these values, the corresponding Δ_G, degree of polarization (DOP) before and after the TDCM, and ellipticity ε after the TDCM are given. Here, DOP is defined by DOP $= \sqrt{S_1^2 + S_2^2 + S_3^2}/S_0$ for the Stokes vector of (S_0, S_1, S_2, S_3). In Table 7.2, ψ_G and the ranges of Δ_G, DOP, and ε are listed. Fortunately, the ranges of Δ_G, DOP, and ε are limited. Hence, we can discuss the polarization states further.

The CP HHs were reported to be partially depolarized, because of the dynamical symmetry breaking by medium ionization and the temporal evolution of the driving laser during the HH generation [58]. The DOP of the 17th harmonic was reported to be approximately 0.6 [58]. CP HHs generated in noncollinear scheme have a DOP of about 0.85 [44]. The depolarized components would be attributable to the ionization of the interacting gas, introducing decoherence in the process of HH generation. The DOP on target in the present work is 0.81 in the worst case, which is higher than that in [58]. On the gratings, only the spatially coherent component with the same polarization can be diffracted. Therefore, the gratings work as filters passing through the polarized component. Higher DOP is one advantage of this scheme.

The obtained ψ_G is close to those of Pt, $\psi = 36.6°$ for the 16th and $\psi = 36.0°$for the 17th harmonic, respectively, at the incident angle of 71° [55]. The phase shift of Pt, $\Delta = 319°$ for 16th and $\Delta = 321°$ for 17 harmonics, are also within the range of Δ_G. Although the harmonics are not reflected but diffracted on the surface of the toroidal grating, the diffraction efficiency depends on the coated substance, Pt. Therefore, it is reasonable that ψ_G and Δ_G have similar values to those of Pt. The ratio of the diffraction efficiency ${r_{TM}}^2/{r_{TE}}^2$ of the toroidal grating is related with ψ_G by $\tan\psi_G = r_{TM}/r_{TE}$, and it is 0.66 when the average value of $\psi_G = 39.0°$ is employed for the 17th harmonic. This value is consistent with the experimentally measured value 0.70 ± 0.05 at 47 nm for linearly polarized light. The experimentally determined range of ε shows that the circular polarization of the selected single-order harmonics was deteriorated by the TDCM, owing to the anisotropy and the phase shift by diffraction.

Table 7.2 Parameters for right (RH)- and left-handed (LH) circularly polarized harmonics after TDCM

Harmonic order	Polarization	ψ_G (°)	Δ_G (°)	DOP before TDCM	DOP after TDCM	Ellipticity
16	LH	39.6	315~338	0.71~1.00	0.81~1.00	0~0.38
	RH	39.8	315~329	0.88~1.00	0.91~1.00	0~0.24
17	LH	39.7	315~330	0.87~1.00	0.90~1.00	0~0.24
	RH	38.2	315~329	0.88~1.00	0.91~1.00	0~0.23

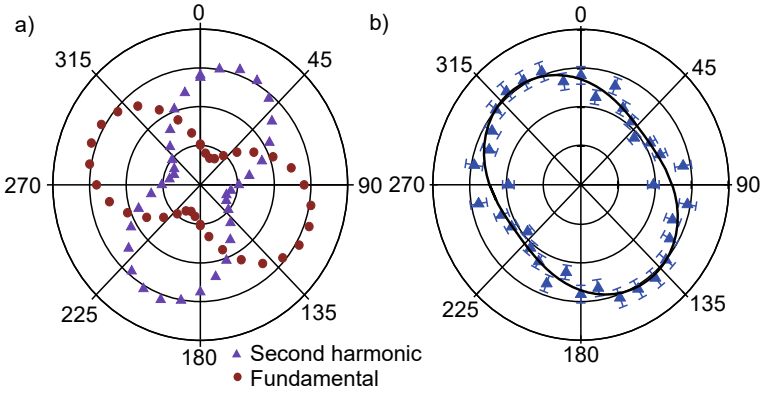

Fig. 7.6 **a** Transmitted intensities of elliptically polarized fundamental light ω (●) and the second harmonic 2ω (▲) as a function of the rotating angle of the polarizer. **b** Transmitted intensities of RH elliptically polarized 17th harmonic as a function of the rotating angle of the linear polarizer. The solid lines are the fitting results of (7.10) and (7.11). These two results are overlapped

7.2.5 Compensation of Ellipticity for Circluar Polarization

One approach to obtain the CP harmonic at focus in this scheme is to generate elliptically polarized HHs and to correct the ellipticity by the anisotropic diffraction and the phase shift of the toroidal gratings. For example, the elliptical polarization along the TM direction is preferred, because the diffraction efficiency of TE mode is higher than that of TM mode. To generate elliptically polarized HHs, the polarization of ω with higher pulse energy than 2ω was set to parallel to TM mode and the ellipticity was introduced to the driving laser field by rotating the AQW from the optimum angle for the quarter wavelength. When the angle was rotated by 20° from the optimum angle, the polarizations of the driving laser field were changed to be elliptical. Figure 7.6a shows the angle dependence of the RH ω and LH 2ω intensities measured using a linear polarizer. The ellipticities of ω and 2ω were 0.48 and 0.52, respectively.

These two laser fields were synthesized and generated the RH 17th harmonic, of which angle dependence of the intensity is shown in Fig. 7.6b. Because the optical parameters of the toroidal grating listed in Table 7.2 are not uniquely determined, $I(\phi)$ of $\overrightarrow{S} = (S_0, S_1, S_2, S_3)$ are evaluated for two extreme cases with $\Delta_G = 329°$ and with $\Delta_G = 315°$. The corresponding $I(\phi)$ are

$$I(\phi) = 1.747S_0 - 0.625S_1 + (0.584S_0 - 1.633S_1)\cos(2\phi) + (-0.750S_2 + 1.328S_3)\sin(2\phi) \tag{7.10}$$

and

$$I(\phi) = 1.747S_0 - 0.625S_1 + (0.584S_0 - 1.633S_1)\cos(2\phi) + 1.525S_3\sin(2\phi). \tag{7.11}$$

The fitting these equations to the experimental data determines S_0 and S_1 uniquely. However, S_2 and S_3 have ambiguities, although the coefficient for $\sin(2\phi)$ can be determined. Table 7.2 suggests that the selected harmonic by the TDCM has higher DOP than ca. 0.9. Therefore, DOP is here assumed to be 0.90 and $\overrightarrow{S}$ was determined, although DOP might be changed when the HH is generated by the laser field synthesized by elliptically polarized lights. The fitting results to (7.10) and (7.11) are shown by the solid lines in Fig. 7.6b. Two fitting results are almost overlapped. $\overrightarrow{S} = (1.00, 0.31, 0.73, 0.43)$ for $\Delta_G = 329°$ and $\overrightarrow{S} = (1.00, 0.31, 0.83, 0.17)$ for $\Delta_G = 315°$ are obtained. The corresponding Stokes vectors after the TDCM are $\mathbf{M}_G\mathbf{M}_G\overrightarrow{S} = (1.00, -0.05, -0.02, 0.89)$ with $\varepsilon = 0.94$ and $\mathbf{M}_G\mathbf{M}_G\overrightarrow{S} = (1.00, -005, -0.18, 0.87)$ with $\varepsilon = 0.80$. The latter case gives the lowest ellipticity under the conditions given in Table 7.2. Therefore, it is confirmed that the diffracted single-order 17th harmonic has an ellipticity better than 0.80. This ellipticity is applicable to the measurement of the photoelectron angular distribution [58] and of magnetic imaging [46]. The compensation of the ellipticity is shown by the shift of $\overrightarrow{S}$ denoted by the sphere (●) before the TDCM to the square (■) after the TDCM on the Poincare sphere in Fig. 7.7.

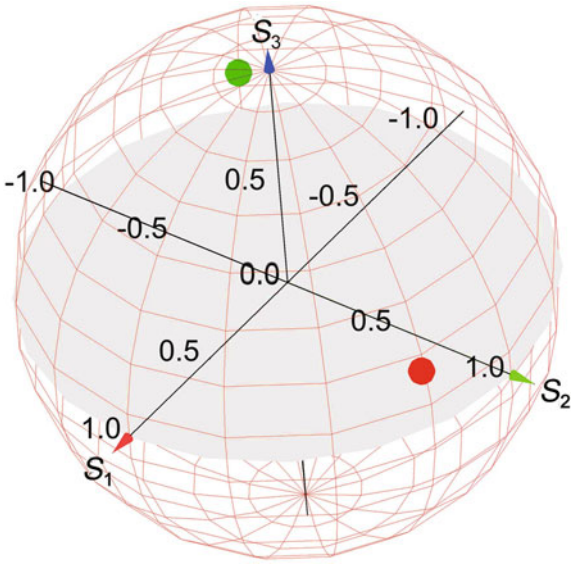

Fig. 7.7 Polarization states on the Poincare sphere. The sphere (●) and square (■) show the Stokes vectors of the 17th harmonic, generated elliptically polarized laser field, before and after the TDCM, respectively

7.3 Summary

In this work, the polarizations of the monochromatized 16th and 17th harmonics of a Ti:sapphire laser by the TDCM were characterized for the development of ultrashort CP EUV light source. It was found that the circular polarization was distorted by the diffraction on the toroidal gratings. However, the diffraction on the grating increases DOP. The compensation of the ellipticity by manipulating the driving laser field was demonstrated for the first time. Here, we assumed DOP = 0.9 in reference to the case driven by CP driving lasers. The single-order CP HH pulses selected by the TDCM will be a versatile light source for the investigation of magnetism and chirality.

In this article, we presented two topics related with molecular chirality. The first topic is the chiral responses of limonene molecules in HHG. We are interested in the nonlinear responses of other chiral molecules. The chirality in the electronic states of a chiral molecules should be related with HHG. We will investigate other chiral molecules. In the second topic, we are interested in the application of the CP HH light source to photoelectron spectroscopy of chiral molecules.

Acknowledgements MEXT Q-LEAP (JPMXS0118068681); JST CREST (JPMJCR15N1); KAKENHI (19H01814).

References

1. R. Cireasa, A.E. Boguslavskiy, B. Pons, M.C.H. Wong, D. Descamps, S. Petit, H. Ruf, N. Thiré, A. Ferré, J. Suarez et al., Nat. Phys. **11**, 654 (2015)
2. D. Baykusheva, H.J. Wörner, Phys. Rev. X **8**, 031060 (2018)
3. D. Baykusheva, D. Zindel, V. Svoboda, E. Bommeli, M. Ochsner, A. Tehlar, H.J. Wörner, Proc. Natl. Acad. Sci. USA **116**, 23923 (2019)
4. F. Krausz, M. Ivanov, Rev. Mod. Phys. **81**, 163 (2009)
5. P.B. Corkum, Phys. Rev. Lett. **71**, 1994 (1993)
6. B. Vodungbo, A.B. Sardinha, J. Gautier, G. Lambert, C. Valentin, M. Lozano, G. Iaquaniello, F. Delmotte, S. Sebban, J. Lüning et al., Opt. Express **19**, 4346 (2011)
7. A. McPherson, G. Gibson, H. Iara, H. Johann, T.S. Luk, I.A. McIntyre, K. Boyer, C.K. Rodes, J. Opt. Soc. Am. B **4**, 595 (1987)
8. M. Ferray, A. L'Huillier, X.F. Li, L.A. Lompre, G. Mainfray, C. Manus, J. Phys. B: At. Mol. Opt. Phys. **21**, L31 (1988)
9. M. Hentschel, R. Kienberger, C. Spielmann, G.A. Reider, N. Milosevic, T. Brabec, P. Corkum, U. Heinzmann, M. Drescher, F. Krausz, Nature **414**, 509 (2001)
10. T. Sekikawa, A. Kosuge, T. Kanai, S. Watanabe, Nature **432**, 605 (2004)
11. Y. Nabekawa, T. Shimizu, T. Okino, K. Furusawa, H. Hasegawa, K. Yamanouchi, K. Midorikawa, Phys. Rev. Lett. **97**, 153904 (2006)
12. K. Zhao, Q. Zhang, M. Chini, Y. Wu, X. Wang, Z. Chang, Opt. Lett. **37**, 3891 (2012)
13. T. Gaumnitz, A. Jain, Y. Pertot, M. Huppert, I. Jordan, F. Ardana-Lamas, H.J. Wörner, Opt. Express **25**, 27506 (2017)
14. Y. Harada, E. Haraguchi, K. Kaneshima, T. Sekikawa, Phys. Rev. A **98**, 021401(R) (2018)
15. K. Ito, E. Haraguchi, K. Kaneshima, T. Sekikawa, Opt. Express **27**, 38735 (2019)
16. P. Fischer, F. Hache, Chirality **17**, 421 (2005)

17. B. Ritchie, Phys. Rev. A **13**, 1411 (1976)
18. N. Böwering, T. Lischke, B. Schmidtke, N. Müller, T. Khalil, U. Heinzmann, Phys. Rev. Lett. **86**, 1187 (2001)
19. T. Lischke, N. Böwering, B. Schmidtke, N. Müller, T. Khalil, and U. Heinzmann, Phys. Rev. A **70**, 022507 (2004).
20. M.H.M. Janssen, I. Powis, Phys. Chem. Chem. Phys. **16**, 856 (2014)
21. D.B. Milošević, W. Becker, R. Kopold, Phys. Rev. A **61**, 063403 (2000)
22. A. Fleischer, P. Sidorenko, O. Cohen, Opt. Lett. **38**, 223 (2013)
23. A. Fleischer, O. Kfir, T. Diskin, P. Sidorenko, O. Cohen, Nat. Photon. **8**, 543 (2014)
24. L. Medišauskas, J. Wragg, H.v.d. Hart, M.Y. Ivanov, Phys. Rev. Lett. **115**, 153001 (2015)
25. O. Kfir, P. Grychtol, E. Turgut, R. Knut, D. Zusin, D. Popmintchev, T. Popmintchev, H. Nembach, J.M. Shaw, A. Fleischer et al., Nat. Photon. **9**, 99 (2015)
26. T. Fan, P. Grychtol, R. Knut, C. Hernández-García, D.D. Hickstein, D. Zusin, C. Gentry, F.J. Dollar, C.A. Mancuso, C.W. Hogle et al., Proc. Natl. Acad. Sci. USA **112**, 14206 (2015)
27. D. Baykusheva, M.S. Ahsan, N. Lin, H.J. Wörner, Phys. Rev. Lett. **116**, 123001 (2016)
28. D. Wang, X. Zhu, L. L. Xi Liu, X. Zhang, P. Lan, P. Lu, Opt. Express **25**, 23502 (2017).
29. D. Baykusheva, S. Brennecke, M. Lein, H.J. Wörner, Phys. Rev. Lett. **119**, 203201 (2017)
30. Á. Jiménez-Galán, N. Zhavoronkov, M. Schloz, F. Morales, M. Ivanov, Opt. Express **25**, 22880 (2017)
31. E.O. Hulburt, Astrophys. J. **54**, 116 (1921)
32. M. Lewenstein, P. Balcou, M.Y. Ivanov, A. L'Huillier, P.B. Corkum, Phys. Rev. A **49**, 2117 (1994)
33. O. Smirnova, Y. Mairesse, S. Patchkovskii, J. Phys. B: At. Mol. Opt. Phys. **48**, 234005 (2015)
34. O. Kfir, E. Bordo, G.I. Haham, O. Lahav, A. Fleischer, O. Cohen, Appl. Phys. Lett. **108**, 211106 (2016)
35. O. Kfir, P. Grychtol, E. Turgut, R. Knut, D. Zusin, A. Fleischer, E. Bordo, T. Fan, D. Popmintchev, T. Popmintchev, J. Phys. B: At. Mol. Opt. Phys. **49**, 123501 (2016)
36. E.S. Toma, P. Antoine, A.d. Bohan, H.G. Muller, J. Phys. B: At. Mol. Opt. Phys. **32**, 5843 (1999)
37. P. Brint, E. Meshulam, A. Gedanken, Chem. Phys. Lett. **109**, 383 (1984)
38. M.M.R. Fanood, M.H.M. Janssen, I. Powis, J. Chem. Phys. **145**, 124320 (2016)
39. M. Carnell, S.D. Peyerimhoff, A. Breest, K.H. Gödderz, P. Ochmann, J. Hormes, Chem. Phys. Lett. **180**, 477 (1991)
40. F. Pulm, J. Schramm, J. Hormes, S. Grimme, S.D. Peyerimhoff, Chem. Phys. **224**, 143 (1997)
41. M.F. Rodrigues, M.G. Bernardo-Gil, J. Chem. Eng. Data **40**, 1193 (1995)
42. T. Adachi, K. Kondo, S. Watanabe, Appl. Phys. B **55**, 323 (1992)
43. D.D. Hickstein, F.J. Dollar, P. Grychtol, J.L. Ellis, R. Knut, C. Hernández-García, D. Zusin, C. Gentry, J.M. Shaw, T. Fan et al., Nat. Photon. **9**, 743 (2015)
44. P.-C. Huang, C. Hernández-García, J.-T. Huang, P.-Y. Huang, C.-H. Lu, L. Rego, D.D. Hickstein, J.L. Ellis, A. Jaron-Becker, A. Becker et al., Nat. Photon. **12**, 349 (2018)
45. D. Azoury, O. Kneller, M. Krüger, B.D. Bruner, O. Cohen, Y. Mairesse, N. Dudovich, Nat. Photon. **13**, 198 (2019)
46. O. Kfir, S. Zayko, C. Nolte, M. Sivis, M. Möller, B. Hebler, S.S.P.K. Arekapudi, D. Steil, S. Schäfer, M. Albrecht et al., Sci. Adv. **3**, eaao4641 (2017)
47. L. Poletto, P. Villoresi, E. Benedetti, F. Ferrari, S. Stagira, G. Sansone, M. Nisoli, Opt. Lett. **32**, 2897 (2007)
48. M. Ito, Y. Kataoka, T. Okamoto, M. Yamashita, T. Sekikawa, Opt. Express **18**, 6071 (2010)
49. H. Igarashi, A. Makida, M. Ito, T. Sekikawa, Opt. Express **20**, 3725 (2012)
50. A. Makida, H. Igarashi, T. Fujiwara, T. Sekikawa, Y. Harabuchi, T. Taketsugu, J. Phys. Chem. Lett. **5**, 1760 (2014)
51. R. Iikubo, T. Fujiwara, T. Sekikawa, Y. Harabuchi, S. Satoh, T. Taketsugu, Y. Kayanuma, J. Phys. Chem. Lett. **6**, 2463 (2015)
52. R. Iikubo, T. Sekikawa, Y. Harabuchi, T. Taketsugu, Faraday Discuss. **194**, 147 (2016)

53. T. Koide, T. Shidara, M. Yuri, N. Kandaka, K. Yamaguchi, H. Fukutani, Nucl. Instrum. Methods Phys. Res. **308**, 635 (1991)
54. W.R. Hunter, in *Vacuum Ultraviolet Spectroscopy I*, ed. by J.A. Samson, D.L. Ederer (Academic Press, San Diego, 1998)
55. W.S.M. Werner, K. Glantschnig, C. Ambrosch-Draxl, J. Phys. Chem. Ref. Data **38**, 1013 (2009)
56. R.M.A. Azzam, J. Opt. Soc. Am. A **33**, 1396 (2016)
57. D. Maystre, *Edited by E* (Université d'Aix-Marseille, CNRS, Popov (Institut Fresnel, 2014).
58. L. Barreau, K. Veyrinas, V. Gruson, S.J. Weber, T. Auguste, J.-F. Hergott, F. Lepetit, B. Carré, J.-C. Houver, D. Dowek et al., Nat. Commun. **9**, 4727 (2018)

Chapter 8
The Role of the Ponderomotive Force in High Field Experiments

Luis Roso, José Antonio Pérez-Hernández, Roberto Lera, and Robert Fedosejevs

Abstract Petawatt lasers are a new tool to understand many basic properties of matter (solids, plasmas, molecules, atoms, and nuclei) in extreme conditions. Radiation reaction and fundamental non-linear QED problems can also be studied with high intensity lasers, as well as many other relevant problems. In all cases we focus the laser to concentrate its energy over a small volume, therefore a huge intensity gradient appears, and it generates a force -the ponderomotive force- that drives the ionized electrons. This driving can be dominant in some situations. A conventional focus has a convex intensity pattern and ponderomotive force expels the electrons out of the focal region. With optimal use of TEM 01 and 10 modes it is possible to generate concave beams that trap and drag such electrons. Such possibilities are reviewed here, particularly for the strongly relativistic intensities available with existing ultraintense lasers.

8.1 Introduction

Origins of the ponderomotive force

A charged particle inside an oscillating electric field experiences a quiver motion and therefore has an average energy larger than zero, even if its motion is perfectly oscillatory and the average displacement is zero. Because the charged particle has an energy larger inside the field than outside the field, there is a force that tends to move it out of the high field region. The potential responsible for this force is known as the ponderomotive potential.

L. Roso (✉) · J. A. Pérez-Hernández · R. Lera
Center for Pulsed Lasers, CLPU, 37185 Villamayor, Salamanca, Spain
e-mail: roso@clpu.es

L. Roso
Applied Physics Department, Universidad de Salamanca, 37008 Salamanca, Spain

R. Fedosejevs
Electrical and Computer Engineering, University of Alberta, Edmonton, AB T6G 2V4, Canada

K. Yamanouchi et al. (eds.), *Progress in Ultrafast Intense Laser Science XVI*,
Topics in Applied Physics 141, https://doi.org/10.1007/978-3-030-75089-3_8

This idea was first developed, well before the arrival of lasers, for radiofrequency waves. The first relativistic description was given in 1966 by Kibble [1] under a very appealing name: *mutual refraction of electrons and photons*. Ponderomotive forces were regarded as forces that modify the average trajectory of an accelerated electron crossing a laser field. As the electron enters the laser field its direction is deflected similar to refraction of light. This similarity is very physical and gives a lot of insight to the problem that has been lost in modern literature about this subject. Kibble also studied key features of the standing wave dynamics.

Today's superintense lasers

Since the invention of the CPA technology by Strickland and Mourou [2], ultraintense lasers have increased in performance dramatically. Petawatt (PW), or multi PW, lasers are a reality now [3] and soon the 10 PW barrier will be broken in several facilities around the world. Peak power gives the possibility to focus to extreme intensities, and intensity is the key to induce extreme effects. A focal spot close to diffraction limited quality requires a good optical quality laser pulse, very precise beam transport and a good focusing mirror (typically an off axis parabolic mirror). In order to suppress nonlinear effects, every element after the amplification chain, including the pulse compressor is kept under high vacuum, typically 10^{-6} mbar.

Laser acceleration

Particle accelerators are a fundamental tool in many fields of science and technology. Besides the TeV particle accelerators such as CERN LHC, designed to study the fundamental building blocks of matter, there are many other systems used to advance material science, biology, chemistry, and many more fields. Such accelerators reach up to GeV energies for electrons after many meters, if not kilometers of acceleration. We know today about the potential of ultra-intense lasers for particle acceleration, particularly for electron acceleration, offering the possibility to achieve similar energy per particle as conventional accelerators but in just a fraction of the size. Laser acceleration of electrons uses collective plasma effects to generate, over a very short period of time, enormous field gradients which have proved to be a very efficient tool to accelerate GeV electrons over a short distance (of the order of one or several centimeters) [4–6]. One of the most studied mechanisms is Laser Wakefield Acceleration (LWFA), where the acceleration of particles is generated inside the wake of a high intensity laser pulse as it travels through an underdense plasma medium. The result is a strong longitudinal electric field that couples to the electrons trapped inside this wave induced by the driving laser, accelerating those electrons over the distance of the plasma channel. Since there is no breakdown limit in plasma, the resulting accelerating gradient is huge [7]. Applications of this mechanism include the generation of ultrashort coherent x-ray beams produced by betatron radiation of the accelerated oscillating electrons, which have potential to be used in a wide range of fields [8].

However, plasma effects are quite nonlinear and subject to intrinsic instabilities and for that reason there is renewed interest in direct acceleration of electrons by a laser field as a potential candidate for laser electron acceleration. The idea of such

direct laser acceleration (we call it direct because it does not need the presence of collective plasma effects) has been attracting a lot of interest during recent decades [9]. In laser acceleration, the electron enters and leaves the beam and the goal is to find the best configuration of fields that provides acceleration.

The aim of this work is to show the effects of the ponderomotive force when a gas is ionized during the turn-on and electrons are driven by the focused beam. Released electrons will be subject to an inhomogeneous electromagnetic field and therefore the ponderomotive force will be fundamental for their dynamics. We are not going to consider situations where electrons are injected at relativistic speeds. Instead we will study something related but conceptually different. We consider electrons ionized during the turn-on of the pulse, so they are born inside the field and we want to see how they move. Our purpose is not to study their final speed after leaving the intense pulse. We are going to study their dynamics while in the field and describe common experimental situations seen from a different viewpoint. We will describe several common experimental situations where such ponderomotive force is present but maybe has not been not properly taken into account, as well as other less considered situations where the ponderomotive force presents interesting features. In most cases the electron cloud will explode, but in other cases part of the cloud can be redirected to one side or trapped inside the field.

Experimental situation

A typical high-intensity experiment is performed in high vacuum. The pulse has to be focused to a tiny spot (microns) in order to reach ultrahigh intensities and interact with a target, that can be a solid, liquid or a gas. Gas targets, which take the form of gas jets, gas cells or capillaries, are of special interest for the sake of this discussion since they are employed in underdense plasma physics experiments such as coherent x-ray sources or LWFA. Gas jets are usually delivered through a pulsed nozzle, which is close to the focal spot, and the gas is released a few milliseconds before the arrival of the pulse. As a consequence, the laser pulse hits a diluted neutral gas and atoms or molecules are ionized in the leading edge of the pulse (by barrier suppression), so electrons are released well before its peak. In this regime pondermotive force is fundamental because it causes electrons to move towards weaker field regions therefore deflecting them out of the ultrahigh intensity region. This force avoids to some extent extreme effects (extreme acceleration, extreme radiation, etc.). We will analyze, based on numerical simulations of the relativistic driven independent electron trajectories, how to control and take profit of this ponderomotive repulsion.

Since the model neglects collective effects, it will be valid just for dilute targets. For solid targets, usually few micron thick foils, liquid and overdense plasma experiments, the study of the ponderomotive force needs to include also the fields generated at the target, and this is outside the scope of the present text.

A third family of targets are the electron injectors. Electrons, pre-accelerated using a conventional accelerator cross the laser field in order to get, if possible, an energy boost. Although this has been a quite common experimental scenario, as we said,

we are not going to consider it. In this chapter we will refer only to independent electrons appearing from atoms or molecules after being suddenly ionized by barrier suppression.

8.2 Relativistic Modelling of Laser Driven Electrons

One of the reasons for the interest in the electron motion is its apparent simplicity: interaction of a charged particle with an electromagnetic field in vacuum. At low intensities, the classical motion of the electron is governed by the laser electric field. Beyond 10^{18} W/cm**²**, however, the laser field is so strong that dynamics becomes relativistic, and the coupling to the laser magnetic field is equally important for the motion description.

Motion is described by the Lorentz force, $\overrightarrow{F} = -e\ (\overrightarrow{E} + \vec{v} \times \overrightarrow{B}/c)$, where $\vec{v}$ indicates the speed of the electron and c is the speed of light. $\overrightarrow{E}$ and $\overrightarrow{B}$ are the electric and magnetic fields of the laser beam. We consider that the electron charge is -e (e being positive). Then the relativistic equation of motion is

$$\frac{d\overrightarrow{p}}{dt} = \overrightarrow{F} = -e\left(\overrightarrow{E} + \frac{\overrightarrow{v}}{c} \times \overrightarrow{B}\right) \tag{8.1}$$

where $\vec{p} = m\gamma\vec{v}$, is the momentum and $\gamma^{-1} = \sqrt{1 - v^2/c^2}$ is the well-known relativistic factor. And thus,

$$\frac{d}{dt}(\gamma\overrightarrow{v}) = -\frac{e}{m}\left(\overrightarrow{E} + \frac{\overrightarrow{v}}{c} \times \overrightarrow{B}\right) \tag{8.2}$$

The relativistic factor is the origin of interesting nonlinear effects, that will dominant as intensity increases.

The electron is a spin ½ fermion, so for high intensities there must be a coupling between the laser magnetic field and the spin. Fortunately, the free electron Dirac equation can be worked out analytically for the case of plane propagating pulses, regardless of the intensity [10]. When working with such huge electromagnetic fields it is reasonable to consider the coupling of the magnetic field with the electron spin. Nevertheless, it has been shown [11] that such coupling is extraordinarily small and can be neglected without introducing any relevant source of error. This justifies the use of a classical (non-quantum) description for the driven electron, and thus the validity of the motion at high intensities.

Probably the most limiting factor for the validity of the forthcoming calculations at ultra-high intensities is radiation reaction [12]. The onset for radiation reaction relevant effects, with a near infrared laser, occurs around 10^{23} W/cm^2. We are going to consider relativistic intensities always below that limit.

Therefore, a description based in the relativistic dynamics will be employed. In components, the Lorentz equation becomes:

$$\begin{aligned}
\frac{d}{dt}(\gamma\, v_x) &= -\frac{e}{m}\left(E_x + \frac{1}{c}\left(v_y\, B_z - v_z\, B_y\right)\right)\\
\frac{d}{dt}\left(\gamma\, v_y\right) &= -\frac{e}{m}\left(E_y + \frac{1}{c}\left(v_z\, B_x - v_x\, B_z\right)\right)\\
\frac{d}{dt}(\gamma\, v_z) &= -\frac{e}{m}\left(E_z + \frac{1}{c}\left(v_x\, B_y - v_y\, B_x\right)\right)
\end{aligned} \tag{8.3}$$

Plane wave analytical solution

For the particular case of a propagating plane wave, monochromatic or pulse, Sarachik and Schappert developed a very elegant and useful exact solution [13] that considers a propagating plane wave pulse of arbitrary shape. Their only condition is that the pulse profile function depends only on a variable $\eta = \vec{s} \cdot \vec{r} - c\,t$ where $\vec{s}$ is a unitary vector indicating the propagation direction. For simplicity we will define z as the propagation direction, and thus $\eta = z - c\,t$ gives the pulse shape. For an electron initially at rest, its energy is given by

$$E(\eta) = mc^2\left[1 + \frac{e^2 A^2(\eta) f^2(\eta)}{2m^2c^4}\right] \tag{8.4}$$

$\vec{A}(\eta)\, f(\eta)$ indicates the vector potential, where $f(\eta)$ is a normalized pulse envelope ($f = 1$ at its maximum) that accounts for the pulse profile of the $\vec{A}$ field. We consider that $\vec{A}$ is oscillating at a laser frequency ω and the pulse envelope function gives the bandwidth. Sarachik and Schappert showed also that the momentum is given by

$$\vec{p}(\eta) = -\frac{e}{c}\,\vec{A}(\eta)\, f(\eta) + \vec{s}\,\frac{e^2 A^2(\eta) f^2(\eta)}{2mc^3} \tag{8.5}$$

This expression is very relevant because it shows that the momentum has a transverse component (in the direction of polarization of the vector potential $\vec{A}$) and a longitudinal component (in the direction of the propagation $\vec{s}$). The electric field is related to the vector potential by the well-known relation $\vec{E} = -\left(1/c\right)\,\partial\vec{A}\Big/\partial\, t$. For a plane wave pulse therefore, the momentum has an exact analytical solution (fully relativistic) indicating its two components, one along the vector potential and the other along the propagation direction (z). The two components lie in the plane defined by $\vec{E}$ and $\vec{s}$. Their relation defines a characteristic angle that indicates the averaged motion direction of the electrons in the field. This motion is the first clear expression due to the ponderomotive force. The electron is forced to move forward due to this effect. Of course, it can't move faster than light and eventually ends behind the pulse.

For a linearly polarized plane wave laser field,

$$E_x = E_0\, f(z-ct)\cos(k(z-ct))$$
$$B_y = B_0\, f(z-ct)\cos(k(z-ct)) \tag{8.6}$$

the situation is shown schematically in Fig. 8.1, This motion is oscillatory and at the end the electron will return to rest (provided that initially it was at rest). The oscillation has some typical features. It has harmonic frequencies based on the fact that E_x accelerates the electron along x, and the corresponding velocity v_x couples with the B_y magnetic field giving a v_z speed. From E_x and B_y it is impossible to get acceleration along the direction of the magnetic field if initially the speed is zero, therefore the trajectory lies in the xz plane. The longitudinal component of the velocity can be quite large and therefore the Doppler shift is very relevant. This can be indirectly seen in Fig. 8.1 because the oscillation is much larger than the initial laser wavelength, marked as λ in the figure. Also, this schematic plot shows a very peculiar characteristic, the cusps. At those cusps the electric field gets its maximum value and the electron experiences the maximum acceleration. Such figure seen from a reference frame moving with the average speed of the electron presents a characteristic figure-of-eight pattern as studied in Sarachik and Shappert paper. More relevant is the fact the v_xB_y term couples two terms oscillating at the laser frequency, so it is going to generate a second harmonic and as a consequence many more harmonics. The oscillatory motion in a laser field becomes anharmonic [14] The pattern of frequencies generated by such relativistically driven electron is quite relevant for a number of applications [15, 16].

Computed electron trajectories, for a propagating plane wave laser field linearly polarized along the x-axis, are shown in Fig. 8.2. This is a numerical simulation but is totally in the region of validity of the analytical expressions of Sarachik and Shappert, and fits them well. The pulse envelope is $f(\eta) = \exp(-(\eta/c\,\tau)^2)$, with a time duration τ equal to 10 laser cycles. The figure corresponds therefore to a plane

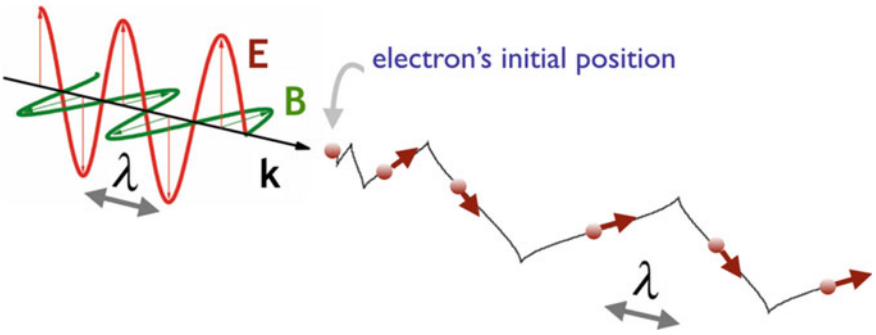

Fig. 8.1 Motion of an electron driven by a plane wave laser. Although this is just a scheme, it is quite realistic for an intensity of 2 10^{19} W/cm^2 and 800 nm wavelength

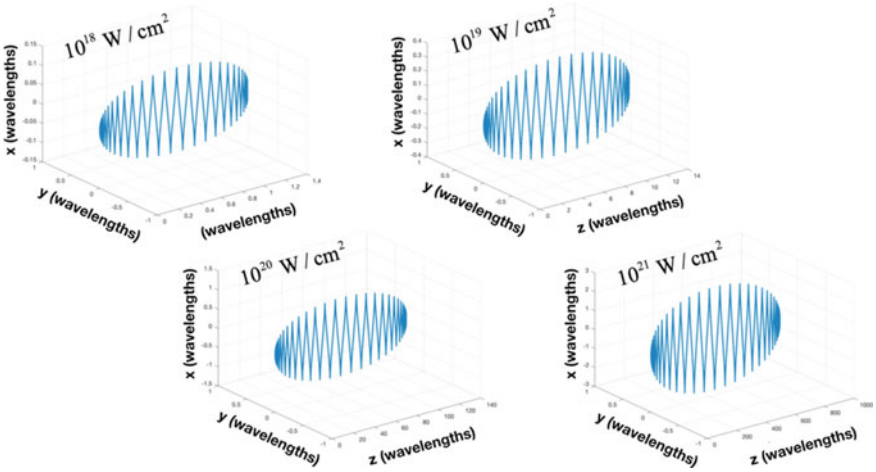

Fig. 8.2 Trajectories of a driven electron initially at rest at the origin of coordinates, in the situation of applicability of the Sarachik-Schappert analytical model. The central wavelength is 800 nm. It corresponds to a plane wave with the pulse envelope $f(\eta) = \exp(-(\eta/c\,\tau)^2)$, and τ equal to 10 laser cycles. The four trajectories correspond to different intensities, all in the relativistic domain. The electrical field is linearly polarized (only E_x component). Although this plot is a numerical computation, it agrees perfectly with their analytical result for plane waves

propagating wave, and four different peak fields are shown, with intensities from 10^{18} W/cm^2, that is the onset of the relativistic effects, to a strongly relativistic case10^{21} W/cm^2. Observe that the four plots look quite similar and only the spatial scales change. This is so because the number of oscillations corresponds to the number of laser periods. In all cases the forward drift (due to the forward ponderomotive force) is evident but its magnitude is quite different. In this case (plane wave) electrons are forced forward, but always at a speed less than c, and sooner or later have to cross the maximum of the field and slow down until the next maximum (or minimum) of the field. This effect is well known and has been described as electron slippage [17].

Initial conditions and ionization dynamics

The aim of this contribution is to show the relevance of the ponderomotive potential in realistic experimental situations of atoms or molecules interacting with intense laser pulses. If one is using an electron beam, then pre-accelerated electrons are there from the very beginning. However, in the atomic or molecular case we start with neutrals. Electrons do not feel the laser field until they are ionized.

In most of the calculations found in the literature, electrons are considered free from the very beginning, so they feel the turn-on of the pulse and they are subject to smooth dynamics that can bring considerations similar to the ones that originate the Lawson Woodward theorem [18, 19]. In the real situation we need a model for ionization, and this would depend on the atomic or molecular species. In the context of relativistic intensities, we can consider that electrons are released when the field

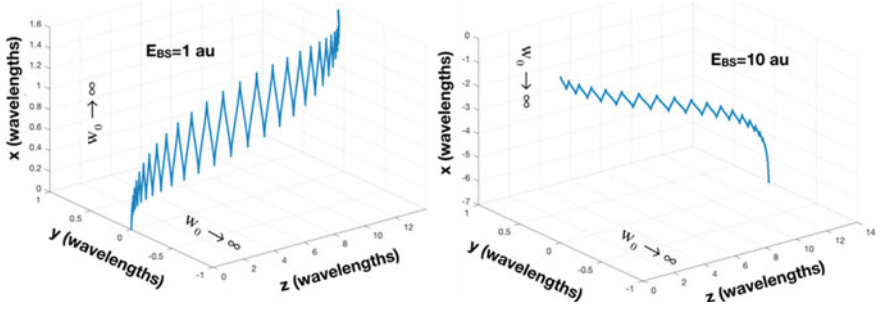

Fig. 8.3 Trajectories for a plane wave pulse for the same conditions as in the previous figure (plane wave 10 cycles long pulse) with intensity 10^{19} W/cm^2. While in the previous figure electron was free from the very beginning, now the electron is released suddenly when the laser field arrives to a given value, E_{BS}, to ionize by barrier suppression. The value $E_{BS} = 1$ a.u. (3.5 10^{16} W/cm^2). Observe the drift induced. This drift is much larger if the electron is released at higher fields as can be the case of inner electrons $E_{BS} = 10$ a.u. (3.5 10^{18} W/cm^2)

amplitude reaches the barrier suppression regime. Well above this barrier suppression field, in the region 10^{14} to 10^{15} W/cm^2 for valence electrons of most atoms, electrons are hundred percent ionized almost instantaneously. This simple model considers that electrons are frozen (inside the atoms or molecules) until the field reaches a given value high enough to fully ionize them. In other words, we wait until the laser field reaches a convenient value (we call this E_{BS}, from barrier suppression) and then the electron is released inside the field. This is not a minor point. To prove that we show in Fig. 8.3 the influence of E_{BS} on the electron's drift. This figure shows two individual trajectories for a plane wave pulse for the same conditions as Fig. 8.2 (10 cycles long pulse) with intensity 10^{19} W/cm^2. While in Fig. 8.2 the electron is free from the very beginning, in Fig. 8.3 the electron is released suddenly when the laser field arrives to a given value, E_{BS}, to ionize by barrier suppression. The value $E_{BS} = 1$ a.u., corresponding to an intensity 3.5 10^{16} W/cm^2 can be a realistic choice for complete ionization. Observe the drift induced, this drift is much larger if the electron is released at higher fields as can be the case of inner electrons, that can be simulated introducing a larger value of the barrier suppresion field, for example $E_{BS} = 10$ a.u. (3.5 10^{18} W/cm^2). This is quite relevant in the present context because the distribution of the released electrons after the pulse will be influenced by the moment where they appear. Inner shell electrons or second or third ionizations will have different transverse distributions in the end.

8.3 Paraxial Beams Close to Waist

An ultrafast ultraintense laser beam is typically a flat-top with some inhomogeneities that can be as large as 10 percent, in intensity. It is focused generally with an off-axis parabola mirror and generates a focal spot and a transverse distribution of intensity in

the focal plane. However, not all of the laser beam energy is concentrated on the focal spot due to the profile of the beam or spatial and temporal aberrations, and a fraction of it is lost. If the beam profile were an ideal flat top, the profile at the focal plane would be the well-known Airy pattern due to diffraction (Fraunhofer diffraction) by a circular aperture. Realistic modelling of the focus is now possible but depends on many parameters, a number of them unknown.

A widely used first approximation that represents a reasonable compromise between realistic description and simple mathematical model are paraxial beams. When focusing the pulse with a long focal, such an approximation is reasonable. Harmonic paraxial beams are solutions of the Helmholtz equation, k being the harmonic wavenumber, $\partial^2 \vec{E} \Big/ \partial\, x^2 + \partial^2 \vec{E} \Big/ \partial\, y^2 = -ik\partial \vec{E} \Big/ \partial\, z$. The problem is that the three components are not independent, they must obey the condition $\vec{\nabla} \cdot \vec{E} = 0$, this condition is fundamental to understand ponderomotive potentials, as we will show. Pulsed paraxial beams can be described with the introduction of a pulse function $f(\vec{r}, t)$, with a gaussian time dependence $\exp(-(t/c\tau)^2)$, τ being the pulse duration, as indicated above**.** Such pulse description is reasonable for pulses of 30 fs (for Ti:Sapphire) or longer. For a few cycles pulses some corrections have to be added. Other $f(\vec{r}, t)$ functions can be used that give a realistic description ($\sin^2$, sech, and more), but we are going to consider only the gaussian pulse shape. In fact we are going to consider only Ti:Sapphire 800 nm laser pulses, with a realistic pulse duration, $\tau = 10\, cycles$. This gives a reasonable descriptition of most of the existing high-field PW or multi-PW lasers around the world, including the Salamanca PW laser.

Hermite-Gauss or Laguerre–Gauss modes (depending on the symmetry we want to explicitly consider), give paraxial solutions of interest. These modes are widely studied in the literature and they are characterized by a waist w_0 and a Rayleigh length z_R, related by $z_R = \pi\, w_0/\lambda$. Their value depends on the F number of the focusing system. If we are close to focus, i.e. if the distance from focus is smaller than the Rayleigh length, wave-fronts are almost constant z planes and it is possible to describe the field in the form,

$$E_x = E_0 \exp\left(-\rho^2 \Big/ w_0^2\right)\, f(z - ct) \cos(k(z - c\, t)) \tag{8.7}$$

Paraxial gaussian beams give very nice and useful descriptions of the fields before and after the waist, including the corresponding spherically converging or diverging wavefront. The generalization to such beams is straight forward, but in the present notes we are going to consider that all wavefronts are planes perpendicular to z. This is reasonable only if we are close to the beam waist, the region where most experiments are performed. We introduce the name CTW (Close-to-Waist) approximation, to refer to this plane wavefront description that is valid just at a distance from the waist much smaller that the Rayleigh length. The big simplifying advantage to the CTW approximation is the fact that we have just a propagating beam. Propagation depends again only on the $\eta = z - c\, t$ variable and the comparison with the infinite plane analytical solutions is more evident. The CTW approximation represents a

nice compromise between a realistic model and a model that is simple enough to get compact expressions of the low order modes. Being close to the waist the Gouy phase has been neglected, however it can be included when a careful consideration of the phase velocity is needed because Gouy phase is a z-dependent phase to be added to the propagation. In the following discussion we neglect the Gouy phase and therefore we neglect the phase slippage it generates.

Scalar modes

The lowest order mode, the gaussian mode, is given by the scalar function,

$$u_{00}(\vec{r}) = u_0 \exp\left(-\rho^2/w_0^2\right) f(z-ct) \cos(kz-\omega t) \tag{8.8}$$

As is well known, the dependence of the next two modes is

$$\begin{aligned} u_{10}(\vec{r}) &= u_0 \frac{x}{w_0} \exp\left(-\rho^2/w_0^2\right) f(z-ct) \cos(kz-\omega t) \\ u_{01}(\vec{r}) &= u_0 \frac{y}{w_0} \exp\left(-\rho^2/w_0^2\right) f(z-ct) \cos(kz-\omega t) \end{aligned} \tag{8.9}$$

To describe more complicated transverse profiles, it is always possible to consider higher order Hermite-Gauss, or Laguerre–Gauss modes, depending of the transverse symmetry of the problem (circular or squared). It is also possible to consider geometries where the waist is not circular, but larger in one dimension that other. In that case one needs to replace the ρ^2/w_0^2 term in the exponential giving the transverse profile by $x^2/w_{0x}^2 + y^2/w_{0y}^2$, w_{0x} being the waist in the x direction and w_{0y} in the y direction (Fig. 8.4).

Clearly, the u_{10} scalar function has a node along the yz plane, while the u_{01} scalar function has a node along the xz plane. Adding these two modes in phase one gets a node plane at 45 degrees. However, adding them $\pi/2$ out of phase generates the simplest beams with one unit of OAM (Orbital Angular Momentum), i.e.

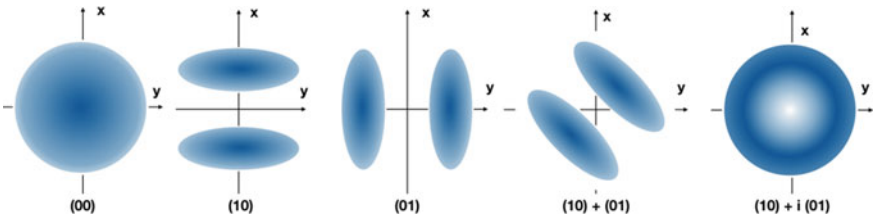

Fig. 8.4 Schematic representation of the amplitude distribution on the transverse plane of the different scalar modes. (00) indicates the u_{00} scalar function; (10) indicates the u_{10} scalar function; (01) indicates the u_{01} scalar function; (10) + (01) is the sum in phase of the two previous ones; and (10) + i(01) indicates the sum with a $\pi/2$ dephasing, that corresponds to u_1, the simplest mode with non-vanishing Orbital Angular Momentum

$$u_1(\vec{r}) = u_0 \ \exp\left(-\rho^2 / w_0^2\right) \ f(z-ct) \ \left(\frac{x}{w_0}\cos(kz-\omega t) + \frac{y}{w_0}\sin(kz-\omega t)\right) \tag{8.10}$$

Vector transverse modes

Those three basic scalar modes, (00), (01) and (10), are enough to get a clear description of the relativistic ponderomotive force. To calculate the trajectory of the electron it is necessary to take a full vector description of the fields, taking also into account the longitudinal fields to fulfill the $\vec{\nabla}\cdot\vec{E} = \vec{\nabla}\cdot\vec{B} = 0$ transversality conditions both for electric and magnetic fields.

For the rest of this chapter we are going to study five of such vectorial modes, that represent modes with internal structure able to generate different dynamics. Most of the ponderomotive potential relevant features can be obtained using these basic modes and combinations of them with convenient phases and/or delays.

Gas density

In the simulations we consider a dilute neutral gas from which electrons appear. The gas density is assumed to be low enough to not modify the laser propagation indicated in Eqs. (8.8) and (8.9). Ionized electron density is assumed also to be small enough to not affect the propagation. In other words, the refractive index (linear and nonlinear) induced by the neutrals, the ions and the ionized electrons is not relevant to change the fields propagation. In our model, moreover, electrons move independently, without interacting between them.

All this can be realistic for Argon, Nitrogen or other gases at low pressures (from 10^{-2} to 10^{-4} mb) and for slightly higher pressures for the case of Helium. Higher densities would imply B integral effects and collisions and the present model will fails. In the collision dominated regime PIC simulations are needed [20].

8.4 Numerical Results for the Lowest Order Mode

Our purpose is to give the reader some degree of intuition about the ponderomotive force that can be useful for the design of high field experiments where relativistic or ultra-relativistic dynamics is dominant. We will present several mode combinations that induce conceptually different ponderomotive patterns.

We start with the simplest mode, the gaussian (00) mode. Because we are going to introduce different polarizations, we introduce a compact notation, labeling this mode as ($\times$00), where x stands for the polarization (electric field in the xz plane) and 00 indicates the mode. The gaussian mode, linearly polarized along x, can be written as:

$$
\begin{aligned}
E_x &= E_0 \exp\left(-\rho^2/w_0^2\right)\ f(z-ct)\cos(kz-\omega t) \\
E_z &= E_0 \exp\left(-\rho^2/w_0^2\right)\ f(z-ct)\ \ \sin(kz-\omega t)\ \frac{2\,x}{w_0}\,\frac{1}{k w_0} \\
B_y &= B_0 \exp\left(-\rho^2/w_0^2\right)\ f(z-ct)\cos(kz-\omega t) \\
B_z &= B_0 \exp\left(-\rho^2/w_0^2\right)\ f(z-ct)\ \ \sin(kz-\omega t)\ \frac{2\,y}{w_0}\,\frac{1}{k w_0}
\end{aligned}
\tag{8.11}
$$

With $E_y = 0$, and $B_x = 0$. Observe that in the E_z and B_z expressions we neglected the space derivative of the pulse profile function f. This can be reasonable in the context of the rest of the approximations made provided that the pulse is not too short. Observe thus that there are two large components, E_x and B_y, and two small longitudinal components E_z and B_z introduced to keep the transversality in the CTW region. The $1/kw_0$ factor gives a reference for the relative size of the longitudinal field. To be consistent, the error introduced when neglecting the z derivative of the pulse shape function f must be much smaller. Although it is well known, it is always convenient to remember that in spite of its small value (even when $kw_0 << 1$) the longitudinal field is fundamental for a proper description of the ponderomotive dynamics [21].

As is well known, within the CTW approximation, the longitudinal components are in quadrature with the transverse components (in our case, considering just the real fields for simplicity, this means that the phase dependence is $\cos(kz-\omega t)$ for the transverse components and $\sin(kz-\omega t)$ for the longitudinal ones). To understand this, it is convenient to write explicitly the components of the Lorentz equation,

Without transverse fields

$$
\left.
\begin{aligned}
\frac{d(\gamma\, v_x)}{dt} &= -\frac{e}{m}E_x + \frac{e}{mc}v_z\, B_y \\
\frac{d\left(\gamma\, v_y\right)}{dt} &= 0 \\
\frac{d(\gamma\, v_z)}{dt} &= -\frac{e}{mc}v_x\, B_y
\end{aligned}
\right\}
$$

With transverse fields

$$
\left\{
\begin{aligned}
\frac{d(\gamma\, v_x)}{dt} &= -\frac{e}{m}E_x - \frac{e}{mc}v_y\, B_z + \frac{e}{mc}v_z\, B_y \\
\frac{d\left(\gamma\, v_y\right)}{dt} &= +\frac{e}{mc}v_x\, B_z \\
\frac{d(\gamma\, v_z)}{dt} &= -\frac{e}{m}E_z - \frac{e}{mc}v_x\, B_y
\end{aligned}
\right.
\tag{8.12}
$$

We can observe that without the longitudinal fields, and when the electron is initially at rest, the motion is in the xz plane. The ponderomotive displacement along the y axis requires the longitudinal magnetic field.

The best way to show the essence of the ponderomotive force is to consider a gaussian 00 mode. In the next figures we show snapshots of the motion of the barrier suppression ionized electrons driven by such a field mode (Fig. 8.5).

We consider a cloud of 10^4 electrons originally randomly distributed over a transverse region of $\pm\, x_{max}$ by $\pm\, y_{max}$. They are placed in the slab $0 < z < 10\,\lambda$. Using a thicker z slab does not add relevant information and at the same time blurs the results. The transverse size, $2x_{max}$ by $2y_{max}$, is chosen in order to span the whole range of

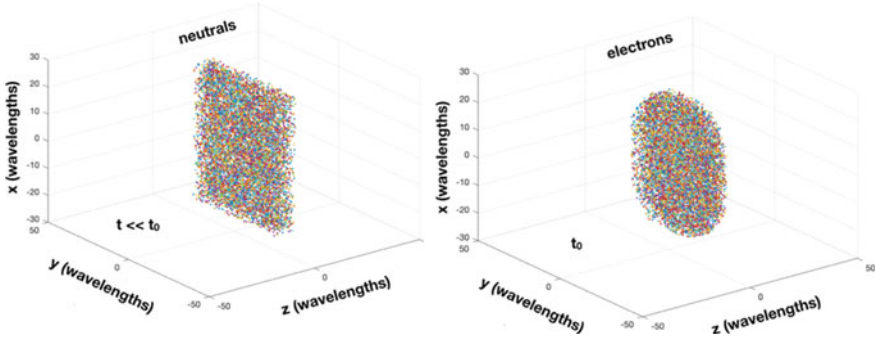

Fig. 8.5 Typical example of the initial cloud of 10^4 points considered in the numerical simulations. Left) Those points represent neutral atoms able to release one electron when the field amplitude reaches a given value, chosen as E = 1 au in the present plot. This is an arbitrary but reasonable value. The profile is a parallelogram of 10 wavelengths in the longitudinal direction (from $z = 0$ to $z = 8\,\mu m$) and enough spreading in the transverse plane to account for all atoms that can be ionized. The initial density of points is uniform. Right) After the arrival of the (×00) pulse ionized electrons appear and start moving. The figure on the right depicts only the ionized electron cloud

transverse positions where the electron can appear by barrier suppression ionization. For a (00) pulse, the maximum transverse radius, $\rho_{\max}$, at which electrons are born, is given by $\rho_{\max} = w_0 \sqrt{\ln\left(E_0 / E_{BS}\right)}$. For other combinations of pulses this may vary. In the simulations we guarantee that the random sampling homogeneously covers the region where electrons can appear (i.e. the region with field higher that E_{BS}).

The number of electron trajectories used in our simulations has nothing to do with the actual gas density in an experiment. The number of computed trajectories has to be large enough to get a visual idea of the electron cloud motion. The gas density can be increased up to the point where collective effects become relevant and this is several orders of magnitude above the density of trajectories considered.

The situation to be described in the following simulations is shown in Fig. 8.6. Some of the mode configurations to be analyzed will have an offset Δ. In the combinations involving the (00) mode, it will be the delayed one. In a real experiment the cloud of atoms from a jet nozzle will be very thick, however we consider that the atoms are localized only in the space between the z = 0, and the z = 8 microns planes. Due to the CTW approximation, the consideration of a thicker electron cloud will be simply a repetition of that. To be sure that the initial dynamics is properly accounted for, we consider that at the starting of the computation we have just neutral atoms. Being precise, we start the computation at a time when the pulse envelope function $E_0 f(z - ct) << E_{BS}$. In order to have a clear reference of the time scale for each of the following plots, we define a time t_0 as the time when the maximum of the first component arrives to z = 0 (i.e. $f(ct_0) = 1$). All figures and discussions will be referred to this time. In the case of an offset Δ (for combinations of the gaussian modes with others) the maximum of the gaussian pulse will arrive to z = 0 at time $t_0 + \Delta/c$. Obviously t_0 has nothing to do with the time where the simulation started

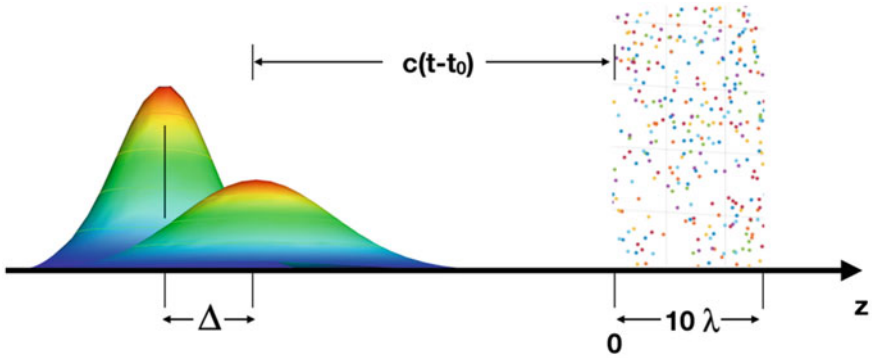

Fig. 8.6 Schematic representation of the initial situation. Randomly distributed neutral atoms (represented as dots) are waiting for the arrival of the pulse in a region 10 lambda thick. When field amplitude arrives to the barrier suppression value, E_{BS}, the atom at that point is ionized, i.e. the electron escapes from the atom/ion and starts moving. Δ is the offset of the (01) and (10), or their combinations. Typically we consider $\Delta = c\,\tau$ or $\Delta = c\,\tau/2$, to get interesting superpositions of intensity. This is just a scheme of the two pulses, of course, in the actual case they will interfere

that, depending on the parameters, particularly on the intensity, can be 20 or mode cycles before.

A simple "well known" case

Just to understand well the transition from plane propagating wave to a real case, we may consider the case of a large waist, 100 wavelengths (80 microns) and an intensity of 10^{19} W/cm^2 ($E_0 = 17$ au). Observe that this may seem a modest intensity however, considering that the waist is quite large this would correspond to about 100 TW of power. Power precisely inside the focal spot, not in other parts of the focal plane. This requires a very good beam quality plus a very high intensity, almost in the limit of today's lasers (Fig. 8.7).

Forward velocity mapping

Depicting electron trajectories, or electron clouds, in space gives direct information on the dynamics but gives an information that is difficult to see in a real experiment. In a number of experiments, it could be possible to measure the signature of the electron trajectories going out of the focal spot driven away by the ponderomotive force by analyzing the angles were electrons are to be found. We computed also the x and y directions, i.e. we plot v_x/v_z and v_y/v_z (v_z being the longitudinal speed), so those plots give the integrated forward pattern of the electron ponderomotive explosion. In principle this could be measured with a scintillator or a radio-chromic plate strategically placed after the focal spot. Although in those cases one would get the integrated pattern, it is also interesting to analyze (but much more difficult to observe) its time evolution because at the beginning, as shown in Fig. 8.8, dynamics is dominated by the $v_x B_y$ term, as in Sarachik-Shappert analytical theory, and the motion is along the electric field polarization. When the v_x velocity combines with

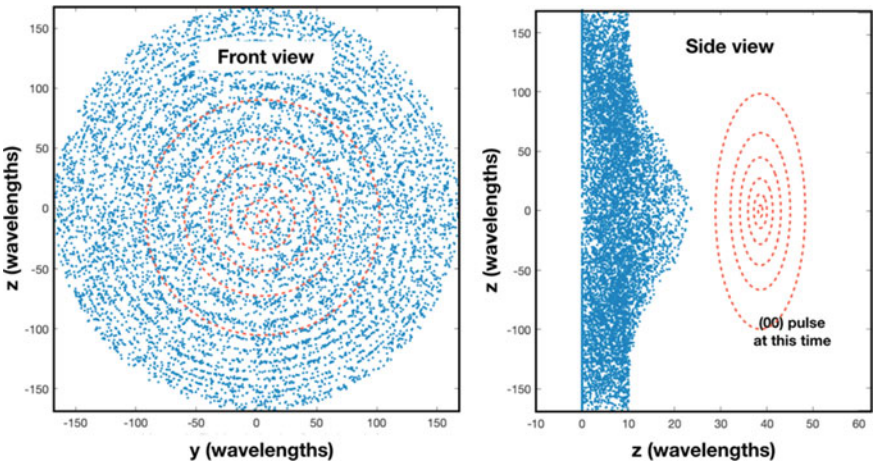

Fig. 8.7 Representation of the position of the electrons just after the pulse, for a large waist (oblate gaussian pulse with waist $w_0 = 100$ wavelengths, and duration 10 cycles) for 10^{19} W/cm^2 ($E_0 = 17$ au). The front view shows the transverse plane (plane xy). The side view shows the y axis projection. Both correspond to the final position of those electrons after the pulse. Dashed lines indicate the pulse contour (the outer one corresponds to 1/e amplitude, i.e. its radius is w_0)

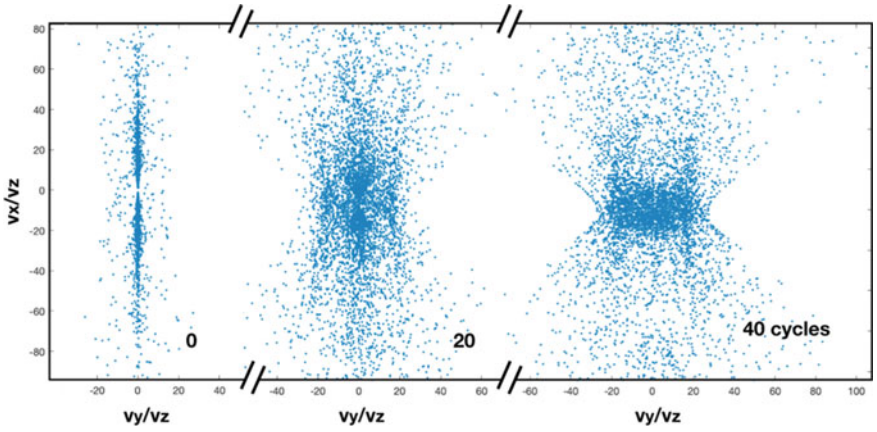

Fig. 8.8 Evolution of the dynamical pattern. Initially the dynamics is driven by the v_xB_y term, as in the Sarachik-Shappert analytical description, later the longitudinal field drives the electron. All parameters as in Fig. 8.7, including the 80 μm beam waist

the longitudinal field we start to have ponderomotive repulsion along the y axis too. This process needs a time because the longitudinal component of the electric field is zero along the $x = 0$ plane and the longitudinal component of the magnetic field is zero along the $y = 0$ plane.

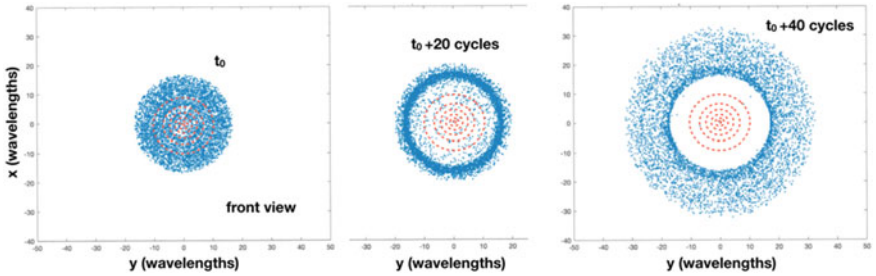

Fig. 8.9 Front views of the distribution for the (×00) mode, for a mildly relativisitic field, Eo = 17 a.u. (10^{19} W/cm^2), spherical pulse ($w_0 = c\tau = 10\lambda = 8\,\mu m$). Time t_0 corresponds to the moment where the maximum of the gaussian pulse arrives to z = 0. The other plots correspond to 20 and 40 cycles later. Dashed lines indicate the pulse contour (the outer one corresponds to 1/e amplitude)

A large waist is closer to Sarachik-Shappert plane wave modelling. In Fig. 8.8 this can be seen, particularly analyzing the direction of the electronic motion. The plot shows the forward angles in the x and y directions (in fact shows the forward velocity tangents v_x/v_z and v_y/v_z). This plot is very interesting because at the beginning the distribution follows the motion in along the xz plane (v_y velocity is very small), but after 40 laser cycles transverse fields wash out the plane dynamics.

The ponderomotive pattern created by a (00) mode is well known. It is shown for the realistic case of an 8 μm waist in Fig. 8.9. This value of the waist will be the same for all the remainding plots in this chapter. The plot at the left, t_0, corresponds to the moment where the peak of the pulse arrives to z = 0 (electrons are, as indicated in Fig. 8.6, filling the region $0 < z < 10\lambda$). Calculations, however started a few tens of cycles before to guarantee that the field is well below barrier supression at the beginning of the computation. The time lapse between each of the three views is 20 cycles. On the right-hand side one the interaction with the pulse is over (the forward drift is small) and the ponderomotive explosion is clearly seen showing a region at the center empty of electrons. Some of those structures may look like as a shock wave, but they are not. Electron–electron repulsion is not accounted for and there are no collective plasma effects. The wave is a caustic of the different electronic trajectories. At higher intensities the dynamics is similar, electrons are pushed outwards and the central region is depleted quickly.

As a partial conclusion of this section, we just can say that the ponderomotive force for a convex pulse acts just as a repulsive force, expelling electrons out of the high intensity region, as expected. Nothing is new here, but these ideas are very relevant for comparison with higher order modes, with nodal planes or axial nodes, that will lead to a different dynamical phenomenology.

8.5 Numerical Results for the 10 or 01 Modes

The scalar modes (01) and (10) are very relevant because they represent a field with a nodal plane. Such nodal plane represents a minimum in in the ponderomotive potential and could deviate or trap electrons. When considering the vector modes, polarization can go along or be perpendicular to the nodal plane, therefore there are four basic modes, ($\times$01), ($\times$10), (y01), and (y10), according to the polarization of the electric field, as indicated in Fig. 8.10. We need to study all four modes because we are going to present some interesting combinations of them with the ($\times$00) gaussian mode. It is relevant to write them explicitly, including the longitudinal component.

In the equations for the different modes, we keep the E_0 amplitude, as we did with the gaussian pulse. However, while for the gaussian pulse E_0 indicates the maximum of the peak (at the center) with a 01 or 10 mode this is not. Because of the nodal plane, the maximum field occurs at a distance 0.7 w_0 (the exact factor is $1/\sqrt{2}$) of the node, and that peak value is $E_{max} = 0.43\ E_0$ (the exact factor is $\exp(-1/2)/\sqrt{2}$). Observe that intensities of those modes are calculated from E_{max} not from E_0.

Mode 10 with x polarization, ($\times$10)

The 10 mode, linearly polarized along x is:

$$\begin{aligned}
E_x &= E_0 \exp\left(-\rho^2/w_0^2\right)\ f(z-ct)\ \cos(kz-\omega t)\ \frac{x}{w_0} \\
E_z &= E_0 \exp\left(-\rho^2/w_0^2\right)\ f(z-ct)\ \sin(kz-\omega t)\ \left(\frac{2x^2}{w_0^2}-1\right)\frac{1}{kw_0} \\
B_y &= B_0 \exp\left(-\rho^2/w_0^2\right)\ f(z-ct)\ \cos(kz-\omega t)\ \frac{x}{w_0} \\
B_z &= B_0 \exp\left(-\rho^2/w_0^2\right)\ f(z-ct)\ \sin(kz-\omega t)\ \frac{2xy}{w_0^2}\frac{1}{kw_0}
\end{aligned} \tag{8.13}$$

The other two components are $E_y = B_y = 0$. The kw_0 inverse dependence in E_z and B_z is kept expicitely because this factor gives idea of the relative value of the

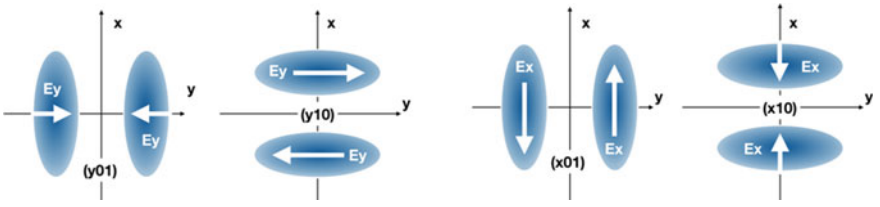

Fig. 8.10 Schematic representation of the four basic modes with one plane node. The four modes are relevant for this paper because we are going to present combined results with the linearly polarized gaussian mode

longitudinal fields. Again, in these expressions we have neglected the z derivatives of the pulse shape function f. Although this would be beyond the scope of the present paper, it is possible to develop these expressions with higher accuracy observing that we have odd and even degree polynomials of x and y. A complete description of those higher orders can be found in [22].

Pulses with a nodal plane are very interesting because the ponderomotive force traps electrons. Within a region of about $w_0/2$ from the nodal plane, the intensity gradient drives the electrons towards the nodal plane, we can consider this as the attraction basin for the nodal plane. Therefore, some electrons are trapped along the x axis in this case (x axis because is a 10 mode, not because of the polarization) and they propagate along the nodal plane. Ponderomotive expansion in the perpendicular direction takes place, as expected. This is clear in Fig. 8.11, that corresponds to a mildly relativistic case, $E_0 = 34$ a.u. (this corresponds to a maximum field of 7.5 10^{10} V/cm, i.e. to a peak intensity of 7.4 10^{18} W/cm^2). The snapshot is taken 45 cycles after the maximum of the pulse crosses the $z = 0$ plane. The side view at the right of this figure shows also the pulse profile (dashed lines). At the time shown, all electrons (initially in the $0 < z < 10\lambda$ slab) lie behind the laser pulse. The results show some tansverse trapping, as expected. The situation changes for strongly relativisitic pulses. Figure 8.12, is similar to the previous one, but now the intensity is 100 times more, i.e. it corresponds to a strongly relativistic case (7.4 10^{20} W/cm^2). Now the trapping is accompanied by a forward acceleration of the electron cloud. An electron eactly at the nodal plane will not feel any transverse field and will pass through the pulse. However, most of the electrons in the attraction basin experience a field that is quite intense. As those electrons bounce back from one side to the other of the nodal plane they experience a field that causes them to drift in the forward direction. The subsequent Doppler shift, makes them experience a longer wavelength field (in their moving frame) and the combined result is that electrons are drifted when trapped. As a consequence they do not go through the nodal plane. They stay for quite a large number of oscillations with the forefront of the pulse.

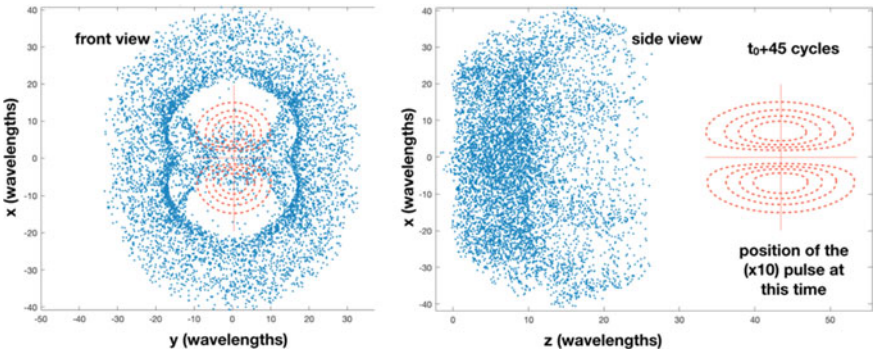

Fig. 8.11 Front view and side view of the electron distribution for a mode (×10) pulse with a mildly relativistic intensity, $E_0 = 34$ au. The pulse at the instant of the plot has already left all electrons behind. Dashed red lines show the pulse position at that time

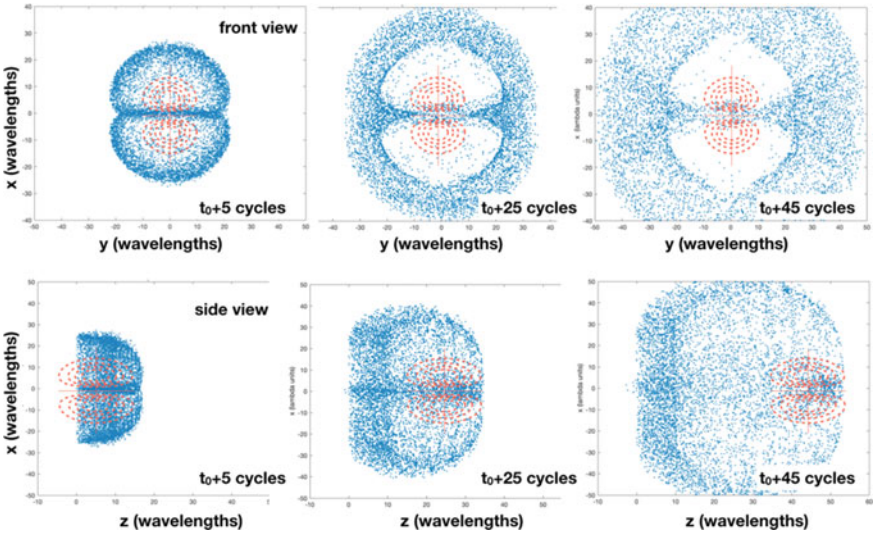

Fig. 8.12 Mode (×10) for a high intensity. The upper plots show the front view of the electron cloud and the lower ones the side view. There is trapping along the mode 01 node. The amplitude is $E_0 = 340$ a.u. (7.4 10^{20} W/cm^2). In this case, the quivering motion due to the electric field is perpendicular to the nodal plane

The simulation shown in Fig. 8.12 indicates a trapping ponderomotive force in one direction and a repulsive motion in the other. In other words, the ponderomotive potential has a saddle point. For that reason, electrons are trapped along the x axis but escape along the y.

Mode 10 with y polarization, (y10)

The 10 mode, linearly polarized along y is:

$$\begin{aligned}
E_y &= E_0 \exp\left(-\rho^2/w_0^2\right) f(z-ct)\ \cos(kz-\omega t)\ \frac{x}{w_0} \\
E_z &= E_0 \exp\left(-\rho^2/w_0^2\right) f(z-ct)\ \sin(kz-\omega t)\ \frac{2xy}{w_0^2}\frac{1}{kw_0} \\
B_x &= -B_0 \exp\left(-\rho^2/w_0^2\right) f(z-ct)\ \cos(kz-\omega t)\ \frac{x}{w_0} \\
B_z &= -B_0 \exp\left(-\rho^2/w_0^2\right) f(z-ct)\ \sin(kz-\omega t)\ \left(\frac{2x^2}{w_0^2} - 1\right)\frac{1}{kw_0}
\end{aligned} \tag{8.14}$$

The other two components are are $E_x = B_y = 0$. There is no need to show specific plots for this case because they are quite similar to the ones shown in Fig. 8.12, trapping along the x axis is due the mode (10) amplitude profile, not to the field polarization. However, in this case the electric field is driving the electrons along the nodal plane, not across it, as in the previous case. The remaining two modes will

have the same ponderomotive characteristics. We write them explicitly, just to have they expressions for the next sections, although they are only rotations.

Mode 01 with x polarization, (×01)

The 01 mode, linearly polarized along x, is

$$\begin{aligned}
E_x &= E_0 \exp\left(-\rho^2/w_0^2\right)\ f(z-ct)\ \cos(kz-\omega t)\ \frac{y}{w_0} \\
E_z &= E_0 \exp\left(-\rho^2/w_0^2\right)\ f(z-ct)\ \sin(kz-\omega t)\frac{2xy}{w_0^2}\ \frac{1}{kw_0} \\
B_y &= B_0 \exp\left(-\rho^2/w_0^2\right)\ f(z-ct)\ \cos(kz-\omega t)\ \frac{y}{w_0} \\
B_z &= B_0 \exp\left(-\rho^2/w_0^2\right)\ f(z-ct)\ \sin(kz-\omega t)\ \left(\frac{2\,y^2}{w_0^2}\ -1\right)\frac{1}{kw_0}
\end{aligned} \tag{8.15}$$

The other two components are. are $E_y = B_x = 0$.

Mode 01 with y polarization, (y01)

The 01 mode, linearly polarized along y, is

$$\begin{aligned}
E_y &= \ E_0 \exp\left(-\rho^2/w_0^2\right)\ f(z-ct)\ \cos(kz-\omega t)\ \frac{y}{w_0} \\
E_z &= E_0 \exp\left(-\rho^2/w_0^2\right)\ f(z-ct)\ \sin(kz-\omega t)\ \left(\frac{2\,y^2}{w_0^2}\ -1\right)\frac{1}{kw_0} \\
B_x &= -B_0 \exp\left(-\rho^2/w_0^2\right)\ f(z-ct)\ \cos(kz-\omega t)\ \frac{y}{w_0} \\
B_z &= -B_0 \exp\left(-\rho^2/w_0^2\right)\ f(z-ct)\ \sin(kz-\omega t)\ \frac{2xy}{w_0^2}\frac{1}{kw_0}
\end{aligned} \tag{8.16}$$

The other two components are $E_x = B_y = 0$.

In the next pages we are going to show simulations of the ponderomotive force induced by some of these modes as well as some combinations of them, with different delays and amplitudes. For simplicity, in all cases we are going to consider the Ti:sapphire wavelength, 800 nm, a beam waist $w_0 = 8\ \mu m$ and a pulse length $\tau =$ 10 cycles. There will be some delays between them, so we will indicate it as delay, for simplicity the gaussian 00 will be the reference and the other mode will come before (in these notes we are going to present only simulations where the 00 is the last one to arrive to the target). The offset or delay between one and the other will be on the order of the pulse duration or half of the pulse duration to have a clear interplay between them. For simplicity we can borrow the quantum mechanics notation of states (using parenthesis instead of brackets), so we are going to have combinations of the form $(\times 00) + a(y10) + b(y01) + c(\times 01) + d(\times 10)$, where a, b, c, d are complex numbers

giving the relative amplitudes and phases of the modes. The offset will be explicitly indicated for each example.

8.6 Numerical Results for Modes with an Axial Node (Donut Modes)

We saw that (10) or (10) modes trap in one dimension only. Therefore, as pointed out by Moore, convenient combinations of them will trap in the transverse plane. In other words, the three-dimensional saddle point will be attractive along the two transverse directions and repulsive along the forward axis. Taking into account the polarizations there are two conceptually different combinations, the standard donut mode mixing two crossed polarizations (and resulting -due to the lack of interference- as a flat-phase mode) and the OAM donut mode (mixing the same polarizations with a $\pi/2$ dephasing (resulting in a helical-phase mode).

Flat-phase donut mode

The more famous combination of those modes is the so-called donut mode. We can make such a mode with equal amplitude combinations of the ($\times$10) and (y01) modes or, alternatively with (y01) and ($\times$10). Regardless of the relative phase among them the mode intensity profile will have the well-known shape. Obviously, different phases between these two modes will result in different field patterns (radial polarization, for example), but the intensity profile is the same because being of crossed polarizations they do not interfere [23].

The idea of confining electrons at the center of an intense laser beam via the ponderomotive potential was suggested initially by Phillips and Sanderson [24] in a very preliminary form and later reexamined by Moore [25] for feasible laser conditions. As was pointed out by Moore such an axial node generates a tunnel that traps electrons in the transverse directions. Electrons born within a cylinder of radius approximately $w_0/2$ can be trapped. Figure 8.13 shows the numerical result for such donut mode ($\times$01) + (y10). Both plots correspond to the transverse projection of the electron cloud (x corresponds to the electric field polarization and z is the propagation). The left plot corresponds to a mildly relativistic case, $E_0 = 34 + 34$ a.u. (or 7.4 10^{18} W/cm^2 peak intensity for each mode), on each of the two modes. It is clear that some electrons went through the ponderomotive potential tunnel, but they are not pushed forward. The center of the donut pulse is at $z = 45\,\lambda$ for the left figure. The right plot corresponds to an intensity hundred times larger, $E_0 = 340 + 340$ a.u. (peak intensity 7.4 10^{20} W/cm^2 for each mode) and the picture corresponds to the time where the center of the donut pulse is at $z = 85\,\lambda$. Here the electron cloud evolution is completely different, the transversally trapped electrons feel a strongly relativistic field with the corresponding forward drift. The cloud of fast forward moving electrons is evident and it is still being pushed forward before the pulse maximum. Thus, at strongly relativistic intensities we can say that besides transverse trapping there is a

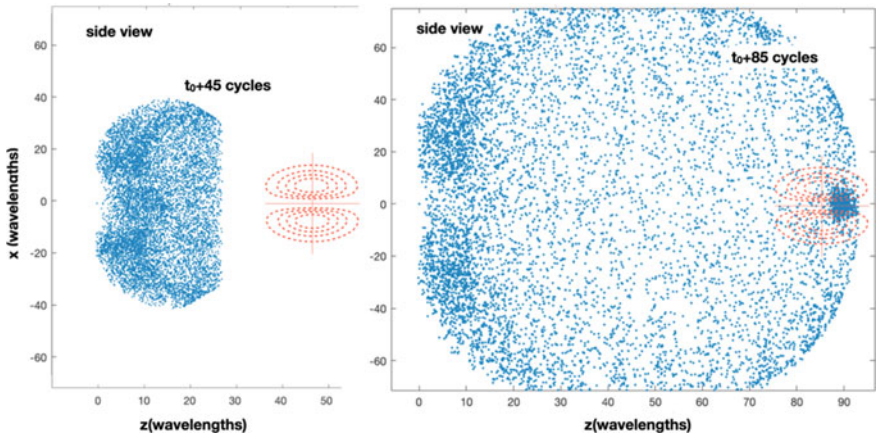

Fig. 8.13 Numerical result for the donut mode (×01) + (y10). Both plots correspond to the lateral projection of the electron cloud The left plot corresponds to an amplitude $E_0 = 34 + 34$ a.u., on each of the two modes (i.e. 7.4 10^{18} W/cm^2 each), and a time $t_0 + 45$ cycles, at that time the electron cloud is behind the pulse (the pulse position is indicated by the red dashed lines). The right plot corresponds to an intensity hundred times larger, $E_0 = 340 + 340$ a.u. (7.4 10^{20} W/cm^2) and to a time $t_0 + 85$ cycles. A number of trapped electrons have a strong drift forward, following the pulse

strong longitudinal drift that acts as a forward trapping. This effect was shown by Miyazaki and co-workers [26], but using an electron injector, instead of a gas of neutral atoms to be ionized. A similar effect will appear for the $l = 1$ OAM mode, because the ponderomotive force pattern is quite similar.

Helical-phase donut mode- (OAM mode, with parallel polarizations)

Combinations such as (×10) and (×01) are also quite interesting. Since both have the same polarization, their relative phase is very important. If both modes are in phase, i.e. combinations as (×01) + (×10), then we just shift the nodal plane and get just a rotation of ponderomotive potential pattern. However, if we introduce a $\pi/2$ phase shift among them, i.e. combinations of the form (×01) + i(×10), then we obtain an OAM $l = 1$ mode [27]. Such a mode has an intensity profile that looks like a donut mode, and it is called as donut many times in the literature. However, it has a helical phase structure. To avoid confusions, we will use the name donut to refer to the flat phase and OAM to refer to the helical phase $l = 1$ mode in this text. Observe that the helical structure of the OAM is in the phase distribution, the field polarization is always in the same direction (except, of course, the longitudinal component). Such Helical OAM modes can efficiently be produced form a (00) mode [28] using simple spiral staircase mirrors. This technique can be used in high intensity laser systems [29]. As a consequence, ultraintense OAM modes are achievable with existing lasers, and their potential for trap electrons in conjunction with other LWFA mechanisms has probably not being fully studied.

The in phase superposition of the (×01) and (×10) modes shifts the node to the $x + y =$ constant plane, however the superposition with a phase shift of $\pi/2$, gives

rise to the well-known OAM mode (with one unit of orbital angular momentum). The other possibility of combining two modes, y01 and y10 is just a rotation and does not add new information.

Figure 8.14 (upper part) shows the OAM mode ($\times 01$) + i($\times 10$) trapping, for E_0 = 34 + 34 a.u., i.e. a mildly relativistic case (7.4 10^{18} W/cm^2 at each component). Electrons are trapped in the minimum, but they are not pushed forward, so at the end there is a cloud of electrons repelled outwards by the ponderomotive force and a number of electrons trapped close to the axis. However, all electrons are out of the high intensity region, as can be seen in the upper right plot in Fig. 8.14. The lower part of Fig. 8.14 shows a case 100 times more intense. Transverse trapping perpendicularly to the beam axis is clear in this front view. However, there is a fundamental difference between them. For the strongly relativistic regime, electrons are pushed forward, so there is the expected trapping plus a relevant drift. This drift is evident in Fig. 8.14.

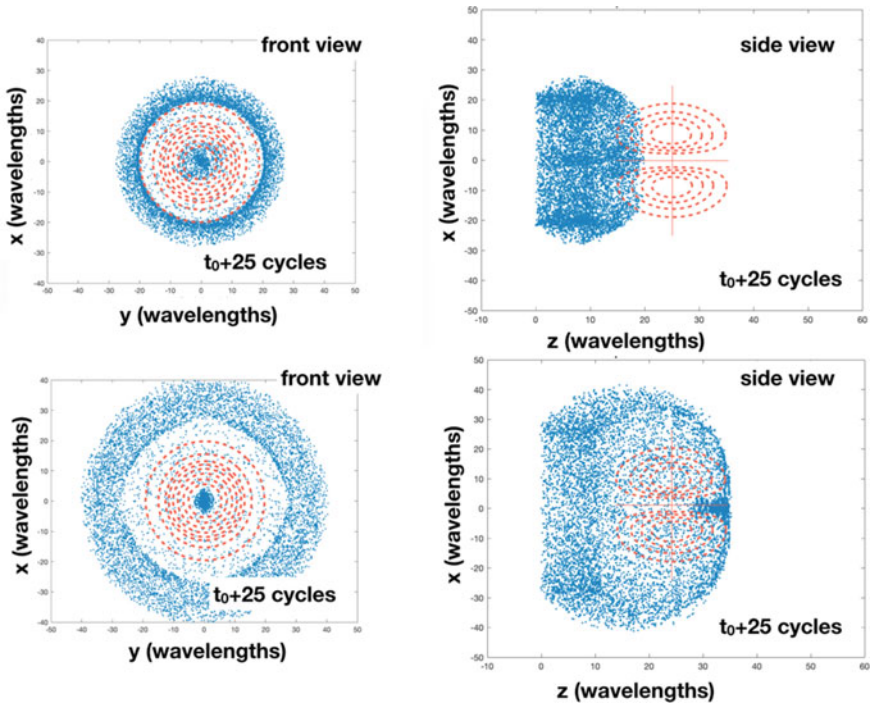

Fig. 8.14 Characteristic distribution of the electron cloud for an OAM, ($\times 01$) + i($\times 10$) of the electron distribution. The two upper figures are the front view and the side view for a mildly relativistic case, with amplitudes E_0 = 34 au (7.4 10^{18} W/cm^2). for each of the two modes. Result seems obvious, and is plotted just for comparison. The two lower plots correspond to the pulse structure but 100 times more intense, E_0 = 340 + 340 a.u. (7.4 10^{20} W/cm^2). In this case, a fraction of the electrons are also trapped in the axial node, but in this case they experience a strong drift forward. Time is 25 cycles after t_0

The OAM mode (×01) + i(×10) traps and drags a number of electrons when the intensity is strongly relativistic. Figures 8.15 and 8.16 correspond to the case E_0 = 340 + 340 a.u. (7.4 10^{20} W/cm^2 at each component) and evidence the electron

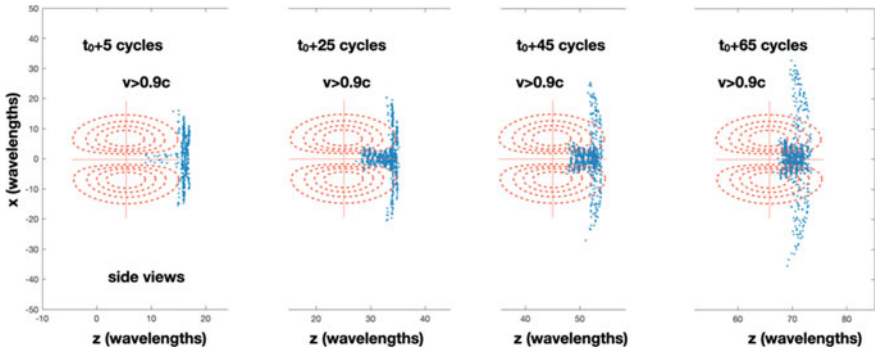

Fig. 8.15 Motion of the electronic cloud for a highly relativistic OAM mode, the same mode and fields as the previous figure. In the present plot only electrons with speed v > 0.9c have been plotted. The presence of a number of electrons close to the axial node and having a large drift is clear. Dashed lines indicate the position of the laser pulse

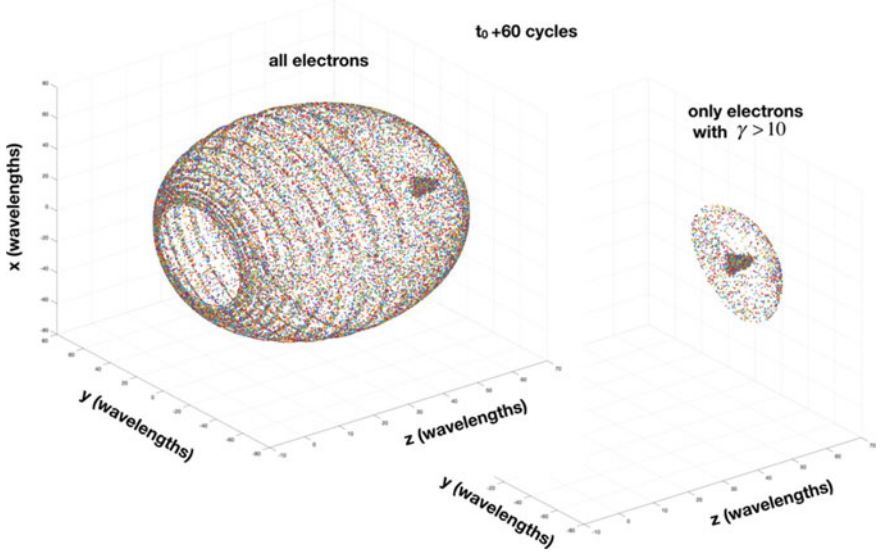

Fig. 8.16 Distribution of electrons at t_0 + 60 cycles. For a OAM mode (×01) + i(×10) with E_0 = 340 + 340 a.u. (7.4 10^{20} W/cm^2), and a waist w_0 equal to ten wavelengths, as in the previous figure. The left plot shows the ionized electrons. A large fraction are expelled by the ponderomotive force, but about ten percent of the electrons remain close to the axis and move forward with the field. The left part shows the electrons that move with $\gamma > 10$. Among those electrons, a few are escaping due to the ponderomotive force and the majority are trapped

trapping and dragging. Figure 8.15 shows only the electrons with v > 0.9 c for different times. The structure is clear, there is a group of trapped electrons that are bouncing back and forth inside the OAM axial node (transverse motion) at the same time that this motion induces a longitudinal drift in accordance to Eq. (8.5). In this back and forth oscillation some electrons escape and generate a flat pattern clearly visible in Fig. 8.15. The same pattern of a central trapped part and escaping cloud is seen in Fig. 8.16 (for the same pulse parameters). At the right part of this figure we depicted only the electrons moving with $\gamma > 10$, while at the left part we plotted all ionized electrons. The structure at the left shows a circle of electrons ionized at the outer part of the field that due to the low intensity are not pushed forward while the inner electrons are expelled generating some sort of bag or fish trap (with the helical structure induced by the OAM helical phase). Electrons at the center are trapped and move forward quickly giving the high density tip. For this case about 9.5 percent of the ionized electrons are trapped and accelerated to $\gamma > 10$ and about one percent of them have a relativistic factor $\gamma > 100$. The attractive (concave) region of the OAM beam corresponds to a radius of about 0.7 w_0.

8.7 Numerical Results for Delayed Mode Superpositions

Now we can analyze combinations of the ($\times$00) mode with only one of the other four modes conveniently shifted in time. The offset is of the order of the pulse duration, or less (otherwise the overlap won't be relevant), and the gaussian pulse is the last to arrive. In this case ponderomotive force shows other interesting features. Some of them can be more or less foreseen from the above considerations and we will skip them, but other features are also surprising and interesting.

Electron steering

Among the surprising possibilities of the different combinations of such modes with different offsets, one of the most relevant is the possibility of electron steering. Combining conveniently the pulses we may get potentials able to deflect electrons. One example of these kind of pulses is the combination ($\times$00) + ($\times$10). Being that the two are polarized in the same direction there will be interference, and the fields add up on one side and show destructive interference on the other side of the 10 nodal plane. Thus, the potential will deviate the electrons to the region of destructive interference because there the intensity is lower. To be sure that the deviation is due to this effect we may compute three different combinations ($\times$00) + ($\times$10), ($\times$00) + i($\times$10), and ($\times$00)-($\times$10).

Results are shown in Fig. 8.17, in all cases the offset is 8 μm(10 cycles) with the (10) mode advanced with respect to the (00). The superpositions ($\times$00) + ($\times$ 10) and the ($\times$00)-($\times$10) are equivalent, deflecting electrons towards the destructive interference side. However the ($\times$00) + i($\times$10) has a symmetrical structure and does not steer electrons. Such combinations are feasible experimentally and moreover a super high intensity is not needed., Thus, ponderomotive steering has a lot of potential

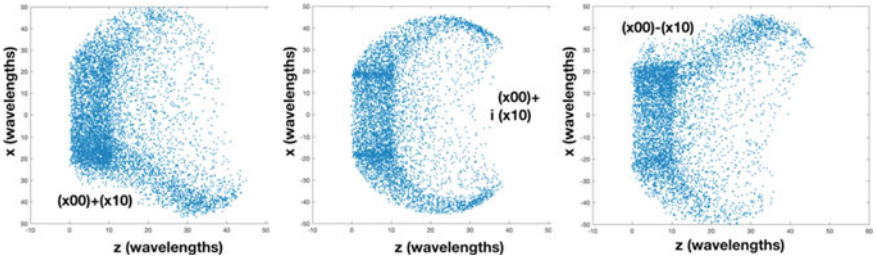

Fig. 8.17 The destructive interference in one side and constructive on the other, generates a ponderomotive force along x that deflects electrons to the region of lower total field. Simulation corresponds to $E_0 = 17$ a.u. (peak at 10^{19} W/cm^2 for the ($\times$00) mode and at 1.8 10^{18} W/cm^2 for the ($\times$10) mode) and 8 microns offset, and for a time 65 cycles after t_0. Electrons born at the edges of the pulse have a very small drift and they constitute the cloud seen between z = 0 and z = 10 wavelengths

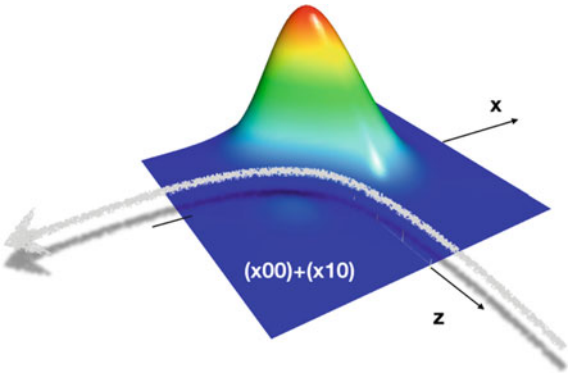

Fig. 8.18 Representation of a cut along the y = 0 plane of the ($\times$00) + ($\times$10) pulse, for 10 cycles offset. Grey arrow indicates the path of the deflected electrons

for coherent control of ionized electrons. Such pulses can push electrons out of one side of the target in a real experiment (Fig. 8.18).

The number of combinations is very large and with five modes and different configurations it is possible to reproduce a huge number of experimental configurations. For example, it is possible to model the horseshoe (or concave) beams, as proposed by Brijesh et al. [30]. They introduced for the first time to our knowledge the concept of concave beams for trapping not only in the transverse directions but also in the longitudinal direction the electrons. Their discussion is very interesting at the onset of the relativistic regime, however, when the dynamics is highly relativistic, electron's drift dominates.

Concave pulses with a gaussian and an OAM mode

To end this investigation of ponderomotive dynamics, let's consider Brijesh horseshoe pulses. The can be modelled here as a combination of the (x00) gaussian pulse and a y-polarized OAM pulse with a few cycles offset. According to our notation those pulses will be ($\times$00) + 2(y10) + 2i(y01), with a 5 cycles offset (always the

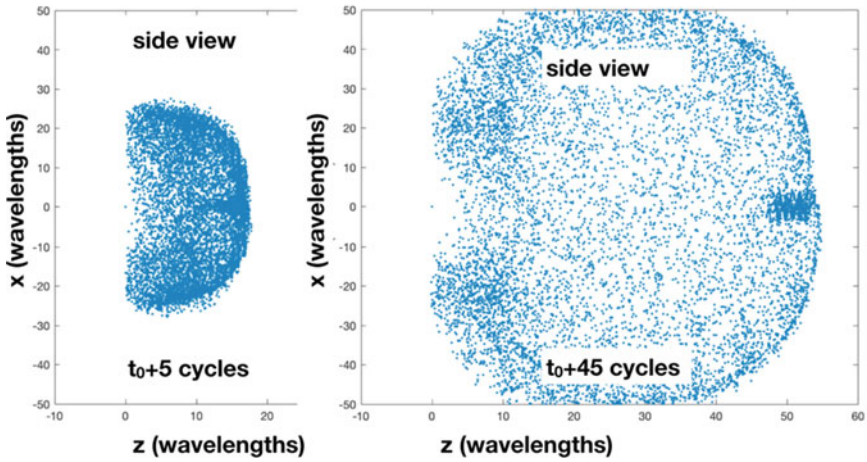

Fig. 8.19 Side views of the electron cloud, during the interaction with the pulse (rigth) and just at the beginning (left). This figure corresponds to a highly relativistic case with $E_0 = 170$ a.u., and a pulse structure $(\times 00) + 2(y10) + 2i(y01)$, with a 5 cycles offset. This corresponds to 10^{21} W/cm^2, peak intensity, for the (00) mode, and 7.4 10^{20} W/cm^2 for each one of the other two

donut in front of the gaussian). Results for that case are shown in Fig. 8.19 for a strongly relativistic case. One can see that the drift of the electron cloud is similar to that observed in Figs. 8.13 and 8.14 for the pure donut or OAM modes themselves and the observed trapped high energy electrons are mainly due to the OAM forward drift itself. The figure corresponds to $E_0 = 170$ a.u. for the gaussian beam (10^{21} W/cm^2). Combining such a peak power gaussian pulse with a similar donut pulse both having smooth profiles is probably on the limit of today's multi PW lasers.

8.8 Conclusions

The ponderomotive potential is ubiquitous in any strong-field experiment where a laser pulse is focused to a small spot. In most cases this is a force that drives electrons out of the focal volume, i.e. it is a force that repels electrons out of the high intensity spot. However, there are modes with a nodal structure that allow trapping and steering of the ionized electrons. While this can readily be understood in the classical or mildly relativistic regime, as intensities enter the 10^{21} W/cm^2 region drifts play a fundamental role in enhancing the trapping and dragging of electrons. With the new multi petawatt lasers and the use of higher order modes, there are a large set of pulse configurations that can be explored and exploited for various applications in electron trapping and steering.

All the present notes are based on the simulation of the Lorentz force dynamics for independent relativistically driven electrons, and without considering nonlinear

effects on the laser propagation. Therefore, the validity of the present results is just for very dilute gases. Study at higher densities would require more complex simulation tools as PIC codes.

Such tools to control the electron dynamics while electrons are still driven by the intense pulse may result in interesting applications such as injection to other accelerators or boosters. Also new coherent radiation schemes seem possible because electrons are self-organized in patterns by the relativistic dynamics. At the present low densities, the number of emitted photons will be small.

Acknowledgements We acknowledge support from the Spanish Ministerio de Ciencia, Innovación y Universidades and the European Regional Development Fund (Grants No. FIS2016-81056-R, and EQC2018-005230-P), from H2020-EU Laserlab Europe V (Grant No. 871124), from Junta de Castilla y León (Grant No. CLP087U16), and from the Natural Sciences and Engineering Research Council of Canada (Grant No. RGPIN-2019-05013).

References

1. T.W.B. Kibble, Mutual refraction of electrons and photons. Phys. Rev. **150**, 1060 (1966)
2. D. Strickland, G. Mourou, Compression of amplified chirped optical pulses. Optics Communications **55**, 447–449 (1985)
3. C. Danson et al., Petawatt and exawatt class lasers worldwide. High Power Laser Science and Engineering **7**, E54 (2019)
4. E. Esarey, C.B. Schroeder, W.P. Leemans, Physics of laser-driven plasma-based electron accelerators. Rev. Mod. Phys. **81**, 1229 (2009)
5. P. M. Woodward, A method for calculating the field over a plane aperture required to produce a given polar diagram, J. Inst. Electr. Eng., 93 Part IIIA (1947) 1554
6. F. Amiranoff et al., Observation of laser wakefield acceleration of electrons. Phys. Rev. Lett. **81**, 995 (1998)
7. V. Malka, Laser plasma accelerators, Phys. Plasmas, 19 (2012) 055501.
8. S. Kneip et al., Bright spatially coherent synchrotron X-rays from a table-top source. Nat. Phys. **6**, 980 (2010)
9. E. Esarey, P. Sprangle, J. Krall, Acceleration of electrons invacuum. Phys. Rev. E **52**, 5443 (1995)
10. J. San Roman, L. Roso and H. Reiss, Evolution of a relativisitic wavepacket describing a free electron in a very intense laser field, J Physics B: Atom Molec Opt Phys, 33 (2000) 1869
11. J. San Roman, L. Roso and L. Plaja, A complete description of the spin force, J Physics B: Atom Molec Opt Phys, 36 (2003) 1
12. I. C. E. Turcu, et al., Quantum electrodynamics experiments with colliding petawatt laser pulses, High Power Laser Science and Engineering 7 (2019).
13. E.S. Sarachik, G.T. Schappert, Classical theory of the scattering of intense laser radiation by free electrons. Physical Review D **1**, 2738 (1970)
14. C.I. Moore, J.P. Knauer, D.D. Meyerhoffer, Observation of the transition from Thomson to Compton scattering in multiphoton interactions with low-energy electrons. Phys Rev Letters **74**, 2439 (1995)
15. C. H. He, et al., Towards an in situ, full-power gauge of the focal-volume intensity of petawatt-class lasers, Optics Express 27 (2019)
16. I. Pastor, et al., Nonlinear relativistic electron Thomson Scattering for laser radiation with orbital angular momentum, Journal of Physics Communications, 4 (2020) 065010.

17. J. Pang, et al., Subluminous phase velocity of a focused laser beam and vacuum laser acceleration, Physical Review E, 66 (2002) 066501
18. J.D. Lawson, Lasers and Accelerators, , IEEE Trans. Nucl. Sci. NS- **26**, 4217 (1979)
19. P. M. Woodward, A method of calculating the field over a plane aperture required to produce a given polar diagram, J. Inst. Electr. Eng., 93 Part IIIA (1947) 1554
20. P. Gibbon, Short pulse laser interactions with matter: an introduction. World Scientific, 2005.
21. N. Cao et al., Accurate description of gaussian beams and electron dynamics. Optics Communications **204**, 7 (2002)
22. L.W. Davies, Vector electromagnetic modes of an optical resonator. Phys. Rev. A **19**, 1177 (1979)
23. W. Kochner, Solid-State Laser Engineering, Springer, 2006
24. N.J. Phillips, J.J. Sanderson, Trapping of electrons in a spatially inhomogeneous laser beam. Physics Letters **21**, 533 (1966)
25. C.I. Moore, Confinement of electrons to the centre of a laser focus via the ponderomotive potential. J. Mod. Opt. **39**, 2171 (1992)
26. S. Miyazaki et al., Generation of a microelectron beam by an intense short pulse laser in the TEM(1,0)+TEM(01) mode in vacuum. J Phys D: Applied Physics **38**, 1665 (2005)
27. M. Padgett et al., An experiment to observe the intensity and phase structure of Laguerre-Gaussian laser modes. Am. J. Phys. **64**, 1 (1996)
28. A. Longman, R. Fedosejevs, Mode conversion efficiency to Laguerre-Gaussian AOM modes using spiral phase optics. Opt. Express **25**, 17382 (2017)
29. A. Longman et al., Off-axis spiral mirrors for generating high-intensity optical vortices. Opt. Lett. **45**, 2187 (2020)
30. P. Brijesh et al., Demonstration of a horseshoe-shaped longitudinal focal profile. J Optical Society of America B **24**, 1030 (2007)

Chapter 9
LD-Pumped Kilo-Joule-Class Solid-State Laser Technology

Takashi Sekine, Norio Kurita, and Toshiyuki Kawashima

Abstract In this chapter, we report our latest work on the technical development of the cryogenically cooled Yb:YAG-ceramics laser as scalable technology toward achievement of repetitive kilo-joule-class lasers. In our first trial, we obtain a high small signal gain of 20.4 with a high stored energy of 149.0 J using a conductively side-cooled Yb:YAG ceramic multi-disk laser amplifier operating at 100-K cooling temperature. In the second trial, we obtain 117-J nanosecond pulsed laser output with a cryogenic-helium-gas face-cooled Yb:YAG ceramic multi-disk laser amplifier. In this study, we obtain 42.3% energy-extraction efficiency from the energy stored in the Yb:YAG ceramic disks. We also determined the specifications of the face-cooled laser amplifier designed for repetitive operation by flowing helium gas on the end faces of the Yb:YAG ceramic disks. The feasibility of a practical design for kilo-joule-class diode pumped solid state lasers with a cryogenically cooled Yb:YAG ceramic disks was demonstrated by the developed high-gain and high-efficiency laser technologies.

9.1 Introduction

Since the first demonstration of laser oscillation in 1960 [1], laser technologies have been progressing rapidly. The most important characteristic of a laser is coherent control of the photons in the temporal, spatial, and spectral domains. Therefore, the progress in laser technologies can be seen as a history of pursuing optimal control in these domains. A nanosecond coherent optical pulse was demonstrated in the temporal domain by Q-switch technology in 1962 [2]. Furthermore, picosecond and

T. Sekine (✉) · N. Kurita · T. Kawashima
Central Research Laboratory, Industrial Development Center, Hamamatsu Photonics K.K., 1820 Kurematsu, Nishi-Ku, Hamamatsu City, Shizuoka 431-1202, Japan
e-mail: t-sekine@crl.hpk.co.jp

N. Kurita
e-mail: norio.kurita@hpk.co.jp

T. Kawashima
e-mail: kawasima@crl.hpk.co.jp

K. Yamanouchi et al. (eds.), *Progress in Ultrafast Intense Laser Science XVI*,
Topics in Applied Physics 141, https://doi.org/10.1007/978-3-030-75089-3_9

femtosecond laser pulses were observed using the mode-locked laser oscillators in 1966 [3–5]. By using the interaction between electron and an electric field generated by a femto-second laser pulse, an atto-second optical pulse generation was demonstrated using high-order harmonic generation in 2001 [6]. In the spatial domain, a mega-watt electric field at micrometer scale were generated by focusing spatially coherent photons from a transverse single-mode laser pulse onto the diffraction limit spot area. An electric-field intensity can be enhanced by increasing the laser-pulse energy by expanding the laser beam size and maintaining the spatial coherence to avoid an optical damage on the material surface. The National Ignition Facility (NIF) at Lawrence Livermore National Laboratory (USA) achieved the highest pulsed laser energy output of 16 kJ with transverse-single mode at 1053 nm wavelength with a beam size of 30 cm by 30 cm in 2012 [7, 8]. Their research made great contribution in the progress of the high power laser technologies, such as fabrication of the high quality optical materials, dielectric coatings with high damage threshold, and optical polish in high precision. A chirped pulse amplification (CPA) technique realized by coherence controlling technologies in the temporal, spatial, and spectral domains invented in 1985 [9] made a significant contribution to increasing the focused electric-field intensity beyond 10^{22} W/cm^2. In Europe, Extreme Light Infrastructure (ELI) laser facilities, including 10-PW laser systems based on the CPA technique, have been constructed to expand the application range of ultra-intense lasers [10].

With the dramatic progress in these laser technologies, the application range of lasers has widely expanded to optical communication, semiconductor lithography, material processing, laser ranging, laser scalpels, microscopes, and so on. For these applications to be practical, many types of lasers, such as gas, excimer, laser diode (LD), and solid-state have been developed. A diode-pumped solid-state laser (DPSSL) was described as "a renaissance in solid-state laser development" by Dr. R. L. Byer (Stanford University, U.S.A.) in 1988 [11], and has recently been widely used as a continuous-wave (CW) based fiber laser with kilo-watt class output in material processing. With the current industrial trends of Internet of Things and Industry 4.0, lasers are one of the most important technologies for constructing manufacturing systems. A pulsed DPSSL is suitable for optimizing the processing conditions of such systems due to the flexibility of its laser characteristics such as pulse duration (shape), repetition rate, pulse energy, and wavelength. Therefore, demand for pulsed laser processing of tempered glass, carbon fiber reinforced plastic (CFRP), and high-tensile steel is now growing.

Figure 9.1 shows the relationship between laser pulse energy and pulse repetition rate of typical laser systems in development or on the market. White plots denote flashlamp-pumped laser systems and black plots denote DPSSL systems. Flashlamp-pumped lasers with high pulse energy but a low repetition rate have long been used in scientific applications and have achieved many important results. However, DPSSLs with low pulse energy but high repetition rate have been developed for material-processing laser systems. From this background, a DPSSL with high pulse energy and high repetition rate is expected to create a new market in not only novel material processing but also scientific applications such as high energy physics, laser acceleration, attosecond generation, quantum beam generation, and inertial fusion

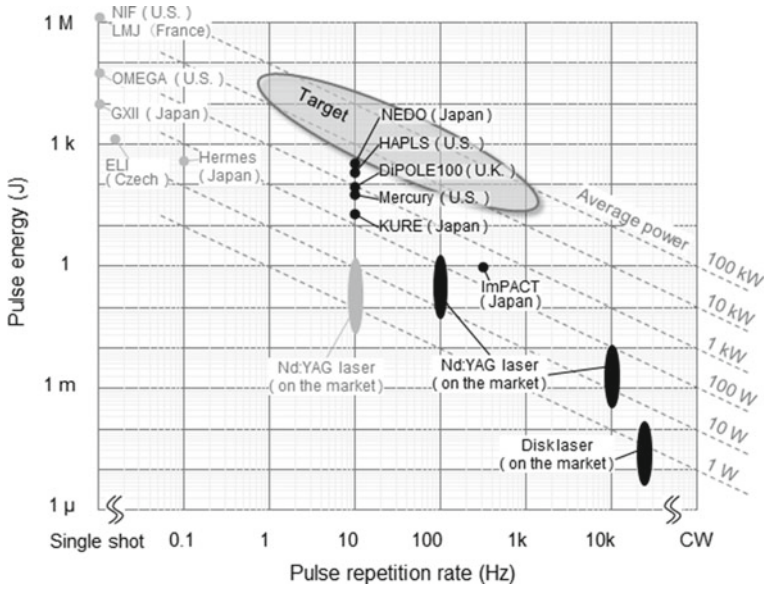

Fig. 9.1 Relationship between laser pulse energy and pulse repetition rate of typical laser systems in development or on the market

energy. Development of a high energy pulsed DPSSL began at the end of the 1990s in the U.S.A., Europe, and Japan. In 2007, 55 J at 10-Hz output from an LD-pumped Yb:S-FAP monocrystalline laser was achieve in the U.S.A. [12]. In 2008, 21.3 J at 10-Hz output was achieved from an LD-pumped Nd:glass laser in Japan [13]. In the latest report, 105 J at 10-Hz output was achieved using an LD-pumped cryogenically cooled Yb:YAG-ceramics laser in 2017 in the U.K. [14].

Since the 1990s, we have developed high-energy pulsed DPSSL technologies as fundamental research for the development of inertial fusion energy laser drivers. For a development of practical application in industrial and academic purposes, that must be processed for achieving our ultimate goal, we are developing high energy laser technology. Recently, such usage requires lasers of over 1-kW class average power in industrial fields; future applications in academic fields will require laser performance exceeding 10-kW average power. Therefore, in this chapter, we report our latest experimental results from the development of a cryogenically cooled Yb:YAG-ceramics laser amplifier as a feasibility study of kilo-joule-class lasers with a 10-Hz repetition rate [15].

9.2 Demonstration of High-Gain with High-Energy Storage Characteristics of Cryogenically Cooled Yb:YAG-Ceramics Laser Amplifier

In this section, we report a demonstration of high small-signal gain of 20 times along with high-energy storage characteristics of 149.0 J. This performance was achieved with an LD-pumped cryogenically side-cooled Yb:YAG ceramic multi-disk laser amplifier [16]. The results indicate the feasibility of developing practical kilo-joule class DPSSLs capable of simultaneously providing high gain as well as high-energy storage characteristics.

9.2.1 Construction of LD-Pumped Conductively Side-Cooled Yb:YAG Ceramic Multi-disk Laser Amplifier

The laser amplifier employed in this work uses Yb:YAG as a laser medium that can be adjusted to stimulated emission cross section suitable for high-energy lasers by cooling to a low temperature. Another advantage is that the established manufacturing technology of transparent Yb:YAG ceramics improves the reliability of high energy lasers. This multi-disk-type laser amplifier configuration is also suitable for a high energy laser amplifier due to its energy scalability made possible by enlarging the disk aperture. Such an amplifier can also be adapted to high-repetition operation by cooling the laser medium from the end-face with coolant. In the case of this laser amplifier, the Yb:YAG ceramic disks are conductively cooled from the side-surface via a copper holder using two Gifford-McMahon (GM) cryo-coolers. Thanks to this simple configuration of this amplifier, a high pulse energy extraction and high amplification gain is demonstrated. Consequently, the results from this amplifier allowed us to develop the cryogenic helium gas face-cooled Yb:YAG ceramic multi-disk laser amplifier discussed in this paper.

This LD-pumped Yb:YAG-ceramics laser amplifier was developed in 2015 by Hamamatsu Photonics K.K. (Fig. 9.2). Ten Yb:YAG ceramic disks, each with a size of 100 mm by 100 mm and a thickness of 10 mm, are placed in a central vacuumed laser chamber as the laser medium. Four LD modules are set around the vacuumed laser chamber. The LD modules pump the Yb:YAG ceramic disks from four diagonal directions. To prevent a difference in stored energy among the disks arranged at both ends and the center, we used five kinds of Yb:YAG ceramic disks with different Yb ion doping concentrations. Thus, lower concentration disks are arranged at both ends, and higher concentration disks are arranged at the center. The ten disks are cooled using two GM cryo-coolers installed in the upper and lower areas of the vacuumed laser chamber. The cooling capacity of the GM cryo-coolers is 180 W at 130 K. The side-surfaces of the Yb:YAG ceramic disks were treated to form a cladding layer for suppressing parasitic oscillation. Figure 9.3 shows a photograph of the Yb:YAG ceramic disks before cladding treatment. As shown by the arrow in Fig. 9.2, a seed

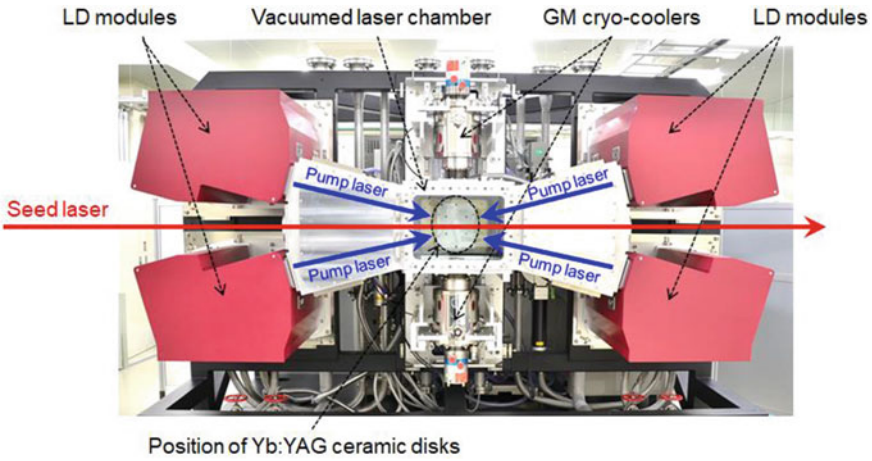

Fig. 9.2 Conductively cryogenic side-cooled Yb:YAG ceramic multi-disk laser amplifier

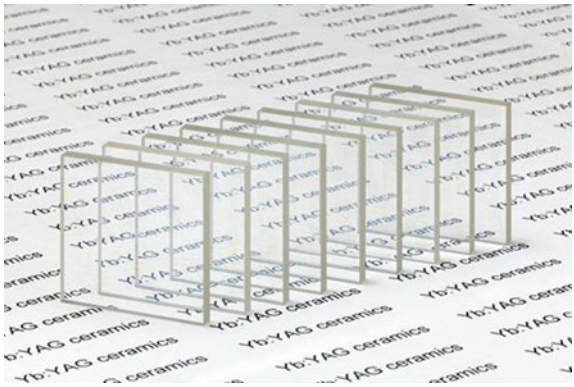

Fig. 9.3 Yb:YAG ceramic disks before cladding treatment

pulse propagates between the upper and lower LD modules and passes through the Yb:YAG ceramic disks after being injected into the vacuumed laser chamber from the vacuum window.

This laser amplifier is equipped with four water-cooled power supply systems for the four LD modules at the back. A total of 80 channels of electric pulse output are connected to each LD stack in the LD modules. The specifications of each output channel include a maximum output voltage of 60 V and maximum output current of 400 A with a pulse duration of 1 ms. Deionized water for the LD modules is supplied from a chiller with the capability of a 500-l/min flow rate with 0.8-MPa water pressure. All of the water is delivered through pipes from the rear-end of the system to cool the LD modules, LD power-suppling system, and GM cryo-coolers.

9.2.2 Characteristics of Pumping LD Modules

Table 9.1 gives the specifications of an LD stack used in the LD modules (shown by photo in Fig. 9.4). Jet-water-cooling LD stacks (model LE0115, Hamamatsu Photonics K.K.) are used. By driving a LD stack at 200-A current, it can output 6 J of energy with a peak power of 6 kW and a pulse duration of 1 ms. The typical repetition rate is 10 Hz. Thirty LD bars have cylindrical micro lenses for divergence collimation in the fast axis.

The specifications of an LD module are given in Table 9.2 (shown by photo in Fig. 9.5). An LD module outputs 110 kW in peak power. The typical irradiation size is 60 × 70 mm at a working distance of 700 mm. One of the unique characteristics of this LD module is that all output patterns from the LD stacks built into the LD module are superposed at the same position and in the same pattern at the working distance. This superposing scheme provides the averaging effects for the various intensities and the various spectrum of each LD stack. This scheme also has the advantage of avoiding spatial intensity defects in the irradiation pattern, even when a failure occurs in an LD stack.

A typical near-field pattern (NFP) at the working distance of an LD module is shown in Fig. 9.6. The intensity distribution in the NFP has a strong modulation at upper and lower areas. A number of vertically linear intensity distributions corresponding to the LD bars can also be confirmed. The intensity modulation at the upper and lower areas are explained from the aberration of the optical components used in the LD module. Another problem of the vertical-line profile is caused by the intensity

Table 9.1 Typical specifications of LD stack

Parameter	Value
Peak power	6 kW
Wavelength	940 nm
Pulse duration	1 ms
Repetition rate	10 Hz
Number of LD bars	30 bars

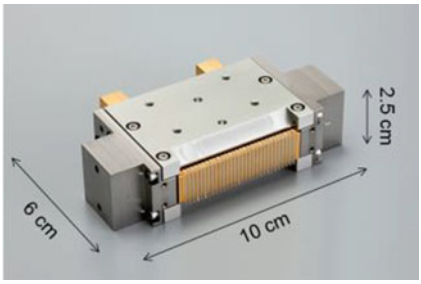

Fig. 9.4 Laser diode (LD) stack

Table 9.2 Typical specifications of LD module

Parameter	Value
Peak power	>110 kW
Wavelength	940 nm
Working distance	700 mm
Irradiation intensity	>2.6 kW/cm^2
Irradiation size (Rectangle)	60 × 70 mm

Fig. 9.5 LD module

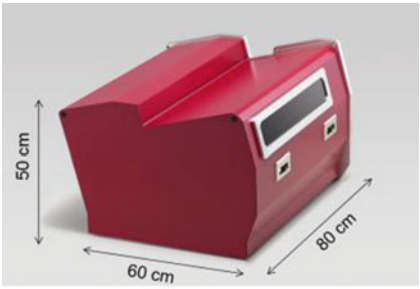

Fig. 9.6 Typical near-field pattern (NFP) of LD module

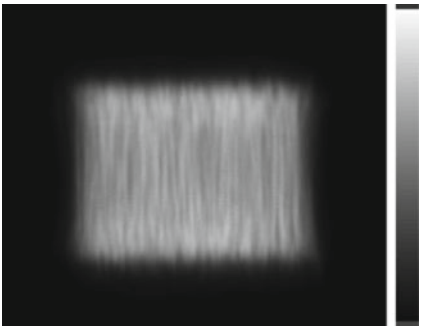

distribution of the LD bars. This pattern is expected to be improved by averaging with a four-direction pumping scheme.

9.2.3 Demonstration of High Small Signal Gain Characteristics with High-Energy Storage

Figure 9.7 shows a typical fluorescence pattern when Yb:YAG ceramic disks were pumped by four LD modules. The fluorescence pattern was measured in the horizontal direction along the same axis of the seed pulse path using a CMOS camera. The cooling temperature of the disks was 100 K, and the repetition rate of the LD

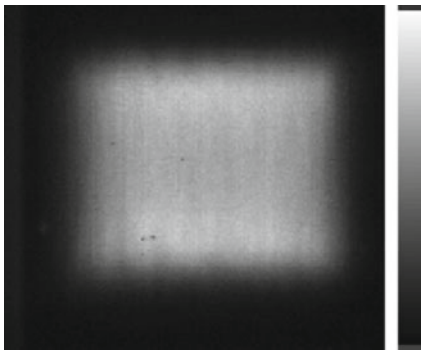

Fig. 9.7 Typical fluorescence pattern from Yb:YAG ceramics

modules was less than 1 Hz to avoid a temperature increase caused by pumping at a high repetition rate. The size of the fluorescent pattern was evaluated as 55 × 63 mm, and a smooth intensity profile in the pattern was observed. From the comparison between the fluorescent pattern (shown in Fig. 9.7) and a typical NFP of an LD module (shown in Fig. 9.6), the longitudinal line profile formed by the LD bars was clearly improved by the superposing effect of the four LD modules. However, strong upper and lower intensity distributions still remained. These distributions will be suppressed by optimizing the optical aberration management of the LD modules.

We conducted an experiment to evaluate the small-signal gain (SSG) characteristics of this laser amplifier. Generally, SSG can be expressed by the following formula.

$$G_0 = e^{\frac{E_{\mathrm{st}}\sigma_{\mathrm{em}}}{h\nu}\times l} = e^{\frac{E_{\mathrm{st}}}{E_s}l} = e^{g_0 l} \tag{1}$$

Here, G_0 is the SSG value, E_{st} is stored energy density, σ_{em} is the stimulated emission cross section, ν is oscillation frequency, c is the speed of light, h is the Planck constant, and l is gain length. In addition, Es is defined as a saturation fluence, and g_0 is defined as a SSG coefficient. In the experiment, a probe pulse with a wavelength of 1030 nm, pulse duration of about 100 ns, and pulse energy of about 1 μJ were input into this laser amplifier, and the amplification factor of the probe pulse with respect to the pump energy by the LD modules was measured. The cooling temperature of the Yb:YAG ceramic disks was 100 K, and the repetition rate of the pumping by the LD modules was less than 1 Hz. To suppress the temperature increase in the Yb:YAG ceramic disks caused by the pumping, the repetition rate was kept low.

The experimental results are shown in Fig. 9.8. The horizontal axis shows the pump energy, and the vertical axis shows the SSG values on a logarithmic scale. The SSG increases exponentially with respect to the stored energy, as represented by Eq. (1). A SSG of 20.4 times was obtained at 450.4-J pumping energy, and the energy stored inside Yb:YAG ceramic disks was calculated to be 149.0 J from Eq. (1) by assuming a pumped volume of 346.5 cm^3. These results show the feasibility of a laser amplifier with high stored energy as well as high gain using low-temperature-cooled Yb:YAG ceramics.

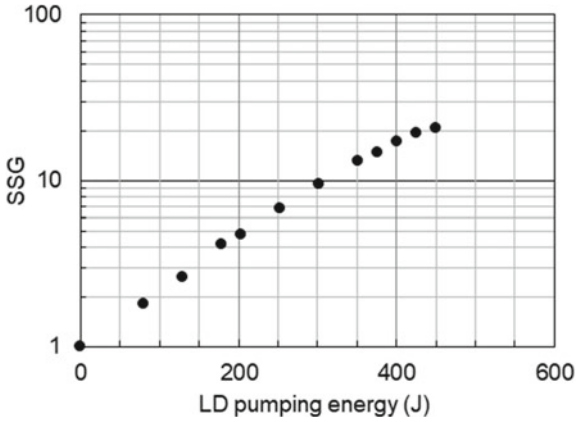

Fig. 9.8 Small-signal gain (SSG) characteristics

The $g_0 \times l$ (an index for generating unexpected oscillation (parasitic oscillation) in the laser medium) on the probe pulse propagation axis was evaluated to be about 3 from a SSG of 20.4 times. If $g_0 \times l$ exceeds 4, parasitic oscillation would start or the amplification of spontaneous emission (ASE) would significantly increase. From this estimation of $g_0 \times l$, the Yb:YAG ceramic disks exhibit a high SSG of 20.4 times while maintaining high stored energy of 149.0 J without parasitic oscillation. From Fig. 9.8, it was confirmed that the SSG showed good linearity in the logarithmic scale with respect to the pump energy up to 300 J; however, there was a tendency for this to gradually saturate over 300 J. The $g_0 \times l$ was calculated to be about 3.89 for 450.4-J pumping when the diagonal length in the three-dimensional pumping region in the Yb:YAG ceramic disks was used as the maximum gain length. Thus, it is assumed that the ASE inside the Yb:YAG ceramics significantly increases at over 300 J of pump energy.

9.2.4 Demonstration of 55.4 J Laser-Pulse Amplification

We conducted an energy-extraction experiment of this laser amplifier. An input pulse with a pulse duration of 20 ns and pulse energy of about 1 J was used. The seed pulse passed through the laser amplifier two times by constructing a pulse propagating system using an image-relaying telescope and a 0-degree reflection mirror. The experimental results of output energy with respect to the input energy are shown in Fig. 9.9. An output energy of 55.4 J was obtained when the input was 0.98 J. The solid line in Fig. 9.9 indicates the calculation results. The calculation code is based on the *Franz-Nodvik* equation model [17]. The stored energy estimated from the SSG measurement was used for the calculation. The results of the experiment were slightly lower than those of the calculation. The extraction efficiency was 36.5%, and the optical-to-optical conversion efficiency was 12.3%. The calculation results indicate that higher output energy could be expected due to the increased input energy.

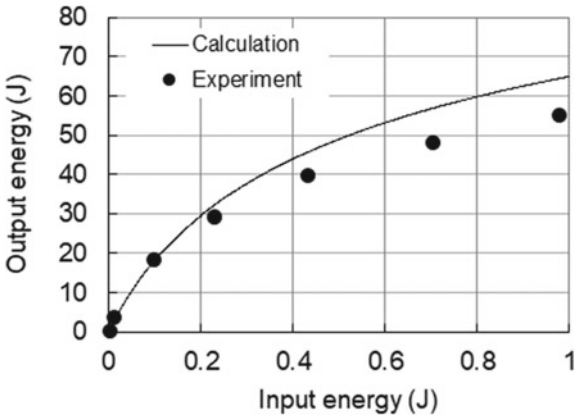

Fig. 9.9 Output energy characteristics as a function of input energy

The NFP of the output pulse is shown in Fig. 9.10. The pattern profile was similar to the fluorescent pattern shown in Fig. 9.7. Then the average fluence was evaluated to be 2.36 J/cm^2 with the pattern size of 46 $\times$ 51 mm.

In this section, we demonstrate high-energy laser amplification with high gain characteristics with an LD-pumped cryogenically cooled Yb:YAG ceramic multi-disk laser amplifier. This serves as a feasibility study of compact kilo-joule class DPSSLs.

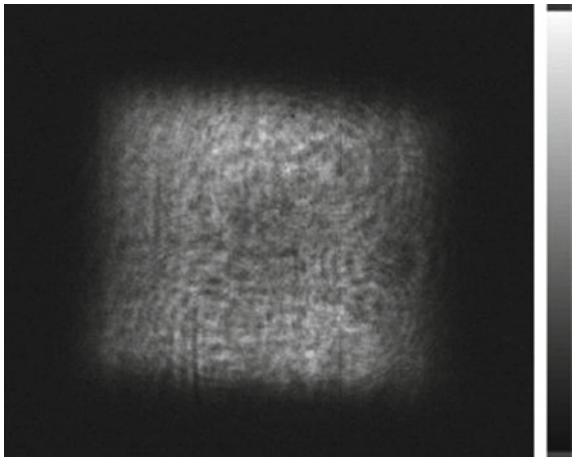

Fig. 9.10 NFP of 55-J output pulse

9.3 Demonstration of High-Energy Laser Output with High Energy-Extraction Efficiency Characteristics of Cryogenically Cooled Yb:YAG-Ceramics Laser Amplifier

In this section, we report a demonstration of 117 J laser output with over 40% energy-extraction efficiency using an LD-pumped cryogenic-helium-gas face-cooled Yb:YAG ceramic multi-disk laser amplifier [18]. The results indicate the feasibility of practical kilo-joule-class DPSSLs by demonstrating simultaneously high energy output and high-efficiency characteristics.

9.3.1 Construction of LD-Pumped Cryogenic-Helium-Gas Face-Cooled Yb:YAG Ceramic Multi-disk Laser Amplifier

A photograph of this amplifier is shown in Fig. 9.11, and its conceptual design is similar to the cryogenically side-cooled Yb:YAG ceramic laser amplifier discussed in Sect. 9.2. Four LD modules are located around a laser chamber as the pumping source. A seed pulse propagates between the upper and lower LD modules. Six Yb:YAG ceramic disks are placed in the center of the laser chamber. The disks are arranged with slight gaps to allow the helium gas to flow on each end-face. Helium gas characteristics can be controlled at a temperature of 150 K to 300 K and pressure of 0.5 MPa or less. Helium gas temperature is controlled with the flow rate of liquid nitrogen at the heat exchanger. The laser chamber has a two-layer structure with an inner high-pressure vessel for helium gas and an outer vacuum vessel for thermal

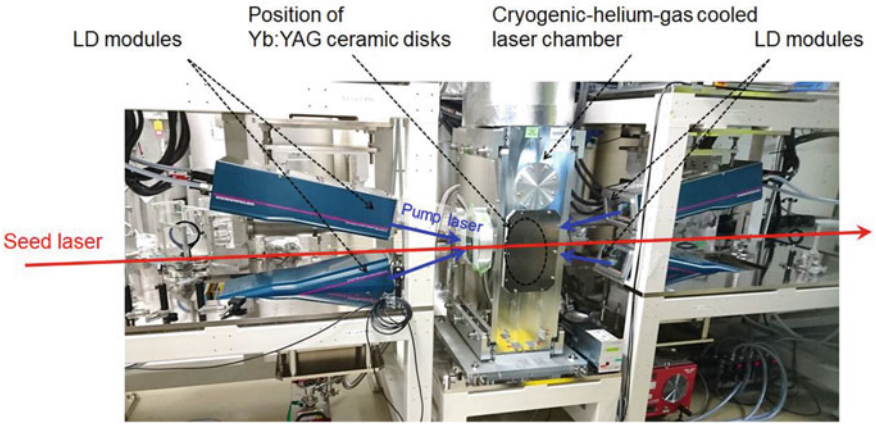

Fig. 9.11 Cryogenic-helium-gas face-cooled Yb:YAG ceramic multi-disk laser amplifier

insulation. Two sapphire windows joined on a metallic flange are attached to the high-pressure vessel as optical windows for delivering a seed pulse and four pump pulses into the Yb:YAG ceramic disks. A sapphire window requires extremely high sealing characteristics for low-temperature and high-pressure helium gas without causing leakage into the vacuum vessel. Cryogenic-helium-gas flows upward from the bottom of the laser chamber and then flows between the laser chamber and a cryogenic-helium-gas circulation device in a closed loop. The returned helium gas from the laser chamber is cooled by liquid nitrogen at the heat exchanger after being pumped up by the fan. The cooling capacity of the heat exchange is over 7 kW.

The size of a Yb:YAG ceramic disk in this amplifier is 120 mm in diameter by 10 mm in thickness and has a 7-mm-wide Cr:YAG ceramic cladding layer on the side-surface. These Yb:YAG ceramic disks and Cr:YAG ceramic layers are joined by sintering. Three types of Yb:YAG ceramic disks with different Yb ion-doping concentrations are arranged to average the stored energy distribution over all of the disks.

9.3.2 Characteristics of Pumping LD Modules

Table 9.3 gives the specifications of an LD stack used for an LD module (shown by photo in Fig. 9.12). For this LD module, a passive-cooled LD stack (LE0703MOD, Hamamatsu Photonics K.K.) was used. This LD stack can output a peak power of 7.5 kW at a driving current of 800 A. Then, output energy reaches 7.5 J at a pulse duration of 1 ms. The maximum repetition rate is 10 Hz due to passive cooling.

Table 9.3 Typical specifications of LD stack

Parameter	Value
Peak power	7.5 kW
Wavelength	940 nm
Pulse duration	1 ms
Repetition rate	10 Hz
Number of LD bars	10 bars

Fig. 9.12 LD stack

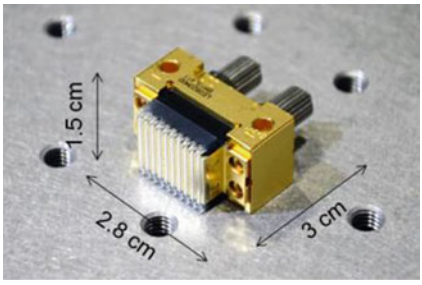

Table 9.4 Typical specifications of LD module

Parameter	Value
Peak power	>100 kW
Wavelength	940 nm
Repetition rate	10 Hz
Irradiation intensity	2 kW/cm^2
Irradiation size (Rectangle)	Adjustable between from 60 × 60 mm to 85 × 85 mm

Comparing this LD stack with that shown in Fig. 9.4, the output peak power of the LD bar is enhanced by more than three times, and the size of the LD stack is reduced to less than 1/10 while maintaining the same output energy.

The specifications of a pumping LD module are given in Table 9.4 (shown by photo in Fig. 9.13). The LD module can output over 100 J by operating at 100-kW peak power with a 1-ms-pulse duration. This LD module was designed using a superposing scheme of all LD stacks used in the LD module, the same as the pre-LD module shown Fig. 9.5. A unique characteristic of this LD module is that the rectangular irradiation pattern at the working distance of 560 mm can be changeable between from 60 × 60 mm to 85 × 85 mm by adjusting the internal optical system. The typical NFP of this LD module is shown in Fig. 9.14. The beam size is 85 × 72 mm. By optimizing the optical design, the uniformity of the intensity on the vertical-line shape profiles

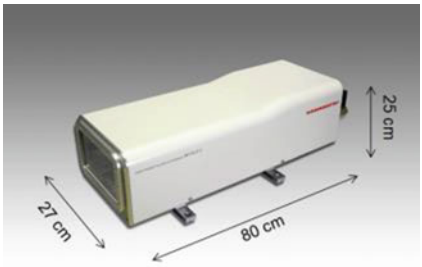

Fig. 9.13 LD module

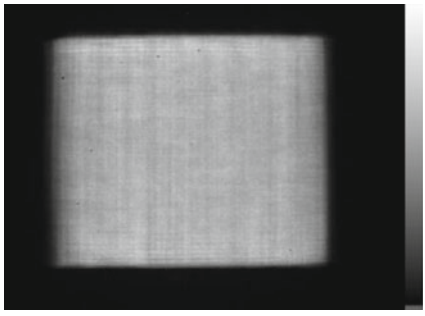

Fig. 9.14 Typical output NFP of LD module

and on the upper and lower distributions dramatically improved compared with the pattern measured in the previous works shown in Fig. 9.6.

9.3.3 *Characteristics of Small Signal Gain and Energy Extraction*

Figure 9.15 shows a typical fluorescence pattern of the Yb:YAG ceramic disks pumped by the LD modules from four direction in this laser amplifier. The cooling temperature of the Yb:YAG ceramic disks was 175 K, and the repetition rate of the LD modules was 1 Hz. A uniform and smooth pattern was obtained by improving the characteristics of the LD modules. The size of the fluorescent pattern was evaluated as 70.0 × 58.6 mm. The pumping intensity on the Yb:YAG ceramics was then evaluated as 2.7 kW/cm^2 for each LD module. It was also confirmed that flowing cryogenic-helium-gas had no effect on the fluorescent pattern on the Yb:YAG ceramic disks.

We measured the SSG characteristics of this laser amplifier. In this experiment, the cooling temperature of the Yb:YAG ceramic disks was 175 K, and the repetition rate of LD modules was 0.5 Hz. The experimental results are shown in Fig. 9.16. The horizontal axis shows the pump energy, and the vertical axis shows the SSG values on a logarithmic scale. A SSG of 4.5 times was confirmed at about 444.4-J pumping energy. The calculation results are shown with a solid line. The experimental results show good agreement with the calculation results up to 300 J. However, a slight deviation was observed over at 300 J. The ASE was much smaller than that in Fig. 9.8 because the SSG of this laser amplifier was around 4 times due to a higher cooling temperature of 175 K. One of the reasons for this saturation in SSG characteristics is assumed to be nonradiative loss in the Yb:YAG ceramics caused

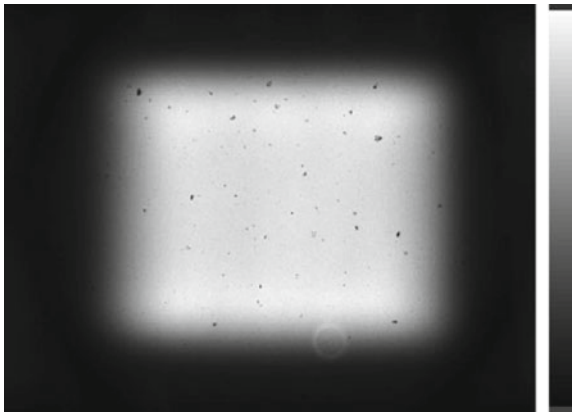

Fig. 9.15 Typical fluorescent pattern of Yb:YAG ceramics

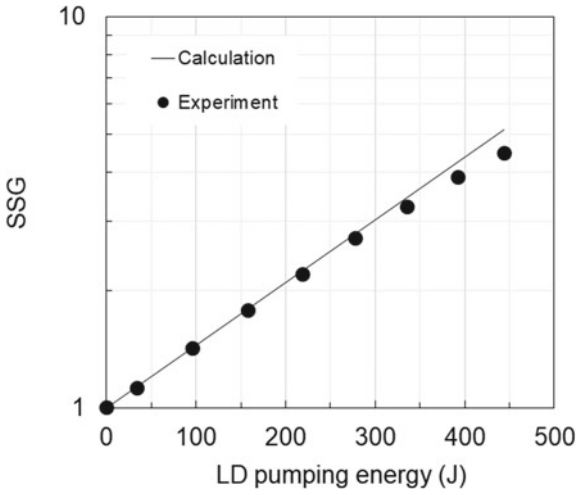

Fig. 9.16 SSG characteristics

by the Stokes shift and quantum efficiency. This nonradiative loss cause temperature increasing in the Yb:YAG ceramics.

We conducted an energy-extraction experiment using this laser amplifier. The input laser pulse had a pulse energy of 5 J, pulse duration of 40 ns in Gaussian shape, beam size of 7 × 7 cm, and pulse repetition rate of 0.05 Hz. We constructed an experimental set-up for single- and double-pass amplification. The seed pulse passed through the laser amplifier two times with different incident angles. The NFP at the first pass on the Yb:YAG ceramic disks was image-relayed to the ceramic disks in the second pass. The experimental results are shown in Fig. 9.17. The horizontal axis shows the pump energy by the LD modules, and the vertical axis shows the

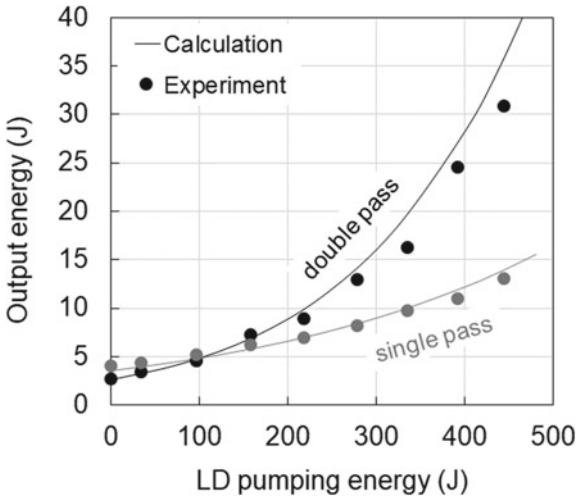

Fig. 9.17 Results of energy-extraction experiment

output energy of the laser amplifier. We obtained a 13.0 J output energy at single-pass amplification and 30.8 J at double-pass amplification. The pumping energy was 444 J. The calculation result simulated using the rate equation model is also shown with a solid line in Fig. 9.17. The calculation used the stored energy in the Yb:YAG ceramic disks estimated from the SSG experiment. The experimental results indicate good agreement with the calculation results, but there was a difference after exceeding a pump energy of 300 J. This difference can be explained by having the same characteristics as those estimated from the SSG experiment.

9.3.4 *Demonstration of 117-J Laser-Pulse Amplification with High Energy-Extraction Efficiency*

Figure 9.18 shows the configuration of a 100-J class high energy laser output demonstration using two cryogenic-helium-gas face-cooled Yb:YAG ceramic multi-disk laser amplifiers. These two laser amplifiers (laser heads 1 and 2) have a similar configuration in which six Yb:YAG ceramic disks are pumped by four LD modules from four directions. The maximum pump energy is 444 J for laser head 1 and 506 J for laser head 2. The pumping size on the Yb:YAG ceramic disks was 70.0 × 58.6 mm for laser head 1 and 75.4 × 58.9 mm for laser head 2. This experimental setup consisted of arranging the two laser heads, which have the double-pass amplification configuration, in series. The output pulse amplified by laser head 1 was input again to laser head 2 for double-pass amplification. An NFP and wave-front of the input pulse was relayed to the Yb:YAG ceramic disks in the two laser heads by

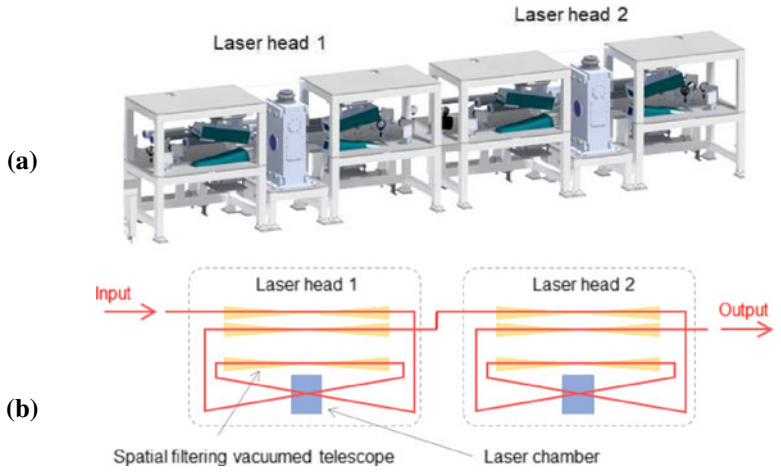

Fig. 9.18 Experimental setup for 100-J output demonstration. **a** 3D image of configuration. **b** Diagram of optical layout

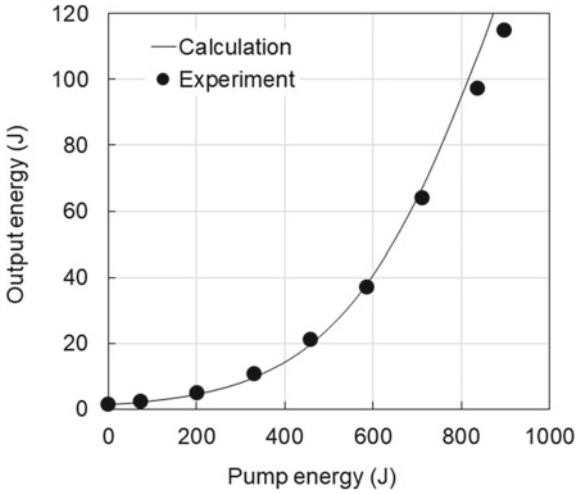

Fig. 9.19 Output energy characteristic

six vacuumed telescopes during every propagation. These telescopes also perform spatial filtering to prevent parasitic oscillation and straying laser pulses inside the two laser heads. The specifications of the input pulse for laser head 1 are the same as those from the SSG experiment for the single laser amplifier and energy extraction discussed in the previous section; the pulse energy was 5 J, pulse duration was 40 ns, and repetition rate was 0.05 Hz. In the experiment, the output energy after double-pass amplification of the two laser heads was measured by increasing the pump energy of the two laser heads simultaneously.

The output energy characteristics as a function of pump energy are shown in Fig. 9.19. A maximum output energy of 117 J was achieved at a total pump energy of 895 J in the two laser heads. The calculation results based on the rate-equation model are shown with a solid line. The optical-to-optical conversion efficiency was 12.5%. This calculation was conducted using actual characteristics of the pump energy and pumping area by the LD modules. In the calculation, pump efficiency defined by the ratio of the stored energy to pump energy was assumed to be 44% in both laser heads. This pump efficiency was evaluated from SSG measurement of laser head 1 as typical value. The experimental results indicate good agreement with the calculation results. The difference between the calculation and experiment results over 700 J is due to nonradiative transition in the Yb:YAG ceramics as in the SSG measurement. Energy extraction efficiencies of laser head 1 and 2 were evaluated as 13.4 and 42.3%, respectively. Here, the stored energies of the two laser heads of 171.3 and 210.5 J were evaluated by the multiplication of pump energy and pump efficiency of 0.44%.

An NFP of 117-J output is shown in Fig. 9.20. A smooth intensity profile without peak spots was confirmed. The smooth pumping profile obtained with four-direction pumping contributed to suppressing damage on the Yb:YAG ceramic disks. The intensity distributions at the upper and lower parts on the NFP are considered the effect of the pumping distribution, which has slight intensity modulation (Fig. 9.15).

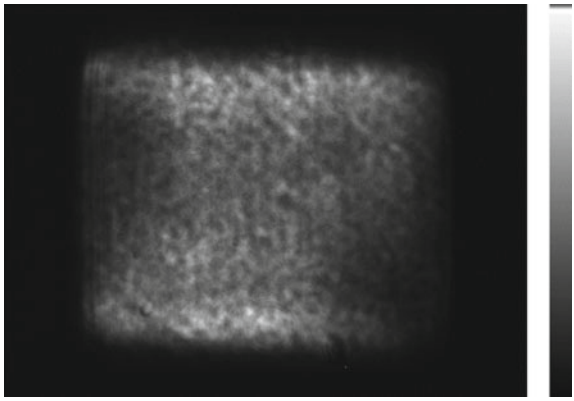

Fig. 9.20 NFP of 117 J output

The output pattern size is about 78 × 56 mm. Then the average fluence at the 117-J output is estimated to be about 2.68 J/cm^2. The reason for the dot-like profile on the NFP will be studied, along with the effect of the B-integral, in our future work.

In this section, we demonstrated high-energy laser amplification of over 100 J with high extraction-efficiency characteristics using an LD-pumped cryogenically cooled Yb:YAG ceramic multi-disk laser amplifier, thus providing a feasibility study of compact kilo-joule class DPSSLs.

9.4 Summary

In this chapter, we reported our current experimental results on cryogenically cooled Yb:YAG-ceramics laser amplifiers. This work was conducted as a feasibility study of kilo-joule class laser technologies. A high gain of 20.4 times with high stored energy of 149.0 J was demonstrated with a conductively side-cooled Yb:YAG ceramic multi-disk laser amplifier having a cooling temperature of 100 K. A 117-J output energy was also demonstrated with a cryogenic-helium-gas face-cooled Yb:YAG ceramic multi-disk laser amplifier having a cooling temperature of 175 K. Consequently, maximum efficiency as energy extraction was evaluated to be 42.3%. The demonstration of a high-gain laser amplifier while operating at a low temperature of about 100 K confirmed the feasibility of a compact and highly efficient design for kilo-joule-class DPSSLs.

We will develop fundamental laser technologies to demonstrate the high-energy and high-repetition capabilities made possible by using a cryogenic helium gas face-cooled Yb:YAG ceramic multi-disk laser amplifier. This further work will serve as a step toward achieving practical kilo-joule DPSSLs.

Acknowledgements A part of this report is based on the results obtained from a project commissioned by the New Energy and Industrial Technology Development Organization (NEDO), Japan.

References

1. T.H. Mainman, Nature **187**, 493 (1960)
2. F.J. McClung, R.W. Hellwarth, J. Appl. Phys. **33**, 828 (1962)
3. H.W. Mocker, R.J. Collins, Appl. Phys. Lett. **7**, 270 (1965)
4. A.J. DeMaria, D.A. Stetser, H. Heynau, Appl. Phys. Lett. **8**, 174 (1966)
5. D.A. Stetser, A.J. DeMaria, App. Phys. Lett. **9**, 118 (1966)
6. M. Hentschel, R. Kienberger, C. Spielmann, G.A. Reider, N. Milosevic, T. Brabec, P. Corkum, U. Heinzmann, M. Drescher, F. Krausz, Nature **414**, 509 (2001)
7. G. Brumfiel, Nature **491**, 170 (2012)
8. O.A. Hurricane, D.A. Callahan, D.T. Casey, P.M. Celliers, C. Cerjan, E.L. Dewald, T.R. Dittrich, T. Döppner, D.E. Hinkel, L.F. Berzak Hopkins, J.L. Kline, S. Le Pape, T. Ma, A.G. MacPhee, J.L. Milovich, A. Pak, H.-S. Park, P.K. Patel, B.A. Remington, J.D. Salmonson, P.T. Springer, R. Tommasini, Nature **506**, 343 (2014)
9. D. Strickland, G. Mourou, Opt. Commun. **56**, 291 (1985)
10. S. Wills, Opt. Photonics News **31**, 30 (2020)
11. R.L. Byer, Science **239**, 742 (1988)
12. A. Bayramian, P. Armstrong, E. Ault, R. Beach, C. Bibeau, J. Caird, R. Campbell, B. Chai, J. Dawson, C. Ebbers, A. Erlandson, Y. Fei, B. Freitas, R. Kent, Z. Liao, T. Ladran, J. Menapace, B. Molander, S. Payne, N. Peterson, M. Randles, K. Schaffers, S. Sutton, J. Tassano, S. Telford, E. Utterback, Fusion Sci. **52**, 383 (2007)
13. R. Yasuhara, T. Kawashima, T. Sekine, T. Kurita, T. Ikegawa, O. Matsumoto, M. Miyamoto, H. Kan, H. Yoshida, J. Kawanaka, M. Nakatsuka, N. Miyanaga, Y. Izawa, T. Kanabe, Opt. Lett. **33**, 1711 (2008)
14. P. Mason, M. Divoky, K. Ertel, J. Pilar, T. Butcher, M. Manus, S. Banerjee, J. Phillips, J. Smith, M.D. Vido, A. Lucianetti, C. Hernandez-Gomez, C. Edwards, T. Mocek, J. Collier, Optica **4**, 438 (2017)
15. http://www.nedo.go.jp/koubo/CD3_100053.html
16. T. Sekine, Y. Takeuchi, T. Kurita, Y. Hatano, Y. Muramatsu, Y. Mizuta, Y. Kabeya, Y. Tamaoki, Y. Kato, Proc. SPIE **10082**, 100820U (2017)
17. L.M. Frantz, J.S. Nodvik, J. Appl. Phys. **34**, 2346 (1963)
18. T. Sekine, T. Kurita, M. Kurata, Y. Hatano, Y. Muramatsu, T. Morita, Y. Kabeya, T. Iguchi, T. Watari, R. Yoshimura, Y. Tamaoki, Y. Takeuchi, Y. Mizuta, K. Kawai, Y. Zheng, Y. Kato, T. Suzuki, N. Kurita, T. Kawashima, S. Tokita, J. Kawanaka, N. Ozaki, Y. Hironaka, K. Shigemori, R. Kodama, R. Kuroda, E. Miura, submitted to High Energy Density Physics

Chapter 10
The Shanghai Superintense Ultrafast Laser Facility (SULF) Project

Zebiao Gan, Lianghong Yu, Cheng Wang, Yanqi Liu, Yi Xu, Wenqi Li, Shuai Li, Linpeng Yu, Xinliang Wang, Xinyan Liu, Junchi Chen, Yujie Peng, Lu Xu, Bo Yao, Xiaobo Zhang, Lingru Chen, Yunhai Tang, Xiaobin Wang, Dinjun Yin, Xiaoyan Liang, Yuxin Leng, Ruxin Li, and Zhizhan Xu

Abstract We report the recent progress on the Shanghai Superintense Ultrafast Laser Facility (SULF) project. The schematic design of SULF is described. The upgrade information from SULF laser prototype to SULF 10 PW laser user facility is presented in detail. A high contrast front is developed to generate high-quality clean seed pulses which are then stretched to about 2 ns by a new double-grating Öffner stretcher. A Dazzler is used to control the high-order phase distortions and shape the spectrum of the laser pulses simultaneously. The laser pulses are amplified to 7 J energy in the 1 Hz pre-amplifiers system before injected into the three stages large aperture main amplifiers system. The first two main amplifiers are pumped by five commercial lasers which can be operated at 1 shot/min. The final main amplifier is pumped by six home-built high energy frequency doubled Nd:glass lasers at a repetition rate of 1 shot/3 min. The final amplifier output energy is ~408 J with high stability under a pump energy of ~530 J. Compressed pulse duration of the amplified laser and the total transport efficiency for compression is measured to be 22.4 fs and 70.52% respectively. The experimental results demonstrate that SULF user facility has the capacity to deliver 10 PW peak power femtosecond pulses.

10.1 Introduction

The invention and rapid development of high-intensity, ultra-short lasers have undoubtedly revolutionized the scientific world. Due to their ability to concentrate a large amount of energy within extremely short time intervals, as well as coherent laser light can be focused to the diffraction limit, people can create extreme physical conditions of ultrahigh-energy density in the laboratory. With multi-terawatt laser

Z. Gan · L. Yu · C. Wang · Y. Liu · Y. Xu · W. Li · S. Li · L. Yu · X. Wang · X. Liu · J. Chen · Y. Peng · L. Xu · B. Yao · X. Zhang · L. Chen · Y. Tang · X. Wang · D. Yin · X. Liang · Y. Leng · R. Li (✉) · Z. Xu
State Key Laboratory of High Field Laser Physics and CAS Center for Excellence in Ultra-Intense Laser Science, Shanghai Institute of Optics and Fine Mechanics(SIOM), Chinese Academy of Sciences(CAS), Shanghai 201800, China
e-mail: ruxinli@mail.siom.ac.cn

K. Yamanouchi et al. (eds.), *Progress in Ultrafast Intense Laser Science XVI*,
Topics in Applied Physics 141, https://doi.org/10.1007/978-3-030-75089-3_10

systems, focused intensities are mostly in the range of 10^{19}–10^{21} W/cm^2. This ability opens for study particle (electron and proton) acceleration [1–4], x-/γ-ray generation [5–8] and plasma physics [9–12]. For the investigation of radiation reaction and quantum electrodynamics effects in plasmas, multi petawatt (PW) or even 100 PW laser systems are desired to achieve focused intensities over 10^{22}–10^{24} W/cm^2 [13, 14].

Modern femtosecond high power lasers usually utilize MOPA (master oscillator power amplifier) configuration, with a mode-locked oscillator generated femtosecond few-cycle seed pulse, then a series of optical amplifiers to boost the output power. However, direct amplification of ultrashort laser pulse will produce very high peak intensities, resulting in detrimental nonlinear pulse distortion or even destruction of the gain medium. It was after the chirped pulse amplification (CPA) technique [15] was introduced in 1985 by Gérard Mourou and Donna Strickland that successful amplification of ultrashort laser pulse was achieved. By passing through a strongly dispersive element (the pulse stretcher, e.g., a grating pair or a long fiber) before amplification, the pulses are chirped and temporally lengthened to a much longer duration. This reduces the pulses peak power, avoids damage to the gain medium, and allows efficient energy extraction from the laser amplifier. After amplification, a compressor is used to remove the chirp and compress the pulses to ultrashort duration. The concept of CPA was then further extended by Audrius Dubietis in 1992 to present the method of optical parametric chirped pulse amplification (OPCPA) [16]. In contrast to CPA where amplification is based on stimulated emission in a laser gain medium, OPCPA transfers energy from a pump pulse to a stretched seed pulse through optical parametric amplification (OPA) in a nonlinear crystal.

CPA and OPCPA have become the standard solutions to build a petawatt class laser system. As showed in the reviews [17, 18], over 50 facilities that are, or have been, operational, under construction, or in the preparatory design phase around the world. Gérard Mourou and Donna Strickland have won the 2018 Nobel Prize in Physics due to their invention of the CPA technique, which made these high-intensity ultrashort lasers possible. After the discovery of ultra-broadband phase matching at the central wavelength of 910 nm can be achieved in the DKDP crystal [19, 20], which aperture can be 30 cm or even larger, several more ambitious projects are proposed to approaching 100–200 PW level outputs using OPCPA as the principal technique [17]. Of course, there is still a long way to overcome the 100 PW barrier. So many problems have yet to be solved, including high-quality large-aperture crystals, large compressor gratings, pump laser systems, and many more. Compared to OPCPA, the Ti:Sapphire (Ti:Sa) CPA technique has a number of important advantages such as higher stability and efficiency as well as lower requirements of the pump laser. These features make the Ti:Sa CPA technique the workhorse in most petawatt class laser systems with outputs of >1PW. The CPA technique is also thought to be on the verge of maturing to achieve 10-PW laser pulses output [21–23].

SULF (Shanghai Superintense Ultrafast Laser Facility) is a Ti:Sa CPA laser user facility built by a team from SIOM's (Shanghai Institute of Optics and Fine Mechanics) State Key Laboratory of High Field Laser Physics. SULF is located in a purpose-built building in the joint laboratory of SIOM and Shanghai Tech University.

The civil engineering construction started in December 2016 and has been completed in June 2018. In a neighboring building, the SULF prototype was constructed in early 2016 to carry out pre-research. Several important subsystems, such as high contrast front end, large-aperture Ti:Sa main amplifiers, dispersion control, wavefront correction and pump laser systems are verified by a performance test in the SULF prototype. SULF user facility began installation in August 2018, we upgrade 10 PW laser system based on pre-research in SULF prototype.

In this chapter, the SULF project is described. After introducing the structure of the SULF user facility, we focus on the SULF 10 PW laser system. The results of previous verified experiments in SULF prototype as well as the latest progress in SULF 10 PW laser user facility are presented. In the end, conclusions are drawn and prospects for future developments are discussed.

10.2 The Schematic Design of SULF

The laboratory structure of SULF is schematically illustrated in Fig. 10.1. It includes four major parts: laser systems, experimental end-stations, auxiliary facilities, and data center.

The laser system will deliver three beamlines: a 10 PW laser operated at 1shot/min, a 0.1 Hz 1 PW laser, and a 1 Hz 100 TW laser. Each laser has its own optical pulse compressor. The 10 PW laser and 1 PW laser are driven by a same oscillator with two parallel amplification arms. The 100 TW laser is generated by a beam splitter on the output port of the 1 Hz preamplifiers of the 10 PW laser. The three beamlines can be used independently or be used simultaneously in some particular experiments.

The laser system outputs, as well as the secondary radiation and particle sources driven by lasers, will be used in three experimental end-stations:

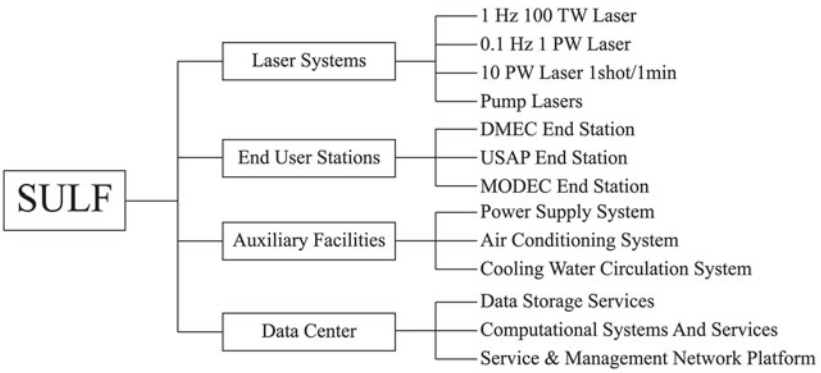

Fig. 10.1 The structure of SULF

(1) DMEC (Dynamic of Materials under Extreme Conditions) end station. DMEC end station will allow researches such as high-order harmonic generation by intense ultrafast laser pulses, dynamic characteristics investigation of critical materials under extreme conditions, non-destructive testing of air materials or nuclear materials, etc.
(2) USAP (Ultrafast Sub-atomic Physics) end station.
USAP end station will allow researches such as accelerating charged particles (electrons and protons) to relativistic velocity, investigation of extreme phenomena in strong-field quantum electrodynamics, photonuclear physics, etc.
(3) MODEC (Molecule Dynamics and Extreme-fast Chemistry) end station.
MODEC end station will allow researches such as detection and control of chemical reactions, study of the structures, movements, and interactions of macromolecules, generating intense terahertz radiation, etc.

The auxiliary facilities include power supply systems, air conditioning systems, cooling water circulation systems, processing and testing equipment, etc. Auxiliary facilities provide necessary support and guarantee for the construction and daily operation of SULF.

The data center is set up to provide informational management of SULF. While realizing the efficient automatic operation of SULF, it can meet users' demands for real-time collection, transmission, processing, storage and sharing of experimental data.

10.3 The SULF 10 PW Laser System

The workhorse of the SULF facility is a 10 PW laser system. In a neighboring building, the SULF prototype was constructed in early 2016 to carry out pre-research and investigate the performance of the subsystems. SULF prototype achieved 5.4 PW output in the end of 2016 [23] and demonstrated 339 J energy output with a 235-mm diameter Ti:Sa CPA amplifier in 2017 [24]. The SULF building was completed in June 2018, the laser systems were then transferred into the new building and were reinstalled as SULF user facility. According to the pre-research experiment results in SULF prototype, we redesigned several subsystems and upgraded the whole 10 PW laser system.

Figure 10.2 shows the block diagram of the SULF 10 PW laser system. In the following section, the design of each subsystem and the upgrade information from SULF prototype to SULF 10 PW laser user facility are presented in detail.

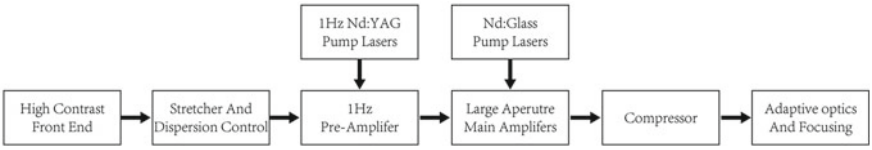

Fig. 10.2 Block diagram of the SULF 10 PW laser System

10.3.1 High Contrast Front-End

The focused peak intensity of the petawatt class laser pulse has now reached 10^{21}–10^{22} W/cm^2, and may reach 10^{23} W/cm^2 in the near future [13, 14]. For experimental studies of the laser matter interaction with such high intensities, pre-pulse or amplified spontaneous emission (ASE) with intensities at the 10^{11} W/cm^2 level can generate significant unwanted pre-plasma on target [9]. Therefore, for focused laser intensity at 10^{21} W/cm^2, the temporal contrast should be better than 10^{-10} to limit destructive pre-plasma dynamics. At the intensities of 10^{22} W/cm^2 to 10^{23} W/cm^2, higher temporal contrast is required.

SULF 10 PW laser is based on double chirped pulse amplification (DCPA) with intermediate temporal pulse filtering. The first CPA stage is a commercial Ti:Sa laser system (Coherent, Astrella). Astrella can deliver a reliable output with pulse energy of 3.9 mJ and pulse duration <40 fs. The spectrum bandwidth and contrast ratio of the initial pulse from the Astrella is measured to be ~30 nm at full width at half maximum (FWHM) and ~2 × 10^{-8} at tens of picoseconds before the main pulse respectively. A novel pulse cleaning technique was developed in SULF prototype to generate high-contrast and broadband seed pulses for the second CPA stage.

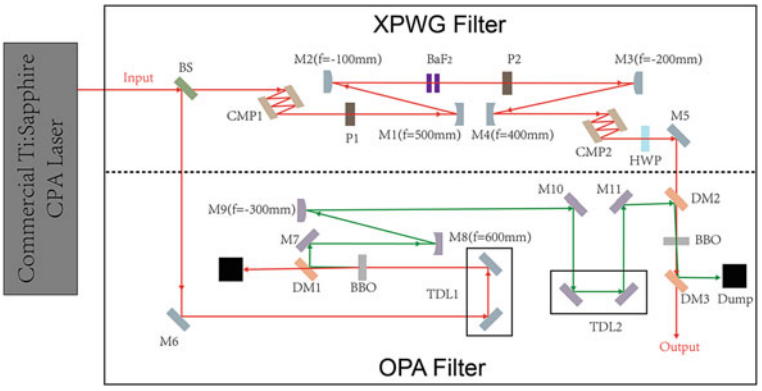

Fig. 10.3 Experimental scheme of the high contrast front end in SULF 10 PW laser. BS, beam splitter; M, mirror; CMP, chirped mirror pair; P, polarizer; DM, dichroic mirror; HWP, half wavelength plate; TDL, time delay line

Figure 10.3 shows the experimental scheme of the high contrast front end in the SULF 10PW laser, which combines cross-polarized wave generation (XPWG) and femtosecond OPA to generate high-quality clean seed pulses [25]. The Astrella output is divided into two laser beams by a beam splitter. The transmitted laser pulse with an ~80 μJ energy is the seed pulse for the XPWG filter, which is constructed using two BaF_2 crystals ([011]-cut orientation, 1.5 mm in thickness), two crossed polarizers with extinction ratios better than 10^5, two sets of chirped mirrors and two telescopes. The BaF_2 crystals are placed in the air and are optimized to ensure good beam quality and long-term stability. After the first polarizer (P1), the seed pulse is focused by an all-reflective telescope (formed by M1 and M2). The second polarizer (P2) extracts the XPWG signal with a 9 μJ energy output, which is then up-collimated by the second telescope (formed by M3 and M4). Two sets of chirped mirror pairs (CMP1 and CMP2) are used to compensate for the residual chirp introduced by optical components. The XPWG signal is then set to horizontally polarized by an achromatic λ/2 waveplate (HWP) and serves as the seed pulse for the subsequent femtosecond OPA.

The 3.82 mJ reflected laser pulse by beam splitter is frequency doubled by a 1-mm-thick beta-barium borate (BBO) crystal with 47% conversion efficiency. The second harmonic generation (SHG) pulse is separated by a dichroic mirror (DM1) and down-collimated by an all-reflective telescope (M9 and M10) to serve as the pump pulse in the femtosecond OPA stage. A 0.5 mm thick BBO crystal is used in the type-I phase matching OPA process. The SHG pump pulse and the signal pulse are synchronized by two time-delay-lines (TD1 and TD2) and combined by a dichroic mirror (DM2). The energy of the signal pulse after the DM2 decreases to ~5 μJ, then it is amplified to ~110 μJ in the OPA process. The energy gain is more than 20 times. Consequently, the temporal contrast of the signal pulse is also promoted by more than 20 times. The energy fluctuation of the final clean pulse in one hour is as low as 1.8% (rms), and a smooth beam profile can be obtained in our experiment [25].

Spectral evolution in the front end is shown in Fig. 10.4. After the XPWG filter, the spectral bandwidth of the seed pulse was significantly enlarged, and the femtosecond OPA process further shapes the spectrum. The final clean pulse has a total bandwidth exceeding 60 nm (FWHM), nearly twice that of the initial pulse, which can support a Fourier-transform-limited pulse duration of 17 fs.

As shown in Fig. 10.5, The measured contrast ratio of the initial pulse from Astrella is approximately 2×10^{-8} at tens of picoseconds before the main pulse. Limited by the dynamic range of the measurement, the measured contrast ratio of the clean pulse is only ~10^{-10} at several picoseconds before the main pulse. According to the extinction ratio of the polarizer (better than 10^5:1) in the XPWG filter and the gain (~22 times) in the femtosecond OPA process, the temporal contrast enhancement should be about 6 orders of magnitude in theory. Correspondingly, the estimated temporal contrast of the final clean pulse should be 10^{-13}–10^{-14}.

The above high contrast front end has been successfully demonstrated in the SULF prototype. The energy of the clean seed pulse was amplified to 7 J in 1 Hz pre-amplifier system, the measured contrast ratio was much better than 10^{-11} at 100 ps

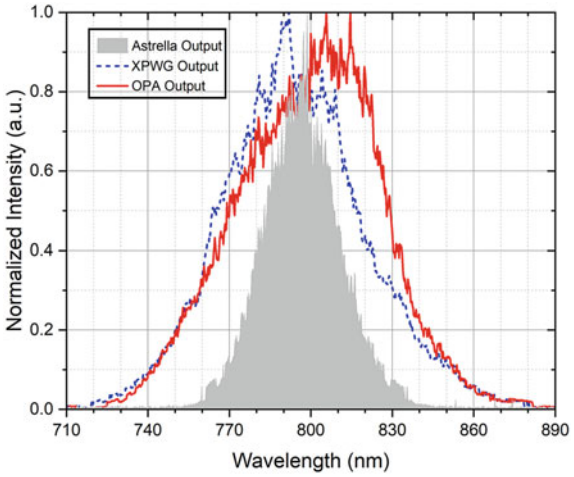

Fig. 10.4 Spectral evolution in the front end. Gray, initial pulse from Astrella; blue, output pulse from XPWG filter; red, femtosecond OPA output pulse

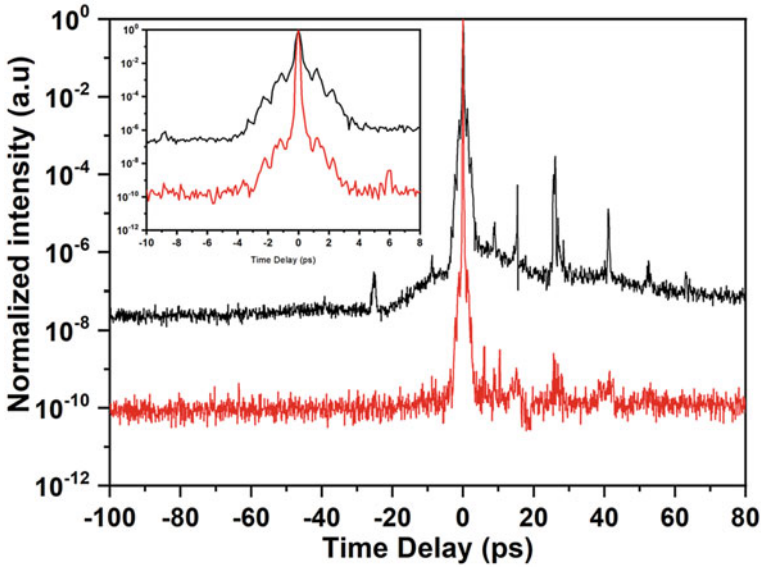

Fig. 10.5 Measured temporal contrast of the Astrella output pulse (black curve) and the final clean pulse (red curve). The inset shows the measured temporal contrast on the 18 ps scale

before the main pulse. We also used a single-shot third-order cross-correlator [25] to measure the temporal contrast of the large aperture main amplifier output with a pulse energy of about 50 J. The measured temporal contrast reached 10^{-10} level at 50 ps before the main pulse, which is the maximal dynamic range of the measurement tool. In SULF 10 PW laser user facility, a high contrast front end with the same structure is applied. The evolution of the pulse temporal contrast in the SULF 10 PW laser was investigated both theoretically and experimentally [26]. The study results provide the guideline for further improvement. We redesign several subsystems of SULF 10 PW laser, as shown in the following sections.

10.3.2 Stretcher and Dispersion Control

The CPA technique employs the concept of laser pulse stretching in the temporal domain and compression to ultrashort duration after laser pulse amplification. In SULF prototype, the high-contrast seed pulses were stretched to about 2 ns by a traditional Öffner stretcher before injected into the second CPA stage. The stretcher was designed as eight-pass configuration. The radii of curvature of the concave and convex mirrors are 1600 and 800 mm, respectively. The stretcher used a 1480 lines mm^{-1}, gold-coated grating with an incidence angle of 50°.

In PW laser systems, diffraction grating pairs are commonly adopted as a pulse compressor to compensate for the spectral phase distortions imposed by large amounts of optical components. The total group velocity dispersion (GVD) and third-order dispersion (TOD) of the laser system can be reduced to zero by adjusting the incidence angle and the slant distance of the gratings in compressor. For broadband laser pulse, the residual fourth-order dispersion over the required spectral range also needs to be compensated to achieve a Fourier-transform-limited pulse. In SULF prototype, a grism pair was utilized to control the high-order dispersion. The grism separation, angle of incidence and slant distance of the grating compressor were carefully controlled to compensate the dispersion up to fourth order. The 5.4 PW peak power recompressed pulse with a duration of 24 fs was obtained in the single-shot mode [27].

The Öffner stretcher and grism pair had played an important role in the SULF prototype. Due to the low grating efficiency, the transmission efficiency of the stretcher and the grism pair was measured to be only 28.5% and 10%, respectively. The study of pulse temporal contrast evolution in the SULF 10 PW laser indicates that the energy loss in the stretcher and grism pair will significantly degrade the temporal contrast of the laser system. Therefore, we redesign and upgrade the subsystem of stretcher and dispersion control in the SULF 10 PW laser user facility.

In SULF 10 PW laser system, grating in the standard Öffner stretcher will be ~375 mm from the center of the sphere. The spherical aberration cannot be neglected. It is also difficult to obtain a high-quality beam from the traditional One-grating Öffner stretcher when pulse spectrum broader than 100 nm. In SULF 10 PW laser user facility, a double-grating Öffner stretcher is adopted, as shown in Fig. 10.6.

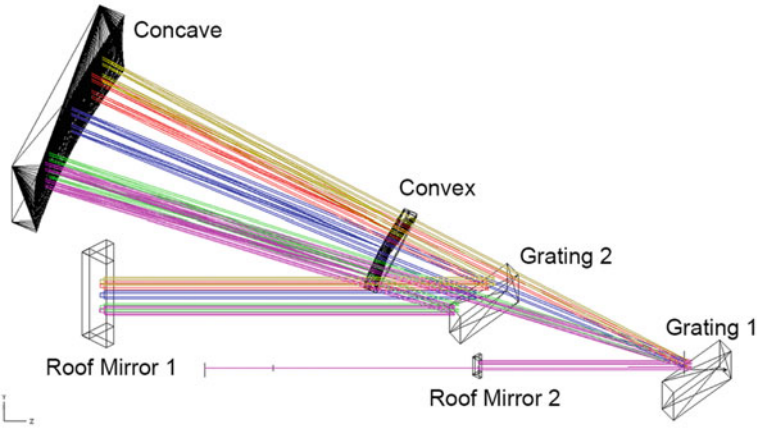

Fig. 10.6 Sketch of the double-grating Öffner stretcher at SULF user facility

Raytracing simulation and experimental study shows that the double-grating stretcher is absolutely aberration-free in both the near-field and far-field when properly aligned [28]. The transmission efficiency of the new stretcher is as high as 40%, which is 1.4 times the previous one.

In SULF 10 PW laser user facility, the grism pair is replaced by an acousto-optic programmable dispersive filter (Fastlite, Dazzler). The Dazzler can compensate for high-order phase distortions and shape the spectrum simultaneously at a higher transmission efficiency (~17%).

10.3.3 1 Hz Pre-amplifiers

In SUFL prototype, the stretcher output pulse was amplified in the regenerative amplifier (FA) with a spectral filter to shape the pulse spectrum and suppress gain narrowing. However, Inserting the spectral filter will increase the FA cavity loss, thus causing degradation of the temporal contrast. Figure 10.7 shows the layout of the new 1 Hz pre-amplifiers system in SULF 10 PW laser user facility. RA are removed from the laser system and all multi-pass amplifications are employed throughout. A Pockels cell (PC) assembly, which consists of two high extinction ratio polarizers and a DKDP PC, is used for pre-pulse suppression and change the pulse repetition rate of the Dazzler output to 1 Hz. The 1 Hz pulses are expanded to 2.5 mm diameter and injected into the first eight-pass amplifier (AMP I), which is pumped at both sides with a total pump energy of 80 mJ and can amplify the pulse energy to 6 mJ. The output pulses from APM I are expanded to 6 mm diameter and then injected into the second six-pass amplifier (AMP II), which is designed to amplify the pulse energy to 70 mJ under pump energy of 260 mJ. A commercial Nd:YAG laser is used to pump both the AMP I and AMP II. The third (AMP III) and fourth (AMP

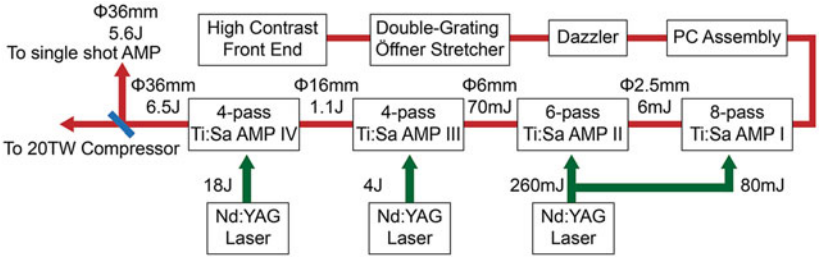

Fig. 10.7 Layout of the 1 Hz pre-amplifiers system

IV) amplifiers are both designed as four-pass configuration and double end pumped by home-built Nd:YAG lasers. The APM II output pulses are expanded to 16 mm diameter, the pulse energy is amplified to 1.1 J in AMP III under 4 J pump energy. Before injected into the AMP IV, the laser beam diameter is further enlarged to 36 mm. Beam homogenizers are applied in AMP IV to obtain a flat-top uniform pump beam profile. The laser pulse is amplified to 6.5 J under 18 J pump energy. The root mean square (RMS) stability of AMP IV output energy is measured to be 1.3% in one hour. The 5.6 J reflected laser pulse by beam splitter (BS) is directed to the single shot, large aperture main amplifiers. The beam profile and wavefront of the BS reflected laser pulse is shown in Fig. 10.8.

10.3.4 Large Aperture Main Amplifiers

To achieve a 10 PW peak power output from the SULF Ti:Sa CPA laser system, crystals with a diameter $\geq$200 mm are necessary for the final amplification stage. when designing such large aperture and high-gain amplifiers, a major challenge is to eliminate or relieve parasitic lasing (PL) effect and amplified spontaneous emission (ASE) [29–31]. PL is due to the formation of a laser cavity through Fresnel reflections at the material interfaces of the gain medium. ASE may place an even stronger restriction in large aperture amplifier, as it definitively increases with increasing pump energy, limiting the maximum stored energy. Flowing an index matching liquid around the crystal cylindrical surface can decrease the Fresnel reflection and increase the parasitic lasing threshold. For Ti:Sa crystals, di-iodomethane derivative (Series M, from Cargille Laboratories) is commonly used as the index matching liquid, which has an index of refraction close to 1.76 (the refractive index of Ti:Sa crystals). However, it is difficult to make sure exact index matching in whole gain bandwidth, as showed in Fig. 10.9. When multi-petawatt pulse output is desired, it is necessary to actively control the transverse gain during the pumping process. One idea is to carefully control the time delay between pump pulses and signal pulse, which is otherwise known as the extraction during pumping (EDP) technique [32]. Figure 10.10 shows the schematic of the EDP technique. In this method, the temporal delay between the

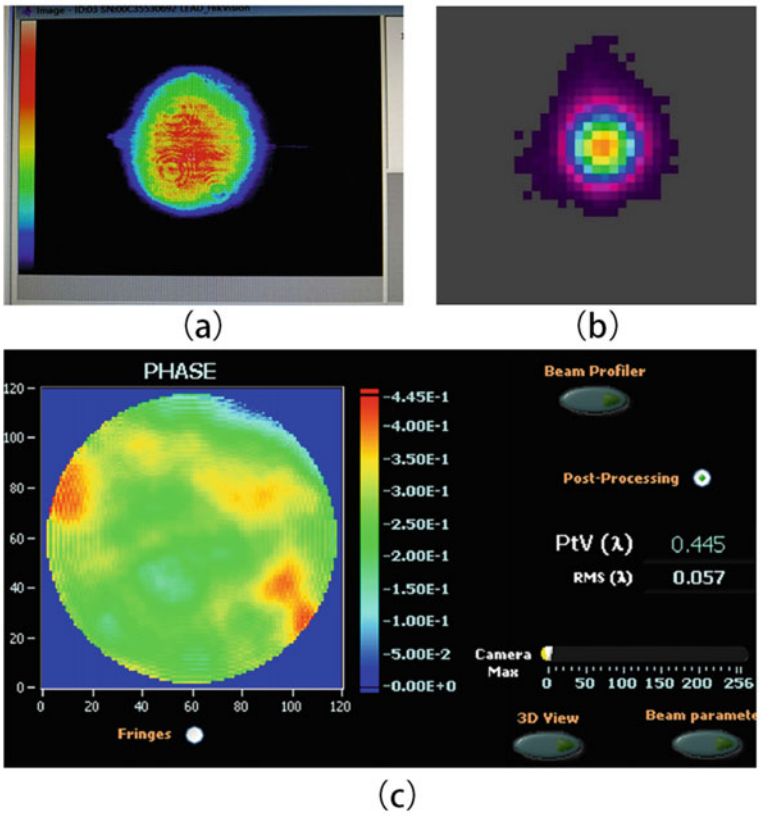

Fig. 10.8 Measured result of the reflected laser pulse by beam splitter **a** Near-field beam intensity profile; **b** Far-field beam intensity profile; **c** The wavefront phase profile

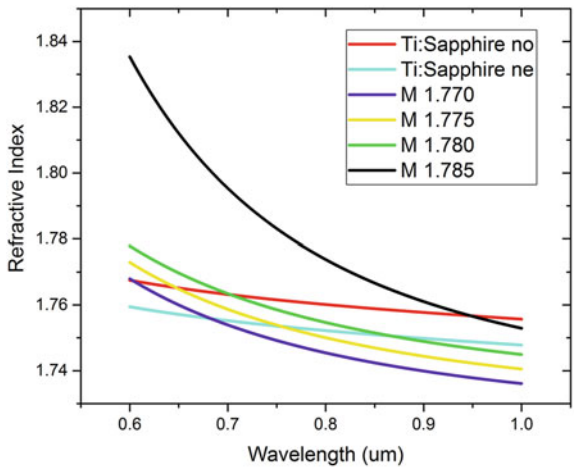

Fig. 10.9 Refractive index with respect to wavelength in different materials

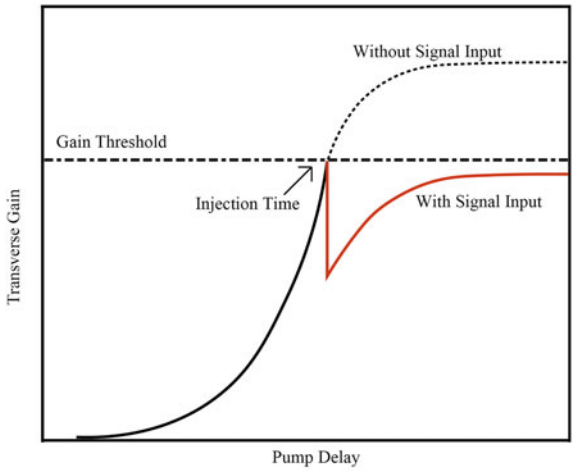

Fig. 10.10 Schematic of the extraction during pumping (EDP) technique

signal pulse and pump pulse is carefully controlled. Only part of the pump energy is stored in the gain medium before the arrival of the input signal. After signal pulse passes through the gain medium, stored energy transfers to the amplified signal pulse and the transverse gain rapidly decreases. The remaining pump pulses keep pumping for the next pass of the amplified signal pulse.

In SULF prototype, we successfully demonstrated 339 J energy output with a homemade 235-mm-diameter Ti:Sa crystal under 620 J pump energy [24]. The pump laser is a home-built frequency doubled Nd:glass disk amplifier which operated at a repetition rate of one shot every two hour. The pump-to-signal conversion efficiency of the final amplifier was only 32.1%. To increase the repetition rate and conversion efficiency of the amplifier, In SULF 10 PW laser user facility, the large aperture Ti:Sa amplifiers as well as their pump lasers are redesigned and upgraded.

Figure 10.11 shows the layout of the large aperture main amplifiers and pump lasers system in SULF 10 PW laser user facility. The 1 Hz pre amplifiers output laser beam is reshaped by a soft edge aperture with a 5 J energy output. The laser

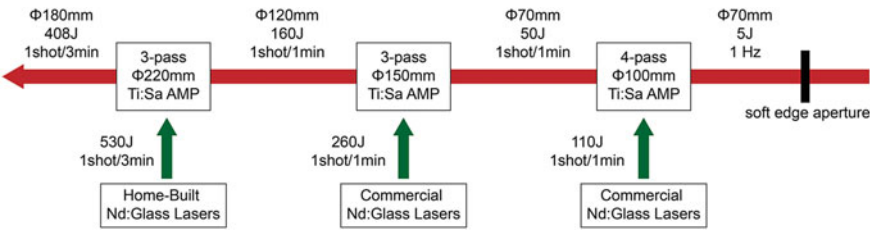

Fig. 10.11 Layout of the larger aperture main amplifiers and pump laser systems in SULF 10 PW laser user facility

beam is then expanded to 70 mm diameter and inject into a four-pass 100-mm-diameter Ti:Sa amplifier (Φ100 mm-AMP). The amplified signal pulse energy is 50 J under a pump energy of 110 J. The signal laser pulse is further expanded to a 120 mm diameter for the next injection into the three-pass 150-mm-diameter Ti:Sa amplifier (Φ150 mm-AMP). Signal pulse energy output of 160 J can be obtained when pump energy is 260 J. Φ100 mm-AMP and Φ150 mm-AMP are pumped by five commercial lasers (ATLAS 100, Thales). An ATLAS 100 laser can deliver two laser pulses with up to 50 J energy @527 nm in each pulse at a repetition rate of 1 shot/min. Prior to the injection into the final three-pass 220-mm-diameter Ti:Sa (GT Advanced Technologies) booster amplifier (Φ220 mm-AMP), the laser beam is enlarged to a diameter of 180 mm. Φ220 mm-AMP is pumped by six home-built high energy frequency-doubled Nd: glass lasers. Each home-built pump laser can deliver pump laser pulses with up to 100 J energy @527 nm at a repetition rate of one shot every three minutes.

To suppress the PL and ASE in Φ220 mm-AMP, a multi-pulse pump scheme is applied [23]. The pump energy absorption before the signal pulse arrival should be relatively large to ensure an adequate gain amplification. However, since the input signal energy is low, after the first-pass amplification, there remains a large degree of inversion population. The pump energy absorption between the first and second passes should refuel the consumed stored energy while avoiding overdriving the gain medium. Since the signal pulse energy increases after the first-pass amplification, a large amount of inversion population can be converted into signal pulse energy in the second-pass. The remaining pump pulses are absorbed by the gain medium to prepare for the third-pass amplification stage.

Figure 10.12 shows the measured output energies of Φ220 mm-AMP, the average output energy is 407.8 J at a pump energy of ~530 J. The RMS stability of the output energy is 0.8% in one and a half hours. The beam profile at the output of Φ220 mm-AMP is shown in Fig. 10.13.

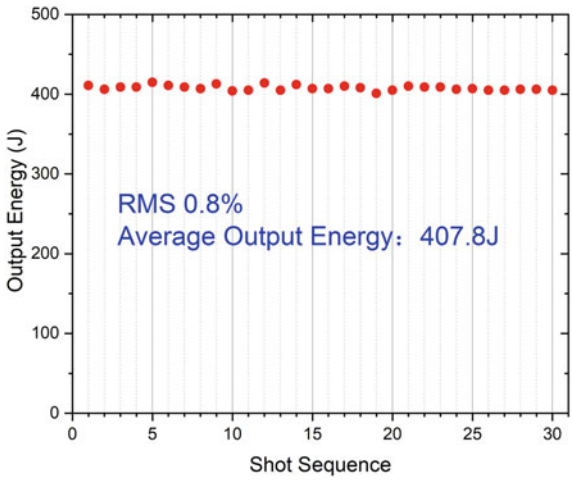

Fig. 10.12 Measured output energies for 530 J pump energy in the final booster amplifier

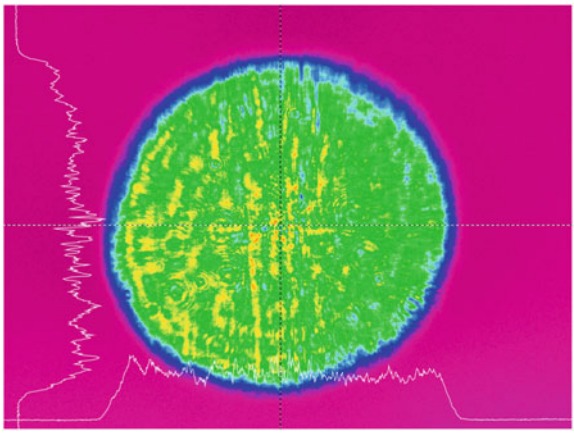

Fig. 10.13 Measured spatial beam profile of the amplified laser beam after the final booster amplifier

10.3.5 Compressor

The output pulses of Φ220 mm-AMP are transported from the ground floor to underground floor where the compressor is installed by a large aperture periscope. An achromatic image relay system is designed and installed to expand the beam size from Φ180 mm to Φ500 mm. The 10 PW compressor consist of four meter-size (575 mm × 1015 mm) gold-coated gratings provided by Horiba, as shown in Fig. 10.14.

We use a commercial measurement device (Fastlite, Wizzler) to measure the characteristics of the recompressed pulse. Meanwhile, a Wizzler–Dazzler feedback loop system is used for dispersion control and optimize the compressed pulse duration.

The final spectrum, spectral phase and reconstructed compressed pulse shape are shown in Fig. 10.15. The FWHM duration of the compressed pulse is measured to be 22.4 fs. The total transport efficiency of the large aperture periscope, the achromatic image relay system and the grating compressor is measured to be 70.52%. The peak power of the final compressed femtosecond laser pulse is estimated to be 12.8PW (compressed pulse energy divided by the compressed pulse width).

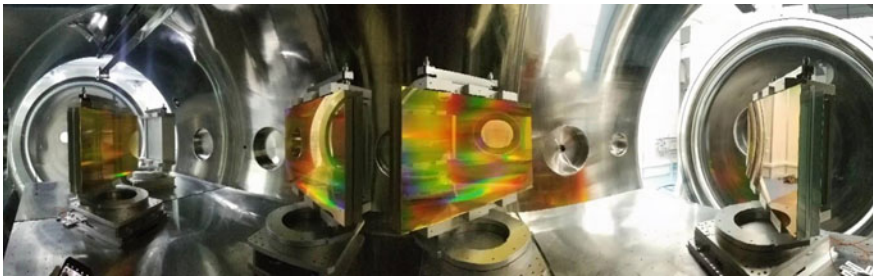

Fig. 10.14 SULF 10 PW grating Compressor

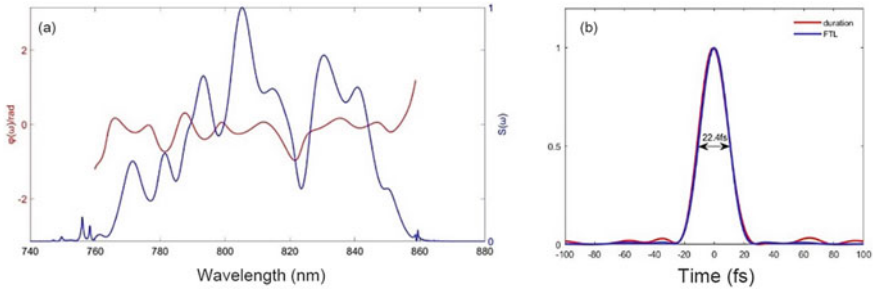

Fig. 10.15 **a** Spectrum and spectral phase of the amplified laser pulse; **b** Reconstructed compressed pulse with a 22.4 FWHM duration

10.3.6 Adaptive Optics and Focusing

Multi PW and even 10 PW lasers are very complex systems. To achieve an ultrahigh focus intensity, it is extremely crucial to correct the wavefront aberrations imposed by a lot of optical components. In the SULF 5 PW laser prototype experiment, we used cascaded double deformable mirrors (DMs) with different actuator densities to optimize the wavefront aberrations [13]. Typically, the first DM with a high spatial resolution compensates for small-scale high-order aberrations, and the second DM with a large stroke corrects large-scale low-order aberrations. In SULF user facility, we use a similar scheme to improve the focusing ability of the 10 PW laser system.

Figure 10.16 shows the layout of adaptive optics systems in the SULF 10 PW laser user facility. The wavefront distortion of the laser pulse is reduced to minimum by carefully controlling the quality of the optical components, the aberration of the beam expanders and the clamping stress of optical assemble. A bimorph DM with a diameter of 130 mm and 64 actuators was inserted after the 150-mm-Ti:Sa multi-pass amplifier, as the first wavefront corrector (DM1), as shown in Fig. 10.17a. The second DM (DM2) is installed after the grating compressor. DM2 has a clear aperture

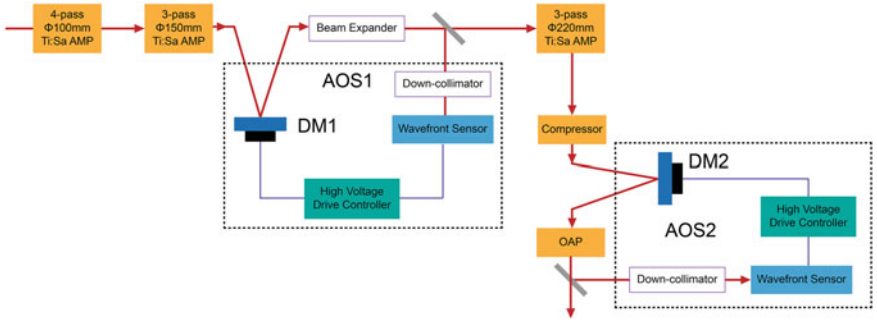

Fig. 10.16 Layout of adaptive optics systems in the SULF 10 PW user facility

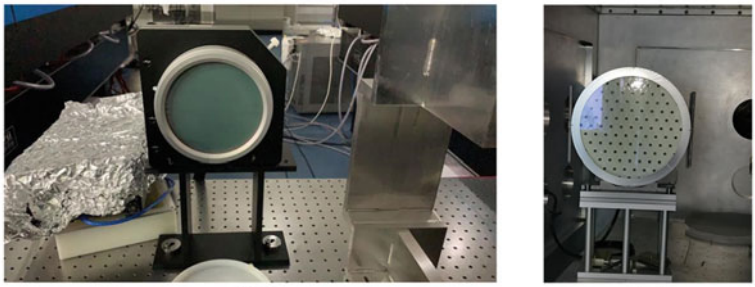

Fig. 10.17 **a** DM with a diameter of 130 mm and 64 actuators; **b** DM with a clear aperture of 500 mm and 121 actuators

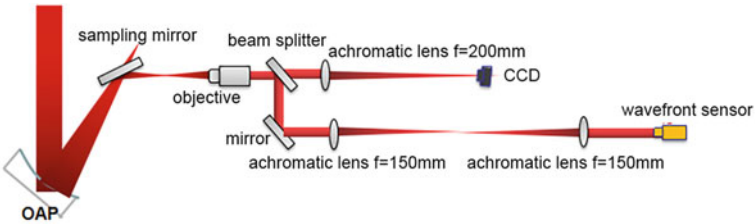

Fig. 10.18 The sampling optical path for wavefront sensor and far-field camera

of 500 mm and 121 actuators, as shown in Fig. 10.17b. After pass through the DM2, laser beam is focused in the target chamber using an f/4 off-axis parabolic mirror (OAP).

The wavefront distortions are compensated by cascaded double DMs in a closed feedback loop with the wavefront sensors. The sampling optical path for diagnostics is shown in Fig. 10.18. The phase profile of the laser beam before and after the correction are presented in Fig. 10.19a, b. There was a decrease in the PV and RMS values of the beam at the measured point from 2.663 um and 0.686 um to 0.261 um and 0.052 um. Far-field profile after the correction confirms the good focus ability of the beam as shown in Fig. 10.19d. The FWHM of the focal spot was 5.5 × 5.5 um^2, which was close to the diffraction limit.

10.4 Conclusion and Outlook

In this chapter, we describe the structure of the SULF user facility and present the latest progress in SULF 10 PW laser system in detail. We improved the design of the SULF 10 PW laser user facility. A new double-grating stretcher and Dazzler are applied to decrease the energy loss of the high-contrast seed pulse. The RA

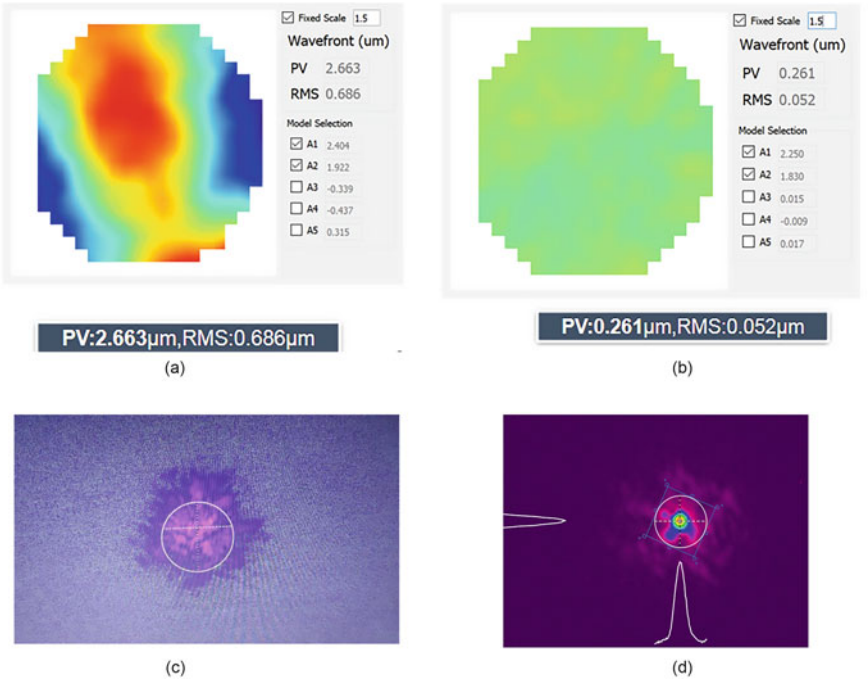

Fig. 10.19 Phase profiles measured after OAP by sampling optical path **a** before and **b** after the correction; **c** and **d** the corresponding focal spots focused by the OAP and obtained by an apochromatic objective lens (10×, Mitutoyo) and low-noise CCD

is replaced by an eight-pass pre-amplifier, which suffers a smaller energy loss and material dispersion and can support a higher temporal contrast during amplification. Large aperture main amplifiers and their pump lasers are redesigned and upgraded to increase the repetition rate to one shot every three minutes. The final Φ220 mm Ti:Sa amplifier output energy is measured to be ~408 J with an RMS stability of 0.8% in one and a half hours. By carefully controlling gain narrowing and high order dispersion, 22.4 fs FWHM duration of the full energy amplified laser pulse is obtained. The total transport efficiency of the large aperture periscope, the achromatic image relay system and the grating compressor is measured to be 70.52%. The peak power of the final compressed femtosecond laser pulse is estimated to be > 10 PW. In addition, good focus ability of the laser beam is confirmed by using cascaded double deformable mirrors with different actuator densities to optimize the wavefront aberrations.

Currently, the home-built Nd: glass pump lasers for the final Ti:Sa amplifier are under upgrade to increase the repetition rate to 1 shot/min. Temporal contrast measurement of the full energy amplified laser pulse is also under research.

References

1. W.T. Wang, W.T. Li, J.S. Liu, Z.J. Zhang, Z.Z. Xu, Phys. Rev. Lett. **117**, (2016)
2. J. Faure, Y. Glinec, A. Pukhov, S. Kiselev, S. Gordienko, E. Lefebvre, J.P. Rousseau, F. Burgy, V. Malka, Nature **431**, 541–544 (2004)
3. C.G.R. Geddes, C. Toth, J. van Tilborg, E. Esarey, C.B. Schroeder, D. Bruhwiler, C. Nieter, J. Cary, W.P. Leemans, Nature **431**, 538–541 (2004)
4. T. Tajima, J.M. Dawson, Phys. Rev. Lett. **43**, 267–270 (1979)
5. C. Yu, R. Qi, W. Wang, J. Liu, W. Li, C. Wang, Z. Zhang, J. Liu, Z. Qin, M. Fang, Sci. Rep. **6**, 29518 (2016)
6. S. Corde, K.T. Phuoc, G. Lambert, R. Fitour, V. Malka, A. Rousse, A. Beck, E. Lefebvre, Rev. Mod. Phys. **85**, 1–48 (2013)
7. M. Fuchs, R. Weingartner, A. Popp, Z. Major, S. Becker, J. Osterhoff, I. Cortrie, B. Zeitler, R. Hoerlein, G.D. Tsakiris, U. Schramm, T.P. Rowlands-Rees, S.M. Hooker, D. Habs, F. Krausz, S. Karsch, F. Gruener, Nat. Phys. **5**, 826–829 (2009)
8. S. Kneip, C. McGuffey, J.L. Martins, S.F. Martins, C. Bellei, V. Chvykov, F. Dollar, R. Fonseca, C. Huntington, G. Kalintchenko, A. Maksimchuk, S.P.D. Mangles, T. Matsuoka, S.R. Nagel, C.A.J. Palmer, J. Schreiber, K.T. Phuoc, A.G.R. Thomas, V. Yanovsky, L.O. Silva, K. Krushelnick, Z. Najmudin, Nat. Phys. **6**, 980–983 (2010)
9. D. Umstadter, Phys. Plasmas **8**, 1774 (2001)
10. S.P.D. Mangles, C.D. Murphy, Z. Najmudin, A.G.R. Thomas, J.L. Collier, A.E. Dangor, E.J. Divall, P.S. Foster, J.G. Gallacher, C.J. Hooker, D.A. Jaroszynski, A.J. Langley, W.B. Mori, P.A. Norreys, F.S. Tsung, R. Viskup, B.R. Walton, K. Krushelnick, Nature **431**, 535–538 (2004)
11. Y.I. Salamin, S.X. Hu, K.Z. Hatsagortsyan, C.H. Keitel, Phys. Rep.-Rev. Sect. Phys. Lett. **427**, 41–155 (2006)
12. D. Umstadter, J. Phys. D-Appl. Phys. **36**, R151–R165 (2003)
13. Z. Guo, L. Yu, J. Wang, C. Wang, Y. Liu, Z. Gan, W. Li, Y. Leng, X. Liang, R. Li, Opt. Express **26**, 26776–26786 (2018)
14. J.W. Yoon, C. Jeon, J. Shin, S.K. Lee, H.W. Lee, I.W. Choi, H.T. Kim, J.H. Sung, C.H. Nam, Opt. Express **27**, 20412–20420 (2019)
15. D. Strickland, G. Mourou, Opt. Commun. **55**, 447–449 (1985)
16. A. Dubietis, G. Jonusauskas, A. Piskarskas, Opt. Commun. **88**, 437–440 (1992)
17. C.N. Danson, C. Haefner, J. Bromage, T. Butcher, J.-C.F. Chanteloup, E.A. Chowdhury, A. Galvanauskas, L.A. Gizzi, J. Hein, D.I. Hillier, N.W. Hopps, Y. Kato, E.A. Khazanov, R. Kodama, G. Korn, R. Li, Y. Li, J. Limpert, J. Ma, C.H. Nam, D. Neely, D. Papadopoulos, R.R. Penman, L. Qian, J.J. Rocca, A.A. Shaykin, C.W. Siders, C. Spindloe, S. Szatmari, R.M.G.M. Trines, J. Zhu, P. Zhu, J.D. Zuegel, High Power Laser Sci. Eng. **7** (2019)
18. C. Danson, D. Hillier, N. Hopps, D. Neely, High Power Laser Sci. Eng. **3** (2015)
19. V.V. Lozhkarev, S.G. Garanin, R.R. Gerke, V.N. Ginzburg, E.V. Katin, A.V. Kirsanov, G.A. Luchinin, A.N. Mal'shakov, M.A. Mart'yanov, O.V. Palashov, A.K. Poteomkin, N.N. Rukavishnikov, A.M. Sergeev, S.A. Sukharev, G.I. Freidman, E.A. Khazanov, A.V. Charukhchev, A.A. Shaikin, I.V. Yakovlev, JETP Lett. **82**, 178–180 (2005)
20. V.V. Lozhkarev, G.I. Freidman, V.N. Ginzburg, E.V. Katin, E.A. Khazanov, A.V. Kirsanov, G.A. Luchinin, A.N. Mal'shakov, M.A. Martyanov, O.V. Palashov, A.K. Poteomkin, A.M. Sergeev, A.A. Shaykin, I.V. Yakovlev, S.G. Garanin, S.A. Sukharev, N.N. Rukavishnikov, A.V. Charukhchev, R.R. Gerke, V.E. Yashin, Opt. Express **14**, 446–454 (2006)
21. D. N. Papadopoulos, J. P. Zou, C. Le Blanc, G. Cheriaux, P. Georges, F. Druon, G. Mennerat, P. Ramirez, L. Martin, A. Freneaux, A. Beluze, N. Lebas, P. Monot, F. Mathieu, P. Audebert, High Power Laser Sci. Eng. **4** (2016)
22. F. Lureau, S. Laux, O. Casagrande, O. Chalus, A. Pellegrina, G. Matras, C. Radier, G. Rey, S. Ricaud, S. Herriot, P. Jongla, M. Charbonneau, P.A. Duvochelle, C. Simon-Boisson, Latest results of 10 petawatt laser beamline for eli nuclear physics infrastructure, in *Solid state lasers xxv: Technology and devices*, ed. by W.A. Clarkson, R.K. Shori (2016)

23. Z. Gan, L. Yu, S. Li, C. Wang, X. Liang, Y. Liu, W. Li, Z. Guo, Z. Fan, X. Yuan, L. Xu, Z. Liu, Y. Xu, J. Lu, H. Lu, D. Yin, Y. Leng, R. Li, Z. Xu, Opt. Express **25**, 5169–5178 (2017)
24. W. Li, Z. Gan, L. Yu, C. Wang, Y. Liu, Z. Guo, L. Xu, M. Xu, Y. Hang, Y. Xu, J. Wang, P. Huang, H. Cao, B. Yao, X. Zhang, L. Chen, Y. Tang, S. Li, X. Liu, S. Li, M. He, D. Yin, X. Liang, Y. Leng, R. Li, Z. Xu, Opt. Lett. **43**, 5681–5684 (2018)
25. L. Yu, Y. Xu, Y. Liu, Y. Li, S. Li, Z. Liu, W. Li, F. Wu, X. Yang, Y. Yang, C. Wang, X. Lu, Y. Leng, R. Li, Z. Xu, Opt. Express **26**, 2625–2633 (2018)
26. L. Yu, Y. Xu, S. Li, Y. Liu, J. Hu, F. Wu, X. Yang, Z. Zhang, Y. Wu, P. Bai, X. Wang, X. Lu, Y. Leng, R. Li, Z. Xu, Opt. Express **27**, 8683–8695 (2019)
27. S. Li, C. Wang, Y. Liu, Y. Xu, Y. Li, X. Liu, Z. Gan, L. Yu, X. Liang, Y. Leng, R. Li, Opt. Express **25**, 17488–17498 (2017)
28. X. Liu, C. Wang, X. Wang, X. Lu, R. Li, Optics **1**, 191–201 (2020)
29. X. Liang, Y. Leng, C. Wang, C. Li, L. Lin, B. Zhao, Y. Jiang, X. Lu, M. Hu, C. Zhang, H. Lu, D. Yin, Y. Jiang, X. Lu, H. Wei, J. Zhu, R. Li, Z. Xu, Opt. Express **15**, 15335–15341 (2007)
30. F.G. Patterson, J. Bonlie, D. Price, B. White, Opt. Lett. **24**, 963–965 (1999)
31. V. Chvykov, J. Nees, K. Krushelnick **312**, 216–221 (2014)
32. V. Chvykov, K. Krushelnick, Opt. Commun. **285**, 2134–2136 (2012)

Index

K. Yamanouchi et al. (eds.), *Progress in Ultrafast Intense Laser Science XVI*, Topics in Applied Physics 141, https://doi.org/10.1007/978-3-030-75089-3